PHD

Enhanced impact resistance and pseudo plastic behaviour in composite structures through 3D twisted helical arrangement of fibres and design of a novel chipless sensor for damage detection

Iervolino, Onorio

Award date:
2017

Awarding institution:
University of Bath

Enhanced impact resistance and pseudo plastic behaviour in composite structures through 3D twisted helical arrangement of fibres and design of a novel chipless sensor for damage detection.

Onorio Iervolino

A thesis submitted for the degree of Doctor of Philosophy

University of Bath

Material Research Centre

Department of Mechanical Engineering

March 2017

“Today is only one day in all the days that will ever be. But what will happen in all the other days that ever come can depend on what you do today.”

(Ernest Hemingway)

Abstract

The future of the aerospace industry in large part relies on two factors: (i) development of advanced damage tolerant materials and (ii) development of advanced smart sensors with the ability to detect and evaluate defects at very early stages of component service life. Laminated composite materials, such as carbon fibre reinforced plastics (CFRP), have emerged as the materials of choice for increasing the performance and reducing the cost and weight of aircrafts, which leads to less fuel consumption and therefore lower CO_2 emissions. However, it is well known that these materials exhibit fragile behaviour, poor resistance to impact damage caused by foreign objects and require a relatively slow and labour intensive manufacturing process. These factors prevent the rapid expansion of composite materials in several industrial sectors at the current time.

Inspired by the use of rope throughout history and driven by the necessity of creating a lean manufacturing process for composites and enhancing their impact properties, the first part of this work has shown that enhanced damage tolerance and pseudo-ductile behaviour can be achieved with standard CFRP by creatively arranging the fibres into a 3D twisted helical configuration. Through an extensive experimental campaign a new method to arrange fibre reinforcement was presented and its effect investigated.

The second part of this PhD work focused on developing a new smart sensor. A spiral passive electromagnetic sensor (SPES) for damage detection on CFRP and glass fibre reinforced plastics (GFRP) is presented in this work. A range of defect types in glass and carbon composite has been considered, such as delamination, perforated holes and cracks. Furthermore, throughout this work, the SPES has been exploited as a multi-sensing device allowing the ability to detect temperature and humidity variation, presence of ice and act as an anti/de-icing device.

Acknowledgments

First and foremost, I would like to express my sincere gratitude to my supervisor Professor Michele Meo for his enthusiasm, guidance, and unrelenting support throughout my PhD course. He has taught me what it means to be a scientist during my time at Bath. Michele has always looked to challenge me during our time together, pushing me beyond what I thought my limits were. I really appreciate his contributions of time and ideas. He has been an amazing role model and mentor, and I truly hope that our collaborations will continue for many years. I still have much to learn from him and aspire to one day be a scholar of Michele's calibre. The work presented herein has been performed as part of ALAMSA project supported and funded by the European Union (EU) in the 7th framework programme (FP7) for research and technological development. My work was also supported by DIVERSUS TECHNOLOGY LTD.

I am truly grateful toward all my office mates which made the PhD enjoyable to work on by providing many distractions, many coffees, and for their invaluable advices and for their contribution with their expertise and work to the realisation of this research. Whilst it is not possible to name everyone, I would especially like to thank in particular: Francesco Ciampa, Daniele Benito Callà, Fabrizio Bucciarelli, Salvatore Boccardi, Mariuele De Simone, Gian Piero Malfense Fierro, Francesco Nicassio, Gennaro Scarselli, Dmitri Ginzburg, Francesco Rizzo and Simon Pickering. A distinctive thank goes to Fulvio Pinto for the countless useful discussions; for being a perfect travel companion for all conferences and meeting with companies. His expertise on impact tests and his help with the experimental campaign provided in Chapter 4 has been essential.

I would like to extend my deepest thanks to my parents for giving me the opportunity of dedicating my-self to my education along a path that started long before this achievement. Thank you for letting me arrive where I managed to get today. A special thanks goes to my sister Elina, that although she lives on the other side of the globe she always finds the time to listen to my problems or for just having a chat.

Last, but not least, I would like to especially thank my wife Nunzia who has always believed in me and for her constant support and unconditional encouragement throughout all these years. Through all these years, I had to face my hard-times but I always found in her and with her the strength to overcome those moments. Words cannot express my gratitude for everything she has done. Thanks for accompanying me on this adventure, I look forward to our next one!

List of Abbreviations

ACTP	Advance Composite Technology Program
ASK	Amplitude Shift Keying
ASTM	American Society of Testing and Materials
BSI	British Standards Institute
BVID	Barely Visible Impact Damage
CAI	Compression After Impact
CAT	Computerized Axial Tomography
CFRP	Carbon Fibre Reinforced Plastic
CNTs	Carbon nanotubes
CT	Computer Tomography
EM	Electromagnetic
FRP	Fibre Reinforced Polymer or Plastic
GFRP	Glass Fibre Reinforced Plastic
HP-PE	high performance polyethylene
IDT	Interdigital Transducer
LC	Inductor-Capacitor
LVI	Low Velocity Impact
NVD	Non Visible Damage
PCB	Printed Circuit Board
RFID	Radio Frequency IDentification
SAW	Surface Acoustic Wave
SHM	Structural Health Monitoring
SMA	Shape Memory Alloys

SPES	Spiral Passive Electromagnetic Sensor
TF	Traditional Fabrics
TPB	Three Points Bending
UAZ	Ultrasonic Assisted Z-fibre
UD	Unidirectional
3DF	3D helicoidal Fabrics

Table of Figures

Table of Contents

1 Introduction

1.1 Background and Motivation

Owing to their high specific strength (strength to mass ratio), laminated composite materials, especially fibre reinforced polymer or plastic (FRP), have been increasingly contributing to the effort to advance the renewable energy enabling development of commercially viable aircraft that leave a smaller carbon footprint. Composite materials may not only improve the weight of the structure, but they will offer design flexibility, corrosion resistance, dimensional stability (composites retain their shape and size when they are hot or cool, wet or dry) and part consolidation as well. In the aerospace industry, the use of carbon fibre reinforced plastic (CFRP) has been instrumental in reducing overall weight (and hence fuel burn savings), reducing lifecycle cost and environmental impact. Aerospace is just one of the many market segments that will see a large increase in the use of these materials. Since the late 1980s, Airbus has increased the use of CFRP, going from 5% for the A310-300 with a composite fin box, up to over 50% for the A350 [1]. The ability of composites to mould complex shapes allows greater potential for consolidating the number of individual components in an assembly and structurally offers the advantage of inherent stability and buckling resistance. This leads to an extended use of FRP for aircraft components, being used for secondary structural components (e.g. fairings, landing gear doors, interior panels etc.) and in the last few years also for critical primary structural components (e.g. outer wing, fuselage, spars) as shown in Figure 1.

Figure 1 Airbus A350XWB materials used by weight; reproduced from [1].

However, the use of composite in the aerospace industry has not reached its full potential yet. In the aerospace industry, following the damage tolerant philosophy, structures made of metal alloys have a safety factor not exceeding 1.5, whereas components made of laminated composite materials require a factor of 2.0 [2]. This means that composite components are intentionally designed in a rather conservative manner in order to account for uncertainties associated with their behaviour during a considerably long and cyclic life of an aircraft. This is primarily because the behaviour of metals is very well understood and practically tested, while even with the extensive research effort over the past decades the same cannot be stated about composites. As part of the effort to overcome these issues, a great part of this thesis focuses on studying an innovative method of arranging fibre reinforcement within the composite material that will allow to produce lighter structure and reduce the safety factors for composite structure. Indeed, the presented invention enhances the impact resistance and gives a pseudo plastic behaviour to the final product.

1.1.1 Composite Materials and Damage Tolerance

Advanced carbon-fibre-reinforced composites offer several distinct advantages over more conventional materials such as their increased stiffness to weight ratio, superior corrosion resistance, and improved fatigue properties. These advantages combined with greater design options make composites one of the most used and promising materials for a wide variety of applications, especially in the aerospace and aeronautical industries. As time progresses, these lighter weight, incredibly strong materials will dominate the materials used in almost any given industry.

Conventional composite materials do, however, suffer some serious limitations. The most significant among these is the sensitivity to mechanical damage from relatively low velocity localized impact loads [3-7] such as that imparted by a dropped tool or runway debris. Indeed, while metal structure can absorb impact energy by deforming plastically (in irreversible or permanent manner), and can be typically detected visually as dents in the structure, laminated composite materials usually absorb impact energy through the formation of internal damage. Such internal damage may be considerably significant and detrimental to structural integrity and yet be undetectable by visual inspection. This internal damage can cause severe reductions in strength and can grow under load. This phenomenon constitutes a class of damage known as Barely Visible Impact Damage (BVID) which requires a use of specialised SHM techniques called Nondestructive Testing (NDT[1]) and Nondestructive Evaluation (NDE[2]) which enables appropriate detection and evaluation of such damage. Delamination is one of the most likely and common types of failure mode in laminated composites due to their weak inter-laminar strength. It is probably the most serious problem, given the difficulty of its visual detection and the extent to which it leads to the degradation of mechanical properties and can cause the failure of the overall composite component and thus limit the life of the structure. It is not straightforward to get good mechanical properties in the out-of-plane direction with conventional designs of fibre reinforced composites. Simple reinforcements may take the form of unidirectional fibres or bidirectional/ fabric layers, in the latter case for example as a woven or unwoven mat. To achieve in-plane quasi isotropic properties plies are stacked together with different orientation. Although these layer reinforcements typically produce greater tensile, compressive and shear strength in the x, y plane; they offer limited stiffness and strength in the z-direction. The properties along the z-direction are mainly governed by the matrix, generally the weaker material in conventional composite structures. Such multiple layer structures are likely to display anisotropic structural properties with relatively poor strength in the z-direction.

Current weaknesses of laminated composite are the lack of strength and stiffness in the z-direction. As consequence, under normal or impact loading, multilayer reinforced composite materials suffer from delamination leading to catastrophic failures. One way to overcome this is to create 3-dimensional composites with quasi-isotropic strength and stiffness in all three directions. Current methodologies adopted for the manufacturing of 3D composites are typically complex, lengthy, expensive, and can lead to a more complex fabrication procedure requiring multiple stages of manufacture and can introduce mechanical stress within the structure and reduce the in-plane properties. Therefore, it is generally desirable to create a fibre-reinforced composite body with a three-dimensional reinforcement that exhibits reduced tendency to delamination as well as to produce more consistent properties in all three dimensions in a fibre-reinforced composite using a lean manufacturing process. Therefore, a major part of this thesis was dedicated to developing and testing the new 3D twisted helical arrangement of fibres which offer the possibility to claim all aspects mentioned previously.

---

[1] Nondestructive testing can be synonymously referred to as nondestructive inspection or examination.

[2] Some authors make a distinction between the abbreviations NDT and NDE, in that NDT is merely a technique used for flaw detection, whereas NDE refers to a more quantitative analysis aimed at determining the size, orientation and sometimes consequences of such defects. In the context of this thesis, no real difference is implied and the terms NDT and NDE are often used interchangeably.

1.1.2 Structural health monitoring for composite structures

Composite structures need to be inspected to check their structural integrity in order to be used more extensively in load bearing structures (e.g. aircraft). Continuous and real time monitoring can increase significantly operational safety. Structural Health Monitoring (SHM) aims to provide information on the current state of structures giving a diagnosis of the “state” of the structure. As mentioned by Balageas [8] it is possible to consider Structural Health Monitoring as a new and improved way to make Non Destructive Evaluation, in which more factors have to be taken into account such as: data transmission, computational power, integration of sensors, possibly use of smart materials and much more. A real-time knowledge of the impact location source and the severity of the damage are fundamental in both Non Destructive Evaluation (NDE) techniques as well as Structural Health Monitoring (SHM) systems.

With the increased number of sensors for SHM, and the relatively high cost associated with the installation of wired sensors [9, 10], wireless sensors have become a promising solution to overcome high cost and design issues. Furthermore, with the steady increase of the use of composite materials in the aerospace industry, much attention has been devoted to smart material structures with embedded sensors, with the functionality to provide an early warning of the damage occurrence, particularly with respect to the known composite problems of Non-Visible Damage / Barely Visible Impact Damage (NVD/BVID), resulting in efficient systems and in safer structures [11-14]. Smart sensors have the potential to change fundamentally the way aerospace infrastructure are inspected, monitored, and maintained.

Smart-Sensors for aerospace applications typically should withstand harsh environment, with extreme temperatures ranging from cryogenic to very high temperature. Hence, production of a Smart-Sensor, which can be flexibly tailored to meet broad requirements and can be integrated into hazardous environment, is required. Operational considerations such as the sensor operating temperature, capability to withstand changes in the sensor environment, and battery life have strong roles to play in the sensor design, and then in the type of sensor to adopt. Furthermore, small sensor dimensions, low costs and a non-contact measurement system for data retrieval are very often required. This leads to designing and investigating a new Passive Wireless Sensor, which does not require battery source, could operate in harsh environment and could monitor the structure wireless being embedded in the structure or being attached on the surface. The SPES sensor presented cover all these features. Moreover, the sensor, offers the functionality to monitor the structural health status as well as other critical parameters, such as temperatures, pressures, flows and vibration levels to ensure they are within known tolerances and to highlight when they are not. Furthermore, the SPES device can act as anti/de-icing device and can work as a continuous network layer of sensors (skin layer) that with the proper design could provide a protection from strike or corrosion.

1.2 Objectives

The objectives for this PhD work can be broadly outlined in a twofold manner:

1. Review the currently available methods adopted to enhance impact properties for composite structures. Present an innovative method to arrange fibre reinforcement for composite that brings pseudo-ductile behaviour as well as higher impact resistance with respect to traditional composite. Furthermore, the presented material leads to a lean manufacturing process and to quasi-isotropic properties without the need for a specific lamination sequence. Subsequently, the presented composite has been compared with traditional composites manufactured with conventional manufacturing process and their properties and behaviour have been studied through a range of experimental studies.
2. Review the passive wireless sensor adopted mainly for the aerospace sector. Develop a new chipless wireless sensor with the ability to perform multiple functions, such as detection of temperature and humidity variation, presence of ice, focusing more on detection of cracks, BVID and delamination in both glass and fibre composite laminated. Moreover, the SPES has been tested as an anti/de-icing device.

1.3 Approach

The twofold objective of this work means that two literature reviews, one for each topic, were required. However, it will be shown that the concepts introduced in one are relevant in the other and vice versa. The first half of the thesis focused on studying the effect of the innovative helical arrangement of fibres on the final properties of the composite, while the second part aimed at developing and designing a new passive smart sensor for structural health monitoring.

Furthermore, this work mainly considers carbon fibre as primary materials of investigation, although, the presented invention can be generally applied to any type of fibre. It is also important to make a note regarding the final application for which the thesis is addressed. Although the innovative fibre reinforcement and the SPES sensor are both presented to be used for the aerospace sector, it must be highlighted that their use can be extended to other fields, such as: automotive, defence, maritime, etc.

The outline of the thesis followed by the original publications is provided next.

1.4 Thesis Outline

Chapter 2 reviews the literature in the field of strategies to increase damage resistance in composites, putting more emphasis in the review of textile structural preform. A second literature review on the passive sensor used in SHM is reported.

Chapter 3 starts with an historical overview on the use of the Rope throughout human history, followed by the illustration of the main concept of the innovative 3D helical arrangement of fibres. Subsequently, the experimental studies involving the manufacturing of rope and cordage and the relative experimental campaign are provided.

Chapter 4 illustrates the use of the 3D helical arrangement of fibre for the manufacturing of rod and plate. An extensive experimental campaign is presented for both structures.

Chapter 5 presents the design, fabrication and testing of the SPES device for an *in-situ* impact detection monitoring system able to identify in real-time the presence of flaws in the structures. The ability of the SPES has been exploited as a multi-sensing device as well as an anti/de-icing device.

Chapter 6 summarises the work carried out and provides suggestions for future work.

1.5 Publications

Meo, M. Pinto, F. Iervolino, O., Fibre Ropes and Composite Materials Containing Fibre Ropes, *Patent pending*

Iervolino, O., & Meo, M., Crack detection, smart sensing and de-icing using a spiral passive electromagnetic sensor (SPES), *Manuscript in preparation*.

Pinto, F., **Iervolino, O.,** Ginzburg, D., Scarselli, G., Meo, M. Helicoidal Composite for enhancement of impact properties and energy absorption, *Manuscript in preparation*.

Scarselli, G., Nicassio, F., Pinto, F., Ciampa, F., **Iervolino, O**., & Meo, M., An enhanced bistable composite power harvesting system, *Manuscript submitted*.

Ginzburg, D., Pinto, F., **Iervolino, O.,** & Meo, M. (2017). Damage tolerance of bio-inspired helicoidal composites under low velocity impact. *Composite Structures*, *161*, 187-203.

Iervolino, O., & Meo, M. (2016, April). Spiral Passive Electromagnetic Sensor (SPES) for composite structural changes in aircraft structures. In *SPIE Smart Structures and Materials+ Nondestructive Evaluation and Health Monitoring* (pp. 979935-979935). International Society for Optics and Photonics.

Scarselli, G., Nicassio, F., Pinto, F., Ciampa, F., **Iervolino, O**., & Meo, M. (2016). A novel bistable energy harvesting concept. *Smart Materials and Structures*, *25*(5), 055001.

Iervolino, O., & Meo, M. (2016). A spiral passive electromagnetic sensor (SPES) for wireless and wired structural health monitoring. *Measurement Science and Technology*, *27*(4), 045601.

Pinto, F., **Iervolino, O.,** Scarselli, G., Ginzburg, D., & Meo, M. (2016, April). Bioinspired twisted composites based on Bouligand structures. In *SPIE Smart Structures and Materials+ Nondestructive Evaluation and Health Monitoring* (pp. 97970E-97970E). International Society for Optics and Photonics.

Iervolino, O., & Meo, M. (2015, April). Spiral passive electromagnetic sensor (SPES) for smart sensing and de-icing. In *SPIE Smart Structures and Materials+ Nondestructive Evaluation and Health Monitoring* (pp. 943528-943528). International Society for Optics and Photonics.

Iervolino, O., Jenks, C. H., & Meo, M. (2014, April). Design, fabrication, and validation of passive wireless resonant sensors for NDT/SHM. In *SPIE Smart Structures and Materials+*

Nondestructive Evaluation and Health Monitoring (pp. 90631K-90631K). International Society for Optics and Photonics.

Iervolino, O., Pinto, F., Ingram, M., Mattia, D., & Meo, M. (2013). CNT Coating for Multiscale Carbon Fibre Composites. *Composite Science and Technology*.

2 Literature Review

2.1 Composite Materials: Past and Future

Composite materials have played an important role as part of man's technology. Apart from natural composites, like wood, people invented many multi-component materials even in ancient times, like the first ancient builders who used straw to reinforce mud bricks. Another use of composite materials was used by the ancient Mesopotamians around 3400 B.C. when they glued wood strips at different angles to create plywood. The final product gives better properties than natural wood. The Mongols, in around 1200 AD, made composite bows that were smaller, more powerful and significantly more accurate than their rivals. The bows were made from a combination of cattle tendons, bamboo, horn, wood, bone and silk bonded with natural pine resin. The Mongolian bow was so advanced that it became the most feared weapon on earth until the invention of gunpowder in the 14th century.

The modern era of advanced composites, as we know it, did not begin until the 20th century. The year 1907 heralded a new era for the composites with the chemist Baekeland and his creation of the first synthetic thermosetting resin (Bakelite) [15]. Until then, only natural resins derived from plants and animals were used. Another important step in the history of composites, was the invention of the glass fibres. In 1935, Owen Corning developed a process for drawing glass into thin strands/fibres and began weaving them into a textile fabric [16, 17]. This was the beginning of the Fibre Reinforced Polymers (FRP) industry as we know it today. Since then, Fibre-reinforced composites have played a very important role in engineering and they have found a tremendous growth in industrial applications due to their outstanding mechanical properties, flexibility in design capabilities and ease of fabrication. Due to their outstanding properties, composites have found many structural applications including aerospace, automotive, medical and construction components, sporting goods, and marine structures.

Although FRPs offer many advantages over conventional materials, they also have some disadvantages. One of the main drawbacks of composites is that their through-thickness properties are limited by the relatively poor properties of the matrix resin and the weak fibre-matrix interfacial bond. While composites have already proven their worth as weight-saving materials, in order to offer better choice over monolithic metallic structures possessing isotropic properties, the current challenge is to make them cost effective, improve their through-thickness properties and prevent or predict their fragile behaviour.

2.1.1 Impact on Composites Structure

Advanced composite materials are generally characterized by high strength fibres bound together by matrices which are generally laminated with fibres oriented in alternating directions to give the material strength and stiffness. Indeed, fibres are the primary load carrying elements of the composite materials and can be used in various forms, including tows, yarns, rovings, chopped strands, and woven fabric mats. According to the fibre architecture, composite materials can be divided in 2D, if obtained by stacking a number of unidirectional lamina; or 3D, if the fibrous reinforcements are arranged in order to create complex structure and/or to exhibit out-of-plane mechanical properties. High-strength fibres used in advanced composites include typically carbon, glass and aramid, as well as new fibres like boron, quartz, basalt, and ceramic. Generally, properties which are matrix dependent are much weaker than those which are governed by the fibre. Nevertheless, the role of the matrix plays a crucial role, transferring any applied load to the fibres, keeping the reinforcement in their position and chosen orientation, as well as protecting the fibres. Moreover, the type of matrices determines the maximum service temperature and in some cases, can influence the failure mode of the composite by providing alternative paths for crack growth.

Although composites are extensively used in several applications, a major concern that limits the use of composites is the effect of external impacts. Indeed, it is well known that composite structures in the form of laminates are extremely susceptible to crack initiation and propagation along the laminar interfaces in various failure modes. A constant warning is the effect of impacts on composites, because significant damage can occur and yet be undetectable by visual inspection. Moreover, if the material fails it can be catastrophic and happen with little warning. One of the most prevalent life-limiting crack growth modes in laminate composites is delamination, and may be introduced by external loading as in static bending, compression or tension, in cyclic fatigue or by impacts of low-to-high energies, during manufacturing or in service [18].

In the aerospace industry, impact loading during service is a common phenomenon (tool drops, bird strikes, runway debris, etc.) and the residual compressive strength of an impact damaged composite is one of the main design limiting factors [19]. In recent years many research programs have been undertaken in an attempt to better understand the impact response of these materials and to produce an impact resistant structure [20] [3, 4, 7] [6]. In the past decades different methodologies and techniques have been developed to improve resistance to the delamination. Delamination is mainly caused by inter laminar stresses and low through thickness debonding resistance. Commonly methods to increase through-thickness properties involve the manufacturing of three dimensional fibre architectures obtained by embroidery [21] , braiding [22], through cross stitching or stapling [4, 5, 23, 24], or by 3D woven fabric using specific and expensive 3D looms [21, 25].

Another drawback of composite materials compared with metal is the lack of plastic deformation. The result is that energy is frequently absorbed through damage mechanisms and in elastic deformation, but not via plastic deformation [3].Thus, impact on composites usually generates large areas of fracture, ensuing reduction in both strength and stiffness. The lack of plastic deformation in composites means that once a certain stress level is exceeded, the structure can fail in a wide variety of modes, and these severely reduce the structural integrity of the component. Furthermore, since damaged composite structures present generally more complex damaged areas than metals the prediction of the post-impact behaviour is generally complex in nature and consequently very difficult to characterize.

In the past year different attempts have been made in order to apply ductile characteristics to composites (pseudo-ductility). The basic strategy to achieve this properties is the incorporation of new ductile matrices and/or fibres. Another approach is creating hybrid structures by introducing thin carbon plies in the laminates, or using fibres with different magnitude of elongations at failure. [26-29].

In conclusion, impacts on composites can cause significant damage that can induce severe reductions in strength of the structures and the damage can grow under load and be undetected for long periods until catastrophic failure happens. These are a major issue in the composite design especially for airworthiness certification [30, 31]. Therefore, there is a need to create damage resistant and damage tolerant structure and at the same time to detect impact damage and any effect correlated to it. Major incidents and catastrophic failure can be prevented with continuous structure health monitoring on the structure and by improving material properties. Different techniques on how to improve damage resistance and on wireless sensor used for SHM are explained briefly in this section highlighting their main advantages and limitation.

2.2 Strategies to increase damage resistance in composites

The aim of this section is to provide an overview on the different methods adopted to improve damage resistance and damage tolerance in composites. The intention of these techniques is to improve the materials’ properties in order to preserve its structural integrity and to reduce or even eliminate the damage caused by an external impact. Generally, this is achieved by through-thickness reinforcement (usually called z-binders) or by improving the material properties of the composite constituents. Enhancing properties in the Z direction is mainly achieved by modification of fibre architecture using techniques such as: 3D weaving, braiding, stitching, knitting, embroidery, tufting and z-anchoring or by embedding high stiffness, high strength rods in the through-thickness direction of the prepreg laminate through the Z-pinning process. Other methods to increase damage resistance involve the use of hybrid structures, combining two or more fibres and/or resins, introducing layers of different material at critical locations in the stacking sequence, or by using specific layup configuration.

2.2.1 Textile structural preforms

Textile preforming is a fibre placement method, prior to the formation of composite structures that play a key role in the manufacturing process by facilitating processing steps and by providing homogenous distribution of matrix and reinforcing fibres. Textile structural preforms are designed to conform to a specific shape and to meet exclusive mechanical, structural and design requirements. One of the main advantages of composite preforms is to improve the through-thickness properties offering a greater resistance to delamination. In addition, production of the composite components, through textile preforming, can have a much lower cost than the same piece obtained by conventional lay-up methods. Moreover, this technique could offer a great benefit for curved components where poor resistance to axial compression can lead to failure due to buckling of axial yarn. Indeed, the geometry and the architecture of the individual tow as well as weave topology play an important role in the properties of the composite and hence the ability to withstand damage.

In the 1960s, in order to reduce the cost and the weight of high temperature metallic alloys in aircraft brakes, 3D preforms of carbon-carbon components were developed and produced using braiding process [32, 33]. A specialized loom was developed, by Avco Corporation, to allow the weaving of hollow cylindrical preforms [33]. This was the first textile process adopted to manufacture 3D fibre preforms. Since then, the interest in 3D woven composites was low, until the 1980s when preforms offered the possibility to overcome the main drawback of traditional 2D laminates, mainly manufacturing cost of complex components and impact resistance. Another important step in the history of 3D preforms was the years between 1985 and 1997 in which the “Advance Composite Technology Program (ACTP)” was launched in order to investigate different techniques for the production of 3D composites [21]. As a result of this rising interest in fabric preforms, and due to the versatility of the textile weaving process various techniques were exploited for producing structural preforms, such as: 3D weaving, 3D knitting, 3D stitching, and non-woven [21, 34]. In the last years, major strides have been made to develop these materials to a commercial level where they can be used in both traditional and emerging markets. Different technology processes can be adopted to produce composite reinforcement materials, but each of them lead to different characteristics with related advantages and disadvantages. The main technique used for 3D complex fabric preforms are interlacing and non-interlacing. With the first category, fabrics are woven by interlacing the warp, weft z-binder yarns to create a fully interlocked structure. Instead, the second category comprises fabrics obtained by non-interlacing fibres, in which warp and weft yarns are stacked as separate ply layers and held in place with z-binder yarns. The architecture of the z-binder reinforcement can vary according to the weaving process and the type of weaving pattern chosen. The main processes employed in the manufacturing of textile reinforcement are: weaving, knitting, stitching, z-anchoring, tufting, embroidery, braiding and non-woven and they will be discussed one by one.

2.2.1.1 Weaving

Weaving is a major process used to make fabrics. The process consists of interlacing two distinct sets of yarns, usually at right angles to each other. The lengthwise yarns which run from the back to the front of the loom are called the warp, while the crosswise yarns are the weft. The simplest two-harness loom is represented in Figure 4 and can be used to fabricate biaxial plain weave fabrics. For weaving different patterns, such as 2/2 twill or sateen (see in Figure 3), looms with more than two harnesses are required. Each weaving pattern will confer different properties to the fabric. An example of different characteristics associated with woven preform is illustrated in Figure 2.

Property	Woven preform					
	Plain	Twill	Satin	Basket	Leno	Mock-leno
Higher stability	4	3	2	2	1	3
Good drape	2	4	5	3	5	2
Low porosity	3	4	5	2	1	3
Smoothness	2	3	5	2	1	2
Balance	4	4	2	4	2	4
Low crimp	2	3	5	2	5	2

Rating scale: (5) Excellent (4) Very good (3) Good (2) Poor (1) Very poor

Figure 2 A comparative properties of some woven preforms, reproduced from [35]

Weave 3D fabrics with complex patterns and with the yarns going through the z-direction, require the use of specific looms. Usually, each company has got its own tailored loom, and most of them are covered by patents [36-40].

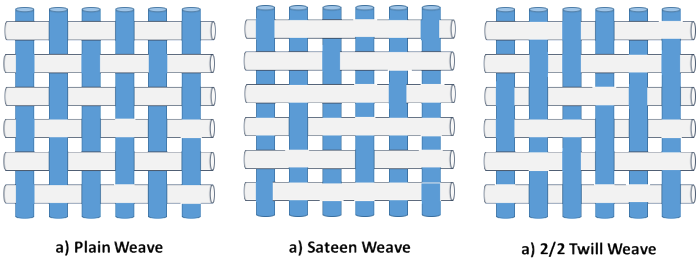

Figure 3 Typical fabric weave styles.

Even though there are different definitions in literature on 3D-weaving [41-46]; here, we refer to it as the process to manufacture fabrics that have pre-designed three-dimensional shapes, or that will be directly manipulated into a 3D shape immediately after being woven. The simplest 3D preform is based on 2D weaves, with no yarns present through the thickness. The thickness is given only by the diameters of the warp and weft yarns. These thin woven fabrics are usually used for motorbike panels or helmets.

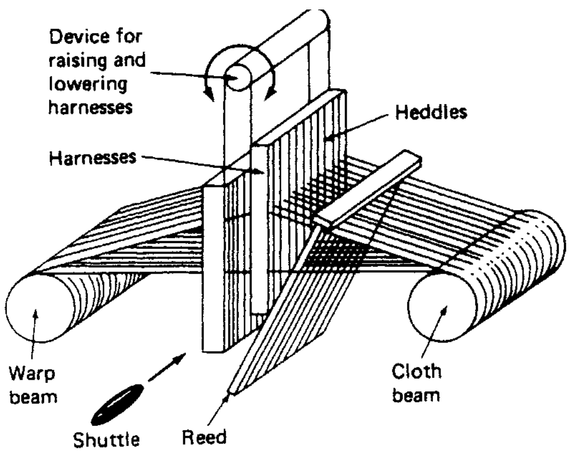

Figure 4 A simple two-harness weaving loom, reproduced from [47]

One of the main advantages of 3D woven preform over other techniques, is the ability to place the through-thickness reinforcement directly during the woven process and not like for other processes, such as z-pinning or stitching, in which the reinforcement is forced through an existing fibrous structure, causing in most cases fibre damage. On the other side, there is still a lot of lack in understanding the effect of the weaving parameters and how they affect the mechanical properties of the composite structure [48-53]. Moreover, the mechanics of woven composite must be considered according to their hierarchical organization that can be divided in four main levels. The first level, comprising the type of fibres, followed by the typology of reinforcement (tows, strands, or yarns) interlocked upon themselves during the weaving process; the third level represented by the fabric, including the weaving pattern chosen and/or the type of technology adopted to make it, and the last level in which the woven preforms can be consolidated with resin to form the composite.

2.2.1.2 Non-Woven

Nonwoven is commonly defined as a web structure or as a sheet of directionally or randomly oriented fibres bonded by means of friction, cohesion, adhesion, or combination of these. Nonwoven fabrics can also be referred to as non-interlaced fabrics or noobed (from an acronym for Non-interlacing, Orthogonally Orientating and Binding) [54, 55]). It is important to underline that there is still a lot of confusion with the definition of non-woven fabrics. Some international agreement refers to the ISO 9092:2011 "*nonwovens are structures of textile materials, such as fibres, continuous filaments, or chopped yarns of any nature or origin, that have been formed into webs by any means, and bonded together by any means, excluding the interlacing of yarns as in woven fabric, knitted fabric, laces, braided fabric or tufted fabric*" while others refer to a more generic definition of the ASTM D 1117-80 "*A nonwoven is a textile structure produced by the bonding or interlocking of fibres, or both, accomplished by mechanical, chemical, thermal or solvent means and combinations thereof. The term does not include paper or fabrics that are woven, knitted or tufted*". The confusion becomes even high for same countries which still prefer to use their own national definition [56-58].

Nonwoven fabrics are classified into three main groups: fibre-web structures (heterogeneous and homogenous), netlike structures, and multiplex [59]. Technologies used to produce nonwoven fabrics are usually based on the following methods: mechanical-frictional forces generated by entanglement or by fibre contact, use of fibres with various lengths and diameters, reinforcement, needle punching, melt-blowing, thermal bonding, etc. Regardless of the process used, one of the major advantages is that the nonwoven fabrics are generally produced directly from the raw materials to the finished fabric in one continuous process, although there are techniques that involve more steps. Non-woven textiles, due to their ability to work as filters or as high absorptive fabric have been used mainly for medical or health care applications, and more recently have found a great application in the composite industries [60].

2.2.1.3 Stitching

Stitching of textile preforms is one of the most used techniques to manufacture complex textile preforms. The stitching process differs from the previous techniques, described above, because is a joint technique rather than a process to obtain textile preforms, and usually involves an extra step in the manufacturing process. Basically, this process involves the insertion of a needle through a stack of fabric layers to form a 3D structure, and can be adopted to assemble sub-structures or to assemble single or multi layered preforms. Stitching can be performed with a variety of sewing machines, usually classified as single- or multi-needle machines, on dry fabrics, preforms, or prepreg laminates. Although, the latter can cause excessive fibre damage and is usually to be avoided. Indeed, dry fibres can move easily compared to prepreg layer, and hence accommodate the stitches avoiding or reducing fibre damage [25, 58]. This technique can be used also to increase impact resistance through the insertion of through thickness reinforcement. Different studies have proven that the stitching process on 2D composites has improved the delamination resistance of a factor of three to twenty [56-58]. However, as highlighted by Mouritz and Cox [56] stitching can reduce in plane properties by up to 20%. One of the main drawbacks is that sewing machines require access to both sides of the preform and most of them cannot stitch thick or curved composite structures with complex shape. Stitching in aerospace structures, is mainly used for lap joints, stiffened panels, and aircraft wing to-spar joints [50, 61-65].

2.2.1.4 Tufting

Tufting, is a one-sided stitching process that require the use of a single hollow needle to insert thread through a multi-layered fabric preform (see Figure 5). The loops are not tied or interlocked but are retained within the preform by simple friction when the needle retracts. The insertion can be total or partial, orthogonal to the preform surface or angled. One of the advantages of this technique is that it requires the access from only one side of the preform, and hence makes this technique suitable for tailor-made reinforcement of complex shapes. It must be highlighted though that the tufting process must be performed on a support that allows the needle to pierce through the structure. This process is best suited for the reinforcement of dry fibre composites. Tufting is a recent technique in the composite industries [66, 67], although has been used since ancient time for the manufacturing of carpet or garments.

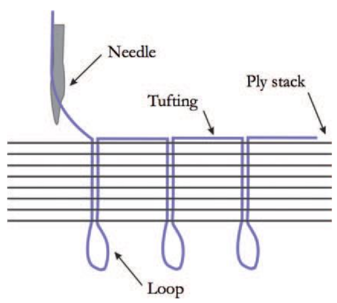

Figure 5 Tufting process description, reproduced from [68]

2.2.1.5 Embroidery

Technical embroidery could be considered as a variant of the stitching technique, in which reinforcement yarn is fed into the path of a stitching needle and pressing through the fabric to make the z-binders. This technique is mainly adopted to provide localised through thickness reinforcement. Usually, the machines used in the technical embroidery are computer-controlled in order to accurately place the yarns along complex paths. This allows to reinforce high-stress regions of composite component and as reported by Crothers et al. also to improve bearing strength of 55% [69].

2.2.1.6 Knitting

Knitted fabrics are produced by intermeshing loops of yarns using knitting needles. Basically, a continuous series of knitting stitches or intermeshed loops are formed by needles (see Figure 6c) catching the yarn and leading it through a previously formed loop to form a new loop. The loops are supported by, and interconnected with, each other to form the fabric. In knitted fabrics, yarns follow a meandering path, which as reported in Figure 6, are named course if the yarns run along the width of the structure forming symmetric loops (bights), while are known as wales if they runs along the length of the fabric.

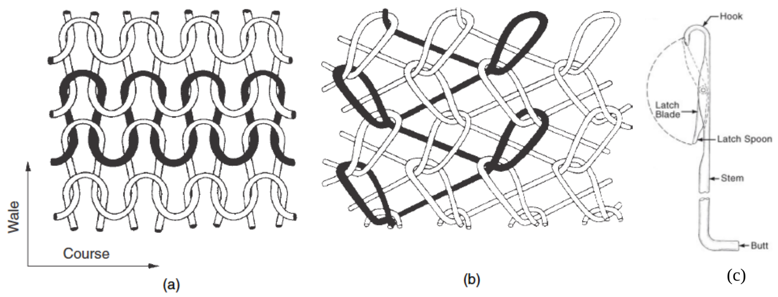

Figure 6 Schematic diagrams of (a) weft-knitted (plain knit) and (b) warp-knitted (single tricot) reinforcement, reproduced from [48]; (c) latch needle, reproduced from [70]

The knitting process can be grouped in two categories according to the direction in which the loops are formed. If the loops are formed through the feeding of the weft yarn in the course direction, the reinforcement is named weft-knitted (see Figure 6 a). Instead, if the loops overlap in alternative wales at alternate courses in the direction of the wale, interloping each yarn into adjacent columns of wales as illustrated in Figure 6b), it is named warp-knitted. Knitting can be used to manufacture complex shapes or to interconnect fibre arrays that have been arranged by other textile techniques. One of the main advantages of knitted fabric is the higher drapability/formability, in particular for the wrap-knit structures, which allow more stretchability of the fabric and then the manufacturing of complex shape. Another great advantage if compared to other conventional textile fabrics, is the high productivity rate and low cost of manufacturing in particular for the warp-knitted [71]. Moreover, knitted fabric composites exhibit a better impact resistance than woven fabric composites [57, 72, 73]. On the other side the knitted architectures bring a reduction in the in-plane stiffness and strength of the composite and hence are not advised to be used as reinforcement unlike the woven and braided fabrics [71].

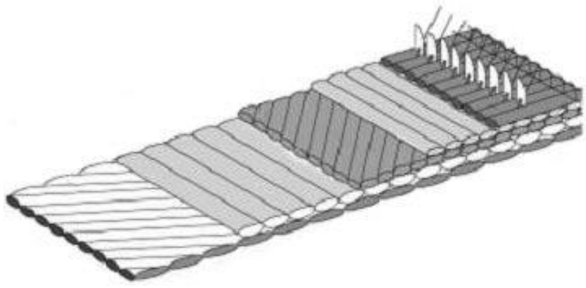

Figure 7 Non crimp fabric, reproduced from [74]

A manufacturing process that combines aspects of weaving and knitting is the structural non crimp knitting also known as multi-axial warp knitting or stitch bonding used to produce non-crimp fabrics in which warp (0°), weft (90°) and (optionally) bias (±θ°) yarns are held together by z-binders inserted through the thickness without penetrating any yarns, but instead going to the sides to form knit loops between the yarns to avoid crimp and damage. This technique usually combine different type of materials, such as Glass, Carbon or Aramid fibres, and it is used to provide high interlaminar strength.

2.2.1.7 Braiding

Braiding is among the oldest textile process used to manufacture 3D fibre preforms for composites [32, 33]. Braided structures are manufactured interwinding two or more sets of yarn fibres. The process involves the counter-rotation of multiple fibrous yarns around a circular frame to intertwine the yarns into braided fabrics. Traditional 2D braided structures are obtained with yarns a ±θ, although for three dimensional braided reinforcement, more complex patterns are used, in which the yarns are mechanically forced into the structure [21]. Braiding can produce complex preform shapes by overbraiding mandrels or by using specific new patterns to form preforms directly (see Figure 8).

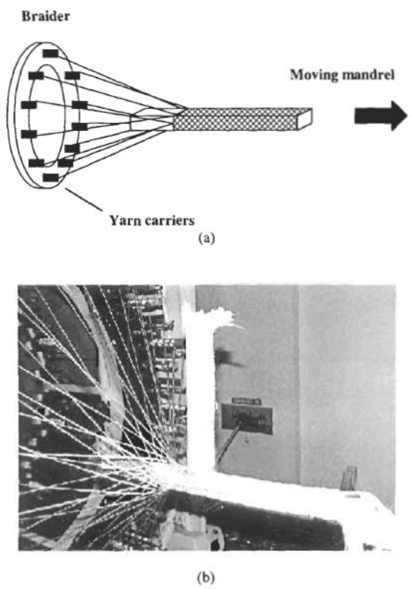

Figure 8 a) Schematic of braiding over a moving mandrel, b) Example of braiding over a T-shaped mandrel, reproduced from [21]

Although, braided fabrics, have relatively low in plane mechanical properties one of their main advantages is to allow them to endure twisting, crush resistance, shearing and impact better than woven fabrics.[21, 25, 75]. Other benefits of this technique include high drapability, capability of forming intricately-shaped preforms and produces holes, bifurcation of curved parts in the final preform. Braiding, due to the production process, is mainly used to manufacture tubular fabric or narrow-width flat fabric. Potential applications for 3D braided composites in the aerospace sectors are tail shaft, connecting rods, fuselage frames and barrels, propeller blades, rocket nose cones, engine nozzles, etc. [21, 22, 25]

2.2.1.8 Z-anchoring

Z-anchoring is a process which use the in-plane yarns of fibre layers to create reinforcement through the z direction. The process involves punching thin rods through a dry fibre reinforcement, bending the fibres towards the through thickness direction, as illustrated in Figure 9. The dimension of the punching rod affect the percentage of fibres bended. The bended fibres take the name of z-anchors. After the rod have crimped the in-plane fibres and the desired number of z-anchors is achieved, the fibre reinforcement is then infused with resin using conventional methods.

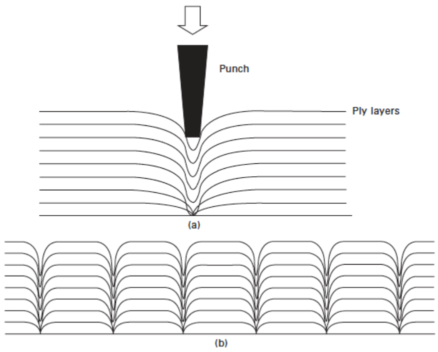

Figure 9 Schematic of the a) local ply deformation forming z-anchor and b) composite with series of z-anchored preforms – reproduced from [74]

Unlike, other through-thickness reinforcement techniques that use separate yarns or pins to create the z-binders, z-anchoring uses the in-plane yarns of the preform to create reinforcement in the z direction. However, this technique can cause damage or undesired crimp to the fibre reinforcement. Moreover, the punching operation became challenging as the fibre reinforcement assume complex shape.

2.2.2 Z pinning

Z-pinning involves the insertion of rigid pins (z-pin) into a laminate prior to consolidation. The z-pin have a diameter of 0.2-1.0 mm and are made of high strength, high stiffened material such as titanium alloy, steel, or carbon composite. The choice of the material is of primary importance. Indeed, a mismatch of thermal coefficients can generate resin matrix cracking during the curing process. Zpin lock the laminate plies together by a combination of friction and adhesion. Before the 80s this pin was inserted individually using a manual process. Successively, different researchers have developed an automated process for inserting thin wire fibres through laminated composite [76-78]. Nowadays UAZ (ultrasonic assisted z-fibre) process is the most common process for the z-pinning laminates [79, 80]. The process involves several steps, in which the first required the use of foam carrier containing the z-pins. The foam is necessary to ensures support prior to the insertion in the fabric and to place the z-pins accurately and with even space. Successively, the z-pins are driven from the foam to the prepreg or dry fabric using an ultrasonically actuated tool. The foam and any z-pin excess length protruding the sample are removed using a blade, ensuring a smooth surface finish. A complete description of the z-pining steps is described by Partridge et al. [81]. Schematic representation of the process is illustrated in Figure 10.

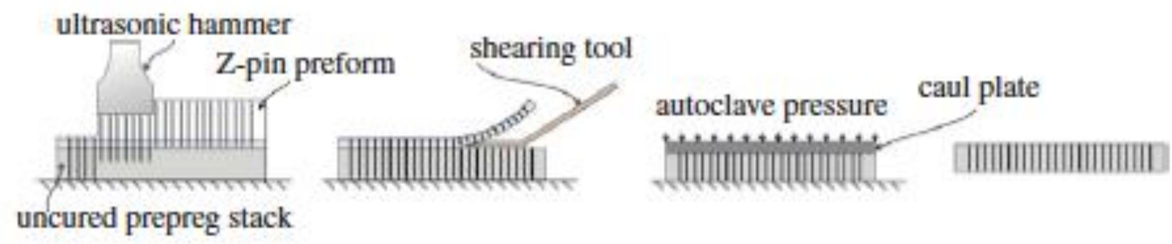

Figure 10 Schematic representation of the Z-pinning process, reproduced from [82]

The main benefits of z-pinning are enhancing of through-thickness stiffness, impact damage tolerance and delamination resistance. An increase in the ultimate strength can be achieved with a relatively small volume fraction of z-pins, 0.5-2% [83]. Z-pin content and their diameter are the main factors that affect the final properties of the composite. Indeed, relatively high volume content of pin with large diameter will maximise damage tolerance but will cause loss in the in-plane strength properties, while thin pins are preferred to minimise loss in the elastic properties mainly due to fibre crimp, fibre waviness, and swelling [84]. Disadvantages of this technique include mainly loss in elastic properties and reduction in tensile strength that are mainly attributed to fibres damage and fibres misalignment due to the introduction of the z-pin. Instead, one of the main advantage of z-pinning is that while other reinforcement techniques are applied on dry fabric which is later infused with liquid resin z-pinning can be directly applied on prepreg. Although further investigations are required for the use of z-pin on dry fabrics, such as the use of z-pinned fabric with resin infusion process. Moreover, the process requires access on only one side of the fabric and can be applied directly on mould. These advantages allow the reinforcements to be applied without the need for radical change in the processing route. However, to our knowledge, nowadays the only current aerospace application of z-pins is in the F/A-18E/FSuperhornet [85]

2.2.3 Enhancements of the material's properties by adding a second phase component

The choice of the resin used for the composite manufacturing is mainly related to design, cost and processing considerations. One of the most broadly used thermoset resins is epoxy, mainly due to its good chemical properties and high versatility in terms of working and curing time, low shrinkage and good mechanical properties. However, the toughness of thermoset resin is relatively poor if compared to thermoplastics. Many investigations, have been carried out in the past years, to improve the thermal and mechanical properties of the resin system. Interlaminar properties of laminated composites can be enhanced by toughening the matrix. An efficient method, already applied in aerospace is to add a second phase component with the matrix. This method has been used on the Torayca 3900 for the empennage and floor beams of the Boeing [86]. Another technique used to improve the toughness of the resins is to include particles in the matrix. The inclusion of particles consume energy mainly by changing the crack patterns or by plastic deformation. In particular, the type of particles and the way in which they are introduced in the resin is mainly related to the toughening mechanism desired. The principle toughening mechanisms adopted are: crack front pinning, crack bridging, crack path deflection, micro crack toughening. According to the chosen toughening mechanism, it is really important to choose the material, the dimension and the volume fraction of the particles to add to the resin system [87].

Apart from applying tougher resins and particles within the resin, another method is to increase the adhesion between the resin and the fibre. This is usually achieved by fibre pre-treatment, and one of the most common material investigated is Carbon nanotubes (CNTs). The incorporation of carbon nanotubes can be achieved by modifying either the matrix resin or the fibre reinforcement. The exploitation of the unique properties of CNTs is strongly dependent on how they are integrated in the structure. The CNTs dispersion method, their orientation, the type of CNTs and the interaction between CNT and the polymer are key factors for determining the performance of the composite [88, 89]. Due their tendency to agglomerate, they are usually mixed in solvent containing surfactants and applied on the fibre reinforcement. As CNT based composites are now entering into use in several industrial fields, there is the need to reduce, as much as possible, the use of toxic reagents for both purification and dispersion processes. Therefore, the traditional procedures, which require the use of toxic solvents such as Tetrachloroethane or N-Methyl-2-pyrrolidone, [90-93] must be reconsidered. In our previous work, we presented two single-step procedures to coat traditional microscale carbon-fibre fabrics with a coating containing CNTs and Gum Arabic in order to create a multiscale reinforcement (see Figure 11). Particular attention was given to the formulation of the solutions used for the impregnation process [94].

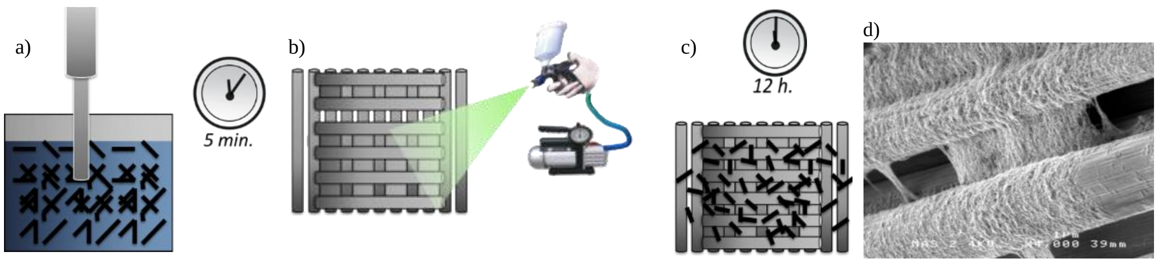

Figure 11 Spray Method Steps: a) CNTs sonication, b) solution sputtered using a spray gun, c) solvent is left to evaporate for 12 hours, d) FESEM image of Sample sputtered with CNT's solution, reproduced from [94].

2.2.4 Hybrid Structures

Hybridization involves the combination of two or more types of reinforcing fibres in a resin system. Different kinds of fibres can be combined in different laminas making an *interply* hybrid laminate, or using different fibres interspersed in the same lamina that takes the name of *intraply* hybrid laminate. Hybrid structures are usually used to enhance the strain failure of the lower elongation reinforcing material of the hybrid structures. Another important effect is to control the way the composite fails. With the right combination of materials, the stress-strain diagram can be smoother or rising a step, avoiding catastrophically failing [95]. The enhancement of strain is usually achieved at the sacrifice of tensile strength and tensile modulus. Factors that can influence mechanical properties are the length of the fibre, fibre orientation, fibre shape and fibre material [96, 97]. Based on the existing literature, the properties of hybrid laminates can be usually predicted using the general rule of mixture, although many research noted the so called “hybrid effect” in which the material property significantly differ from those predicted [98]. Possible explanation of the hybrid effect have been found in the internal compressive strains induced in the carbon phase by differential thermal contraction relative to second type of fibres (e.g. glass fibre) as the composite is cooled from its cure temperature [99]. Or by the crack-constraint theory, in which the load released by the fracture of carbon fibres is transferred to surrounding fibres (usually glass or basalt) which prevent cracks from spreading [100, 101]. Bunsell and Naik [102, 103] observed an improvement of fracture toughness, impact strength, notch sensitivity by using a combination of carbon and glass fibres. Although the higher glass fibres density cause a higher total weight of the sample. Other researchers investigated the effect of carbon/basalt hybrid laminated on impact behaviour [104-106]. The introduction of basalt fibres in the carbon fibre laminates promote an increase of the adsorbed impact energy, with an enhancement of the fracture propagation component and with the ability to sustain the damage propagation and delamination without leading to catastrophic failure. Another approach was suggested by Marom et al. [107], that obtained an improved fatigue response but reduced stiffness combining carbon and Kevlar fibres. Peijs et al.[108-110] studied the effect of the addition of high performance polyethylene (HP-PE) fibres in carbon laminates. The addition of HP-PE cause a change in energy absorption mode, impact energy is stored elastically in the polyethylene fibres and consequently less energy is available for damage in the structural carbon component of the hybrid, resulting in impact damage and improved post-impact properties.

Hybrid structures can also be obtained by the insertion of thin aluminium sheets. Two commercial metal hybrid structures, that has been accepted by aeronautical and aerospace industries, are ARALL[111, 112] (layers of aluminium sheet and unidirectional aramid fibre epoxy laminates) and GLARE [113, 114] (layers of aluminium sheet and either unidirectional or bidirectional S-glass fibre–epoxy laminates) [115] that showed interesting corrosive resistance, fatigue and impact damage tolerance but higher manufacturing costs.

Another method to enhance the impact performance of composite laminates is the insertion of a thin layer of tough, ductile polymer or adhesive between plies within the laminate [116]. Although, this method allows interlaminar fracture toughness to increase, it can cause a decrease in fibre-dominant properties, such as tensile strength and modulus due to a reduction of the overall fibre volume fraction. The insertion of an interleaf with low stiffness could reduce shear stress concentration when used as strategic plies. Krieger found that the insertion of a new thermoplastic resin interleaf presents higher crack growth resistance with a threshold value of 3.5 times higher than the base laminates [117]. An alternative method is to use resin layers with toughening particles as outer layers [118], or using a high energy absorbing materials such as cork [119]. Both approaches offer a mechanism of energy absorption and thus decrease the maximum force during the impact, reducing the energy absorbed in the structural laminate. The main drawback of these techniques is that they add extra cost, unwanted weight and thickness to the structures.

2.2.5 Stacking sequence

The stacking sequence of fibre layer through the thickness of composite can affect delamination mechanism and crack growth [120]. Indeed, inter-laminar toughness decreases as the fibre angle between lamina increases from 0° to 15°, this happens because of the mismatch of the elastic properties between different lamina, therefore the energy required to open a crack or a delamination between two adjacent plies is proportional to the difference between their orientations [121]. This is evident in the work by Tao and Sun on the crack-jumping behaviour in various laminates between two subsequent layers with an orientation difference ϑ equal to 90, 60, 45, 30 and 0 degrees. They found out with an experimental investigation, that the delamination cracks always end up along the $0/\vartheta$ interface and that the interlaminar toughness increases as the off-axis angle ϑ decreases [122]. As consequence, in our previous work, we found that composite mimicking the Bouligand structure along the thickness could provide a nearly continuous grading of the in-plane stiffness in the thickness direction reducing the interlaminar shear stresses significantly [123, 124]

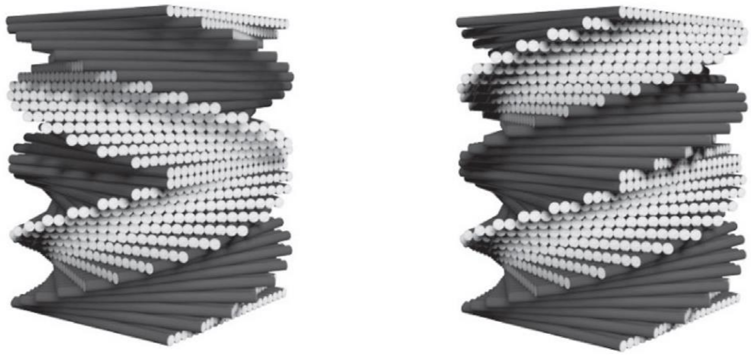

a) b)

Figure 12 Computer generated visualisation of the helicoidally lamination schemes: a) symmetric, b) continuous, reproduced from [124]

2.3 Pseudo-Ductility in Composite

The techniques illustrated in the paragraph 2.2, except for specific hybrid structures, are successfully used to increase impact resistance, but do not address the issue of brittleness and catastrophic failure, except for specific hybrid configurations. These limitations are the main aspects that render composites unsuitable for many applications in which loading conditions are not fully predictable, but catastrophic failure cannot be tolerated. The possibility of manufacturing FRP composite with pseudo-ductile behaviour, and hence assuring safe and progressive failure mechanisms, allow to reduce conservative design which nowadays hinders component manufacturers from fully exploiting their applications. Moreover, pseudo-ductile behaviour in composites will permit detectable warning with a reasonable margin between damage initiation and final failure like in the metals' structures. Basic strategies to add ductility to fibre reinforced composites are either the incorporation of new ductile constituents, or modifying the structure of the composite laminates manufactured (e.g. creating hybrids). The latter method is usually preferred, especially in sensitive sector as aerospace where introduction of new constituents is particularly difficult and can take at least a decade. Several studies have been performed in the past years studying the effect of metal wires inserted in composites, focusing on the type of metal to use and their disposition. Bradley et al.[125] reported an increase in impact properties when metal wires are located close to the impacted area. Paine et al. [126] adopt the use of Shape Memory Alloys (SMAs) wires as secondary reinforcement. Paine showed that the inclusion of SMAs wires limited the damage growth under LVI conditions, hypothesizing that this effect was due to the dissipation of impact energy through the nitinol stress-induced martensitic phase transformation. Allaer et al. [2] and Callens et al. [127-129] experimented excellent ductile properties of composite reinforced with low diameter stainless steel fibre, although the density of the hybrid composite was at least twice as high as that of the traditional carbon/epoxy sample. Hayashi et al. [130] was the first to demonstrate the hybrid effect studying unidirectional (UD) layered glass/carbon hybrid composites. Successive works on hybrid composite have shown their potential to obtain gradual failure over a range of strains by mixing different types of fibres either by intimately mingling them [98, 131, 132] or by creating a ply-by-ply hybrid structure [99, 102, 130]. The effect of different types of carbon fibres [133]or the effect of carbon layer thickness [26] in the so called all-carbon hybrids were also investigated in the past years. Curtis et Brown[134] prove that using lower performance carbon fibres in secondary direction, while keeping high performance fibres for the primary direction lead to 20% cost saving while keeping the mechanical properties at almost the same level as that of the composite made using high performance fibres for all layers. Recently some authors [26] [135-138] studied the effect of the insertion of thin carbon plies in either all-carbon and glass/carbon laminated composite. They demonstrate that the thin layer delay the propagation of intra- and interlaminar cracks, lowering the energy release rate and leading to superior mechanical properties (this phenomenon can shift the onset of damage in composite). In particular G. Czél et al. [139] and [26], demonstrate that by combining the benefit of conventional carbon/glass composites with the use of thin ply composites a pseudo-ductility can be achieved (see Figure 13). They reach a stable pull out of a sufficiently thin central carbon reinforced layer from thicker glass reinforced layers

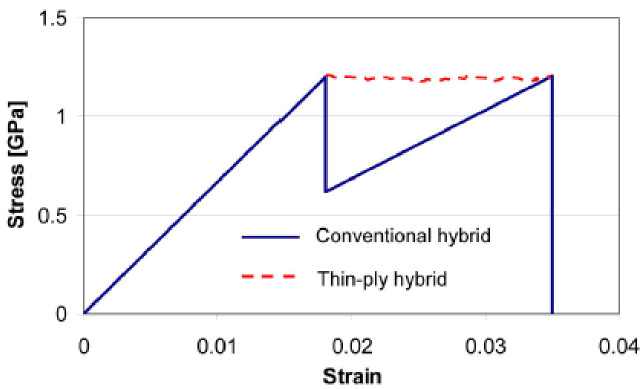

Figure 13 Schematic of the stress-strain graph of a conventional and a thin ply hybrid composite laminate, reproduced from [26]

Ductility during manufacturing can be achieved using discontinuous, but highly aligned fibres. Research is underway to develop manufacturing technology which is adaptable for mass production (e.g. [140].

2.4 Structural Health Monitoring for composite structures

As reported in the previous paragraphs significant amount of work has been done in order to enhance the impact properties and the life of composite structures. This work is always done in parallel with the development of non-destructive inspection/evaluation/ testing techniques. Designing an effective SHM system requires considering all kinds of defects and all possible environmental conditions. Due to the extended variety of damage and materials used, SHM is a multidisciplinary science that adopts several techniques to detect and monitor defects. A good overview on the state-of-the-art on NDT techniques for composite materials can be found in [141-143] and the main ones are: Visual Inspection; Optical methods; Eddy-current (electro-magnetic testing); Ultrasonic Inspection; Laser Ultrasonics; Acoustic Emission; Vibration analysis; Radiography; Thermography; Lamb waves. The types of sensors that can be used, for each sensor technique, are varied and make use of different physical phenomena. The number of techniques and sensors used in SHM is growing rapidly, and there are several ways to categorize the wide range of sensors in use. Following the convention adopted by Balageas we have reported in Table 1 the principal physical phenomena and sensor materials usually adopted.

Table 1 Materials for sensor design, reproduced from [8]

Physical effect	Materials	
	Polymers	Inorganics
Passive sensors		
Piezoelectricity	Polyvinylidene fluoride Polyvinylidene fluoride trifluoroethylene Polyhydroxibutyrate Liquid crystalline polymers (flexoelectricity)	Piezoelectric zirconate titanate Zinc oxide Quartz
Pyroelectricity	Polyvinylidene fluoride Langmuir-Blodgett ferroelectric superlattices	Triglycine sulfate Lead-based lanthanum-doped zirconate titanate Lithium tantalate
Thermoelectricity (Seebeck effect)	Nitrile-based polymers Polyphthalocyanines	$Cu_{100}/Cu_{57}Ni_{43}$ Lead telluride Bismuth selenide
Photovoltaic	Polyacetylene/n-zinc sulfide Poly(N-vinyl carbazole)+merocyanine dyes Polyaniline	Silicon Gallium arsenide Indium antimonide
Electrokinetic	Polyelectrolyte gel ionic polymers	Sintered ionic glasses
Magnetostriction	Molecular ferromagnets	Nickel Nickel-iron alloys
Active sensors		
Piezoresistivity	Polyacetylene Pyrolized polyacrylonitrile Polyacequinones Polyaniline Polypyrrole Polythiophene	Metals Semiconductors
Thermoresistivity	Poly(p-phenylene vinylene)	Metals Metal oxides Titanate ceramics Semiconductors
Magnetoresistivity	Polyacetylene Pyrolized polyvinylacetate	Nickel-iron alloys Nickel-cobalt alloys
Chemioresistivity	Polypyrrole Polythiophene Ionic conducting polymers Charge transfer complexes	Palladium Metal oxides Titanates Zirconia
Photoconductivity	Copper phthalocyanines Polythiophene complexes	Intrinsic and extrinsic (doped) semiconductors

The type of sensors used to monitor and control structures are strictly dependent on different factors, as: the type of structures, the materials, and the damage to be monitored. Classification of sensors may be made based on the nature of the sensor being networked for the data and energy transfer, being group into wired or wireless. A standard transducer requires for its operations an electrical current, usually generated by a power supply. Moreover, a sensor typically needs to detect a specified change and transfer the information to the data acquisition system. Wired transducers due to the necessity of connecting by wires for power and data transmission become more complex to install and maintain, becoming typically a cost increase. Often batteries cannot be used due to inaccessible locations or exposure to large temperature extremes (as for aerospace applications), thus power sources for wireless sensors is one of the main challenges [144]. As a consequence much effort has been focused in design and manufacture of passive wireless sensors [145, 146]. The majority of the wireless sensors contain active circuitry, which requires an on-board battery, and is therefore classified as active sensors. Active devices operate much in the same way as radio transmitters. Hence, a form of on-board active signal processing circuitry (i.e. amplifying, mixing, demodulation/ modulation etc.), required for the modulation of the signal should be integrated into the remote sensor. Unlike the active devices, passive wireless sensors do not require on-board batteries. Therefore, they are less complicated, smaller, and cheaper and they require no maintenance resulting in unlimited lifespan. Furthermore, excluding the lossy characteristics of the active circuitry can be advantageously placed on moving or rotating parts, within closed areas and in hazardous environments such as high temperatures or pressures, or in the presence of hazardous chemicals. A disadvantage of the passive devices is that the signal is weak unless the sensor is in the neighbourhood of the element to detect (i.e. delamination or crack). Moreover, the interrogation distance is usually shorter than the active devices. Lack of need for bulky batteries and wire connections make passive sensors ideal candidates for applications where location of the sensors, or access to them, is prohibited by the remoteness of the system's location or the harshness of the environment in which it is operated such as engine testing or landing gear in-flight. Consequently, the past decades have witnessed an extensive investigation in the Wireless transfer of power and data based on inductive coupling [147-151]. Over the past decade, many damage detection methods have been proposed, mainly concerning Passive and/or Wireless Smart Sensor [14, 145, 146, 152-155]. Common passive wireless sensors for SHM are: Surface Acoustic Wave (SAW), radio frequency identification (RFID), electrical resonance circuit sensors, Patch Antenna and Metamaterial resonators.

2.4.1 Resonance Sensors

Resonance sensors relate the change in the resonance frequency of a mechanical, acoustical or electrical structure to physical state for which the sensor is measuring [156]. Typically, RC or LC tank circuits (see Figure 14) could be designed to change their inductance, capacitance or resistance, which in turn changes the resonant frequency of the circuit, according to a measured quantity. A reader device coupled with the sensor acquires the information wirelessly by measuring the impedance of the RLC-resonator that depends on the coupling between the reader and the sensor.

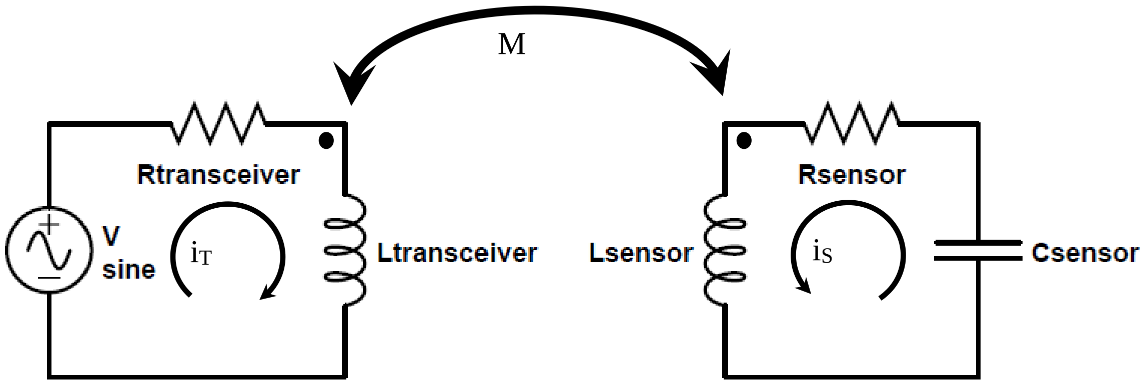

Figure 14 Equivalent circuit model of a resonance sensor

The mutual inductance (M) between the reader and the sensor can be modelled as the primary and secondary sides of an air-core respectively and defined as:

$$M = K_c\sqrt{L_{transceiver}L_{sensor}}$$

where K_c is the inductive coupling coefficient, defining the relationship between magnetic flux linkages in the circuit. K is a dimensionless number in the range zero to unity, where a value of 1 means that all the flux produced by the primary is linked with the secondary and vice versa. The coupling constant gives information on how the lines of magnetic force interact between two air-spaced coils, and so it depends only on their physical size and disposition in space.

For inductively coupled passive wireless sensors the change of capacitance, inductance or resistance can be obtained wirelessly when the impedance is measured at several frequencies. A limitation for the resonance sensors is that their read-out distance is only a few centimetres since they require a near field coupling to the reader device [157-160]. Another limitation of resonance sensors is that their resonance may be affected by proximity to conductive objects or if a short circuit between the conductive traces occurs. Inductively coupled electrical resonance sensors have been used to measure pressure, temperature, PH, structural properties [158, 160-162] and all physical characteristics affecting the parameter of the RLC circuit.

A strain sensor with an inductively coupled resonant circuit (LC tank circuit) for damage detection has been developed by Butler, Viglio, Vendi and Walsh [163]. The sensor measures the resonant frequency change that occurs when a strain is applied to the cross-section area of the solenoid. A similar device was also realized using a coaxial resonant RF cavity in place of the solenoid [164]. Another sensor for structural health monitoring was realized coupling a plane spiral inductor with an interdigital capacitor to form a LC oscillating circuit (see Figure 15) [165].

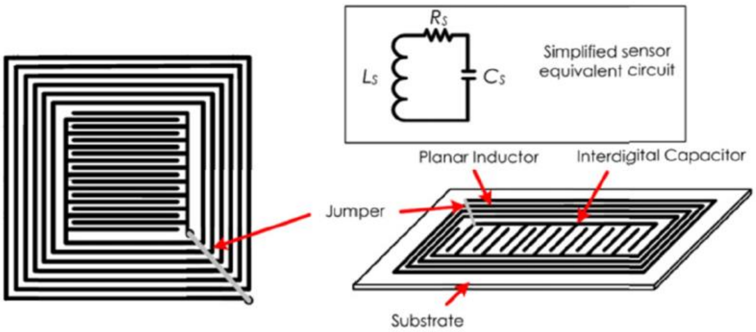

Figure 15 Sensor unit with a laminated sandwich structure, reproduced from [165]

2.4.2 SAW Sensor

Surface Acoustic Wave (SAW) sensors utilize the modulation of surface acoustic waves to sensor a physical phenomenon like structural properties. A basic SAW device consists of an input and an output interdigital transducer (IDT) on a piezoelectric substrate as illustrated in Figure 16. The IDTs are interleaved electrodes that work as a sender to transfer electrical waves to acoustic waves and a receiver to transfer acoustic waves into an electrical signal.

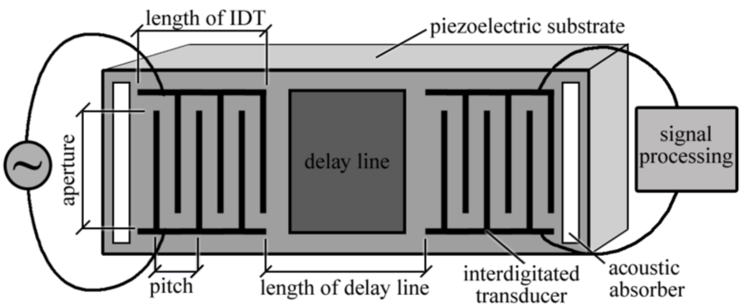

Figure 16 Surface Acoustic Wave Sensor Interdigitated Transducer Diagram

The operation principle is based on converting a sinusoidal electric signal (AC) into a mechanical wave that can be easily influenced by physical phenomena. The electric signal is sent through the first interdigitated transducer, in which the electrodes will alternate polarity according to the electrical signal, creating regions of electric field between fingers. Due to the piezoelectric effect, those regions will cause a tensile and compressive strain, producing a mechanical wave at the surface. The surface acoustic wave, a form of Rayleigh wave, will propagate in both directions of the input IDT, hence only half of the energy will propagate through the delay line in the direction of the output IDT, which transduces this wave back into an electrical signal. By comparing the input and output signals, we can quantify the measure which modulated the acoustic wave. Indeed, changes in amplitude, phase, frequency, or time-delay between the input and output electrical signals can be used to measure the presence of the desired phenomenon. The wave propagation on the piezoelectric substrate depends on the physical quantities like temperature and strain. All SAW sensors can be operated wirelessly by coupling the input IDT to an RF antenna and replacing the output IDT with a reflector. The wave passes through the delay line twice before arriving back at the input IDT transformed in an electrical signal sent to an antenna (the same transmitter antenna can be used).

SAW sensors can operate across a large temperature range and not require batteries. Furthermore SAW technology offers the possibility to transmit data with higher rates with respect to the RFID technologies, being investigated as potential sensor for SHM and Integrated vehicle health management (IVHM) [166] [167]. Moreover, more data can be collected at the same time, as for the sensor reported in Figure 17 where seven chips are integrated in the same device.

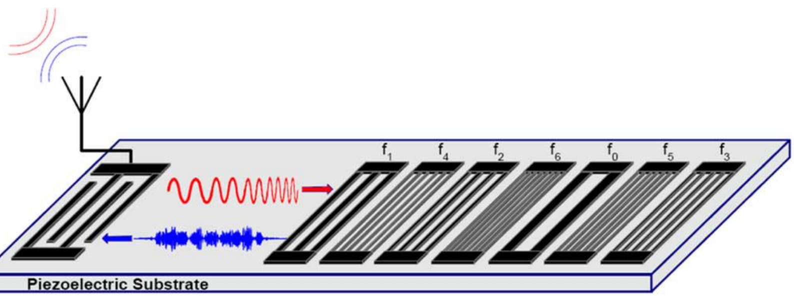

Figure 17 Schematic diagram of a seven-chip OFC RFID tag, reproduced from [166].

2.4.3 PATCH-ANTENNA Sensor

The patch antenna sensor consists of a layer of dielectric substrate, an antenna patch on one side of the substrate and a ground plane on the other side of the substrate. The ground plane and the antenna, both conductive, form an EM resonant cavity that radiates at distinct frequencies. The performance of the sensor is mainly related to the return loss, describing the radiation efficiency of the antenna, and the resonant frequencies at which the return loss is a local minimum. The patch antenna could be rectangular or circular, the rectangular shape radiates at two fundamental resonant modes; the TM_{10} mode whose electric field is parallel to the physical width of the antenna patch and the TM_{01} mode whose electric field is parallel to the physical length of the antenna patch. Tata in [168] shows that rectangular microstrip patch antennas could be used not only for communication between sensor and receiver, but also, as a strain sensor itself. The rectangular antenna only detects strain in two directions while a circularly polarized circular patch antenna could be able to detect strain regardless of its direction (see Figure 18) [169, 170].

The conductivity of the ground plane also influences the resonant frequencies. If a crack is present in the ground in the direction of the width, the current is forced to flow around it increasing the electrical length of the TM_{10} mode. Since the resonant frequency is inversely proportional to the electrical length, the resonant frequency f_{10} reduces with the crack growth. Instead the f_{01} and so the TM_{01} current flow is slightly affected by the presence of the crack being parallel to its current flow. Therefore, the resonant frequency f_{01} remains the same, or almost the same, as if there is no crack present. Instead, the presence of an inclined crack affects the current flows along both directions increasing the electrical lengths of both radiation modes. This will be reflected by changing both resonant frequencies, which will both shift toward lower frequencies.

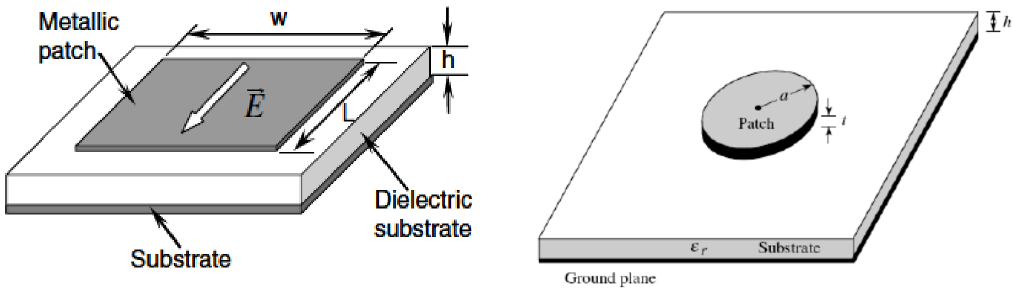

Figure 18 A typical a) rectangular, b) circular microstrip patch antenna

2.4.4 RFID Sensor

RadioFrequency Identification (RFID) identifies a class of device that use radio waves to automatically identify objects. Its power supply and data exchange are done via electromagnetic waves. An RFID system consists of two parts, an RFID reader that sends out a modulated RF signal to the RFID tag (consisting of an antenna and an integrated circuit chip

IC). When the signal hits the tag, a wave at a different frequency with the chip's information encoded in it, is "scattered back" to the reader.

A passive RFID system does not contain its own power source; so needs to gather energy from an outside font. The device becomes active only in presence of a reader. In particular, when a passive tag enters within an electric or magnetic field, the tag draws enough energy from that field to power itself and broadcast its information. Indeed, the chip receives power from the antenna and responds by varying its input impedance and thus modulating the backscattered signal. The chip often uses an amplitude shift keying (ASK) modulation, where the chip impedance switches between two states: one is matched to the antenna (chip collects power in that state) and another one is strongly mismatched.

RFID technology has founded different applications for sensing, such as strain sensors or for structural health monitoring. In the first application the antenna of the tag is a folded patch antenna responsible for the strain detection [171], while for SHM application a wireless sensor is integrated with a passive RFID that when activated, the chip responds with a digitally encoded signal that not only identifies the sensor but also contains information about the sensor state [172]. The use of the RFID tag allow the sensor to be implemented in an array, where different sensors can be activated individual following the RFID tag protocols (Figure 19) [173].

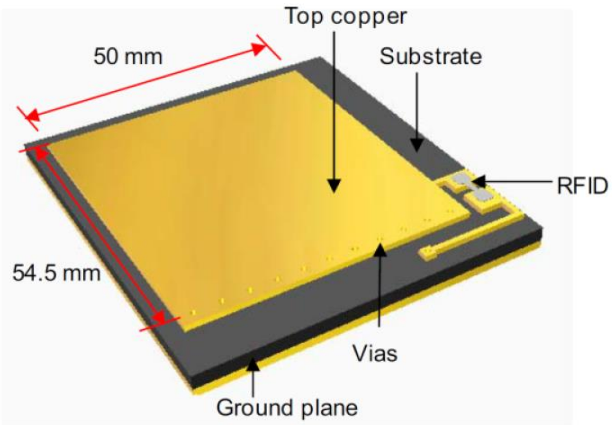

Figure 19 The RFID folded patch antenna strain sensor, reproduced from [173]

2.4.5 Metamaterials

Metamaterials are synthetic materials with a structure such that they exhibit specified properties, which are not readily available in natural materials. In particular, an electromagnetic metamaterial consists of periodically arranged metallic elements, which are less than the wavelength of incident electromagnetic (EM) waves in size. Microwave engineering and physicists, in recent years, have investigated and extended the range of metameterials that can manipulate electromagnetic waves and can exhibit some exotic electromagnetic properties that could find application as sensing systems [174]. These metamaterials are very well suited for telemetric sensing applications having the advantage to obtain higher quality factors (Q factors) [175] Split Ring Resonator (SRR) is one of the geometrical configurations used in the fabrication of metamaterials. Singh et al. analysed the inter-SRR distance and its number density in a fixed area and found that tailoring the periodicity of metamaterials can control the Q factor and the strength of the inductive capacitive (LC) resonance of SRRs[176]. The gaps between the ring of an SRR has been used for strain sensing, monitoring the change during compression and tension that affects the value of the capacitance causing a shift of the resonant frequency[177].

2.4.6 Structural component acting as Sensor

The structure sensed, could be itself used as a sensing system, monitoring how its electrical properties change. The integrity of the structures can be monitored based on the conductive properties of the samples, measuring the flow of current for conductive materials (CFRP); or evaluating the dielectric properties in presence of nonconductive samples (GFRP, Concrete). Data are read wiring the electrode directly to a reader or using a wireless circuit connected with the electrode.

The experiment reported by Matsuzaki and Todoroki [178] belongs to the first category. Two electrodes were attached to two sides of the CFRP composite and were connected to an oscillating circuit. Presences of cracks cause electrical resistance change, resulting in a variation of the oscillating frequency of the circuit. The resonant frequency of the circuit can be read wirelessly through an external antenna. The location of the electrode and the electrical current flow through the carbon fibre are shown in Figure 20.

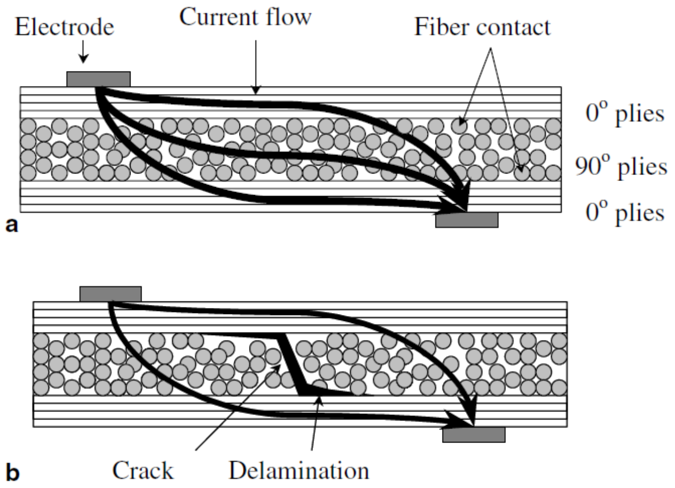

Figure 20 Schema of a practical structure of a carbon/epoxy composite when an electrical current is applied. (a) Electrical network structures of the fiber in a CFRP laminate. (b) The electrical network is broken with a delamination, reproduced from [178].

Another experiment reported by Todoroki et al. [179], for crack monitoring, is the use of CRFP structures as an antenna/sensor. More precisely as a dipole antenna, feeding one end of the dipole with current, and grounding the opposite end. If there is serious damage such as fiber breakage, the antenna properties of the CFRP may change. The damage can then be detected wirelessly by evaluating the change in the antenna property. In order to estimate the sensitivity of the antenna to the presence of cracks the experiment was set out to replicate Todoroki's important results. The CFRP were tested, as reported in Figure 21, both as dipole and monopole antenna, and shift in resonant frequency was found only if the damage caused a bending or a reduction of the samples.

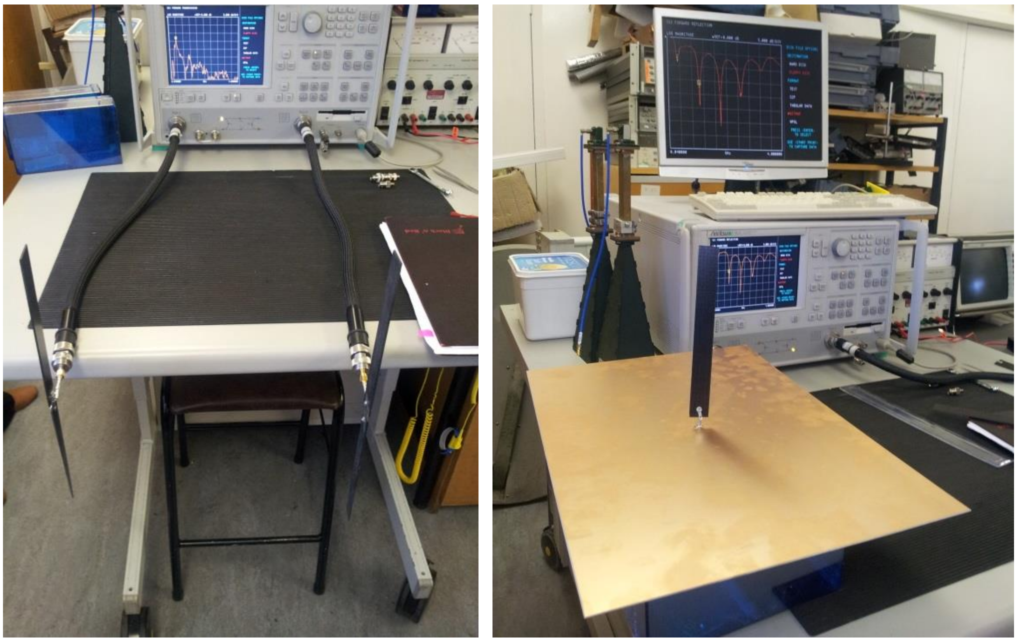

Figure 21 Experimental setup for wireless damage detection tests. The CFRP samples were used as a transmitting and receiving antennas, with two different configurations: a) as dipole antenna, b) as monopole antenna

Indeed, different samples were impacted and tested with both configurations, presenting the same resonant frequency as long as the length and the shape of the sample remained unchanged; even if the crack passed through the entire section of the specimen as reported in Figure 22.

Figure 22 Damaged CFRP rectangular specimen after impact.

Regarding the nonconductive specimens, damage causes a change in dielectric permittivities inside the composite material. Nassr and El-Dakhakhni applied two adjacent electrodes to the composite material from one side [180]. The dielectric material between two conductor plates, forming a parallel plate capacitor, acts as an insulator to increase the charge storage capabilities of the capacitor.

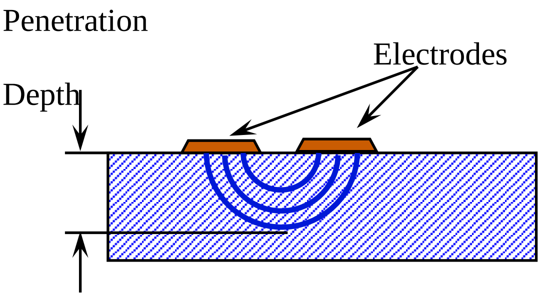

Figure 23 The electric field penetration depth throughout the material

The capacitance across the sensor depends on the dielectric values of the material compositions, material thicknesses and the sensor's geometrical parameters. The presence of delamination or other flaws could be associated with a change of the measured capacitances. The output could result in an increase of the Capacitance, in case of delamination, attributed to the low value of the dielectric permittivity of air ($\varepsilon_a = 1.0$) compared to that of the composite ($i.e. for\ Fiber\ Glass\ \varepsilon_{FRP} = 3.12$). Instead, in case of water intrusion, the high value of dielectric permittivity of water ($\varepsilon_{water} = 81$) compared to that of the FRP plate caused a decrease of the measured Capacitance. Another important factor, to take in account during the analysis of the data is the sensor's penetration depth, which indicates how deep the electric field effectively penetrates a test specimen or the material thickness, as shown in Figure 23.

3 3D twisted helical arrangement of fibres

3.1 Introduction

In this thesis, an innovative method has been presented to create a quasi-isotropic material that can provide pseudo-plastic behaviour, lead to superior impact properties and follow a lean manufacturing process. This innovative method has been developed in collaboration with Dr Michele Meo and Dr Fulvio Pinto and is now under filing.

This method aims to bring some of the rope's advantages to the composite field through the use of a "rope-like" fibres substructure as reinforcement in composites. In its more complete embodiment, the present invention involves the use of a 3-dimensional fibre reinforcement structure based on multiple bundled lengths of fibre substructures, at least some of which embody the underlying principle that they are built up of at least three fibre tows which have been helically wound. The effect of the twisted tows creates a "rope-like" fibre substructure with fibre reinforcement effective in three dimensions. Figure below shows the three-dimensional arrangement of each single strand that forms the wound structure.

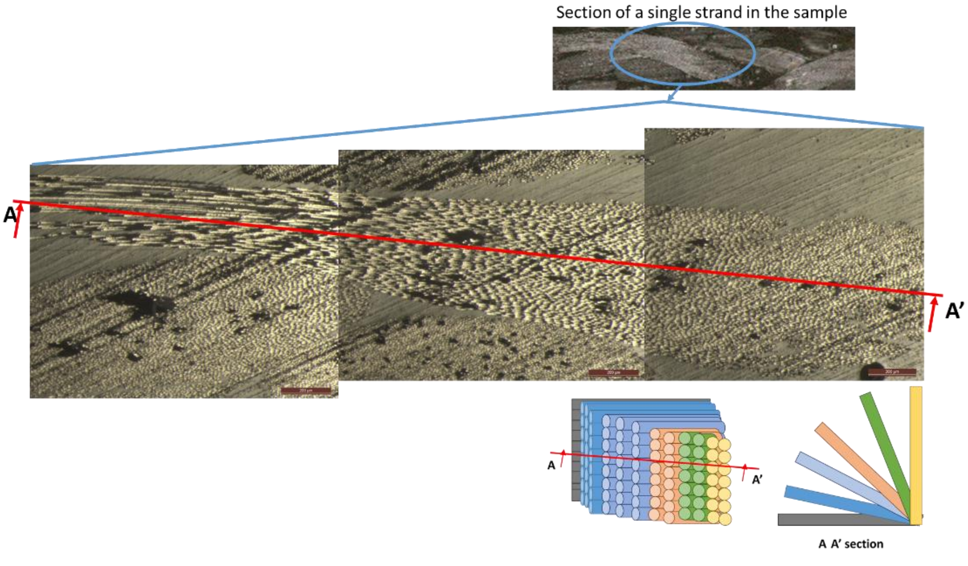

Figure 24 Optical microscope image of 3D twisted helical arrangement showing the orientation of the fibres along the cross section

As it is possible to see from the image, the fibres start from 0 degrees (parallel to the image direction) looking like a straight line on the left side of the image and change their orientation in space until they reach a complete perpendicular arrangement on the right side of the same image, where it is possible to see only their circular section. The proposed invention overcomes common issues related to the laminated composites industries. For many applications, it may be desirable to produce more consistent properties in all three dimensions. As reported in the previous chapter, current solutions to create 3-dimensional composites with quasi-isotropic strength and stiffness in all three directions are typically complex, lengthy, expensive, and to the detriment of in-plane properties. Moreover, laminated composites are often obtained by multiple unidirectional plies or fabric layers stacked together. Due to directionality of the mechanical properties of the individual plies (strong in the direction of the fibres and weak in the perpendicular direction), there is the need to stack layers of material in different directions to achieve in-plane quasi-isotropic properties like metals. This manufacturing process is lengthy and complex. Our solution can simplify the current manufacturing process by reducing or eliminating the lamination process (stacking a sequence of layers) since a quasi-isotropic material configuration could be achieved using a single or fewer 3D twisted rope fabric layers. Mechanical, physical and electric magnetic property can be obtained by blending different type of materials. This allows one to achieve tailored properties, such as the ability to resist unravelling of tows when twisted, by the insertion of specific numbers of shape memory wires within the twisted configuration. A new range of applications can emerge when fibre reinforcing materials extend beyond glass and carbon fibres and include yarns of different nature (metal, polymer, etc.,) that can be shaped in the same way through fibre placement techniques (weaving, tape laying, filament winding, etc.). Fibres blending can be done by mixing uniformly different fibre types in the system, taking the name of intimate blending, or by positioning fibre in specific location to obtain desired characteristics taking the name of structural blending. Finally, composite materials generally suffer a lack of ductility (small failure strain) as metals, lacking the mechanism to absorb energy while composites manufactured using the new 3D structure offer an improved mechanism to absorb energy and in certain conditions can show ductility-like behaviour. In addition, under impact loading, our proposed single layer fabric does not experience delamination unlike an equivalent traditional composite laminate. Improving the properties through the z-direction can reduce the requirements for conservative designs leading to weight saving and to safer structures.

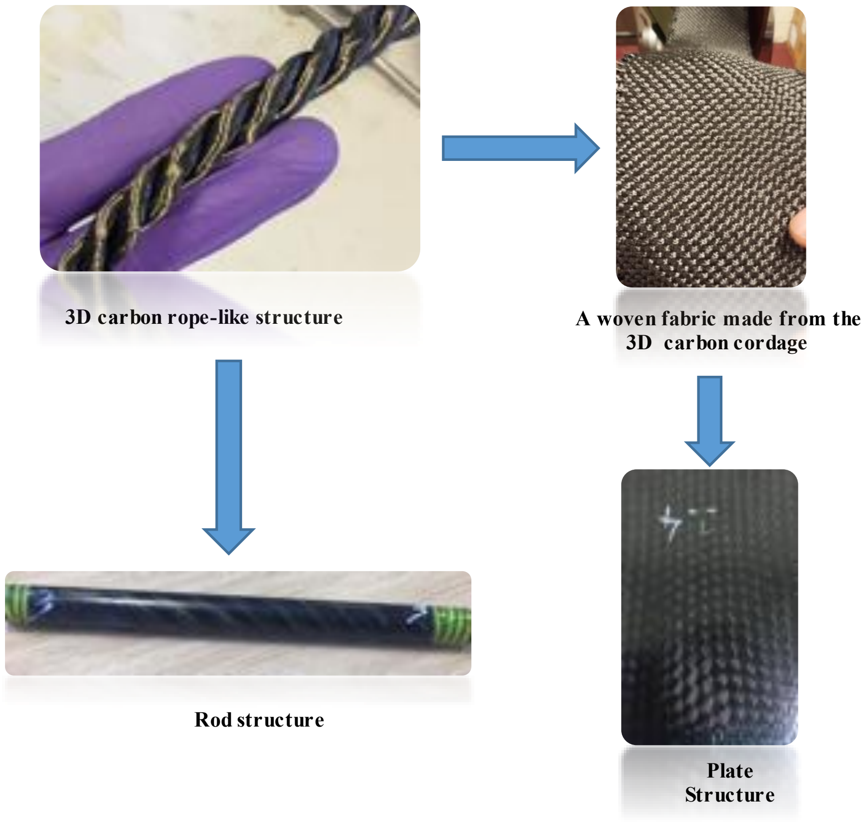

Figure 25 Flow chart for 3D twisted rope-like structures

As illustrated in Figure 25 the proposed invention has been investigated in two different geometrical arrangements:

a) In the first case the three-dimensional arrangement of the fibres can be used to manufacture elongated rod-like structures which comprise a single twisted element. In particular, at least two strands formed by multiple tows are first twisted on themselves and then together to form a balanced helically wound arrangement. This quasi-isotropic arrangement of the dry fibres can be impregnated with resin by direct infusion of the dry reinforcement. Generally, this embodiment is aimed at the manufacturing of thick rods that can be employed for the development of frames or other tubular assemblies.
b) The second embodiment is based on multiple fibres in a helically wound arrangement as for the first case, arranged together to build up a fabric-like or unidirectional reinforcement structure. The helical fibres are used as substructures and can be woven or stitched together using conventional techniques. The resultant 3-D dry reinforcement structure can be impregnated with resin to create a composite material which can potentially possess the same or similar strength and stiffness in-plane and out-of-plane. If the reinforcement material is used in a unidirectional manner, transverse and

longitudinal properties will also be similar. A composite manufactured with the proposed solution would not suffer delamination problems, because of increased properties in the third direction and since similar properties could be achieved in all three directions a single layer could be used rather than layering multiple traditional straight fibre layers.

The presented arrangement of the dry fibres can be used in their dry form, impregnated with resin to create prepreg, or solid parts (by direct infusion of the dry reinforcement with resin that is subsequently consolidated).

3.2 Rope History: from ancient pyramid to space elevator

The invention of rope is one of the most ingenious ideas of ancient mankind. Men discovered that they could take short pieces of fibres or coarser strand found in nature, twist them together to make long, strong yarns, and then twist the yarns and turning them into strong extended lengths of rope which had numerous uses. The twisting operation is required to hold the fibres together in a yarn. As the fibres wrap around each other, they press inwards and grip each other. The ability to spin or plait fibres into ropes or cords is one of the oldest of man's primitive skills. The true origins of the rope maker’s craft are lost in antiquity [181]. Cave-painting of late Palaeolithic or Mesolithic depicting a man climbing down a cliff using a rope has been found in eastern Spain. The manufacturing process for making rope is simple and today's complicated machines follow precisely the same stages used in the past. Since ancient time ropes were made twisting or braiding fibres by hand. Probably the first civilization to develop special tools to make rope were the ancient Egyptians. In Figure 26 are illustrated three rope-makers making a two strands rope. Above the labourers are depicted the tools of their trade, a bundle of raw material, and four finished coils of rope.

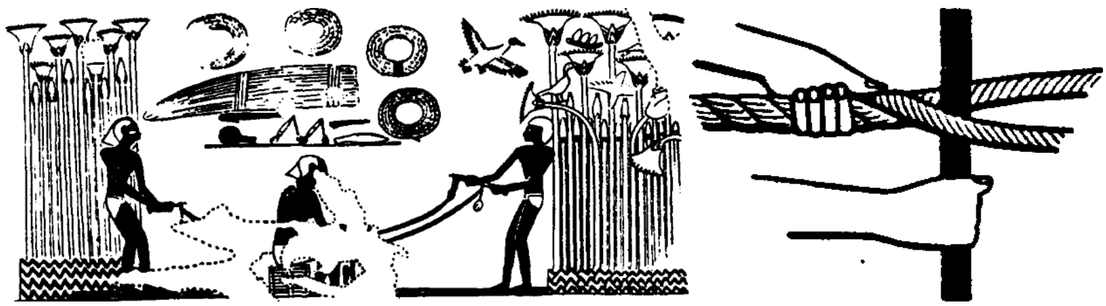

Figure 26 Figure 285—(Left) Rope-laying. From a tomb at Thebes, c 1500 b.c. (Right) Detail showing how the man in the centre controls the closing of the two strands, reproduced from [182]

Although the term rope is of common knowledge, its precise definition is not so straightforward. There are different definitions [183-185] for rope and cordage[3], we refer to the one reported in the American Society of Civil Engineers [186]:

Rope:

1. A long, flexible assembly of fibres, laid, braided, or bundled together, to serve as a tensile strength member.
2. By tradition and some US Government regulations, cordage greater than 3/16 in. diameter (see Cordage).
3. By British Standard, cordage greater than 4mm diameter.

Cordage:

1. The product formed by twisting or braiding fibres into an essentially circular cross-section, which is capable of sustaining load. Usually applied to smaller products.
2. Traditionally and by some US Government regulations, under 2/32 in. diameter = twine, to 3/16 in. = cordage and above = rope.
3. The collective term for rope, line and cord.

Ropes have countless application, they have been used for hunting, pulling, fastening, carrying, lifting, climbing, etc. The main advantages of using twisted fibrous structures are for their strength and flexibility. The use of bundle of fibres/wires/threads twisted together offer several advantages over a single strand of the same cross sectional area. The use of thin fibres often shows higher strength than thick ones made of the same material. A good example is drawn polymer fibres that present better mechanical properties than the same polymer made with ordinary process. Better properties can be due also to the unlikely probability of containing a strength limiting defect due to the smallest dimension as for the case of glass fibres. The use of multi-stranded rope shows more flexibility than a single strand of the same diameter as for example of metal rope. Another great advantage is that in a multi strand setups if one or few fibres fail the rope remains still intact, and broken fibres can still contribute to the tensile strength of the entire rope [187]. Moreover, due to the wide range of materials and manufacturing methods used for manufacturing ropes, their properties can be tailored to

[3] In the context of this thesis, no real difference is implied and the terms Rope and Cordage can be used interchangeably.

specific applications. Nowadays, industrial twisted fibrous structures are mainly applied to load-carrying situations such as fastening, transporting, lifting and impact operations.

The future of rope making, and hence improving their properties is directly linked to improvements in materials and arrangement configurations of the fibres. Over the years, rope makers have refined their machinery to allow different configurations and reduce fibre damage. Nowadays it is possible to braid or twist ropes covering a wide variety of diameters and manufacture hollow, solid or flat ropes, and new machines are emerging able to perform complex and programmable patterns with the use of robotic arms that reduce fibres damage that usually occurs with traditional machines. On the other side the discovery of new materials has allowed rope makers to reduce rope diameters while maintain the tensile strength and improving the resistance of weathering and abrasion, achieved mainly with the use of external jacket that cover the rope.

Although a lot of progress has been made in the rope industry, there are still a lot of challenges to overcome. Steel cable used for elevators does not allow to reach high altitude due to their sheer weight. Indeed, for the Burj Khalifa tower in Dubai (828 metres), people must switch lifts to go above the 500-metre mark. The challenge becomes even higher when we speak of cable for space elevators. It has been estimated that an untampered space elevator cable would need a material capable of sustaining a length of 5000 kilometers of its own weight. That means that nowadays, although there are undoubtedly many obstacles to overcome, "Finding the material to make the tether is the main remaining technological challenge," says Peter Swan, President of the International Space Elevator Consortium. In the past years, different attempts have been done to find a material able to withstand this weight with a large tensile strength/density ratio. The leading contenders are cables made of carbon nanotube [188] or the new emerging diamond nanothreads [189]. It is expected that a new generation of materials combined with emerging technologies and innovative material combinations will open the rope manufacturing process to new fields of application.

3.3 Tensile behaviour of rope structures

The primary mode of deformation of twisting a rod to a small strain is pure shear, while when a yarn is twisted, there is virtually no resistance followed by an immediate and catastrophic shear failure. Resistance to twisting yarns is very low and it only builds up significantly at large strains [190]. Tensile behaviour of rope is complex and when tension is applied to a twisted rope it will generate torque, which, unless fully resisted at the termination, will cause the rope to twist to relieve the torque. The twisting, or untwisting, will contribute to rope elongation in addition to the direct effect of tension. So, when the rope is stretched, the yarn deformation not only includes tensile, but also bending and torsional deformations that are thus inextricably linked. Figure 27d shows several forces acting on the rope when subjected to tensile load. The force in the same direction of the load applied, red arrow (1), result in rope elongation. The force, in green (2) parallel to strand axis compact the strand by stretching it and hence reducing the rope diameter. The force represented by the blue arrow (3), is related to the type of twist inserted in the strand and result in a tendency of unlaying of the rope. The force acting toward the centre of the rope, yellow arrow (4), generate a radial pressure on the rope resulting in a tightening compression of the strand. Hearle et al [191, 192] presented a classic theoretical treatment to explain the yarn mechanics. He analysed continuous filament yarns and extended the theory to include also spun yarns. The translation from fibre properties into rope properties is largely dependent by the angle at which the fibres lie in respect to the rope axis. They considered an idealised geometry illustrated in Figure 27, where each filament follows a helical path of constant pitch h and radius r, with r going from zero to R (where R is the rope diameter). The helix angle θ increasing from 0 at r = 0 to a α at r = R. For each turn the filament has a length l, defined by the triangles in Figure 27b, reaching the maximum length of L on the rope surface.

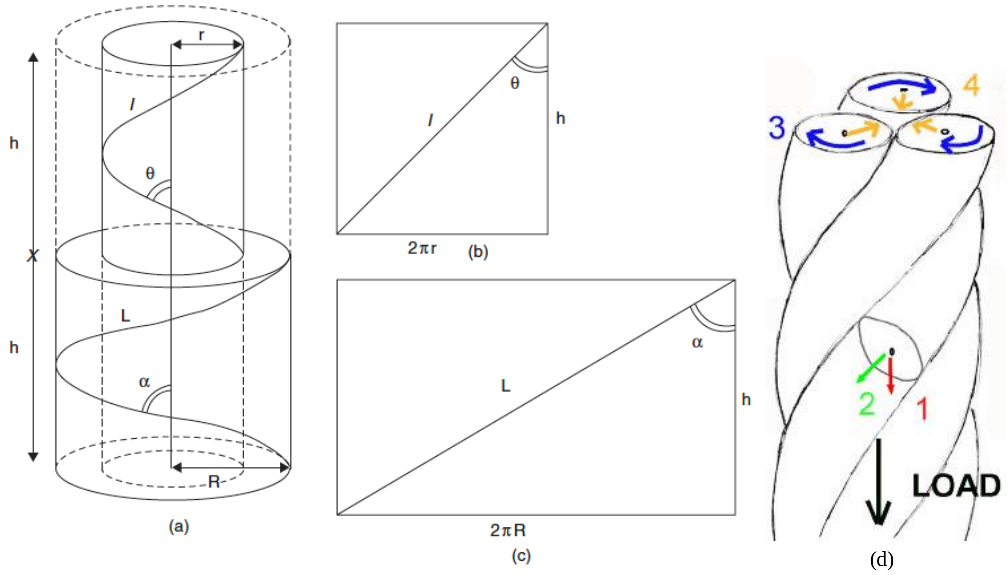

Figure 27 (a) Idealised twisted yarn geometry. (b) and (c) Opened-out diagrams at intermediate and surface radii, reproduced from [183], (d) forces acting on the rope.

Based on this geometry, Hearle found that there are four major factors that influence the tensile properties of ropes:

1. *Obliquity*: the contribution to rope stress of the single fibre lying at an angle θ is reduced by specific factor that depends on the helix angle θ. This factor can be determined considering the following reasons:
   - the fibre elongation is less than the rope elongation by cosθ,
   - the fibre length is longer than the rope length by secθ, hence the strain is reduced by $\cos^2\theta$;
   - the component of fibre tension acting along the rope axis is given by cosθ;
   - the stress on the rope acts on a larger area than the stress on the fibre by a factor secθ, hence stress is reduced by $\cos^2\theta$;

   The factor cosθ comes four times, with the stress and the strain both reduced by $\cos^2\theta$, hence to a first approximation, we therefore have a conversion factor for stress at a given strain between yarn and rope, which is the mean value of $\cos^4\theta$ (it can be shown that the $\cos^4\theta$ through the idealised yarn illustrated in Figure 27 is $\cos^2\alpha$).

$$\frac{rope\ specific\ stress\ at\ a\ given\ strain}{fibre\ specific\ stress\ at\ same\ strain} = mean\ value\ of\ \cos^4\theta \qquad (1$$

   This analysis was extended to accommodate the more complex spun yarns, taking in account the reduction in tension in the surface layers of the yarn as a consequence of using staple fibres. A second component was added to the conversion factor, yielding to the following equation, in which the terms in the bracket are equal to 1 in case of continuous filament yarn (as for the case treated in this thesis):

$$\frac{rope\ strength\ (or\ modulus)}{fibre\ strength\ (or\ modulus)} = \cos^2\alpha(1 - k\csc\alpha) \qquad (2$$

   where k is equal to:

$$k = \frac{\sqrt{2}}{3L_f}\left(\frac{aQ}{\mu}\right)^{1/2} \qquad (3$$

where L_f is the fibre length, a is the fibre radius, Q is the migration period and μ the friction coefficient. The term $\cos^2\alpha$ yields a decreasing strength with the increase in twist angle, while the term in the bracket yields an increasing strength with twist. This explains the complex nature of twisted fibres under tension, which have a unique strength generating mechanism. The force that tends to break the structure also strengthens it. Figure 28 illustrates the plot of yarn strength versus surface helix angle for staple yarn structures.

Figure 28

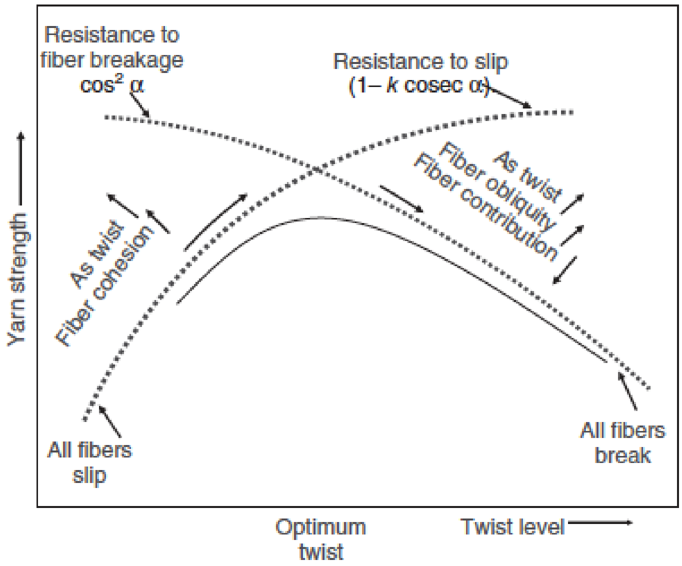

Figure 28 Yarn strength versus surface helix angle (twist level), reproduced from [193]

At low helix angles, as the twist slightly increases, the force required to stretch the structure increases due to the radial pressure in the yarn which causes binding between fibres to strengthen as the twists increase. This trend will continue until the obliquity effects in the fibres become dominant. Fibres are so inclined (high helix angle) that their contribution to the strength will decrease (the component of fibre stress contributing to the strength is proportional to the square of the cosine of the helix angle of the fibre path). Because of these two competing effects there exists a twist level, called optimal twist, determined by the intersection between the two trends, as shown in Figure 28 where the maximum yarn strength is achieved.

2. *slip at fibre ends*: this factor play a part only for discontinuous filament structures. In which, as mentioned before, discontinuous fibres are hold together in twisted structures by radial pressure. At the end of the individual fibre there will be zero tension (see Figure 29), but due to the frictional resistance to slip between fibres, tension builds up along the fibre.

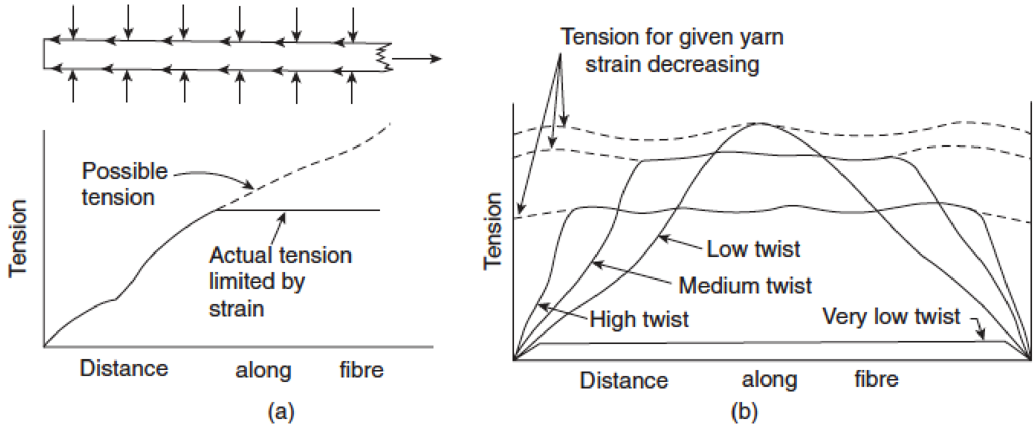

Figure 29 (a) Build-up of tension along a gripped fibre. (b) Effect of twist level, reproduced from [191].

As illustrated in Figure 29, at high twist the tension is considerably reduced mainly due to obliquity effect, but the slip length is small. As the twist is reduced the tension increases, until an optimum twist level is reached for a maximum tension. Beyond the low twist line reported in Figure 29b, any further reduction of the twist causes the fibres to be fully gripped nowhere, and they can slide over one another. For a specific rope geometry and for a given fibre friction it could be possible to predict the minimum staple length and forecast the rope strength. Moreover, the use of shorter fibre in a twisted structure, makes the structure more elastic than the same structure made with continuous filament. Indeed, for dynamic climbing line, core fibres are usually made with synthetic fibres chopped into shorter length and twisted, which makes the rope more elastic. Another importance feature, is the aspect ratio of fibres. Indeed, long, fine fibres will be more effectively gripped than short, coarse fibres.

3. *variability, load sharing and weak places*: Any weak spot along the rope or the fibre length can act as stress raisers and is where breaks will occur. Moreover, if fibre properties are different, load will be unevenly shared. The effect of rope or fibre break is influenced by the transfer of stress from one fibre to another. When fibres start to break they can continue to contribute toward the overall system strength carrying its own load thanks to the effect of load sharing. The importance of lateral pressure on load transfer form fibre to fibre in a twisted fibrous structure was recognized as far back as Galileo [194]. In 1769 Duhamel [195] endeavoured to ascertain what degree of twist in rope would produce the highest strength. At the time ropes were made usually, so that only one third of the length of the yarns was absorbed in twisting, instead he tested the effect of rope made with a different number of twists. The results shown that ropes with

the smallest degree of twist led to high strength. Those conclusions guided Duhamel to try making ropes without any twists (with yarn being wrapped round to hold them together). These ropes had great strength, but very little durability (this type of ropes where unfit for most of the purposes). Over the years, the use of parallel-yarn rope has been possible thanks mainly to the use of braided jacket to hold the fibres. Parallel-yarn(untwisted) have shown a different behave from twisted structure mainly because the effect of fibre interaction is negligible. Although rope made with parallel yarns do not experience reduction in stress at a given strain due to obliquity, present a conversion factor from yarn to rope comparable to that used for twisted structure. The only source of gripping force between fibres comes from the radial pressure of the external jacket and the pressure is kept constant with increase in rope tension. Hence the yarn is free to break at its weakest place, and they breaks independently. Instead, for twisted structure under tension, due to stress transfer the rope tend to break at its single weakest place instead of having each yarn to break at its weakest place. This cause to an initially increase of strength with the insertion of twist, followed by a decreasing in strength, with a further increase of the inserted twist, due to fibre obliquity.

4. *changes in rope structure, bedding-in*: another factor is the indeterminacy of rope and yarn structures. Packing of the fibres can assume different geometries according to the number of strands and fibre properties and to the number of twist. When the rope is put under tension, the strands can be compressed into a wedge shape, and change in geometry affects their mechanical properties. Another phenomenon to take in account is the bedding-in, in which a rope under tension for a number of cycles, increase in length due a tightening effect of the rope structure.

3.4 Rope Manufacturing

This paragraph gives the details on the procedure adopted for the manufacturing of ropes for this research. All ropes manufactured in this research are made by three strands, except if otherwise specified. Three strands ropes have been the commonest form of rope for thousands of years. The advantage of three strands rope over two strands has been known for centuries, as illustrated by the metaphor on the use of rope in the book of Exodus in the Bible. Ecclesiastes 4:12 states "*Though one may be overpowered, two can defend themselves. A cord of three strands is not quickly broken.*" Moreover, three strands ropes when twisted do not require a core or central strand as for ropes made with more than three strands. Indeed, the angles formed by the union of the three cylindrical strands are so obtuse that the pressure of the operation of laying or closing the rope causes the strand to fill them up completely. In this research, ropes and short length cordages have been manufactured using a tailored equipment, designed on purpose for the type of fibres and samples to manufacture. The machine is illustrated in Figure 30 and three independent parts can be identified as follow:

1. *The twisting machine*, consisting of three or more hooks that can be activated by an electric motor. The number of hooks is related to the number of strands to twist.
2. *The sledge*, the hook on the sledge is not fixed to the structure and it is connected to a weight that put the strands in tension during the twisting operation. The distance between the sledge and the twisting machine can be adjusted according the desired rope length. Each rope made by this method is tailor–made to the exact length required. The longest rope that can be made on our premises is around 3.5 meters. With the proper adjustment to the machine is possible to manufacture longer ropes.
3. *The top*, keep the strands apart while the yarns are twisted and twist the strands together as it moves from the sledge to the twisting machine. In the second prototype of the metal-rope machine (Figure 30b), all parts in contact with the fibres were made in Teflon to reduce damage to the fibres.

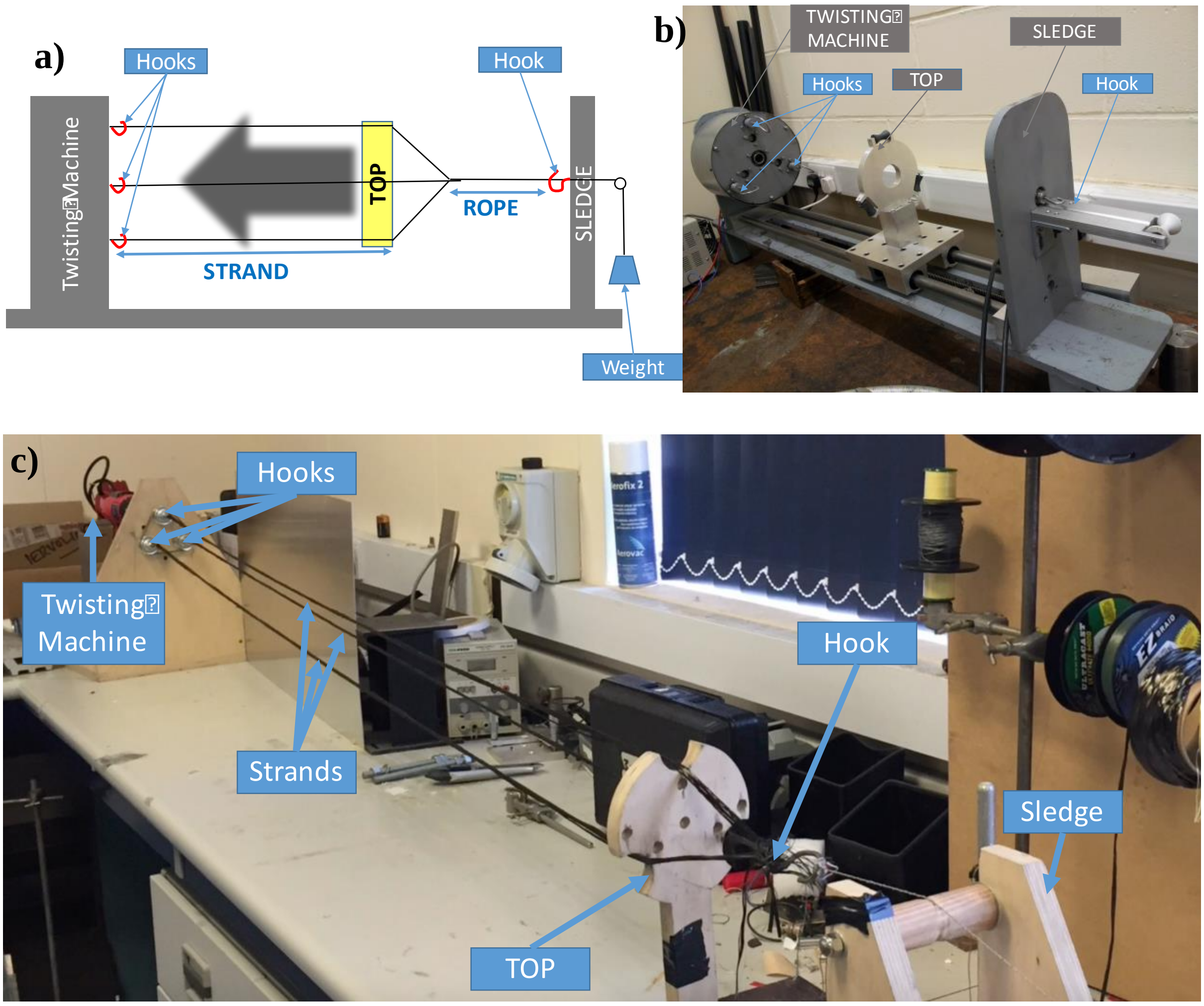

Figure 30 a) Schematic representation of the rope making machine; b) Metal-Rope making machine – Second Prototype; c) Wood Rope making machine – First prototype

The manufacturing process is based on the traditional way of making a three-strand rope using hand held equipment or with the rope walk. Some modifications have been introduced to achieve specific properties. The whole process can be divided in the following steps:

Stage 1 - setup

Yarns/Tows are run from the three hooks on the twisting machine to the single hook on the sledge. The number of hooks used on the twisting machine can be increased or decreased in function of the number of strands desired for the rope manufactured. The number of tows for each strand is added increasing the number of fibres windings between the hooks on the twisting machine and the sledge. The final diameter of the rope must be decided during this step. The distance between the sledge and the twisting machine depends on the length of the rope to be made (typically the final rope is approximately two thirds of the length of the yarns used). The hook on the sledge must be in tension during all the setup in order to have all the yarns straight.

Stage 2 – Strand Twist

Twist is inserted into the separate strands by twisting the hooks on the twisting machine. The top is fixed during this operation and it is used to keep the strands apart while the twist is put in. The strand twist is usually made as high as possible avoiding any kink.

Stage 3 – Rope Twist

When the desired number of twists is put in the single strand, the rope is made twisting the single strands together when the single hook on the sledge is released. The high torque in the strands causes the hook to rotate. The level of twist is controlled by moving the top in the direction of the twisting machine. While strand twisting is due to the hooks on the twisting machine, the rope twist is due to the hook on the sledge that can revolve freely, allowing the strands to twine up together as the top is moved forward. Due to the construction of the machine, the twisting orientation of the single strand is opposite to the twisting orientation of the rope. Twist causes the rope lengths to contract, so the hook on the sledge must be left free to move. To balance the rope (so it will not snarl up) a backtwist can be put in the rope turning the hook on the sledge (this operation is not always required).

Stage 4 – End

Once the rope is complete, it must be bound at its ends by some means to prevent untwisting. According to the applications and the type of material used for the rope manufacturing, different techniques are adopted to prevent the rope from unravelling. Different traditional techniques and two innovative solutions are reported in the following section.

3.4.1 Rope locking mechanism. Methods adopted to prevent fraying

Twisted ropes present a natural tendency to fray. Different techniques have been adopted over the years to prevent strands from untwisting. Fibres can be hold together temporarily by a constrictor knot or by using a self-adhesive plastic tape. Permanent solutions can be performed by applying a semi-permanent rubbery coating by dipping the cut end of the rope in a bath or by applying external polymer jacket. Mechanical hold can be applied using a permanent ending aglet (typically a metal or plastic cap) placed at the end of the rope. Fraying can be prevented also by back splicing; in which the strands of the end of the rope are spliced directly back into it. Synthetic fibres can be held together by simply melting the cut end by heating blade or flame. Although different methods have been presented to avoid fraying of the twisted fibres, as reported earlier, two alternative methods were investigated and presented in this section. The alternative methods present two main advantages, introducing unravelling resistance of tows directly during the rope manufacturing process and the properties will be for the whole length of the rope. Hence, the rope can be easily cut to the desired length without worrying about unwanted fraying. In the first method, the resistance to fray is given by inserting Shape Memory Alloy (SMA) wires within the stands, while the second method the tows have been treated with adhesive spray.

3.4.1.1 Additional material inclusion (SMA)

Shape memory alloys, nitinol wires (NiTi) were introduced in two different steps of the rope manufacturing process: within the tows before the twisting operation (stage 1), as illustrated in Figure 31a and within the strands before twisting them to make the rope (stage 2). The embedded nitinol wires present the ability to retain the shape of the rope when this is cut by exploiting their shape memory effect. To activate the shape memory effect, the twisted shape of the rope is registered while still in tension by increasing the temperature of the entire rope (see Figure 31b). Once the shape memory effect is activated, if the rope is cut, the material is able to retain its initial shape avoiding unravelling of the strands

a) **b)**

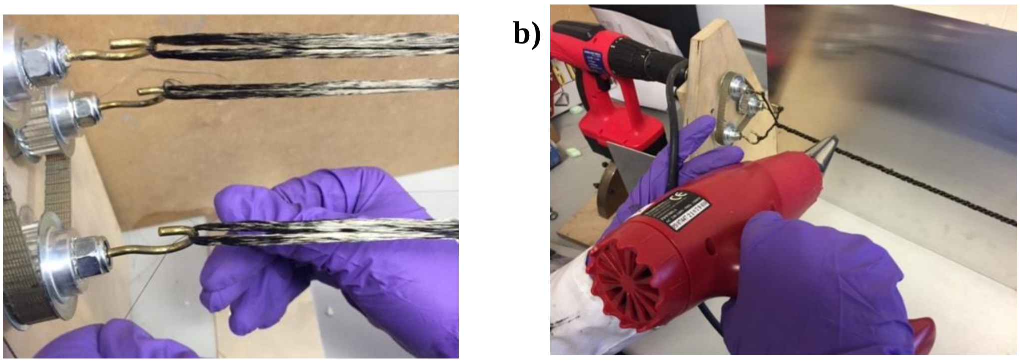

Figure 31 a) SMA inserted within the strands; b) activation of the shape memory effect by heating the rope.

The unravelling properties have been tested by visual inspection cutting the rope and laying the rope freely to move on a table. The effects of the nitinol wires were tested on cordages and on ropes, before and after the activation of the memory effect. Cordages in three strands configuration were manufactured with two carbon tows 12K T800 and two nitinol wires for each strand (see Figure 32 and Figure 33).

Figure 32 a) three strands cordage with Nitinol wires inserted in the first stage; b) fraying of the strands after cut the cordage without activating the Nitinol wires; c) unravelling effect of the cordages after activating the Nitinol wires

The presence of nitinol wires gives the cordage the properties of not frays, regardless of the stage in which the wires are inserted, only if the shape of the cordage is registered by increasing the temperature of the twisted bundle.

Figure 33 a) three strands cordage with Nitinol wires inserted in the second stage; b) fraying of the strands after cut the cordage without activating the Nitinol wires; c) unravelling effect of the cordages after activating the Nitinol wires

Ropes in three strands configuration were manufactured with twenty carbon tows 12K T800 for a total diameter of 10 mm and were inserted ten or twenty nitinol wires for each strand during the first stage. The sample with ten wires for each strand after cut shows fraying (see Figure 34) of the strands although the shape of the rope was registered with the heat gun. Instead, the sample with twenty wires for strands retains the twisted configuration also after cutting (see Figure 35).

a) b)

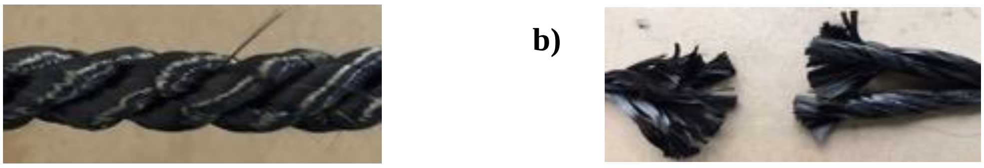

Figure 34 a) three strands rope with 10 Nitinol wires inserted during the first stage; b) frying of the strands after cutting the rope

a) b)

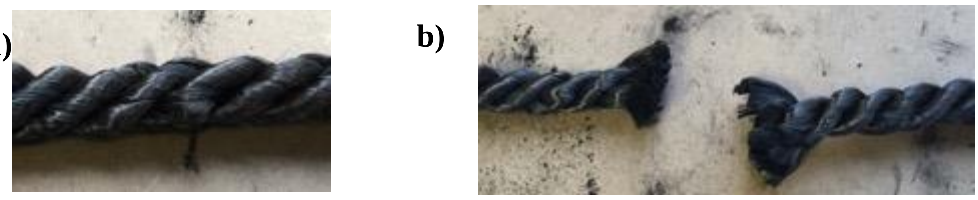

Figure 35 a) three strands rope with 20 Nitinol wires inserted during the first stage; b) unravelling effect of the rope after activating the Nitinol wires

As for the cordage, the effect of the SMA wires was effective only after heating the rope (see Table 2). In conclusion, the use of nitinol wires show good properties to record the configuration of the twisted bundle if properly heated. The rope samples illustrate that the unravelling effect of the SMA is dependent on the number of tows per strand.

Table 2 Effect of the nitinol wires on carbon cordages and rope for different configurations.

Materials	Additional material			
	Cordage		Rope	
	NiTi in stage 1	NiTi in stage 2	NiTi in stage 1	NiTi in stage 1
Carbon Tow 12k – T800	2x3	2x3	20x3	20x3
NiTi wires	2x3	2x3	10x3	20x3
Diameter [mm] ± 0.3	3.0	3.1	10.0	10.0
Unravelling property	Yes	Yes	No	Yes

3.4.1.2 Fibre treatment (adhesive spray)

Fibre treatment requires the application of a specific adhesive (Aerofix) on the surface of the tows before the twisting operation. According to the manufacturer, Aerofix is a spray adhesive which has been formulated to hold glass/carbon fabrics in place in the moulds during the resin infusion process. Ropes and cordages in three strands configuration were manufactured with twenty and two carbon tows 12K T800 respectively, for a total diameter of 10 mm for the rope and 3 mm for the cordage (data reported in Table 3).

Table 3 Effect of the nitinol wires on carbon cordages and rope for different configurations.

Materials	Fibres modification	
	Cordage	Rope
Carbon Tow 12k	2x3	20x3
Adhesive spray	Stage 1	Stage 1
Diameter [mm] ± 0.3	3.0	10.0
Unravelling property	Yes	Yes

The adhesive is compatible with the traditional resins used for composite manufacturing so that it will not create discontinuities in the cured part once the reinforcement is infused with resin. Moreover, adhesive is clear to avoid unwanted visible traces and is easy to use allowing rapid coverage of large areas. As reported in Figure 36 and Figure 37 the use of the adhesive spray helps to keep the carbon yarns in place and avoids untwisting after cutting the rope/cordage.

a)

Figure 36 a) three strands cordage with tows treated with adhesive spray; b) unravelling effect of the cordages after cut

a)

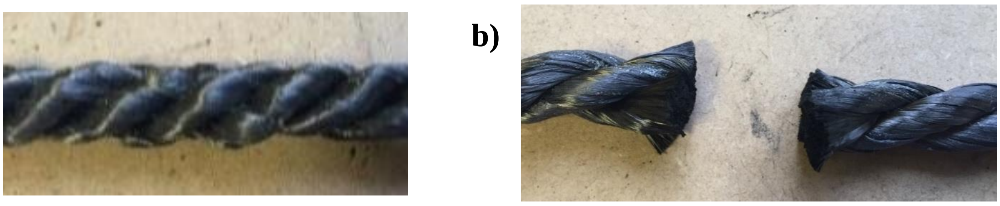

Figure 37 a) three strands rope with tows treated with adhesive spray; b) unravelling effect of the rope after cut

3.5 Cordage Manufacturing

Cordages manufactured with the rope machine illustrated in Figure 30 can have a maximum length of 3.5 meters, with the configuration in use in our premises. To use the cordages for fabric manufacturing, the cordage length must be long enough to be fed continuously within the loom. Cordages have been manufactured using a modified ring and doubling twisting machine (see Figure 38). The machine was designed and manufactured in collaboration with Galan Textile machinery (Spain) with specific adjustment to work with carbon fibres, with the possibility to twist hybrid bundles of wires and fibres with and without a central core.

Figure 38 ring and doubling twisting machine

The cordage manufacturing follows the same steps seen before for the rope, with the main difference that the process is continuous allowing to produce longer cordage. The twisting operation involves two main steps. In the first step, one or more yarns are fed in the machine and twisted together to form a single strand. Once the desired strands (usually three or four) are ready, they are reintroduced in the machine and twisted together to obtain the cordage (the final rope-like structure). To avoid any instabilities in the geometry of the final product, the cordages have been manufactured with the strands twisted in the opposite direction of the one used to twist the yarns (regular lay[4]). In other words, if during the first twisting the yarns were twisted in a clockwise direction to form a single strand, when more of these strands are twisted together in the second twist operation, the twisting direction will be anti-clockwise and vice-versa. Indeed, due to the opposite direction between the two twists, the final cordages are less likely to untwist or kink. This helps to give more stability to the twisted structure.

According to the ISO 2 [196] a left-handed twist is indicated with the upper-case letter S, while the right-handed twist with the letter Z (see Figure 39).

Figure 39 Illustration of the S and Z naming convention [197]

The second twist operation denotes the angle of the strands respect to the cordage axial directions. Being relevant for our application, this parameter has been investigated and different angles have been correlated to the twisting operation. Another essential factor is the strength of the cordages and hence damage of fibres must be avoided or minimized. Several tests were carried out at the Galan premises to establish the correct setup of the machine. Cordages were inspected by visual inspection, looking for defect, damaged areas and geometrical instabilities.

[4] The helix or spiral of the yarns and strands in a cordage is called the lay

Figure 40 JBA 850 - J Bot SA instrument Tensile Machine

Damaged fibres were checked using the cotton-technique (a pad of cotton is rubbed on the rope to collect the broken filaments that are then analysed), while their mechanical properties were evaluated using a tensile machine (JBA 850 - J Bot SA instrument Tensile Machine with a load cell of 5kN which is part of Galan testing equipment, Figure 40) to measure the maximum load reached by the different products. The results from the tests are collected in the Table below which indicates the different process parameter used for each configuration and the relative maximum load as measured from the tensile machine.

Table 4 - results of the experimental campaign on the first twist variables

Test Label	*TPM*	*rpm*	*spring diameter*	*Tow Tension*	*Feeding Setup*	*cursor*	*Tensile strength [N]*
1a	160 S	1600	1.4 mm	160 gr	single hole	metal 6500 mg	248.9
1b	160 S	1600	1.4 mm	160 gr	multiple holes	metal 6500 mg	383
1c	160 S	1600	0.9 mm	90 gr	single hole	metal 6500 mg	383
1d	160 S	1600	0.9 mm	90 gr	multiple holes	metal 6500 mg	451.9
2a	120 S	1600	0.9 mm	90 gr	multiple holes	metal 6500 mg	675.3

3a	100 S	1600	0.9 mm	90 gr	single hole	metal 6500 mg	682.5
3b	100S	1600	0.9 mm	90 gr	multiple holes	metal 6500 mg	748.2
3b bis	100S	1600	0.9 mm	90 gr	multiple holes	nylon 6400 mg	822.8
3b ter	100S	1200	0.9 mm	90 gr	multiple holes	nylon 6400 mg	832.5
4a	40S			*handmade*			1463.9

Several parameters were taken in account during this experimental campaign and they will be analysed one by one.

3.5.1 Geometrical disposition of the wires during the twisting operation in the ring twister.

Four tows of Toray T800HB-12K-50B (4600Dtex x 4 = 18400Dtex) were twisted together using two different configurations and analysing how they affect the property of the strands.

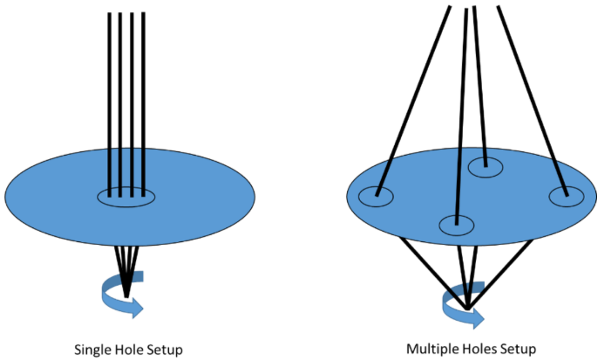

Figure 41 - differences between single and multiple holes setup

As it is possible to see from the image, the difference between the two setups is the feeding configuration of the four tows in the ring twister. In the Single Hole configuration (which is the traditional one used for the manufacturing of twisted ropes), the tows are inserted all together within a circular support and then twisted, while in the multiple holes setup each tows is passed through its own feeding hole in order to reduce the friction between the tows during the twisting process. Figure 42 represents the effect of the hole setup on the mechanical properties of the twisted tows.

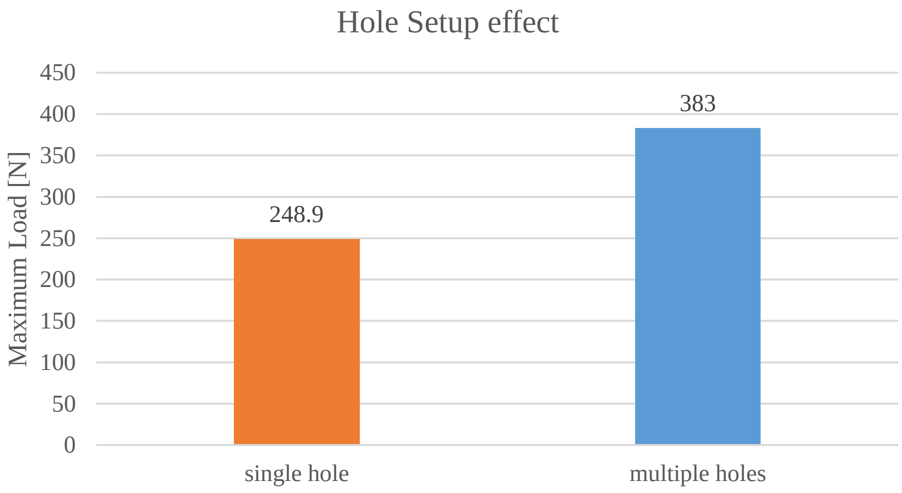

Figure 42 - effect of the different feeding configurations for the tows in the twisting process

As it is possible to see from the different values of the maximum load achieved by the two samples after being subjected to tensile tests, the disposition of the different tows during the twisting operation plays an important role in the mechanical properties of the final product. In particular, the multiple holes configuration is able to provide a lower level of friction between the different tows, reducing the angle during the twisting operation. This leads to a lower level of damaged fibres during the manufacturing process, enhancing the maximum load of the final product going, for the sample tested, from 248.9N of the traditional single hole configuration to 383N for the multiple holes setup (+53.8 %).

3.5.2 Twisting Cursor

The cursor (or flyer) used in the ring twister is the part that rotates and twists together the different tows and its weight and material can affect the level of stress on the tows during the manufacturing process.

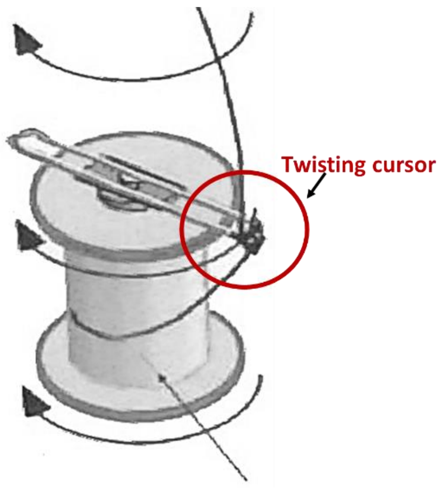

Figure 43 - cursor of a typical ring twister machine

Data from Figure 44 show that also the cursor characteristics affect the mechanical properties of the twisted bundle of fibres. Indeed, as it is possible to see from the chart, changing a metal cursor (6500 mg) to a nylon one (6400 mg) increases the mechanical properties by almost 10% going from 648.2 to 822.8 N. This effect can be explained with the lower friction on the carbon fibres given by the better tribological properties of the nylon cursor in comparison with the metal one.

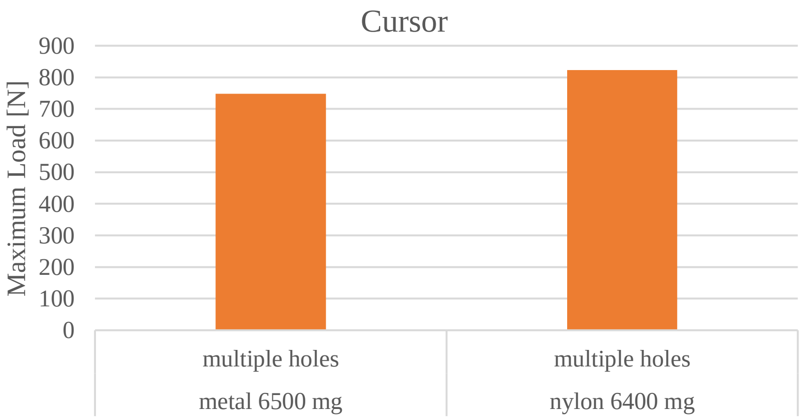

Figure 44 - effect of the cursor material and weight

3.5.3 Tensioning Device

Another fundamental aspect of the manufacturing process is the tension applied to each tow during the twisting procedure. Tow tension is regulated with a spring stopper (see Figure 45), increasing the friction of the feeding bobbins before the twisting operation. Using springs with different diameters and then weight (springs are identified in function of their weight), it is possible to increase the tension and hence force required to unwind the tows from their supports on the creel before the twisting operation.

Figure 45 Spring stopper

Two different spring stoppers were tested, one having a weight of 160 gr and one lighter with a weight of 90 gr. The lighter the spring is, the lower the tension in the tow. This reduction lowers the stress levels in the carbon fibres during the twisting operation, reducing the number of damaged fibres during the manufacturing process. The effect of the different spring stoppers was tested by subjecting the cordages to tensile testing. The use of 90 gr spring, as illustrated in Figure 46 showed better properties for both holes configurations.

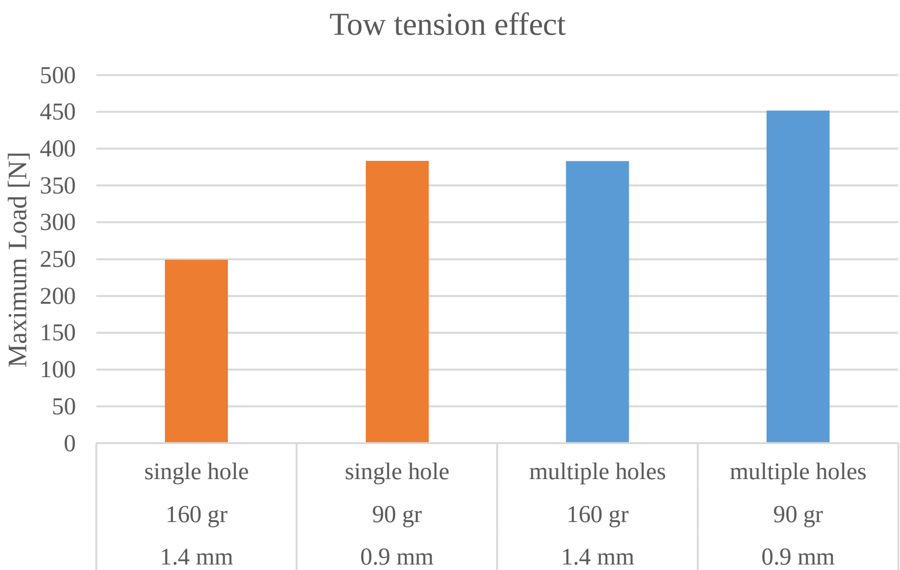

Figure 46 - effect of the tension on each tow for both the single and multiple holes configurations

It is important to underline, that although a lighter tension causes less damage to the fibres, the spring must be rigid enough to put the yarn in tension. Hence, springs with lower weight were not considered for our test campaign.

3.5.4 Number of twists per meter (tpm) during yarns' twisting operation (First Twist)

The number of twists per meter for the yarns is one of the principle parameters that influence the final properties of the cordage. It is strictly related to the second step in which the strands are twisted together. Cordage/strand strength, handling properties and the final structure of cordage is strictly dependent on the twisting operation. Based on a visual inspection of the strand filament, the maximum twist per meter for the first twist was found at around 160 tpm. Increasing the number of twists per meter (tpm) above this threshold causes unstable deformations and fibre damage. Indeed, increasing the first twist at 200 tpm causes corkscrew defects as illustrated in Figure 47.

Figure 47 Single strand (200 tpm first twist) showing corkscrew defect

Different twists per meter were tested, and the highest twist per meter used during our test campaign was found at 160 tpm and was chosen based on visual inspection, checking that it does not cause instabilities of the rope. Different twists per meter were manufactured and tested at tensile test. Analysing the different values of the maximum loads for different twists per meter, it appears evident that decreasing the value of twist increases the maximum load of the final product. More exactly, by going from 160 to 100 tpm it is possible to observe an increase of almost 65%, going from 451.9 to 748.2 N (see Figure 48). A lower twist per meter at 40, was manufactured with a manual procedure. The data is reported in the chart by a red column to remind that the cordage was manufactured using a different method, and the data must be used only as to have an idea of the trend between tpm and maximum load of the cordage.

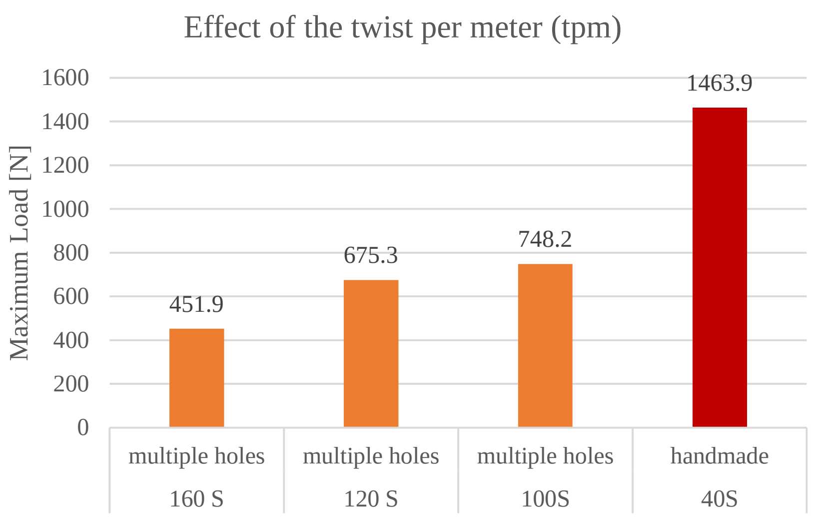

Figure 48 - effect of the twists per meter

Although a lower first twist has shown to bring higher strength to the strand, its value is strictly related to the second twist, and must be chosen accordingly. Indeed, to obtain a stable cordage, it is recommended to have a first twist higher than the second. Usually rope manufacturers suggest setting the ratio between the first and second twisting operation between 3:2 or 2:1.

3.5.5 Number of twists per meter (tpm) during strands' twisting operation (Second Twist)

The second twist operation denotes the angle of the strands in respect to the cordage axial directions. Being relevant for the final properties of the cordage and hence of the woven fabric, this parameter has been investigated and different angles have been correlated to the twisting operation. To investigate the effect of the second twisting operation on the final geometry of the twisted arrangement, the first twist was kept constant at a medium-low twist per meter rate (100 tpm), while the second twist was increased from 75 up to 200 tpm. The corresponding angles for the second twist are illustrated in Figure 49.

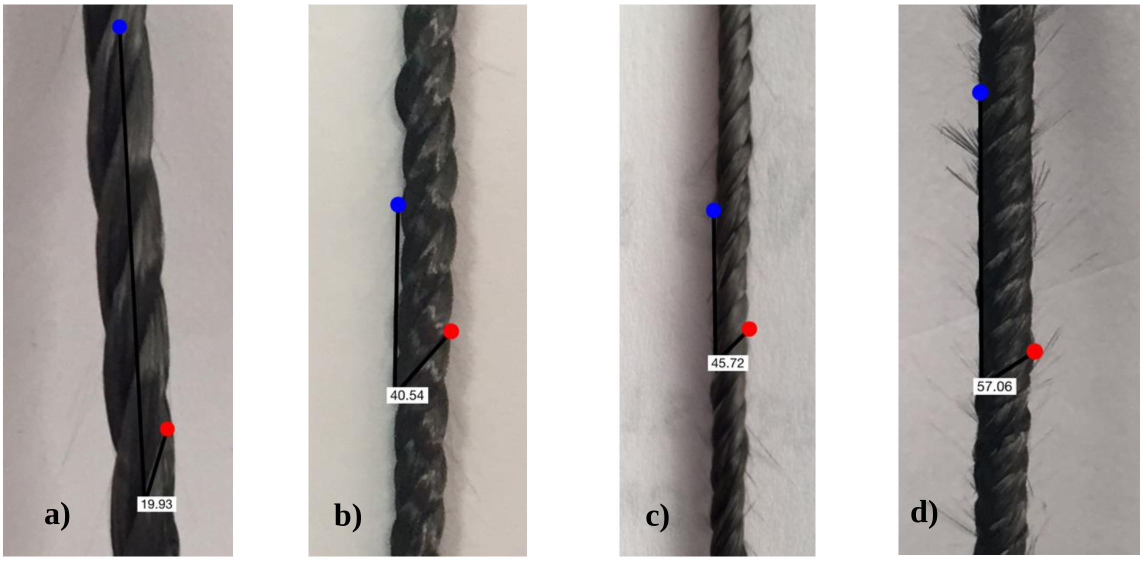

Second twist 75 Second twist 125 Second twist 150 Second twist 200

Figure 49 Angles obtained with the second twist operation

Moreover, from a visual inspection and using the cotton technique it is possible to check the amount of fibre damaged during the second twist operation. As reported in Figure 49, keeping the first twist constant at 100tpm and increasing the second twist at 150 tpm causes compression of the fibre and a high percentage of fibre damaged (Figure 49c). When the second twist is set at 200 tpm the rope touches the bobbin during twisting operation causing higher percentage of fibres damaged as illustrated by the small fibres spreading around the rope (see Figure 49d). Hence, by a first inspection the highest second twist suggested is 125 tpm having a first twist of 100 tpm.

To establish how the second twist, affects the mechanical properties of the final cordage several tensile tests were performed. Due to the number of configuration examined and hence samples tested; the tensile tests for the second twist configurations were carried out at Bridon International Technical Centre in UK. The tensile strength was determined using a computer controlled tensile test system MultiTest 25-i from Mecmesin (see Figure 50) with the rope wrapped around the clamps. For each configuration 5 samples of 4 metres were tested and the tensile strength was determined.

Figure 50 Tensile machine for testing cordages (Bridon International Technical Centre)

Based on the results found during the visual inspection described in the previous section, the first twist was set at its maximum to reach the higher value of the second twist. Setting the first twist at 160tpm, samples were manufactured varying the second twist. The second twist was tested from 50 up to 200tpm with increments of 25tpm. Results from tensile tests show that having the first twist of 160tpm, the cordage shows its highest tensile strength if the second twist is set at 100tpm. It was found that increasing the second twist from 50 to 100tpm causes an increase in tensile strength, while above 100tpm the tensile strength drops and reach its minimum at 150tpm. The results are in accordance with the observations done during the visual inspection.

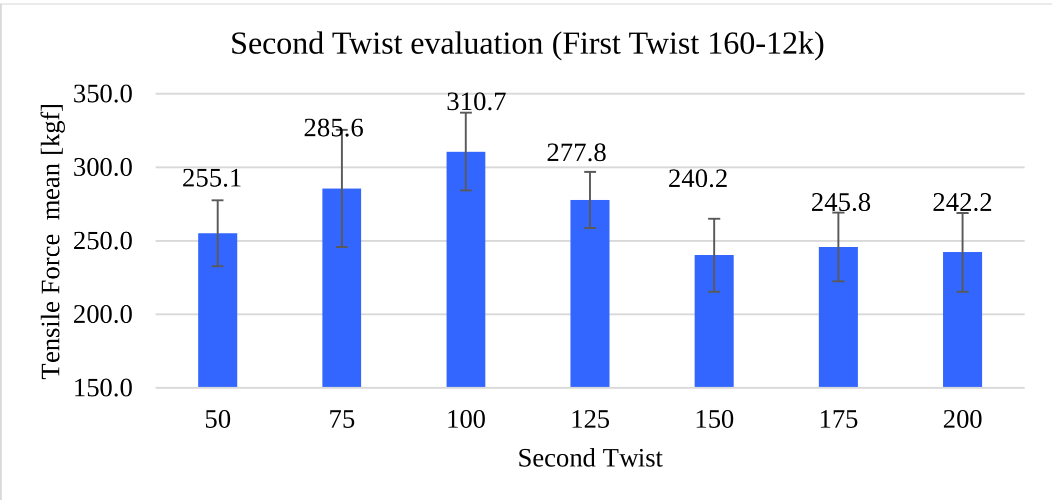

Figure 51 Second twist evaluation keeping the first twist constant at 160 tpm

A second experimental campaign was conducted to check the effect of the first twist on the final cordage. Based on the result on the first twist evaluation, the first twist was set at 100 tpm while the second twist was varied from 50 to 100tpm with increments of 25tpm. The results from the tensile tests were compared with the sample with the same second twist per meter and with a first twist of 160tpm. It is important to highlight that the cordages produced with 100tpm for the first twist show a tensile strength higher in respect to the cordages manufactured with a second twist of 160tpm (see Figure 52). Both configuration show the same trend, with the tensile strength increasing as the second twist increases, reaching its maximum at 100tpm.

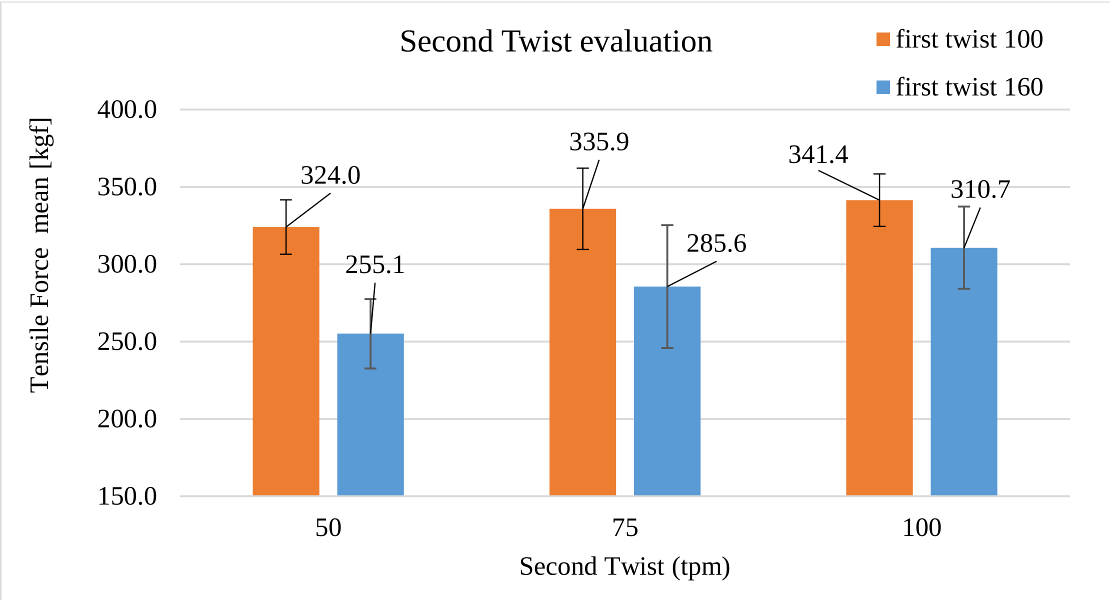

Figure 52 First Twist evaluation for different second twist per meter

These tests confirmed the results found during the first twist evaluation on the single strand. Based on these results, it is possible to conclude that a fundamental parameter in developing an optimal process to manufacture carbon fibre cordages, is the relationship between the number of twists per meter used in both the first and second twisting operation. It appears that the first twisting operation is the most delicate step as it strongly affects the tensile strength of the twisted single strand. While the second twisting operation appears less dramatic in terms of negative effect on the final structure of the cordage.

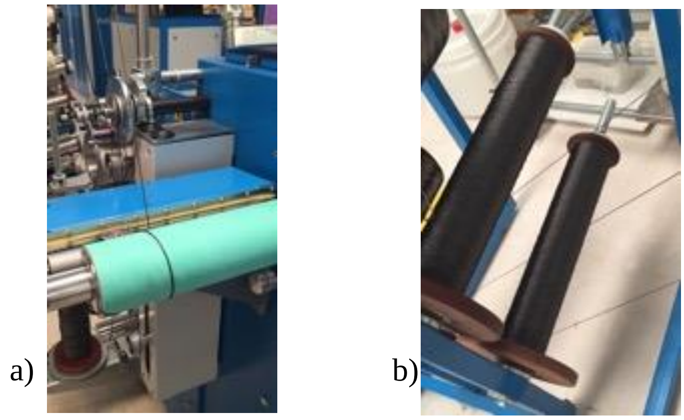

Figure 53 a) winding machine transferring the cordage from the bottle to a cardboard roller; b) two metal support (bottle) with one strand on it

Another important step that can cause fibre damage in the cordage manufacturing process, is the unwinding and winding process which is necessary to remove the manufactured product from the metal support, called “bottle” (see Figure 53a), used in the ring-twisting machine and transfer it to traditional cardboard rollers (see Figure 53b), that can be easily transported. This operation is delicate and can cause damage to the fibres. This is due to the very tortuous path of the unwinding process which forces the manufactured cordage to flow on several pulleys, some of them with a relatively small radius, which apply stresses in the helical arrangement and can cause damages and instabilities especially when high velocities are involved. All cordages tested during our experimental campaign have been wound from a metal bobbin to a cardboard bobbin using a winding machine. This operation can cause damage to the fibres and explains the high standard deviation of the samples.

3.5.6 Evaluation of the number of strands

To investigate the effect of the geometric distribution of different twisted structures based on the same number of fibres, three and four-strand ropes have been compared keeping constant the total number of fibres. Indeed, a 3 strand cordage with each single strand made of four 6K tows, was compared with a 4 strand cordage with each single strand made of three 6K tows (both cordages have been manufactured with a first twist of 120tpm and a second twist of 100tpm). Results are shown in Figure 54.

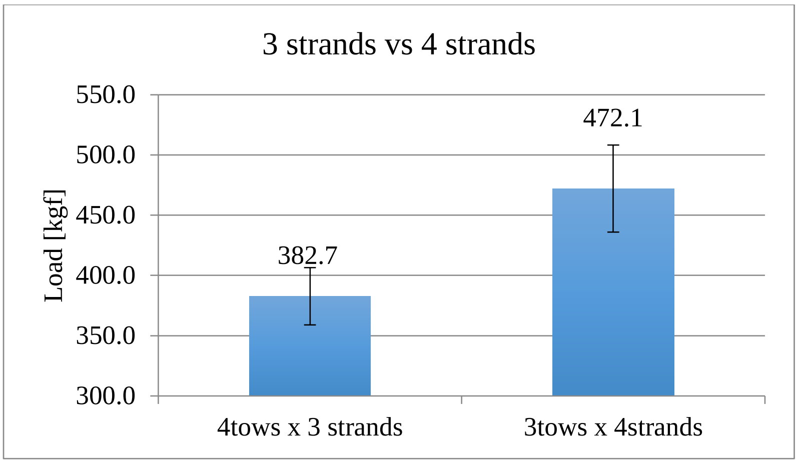

Figure 54 tensile strength for three strands and four strand cordages with the same number of fibres

Based on these results, it possible to conclude that the number of strands, keeping the number of fibres constant, is a fundamental parameter that affects the tensile strength of the final product. In particular, it appears that keeping the cross-section constant, reducing the section of the single strand, and so increasing the number of the strand from three to four increase the tensile strength of the cordage.

3.6 Hybrid Twisted Structure

Ropes' properties can be enhanced introducing different materials to the carbon structure (e.g. aramid, Dyneema, SMA (*shape-memory-alloy*), titanium, copper, etc.). When fibre filaments extend beyond carbon fibres and include yarns of metal and polymer fibres that can be shaped in the same twisted arrangement a new range of applications can emerge. This allows to achieve tailored properties. Indeed, mechanical, physical and electric magnetic property can be obtained by blending. The use of materials with properties different from carbon fibre may require the use of multiple tensioners. Materials can be included in the following methods:

- Replacing, totally or partially, one or more strands (see Figure 56 and Figure 57c)
- include the material as internal core (the core can be made of twisted or parallel fibres). This operation requires the use of specific tool, as the one illustrated in Figure 55 for the cordage manufacturing.
- Braid the fibres externally (jacket) in such a way to have the twisted rope as core of the braid (Figure 56).

If the twisted fibre structure is used for composite manufacturing (as for the case of the rods tested in the Chapter 4) one or more strands can be covered with protective materials (e.g. nylon, silicone, latex, etc.) in order to keep the strand dry during the infusion process (see the red strand in Figure 57a and b).

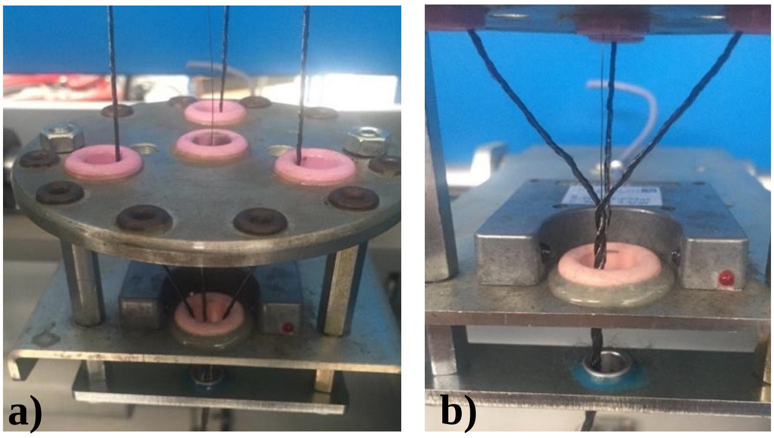

Figure 55 Four holes support to insert material as internal core in a three strands configuration a) upper view; b) bottom view showing three strand carbon cordage with SMA wire as internal core:

Figure 56 Three strands rope with external carbon fibre jacket

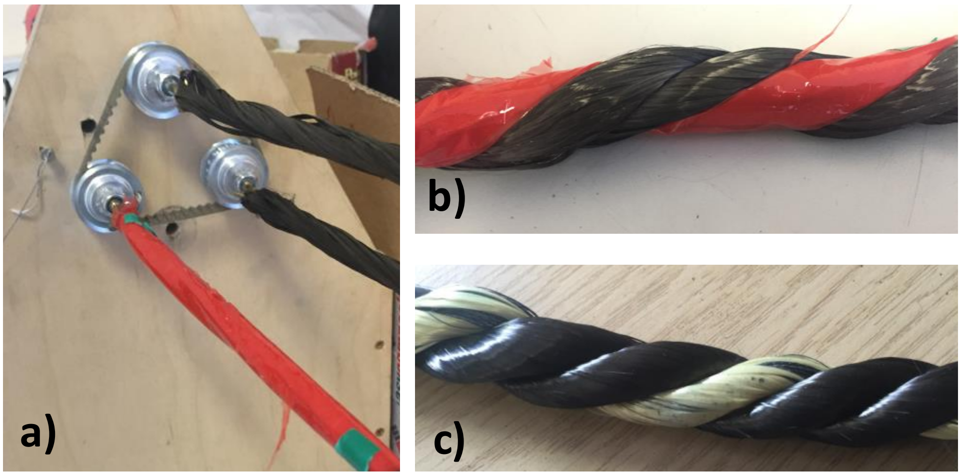

Figure 57 Examples of hybrid twisted structures: a) and b) three strands rope with one "isolated" strand; c) three strands rope having two carbon fibres strands and one Kevlar/Dyneema strand

4 3D Composite reinforcement

4.1 Introduction

The twisted helical arrangement of fibres, as reported in the previous chapter, has direct consequence on the mechanical properties of the final structure, leading to a different behaviour in comparison to the one shown using parallel fibres bundle (e.g. tensile behaviour in paragraph 3.3). In this chapter, the behaviour of the proposed twisted helical fibre arrangement will be investigated by experimental tests when combined with polymer resin for composite manufacturing.

4.2 Effect of resin flow on the twisted helical arrangement

In contrast to yarns used in their “dry form” applications (textile, cable, etc.) the optimal yarn typically used for composite applications needs to take in account the effect or the manufacturing process adopted. For dry preform, the level of twist should be sufficient to enable the use of textile process (such as weaving or knitting) but not high enough to avoid undesired effects such as fibre misalignment (which cause detrimental effect on the composite properties). The effect of twist has a direct consequence also on the resin impregnation, as shown by several works [198, 199]. High level of twist can form compressed fibre bundles with a poor impregnation by the polymer resin. As is well known, there are two scales of flow during resin infusion process: one is the macro flow in the gaps between/around the tows, and the other is the micro flow within tows. For composite structures, the two resin flows must be controlled to ensure that the resin properly impregnates the preform. Indeed, the strands geometry, the level of twist and the weaving pattern, play a crucial role in resin flow. During the resin transfer process the liquid resin flows preferentially through the void spaces between the densely packed yarns, and this is often referred to as ‘race-tracking. If we consider a fabric made using the twisted helical arrangement (Figure 25) the resin we will have two ‘race-tracking’ channels: one between the ‘cordage’ forming the fabrics, and another between the strands forming the single cordage. At high twist, impregnation within the strand is difficult as high overall permeability and low strands permeability leads to fast infusion elsewhere and slow infusion within the strand. Essentially, the resin moves faster in the channels (race track) than in the strand. The resin flow is dominated by inter-strand (macroscale) flow, leading to a fast infusion process that can cause poor impregnation and tendency to form inter-strand voids in the structure. Instead, for low twist the resin is dominated by intra-strand (microscale) flow, where there is a small compaction between fibres allowing the resin to penetrate between the yarns. If the flow run to fast between the yarns can cause inter-strand voids. In conclusion, while for a traditional fabric (woven yarns) there are only two type of resin flows: inter- and intra-yarns, for the proposed 3D fabric (woven twisted helical fibres) there is a further preferential channel for the resin. The resin can flow around the strands following a helical pattern that help to distribute more uniformly the resin around the strands.

4.3 Rod structure

Carbon fibre rods are usually used in applications where light weight is crucial (e.g. aerospace, automotive or sport sectors) and although they can replace steel they are frequently used to substitute aluminium tubes. In many instances, carbon fibre tubes can weigh 1/3rd of an aluminium tube and have the same or better strength characteristics. Carbon fibre tubular structures can be manufactured by vacuum infusion, autoclave processing or compression molding, although the most cost effective methods, and hence the most common is pultrusion. In general, according to the type of desired properties, carbon fibre rods can be manufactured using unidirectional fibres to provide longitudinal tensile strength in the length of the profile, or to provide transverse strength across the width of the rod usually mat fibres are used [200, 201]. One of the main disadvantages of carbon fibre rods are low flexible strength and short fatigue life. Cracks and delamination can weaken the rod and can cause sudden, catastrophic failure of the base structure. This usually leads to over design of carbon structures when used for structural applications, or in the worst-case leads to the necessity to substitute composites with metal structures. Indeed, although the use of metal increase the weight, it gives to structures a ductile behaviour. To overcome these problems, samples manufactured following the new proposed method were tested to evaluate their flexible strength and the behaviour of the rods under impact. The twisted helicoidal samples, named “Corda”, show quasi isotropic properties, pseudo-plastic behaviour and high flexural strength if compared to the traditional unidirectional rod, named “UD”.

4.3.1 Manufacturing process

The helical fibrous reinforcement, made up of a three strands rope, was manufactured using the wood rope making machine illustrated in the chapter 3. Each of the three strands was obtained by twisting together 56 carbon fibre tows (T800 12K from Toray). The rope was obtained by twisting together the strands with a second twist density within a range of 17-22 tpm. The fibres rope was than infused with epoxy resin (Araldite® LY 5052 / Aradur® 5052) through a two steps process. In the first step the fibre reinforcement was impregnated with epoxy resin (Araldite® LY 5052 / Aradur® 5052), by immersion in a resin bath, and put under vacuum to remove air trapped between fibres. In the second phase the wet rope was placed in a custom mould (Figure 58) and extra resin was poured on the sample before closing the mould.

Figure 58 - mould used for the manufacturing of the rods

Following the resin cycle indicated on the manufacturer's datasheet [202] the sample was held in the mould at 80°C for one hour and postcured at 100°C for 4 hours. Rods manufactured with this procedure have about 50 wt.% of fibres, a length of 260 mm and a diameter of 12.7 mm (see Figure 59b).

a) **b)**

Figure 59 a) Unidirectional rod sample "UD", b) 3D helical twisted rod sample "Corda"

All 3D helical samples were compared with the reference rod produced as for the previous sample except that instead of using twisted fibres, a bundle of unidirectional tows was used having the same number of individual carbon fibres used for the Corda sample (see Figure 59a). The fibres, after being impregnated with resin, were aligned under tension and inserted into the mould. All the samples were manufactured using the same type of fibres and resin.

4.3.2 Mechanical tests

The effect of the new helical twisted fibre reinforcement on rod composite samples was evaluated by carrying out a test campaign aimed to identify the differences with rods made with unidirectional fibres. Three mechanical tests were performed:

1. *Flexural behaviour* was studied through *three points bending tests*, identifying flexural modulus, flexural strength and flexural strain of the 3D helical rods against the UD samples.

2. *Impact behaviour* was studied through *charpy tests*. Optical microscope analysis of the impacted area, impact energy for unit of area and mass was evaluated for the 3D helical rods and compared with the UD samples.
3. *Crush/compression behaviour* was evaluated through *crushing tests* of rods under compression load.

4.3.2.1 Three points bending test (flexural behaviour)

Three points bending tests were carried out to study the flexural behaviour of the 3D helical rod against the UD samples. Rods were tested using an Instron Universal Tester (100kN Dartec Universal MJ6813) and following the ASTM D790 (D790 (2010) Standard test methods for flexural properties of unreinforced and reinforced plastics and electrical insulating materials) machine [203] adapted to a cylindrical geometry rather than a rectangular geometry. Table 5 below lists the samples used during this test campaign, showing their dimensions and span length which was calculated by imposing a ratio of 1:16 with the diameter as per standard.

Table 5 - Samples used for the three points bending test campaign

Sample Label	Fibre Type	Total Weight (g)	Length (mm)	Diameter (mm)	Diameter/Span ratio
RC-08	Corda	41.60	225	12.6	1:16
RC-09	Corda	40.03	225	12.6	1:16
RC-10	Corda	40.01	225	12.6	1:16
RUD-12	Unidirectional	40.40	225	12.6	1:16
RUD-13	Unidirectional	41.80	225	12.6	1:16
RUD-14	Unidirectional	40.00	225	12.6	1:16

Each sample was placed on two supporting pins at a set distance apart and a third loading support (see Figure 60) was lowered from above at a constant rate until sample failure and the applied load measured to provide values for the flexural stress-strain response of the material.

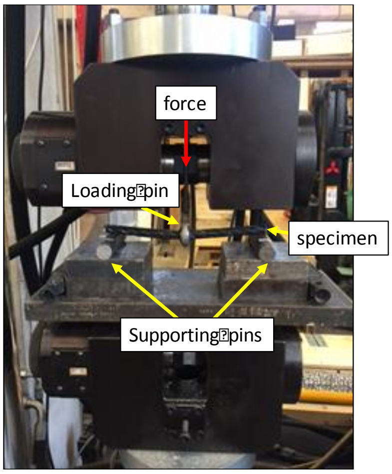

Figure 60 Three points bending test setup

The three points bending flexural test provides values for the modulus of elasticity in bending Ef, flexural stress σf, flexural strain εf and the flexural stress-strain response of the material. Results are reported below and each property will be examined individually for sake of clarity.

4.3.2.1.1 Flexural Stress

Figure 61 illustrates the values of the flexural strength calculated for the CORDA and the UD straight samples. The flexural strength was evaluated from the load-displacement curves by following the equation:

$$\sigma_f = \frac{3LS}{2d^3} \tag{4}$$

where L represents the value of the Load recorded by the machine during the test (kN), S is the span length between the two support (mm) and d is the diameter of the specimen (mm). As it is possible to see from the different trends of the curves, the twisted helical samples show lower values for the flexural strength than the unidirectional ones, going from an average value of 0.436 GPa to 0.202 GPa (-53.66%). The value of the flexural strength for both samples was determined as the highest point of the curve and is indicated by an orange arrow in the stress strain graph (see Figure 61).

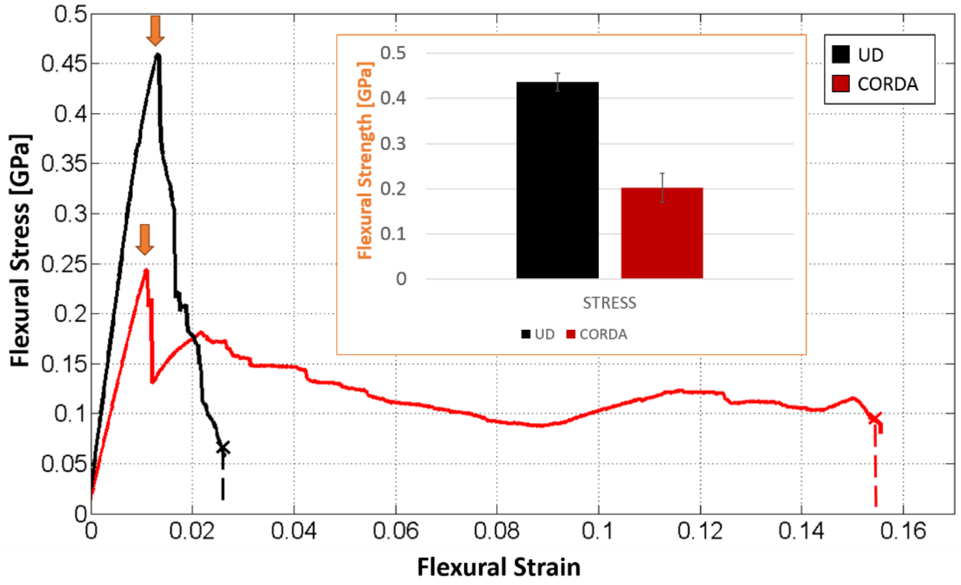

Figure 61 - Three-point-bending: flexural strength

This behaviour is due to the presence of the twists along the axial direction which increase the total flexibility of the corda samples making them more susceptible to bending than the straight fibres. This result is more evident comparing the flexural strain for both rod typologies.

4.3.2.1.2 Flexural Strain

Flexural strain was evaluated by following the equation below:

$$\varepsilon_f = \frac{6(zd)}{S^2} \tag{5}$$

where z represents the vertical displacement recorded by the machine during the test. As it is possible to see from the different trends of the curves (see Figure 62), the corda samples allow a larger deformation of the composite when it is subjected to an axial load showing a flexural strain of 14.6% if compared to the value shown for the unidirectional sample of 3.3% (-78.12%).

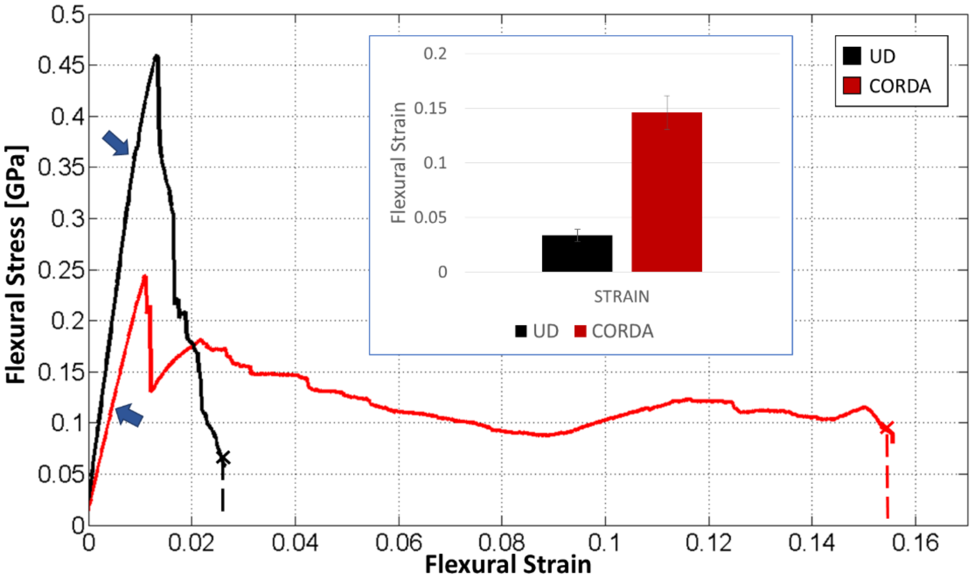

Figure 62 - Three-point-bending: flexural strain

4.3.2.1.3 Bending Modulus

The stiffness was determined as the tangent modulus of the linear part of the load-deformation curve. Bending modulus was calculated as per standard according to the following equation:

$$E_b = \frac{S^3 m}{4d^4} \tag{6}$$

where S is the span length between the two supports (mm), d is the diameter of the specimen (mm), and m represents the gradient (i.e. slope) of the initial straight line portion of the load deflection curve. The higher pliability of the corda samples shown for the flexural stress is also reflected in the behaviour of the Flexural Modulus Ef. The Corda samples show a bending modulus of 22.41 GPa that is 30% lower in respect to the one estimated for the unidirectional samples (31.73 GPa) to the corda ones (22.41 GPa).

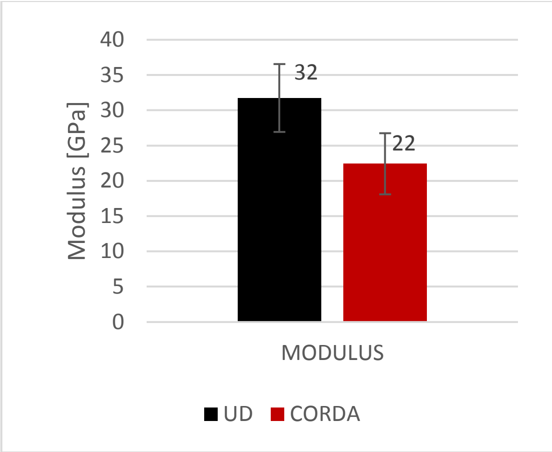

Figure 63 - bending modulus

An important consequence of the different grade of flexibility shown by the two arrangements in the passage between the straight fibres and the twisted ones is the variation of the specific strain energy (energy per unit of volume) absorbed by the samples during the bending test. The strain energy was determined as the area under the load-deformation curve until the point of failure (breaking load) for the UD sample and until the maximum deformation allowed by the machine for the Corda sample Figure 64.

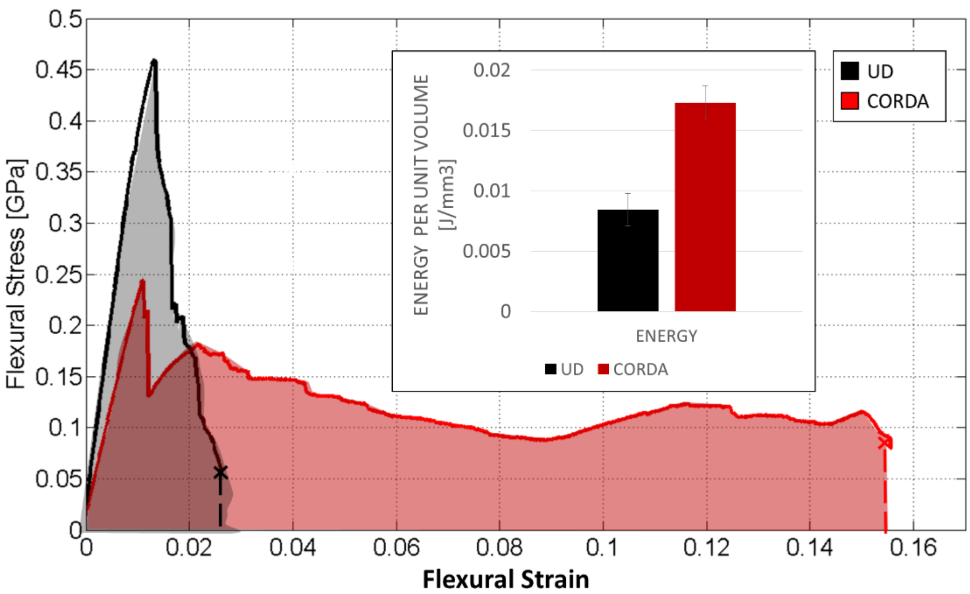

Figure 64 - Three-point-bending: energy per unit volume

The larger flexibility of the corda samples allows the rods to store more than 50% of energy per unit of volume during the bending test with respect to the unidirectional samples. Indeed, the strain energy during the tests for the twisted helical configuration is 0.0173 J/mm3, while the UD samples absorb 0.084 J/mm3. It must be highlighted that the Corda samples did not break, and the maximum strain reached is the maximum allowed by the instrumentation. Hence the analysis of the strain energy is used only as qualitative comparison between the two fibre reinforcement configurations for this specific test procedure.

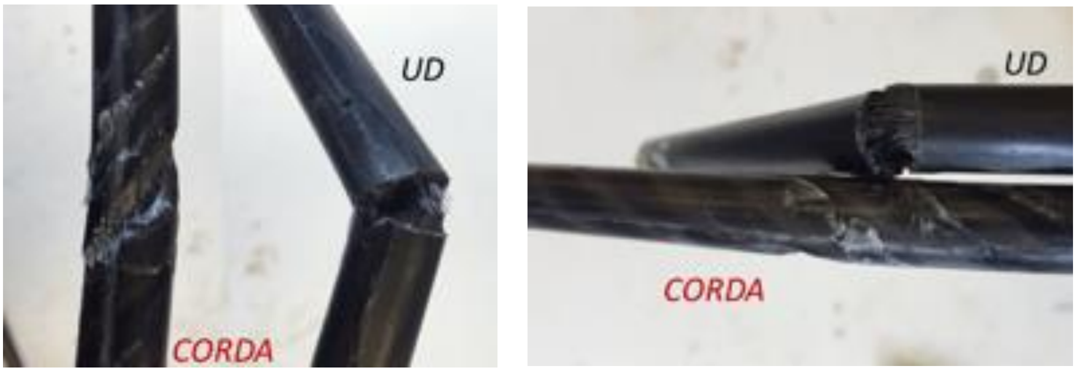

Figure 65 - Three-point-bending: fibres fracture for unidirectional samples vs matrix damage in the corda samples

Analysing all the results listed above it is possible to conclude that the twisting procedure strongly affects the flexural behaviour of the CFRP rods. In particular, the unidirectional samples show fragile fracture which is typical of carbon composite structures with cracks propagating through the thickness of the specimens breaking the fibres in the area under tensile stress. At the end of the tests the samples do not survive and are formed by two straight parts separated by a breakage zone in which the fibres damage occurred (see Figure 65). On the other hand, Corda samples show mainly matrix cracking. It is mainly evident in the resin rich regions, where the resin fall off showing the helical fibre reinforcement (see Figure 65).

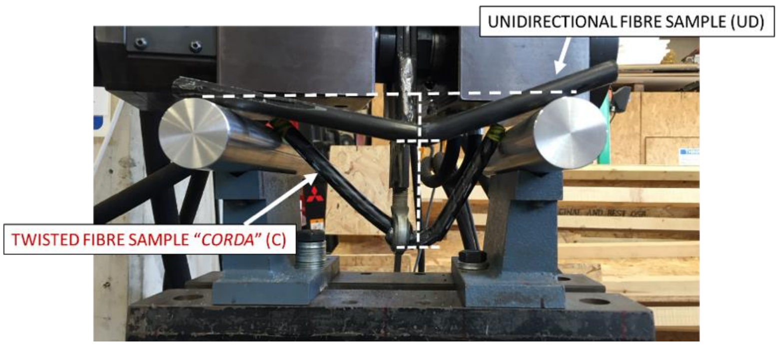

Figure 66 - difference in the flexibility between straight and twisted fibrous arrangements

Moreover, twisted corda samples show a pseudoplastic behaviour like the one observed in metals and polymers. Indeed, the sample can accommodate large displacements by deforming its structure due to the twisted carbon fibres that act as a sort of spring. The deformation in this case is accompanied by cracks only in the resin rich areas which are localised between the twists. At the end of the tests the samples present a plastically deformed curve in the correspondence of the closest twist from the load application point. All the corda samples survive the test showing few fractures or cracks in the fibrous reinforcement.

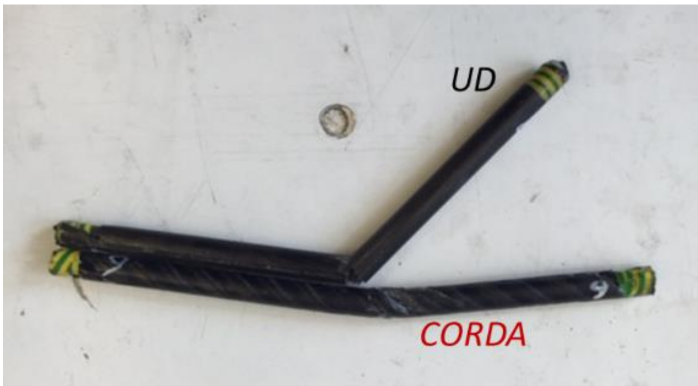

Figure 67 - post impact behaviour of unidirectional and twisted samples

It is important to underline that although the corda samples showed a very large displacement in comparison with the traditional unidirectional samples, the final shape of the specimens showed a smaller bending angle coupled with less damaged fibres. The twisted arrangement of the fibrous reinforcement allows an elastic recovery once the load is removed from the mid-section of the sample (see Figure 67).

4.3.2.2 Charpy test (Impact behaviour)

Charpy test is a standardised high-strain test able to evaluate the energy absorbed by a material during a fracture. The experimental apparatus consists in a pendulum of known mass and length that is dropped from a known length to impact a sample. The energy absorbed by the material during the impact can be evaluated by comparting the difference in the height reached by the hammer before and after the test (see Figure 68).

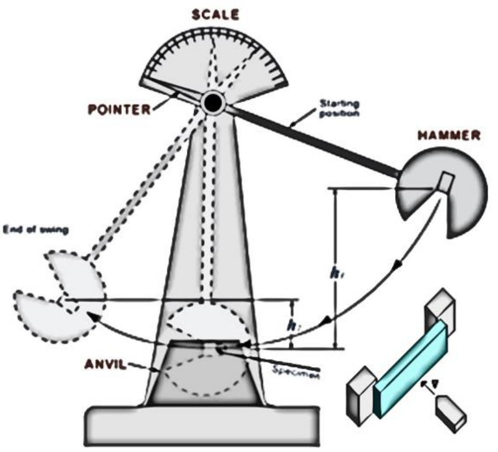

Figure 68- Charpy test: experimental apparatus and test setup

In this specific experimental campaign, the samples were tested with an unnotched geometry because the properties of the corda specimens would have been strongly affected by the location of the notch in relation with the position of the twist, making the results not comparable with the UD samples (see Figure 69a).

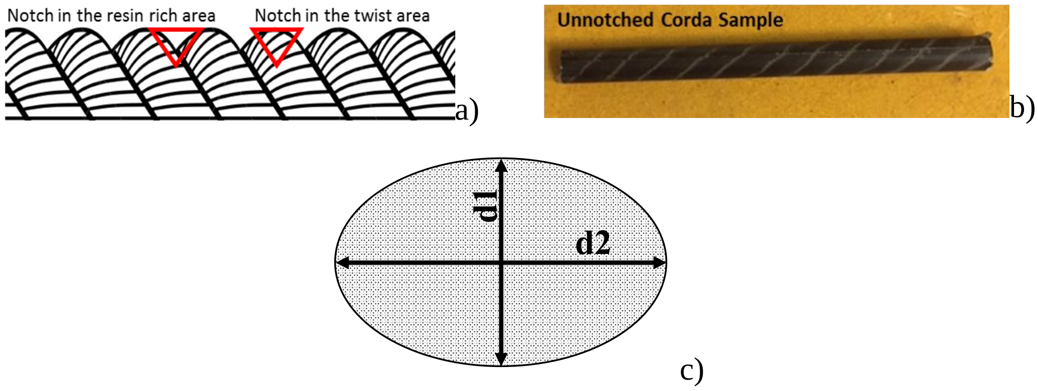

Figure 69 - Charpy test samples: a) influence of the notch location on the flexural behaviour; b) one of the twisted samples used during the experimental campaign, c) cross section of the rod reporting the major and minor axis.

Samples were dimensioned based on BS EN ISO 179-1-2010[204] taking in consideration that they were rods and not small beams (see Figure 69b). All samples were cut with a length of 80mm and a nominal diameter of 6mm. The charpy pendulum used during the test campaign is characterised by a strike energy of 5J with a velocity of the hammer of 3.8 m/s. Test results are illustrated in the table below, which lists the tested samples, their dimensions and calculated charpy impact strength evaluated according to the equation:

$$a_{cU} = \frac{E_c}{d_1 d_2} \times 10^3 \tag{7}$$

where Ec is the corrected energy expressed in J recorded by the instrument during the test and d_1 and d_2 (see Figure 68c)are the dimensions of the section of the rods, expressed in mm. Since the samples presented a small variation in terms of weight due to the slight variation of resin in the samples, the absorbed energy was also evaluated in terms of energy absorbed per unit of weight.

Table 6 - Results from the Charpy test campaign

LABEL	Ec [J]	d1 [mm]	d2 [mm]	weight [g]	length (mm)	Charpy Impact Strength a_{cU} [kJ/m^2] modified	Energy/weight [kJ/kg]
UD-1	1.75	6.10	8.02	3.70	80.00	11.39	0.47
UD-2	1.40	6.10	8.02	3.90	80.00	9.11	0.36
UD-3	1.45	6.10	8.02	4.00	80.00	9.44	0.36
Average	**1.53**	**6.10**	**8.02**	**3.87**		**9.98**	**0.40**

CORDA-1	4.00	6.10	6.51	3.50	80.00	32.08	1.14
CORDA-2	4.80	6.10	6.51	3.45	80.00	38.49	1.39
CORDA-3	4.55	6.10	6.51	3.40	80.00	36.49	1.34
CORDA-4	4.70	6.10	6.51	3.40	80.00	37.69	1.38
Average	**4.51**	**6.10**	**6.51**	**3.44**		**36.19**	**1.31**

a)

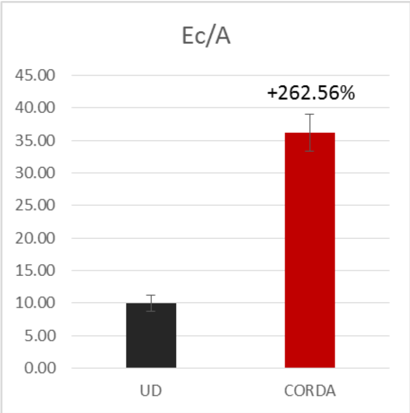

b)

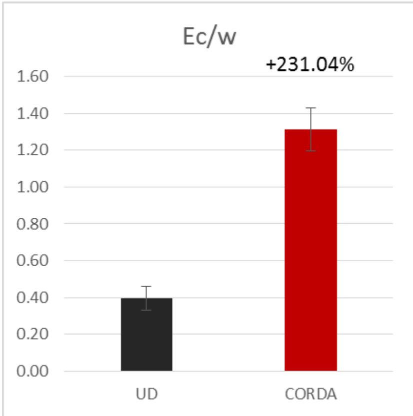

Figure 70 – Charpy test: difference between unidirectional and twisted samples in the absorbed energy: a) per unit of surface and b) per unit of mass

Analysing the results in Table 6 it is possible to observe that corda samples show an enhancement in the energy absorbed by more than 200%. In particular, in terms of energy for unit of surface the energy absorbed is more than 265% higher, while it is 231% for unit of weight (see Figure 70). This behaviour confirms the large energy absorption property given by the twisted arrangement of the fibrous reinforcement shown in the three-point bending tests. Moreover, twisted corda samples can accommodate large displacements by deforming its structure due to the twisted carbon fibres. The deformation in this case is accompanied by cracks mainly in the resin rich areas which are localised between the twists. At the end all the corda samples survive the test and absorb the impact energy through plastic deformation and resin fracture, while the UD samples absorb the energy through fibre fractures leading to a catastrophic failure. Indeed, the UD samples did not survive the test as it is possible to see from Figure 71.

Figure 71 – Post-test images of impacted samples

A second test campaign was performed impacting samples with a diameter of 12.5 mm. The samples were tested with the same apparatus, impacting the rods using a Charpy pendulum with a strike energy of 5J with a velocity of the hammer of 3.8 m/s. The larger samples were impacted with the same energy used for the previous rod to avoid specimen failure and hence investigate the different behaviour of the two fibres arrangements when subjected to an impact in the out-of-plane direction before failure. The impacted surface was analysed with a Leica Optical Microscope to visually compare the indent area and the presence of cracks around the impact zone between the two types of fibre arrangement.

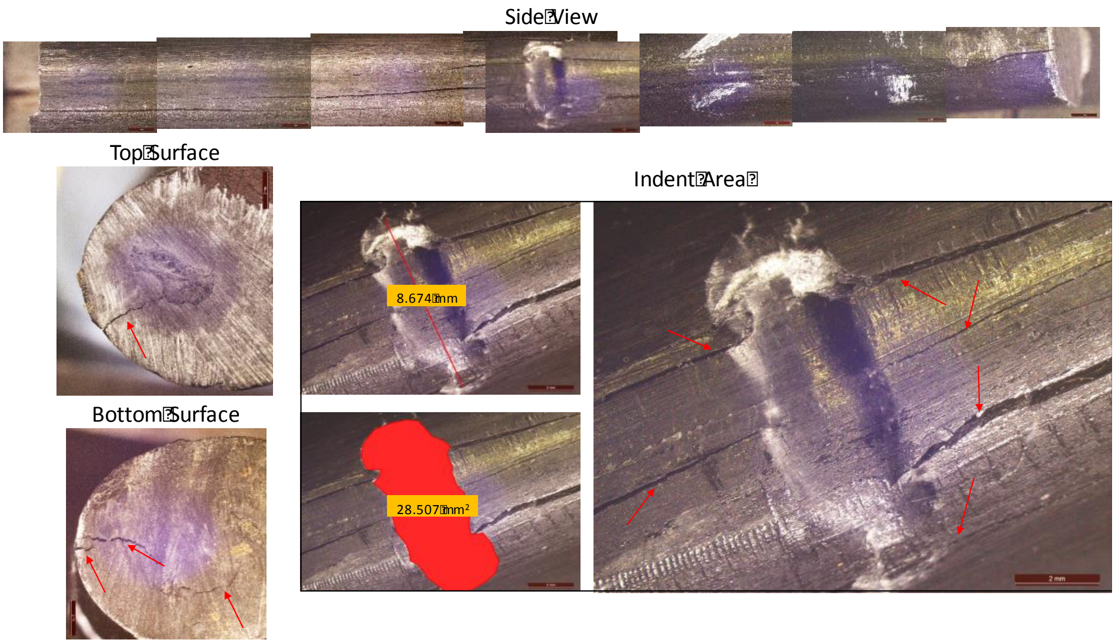

Figure 72 - Evaluation of indent area and cracks propagation for samples with unidirectional fibres with 12.6mm diameter – Pendulum Strike 5 Joule with a velocity of 3.8 m/s

Unidirectional samples present a fragile fracture with sharp edges and cracks propagating from the impact area through the entire length of the samples (see Figure 72). Moreover, the straight alignment of the fibres cause cracks to generate in the proximity of the impact location and to propagate along the fibres' direction. Presence of cracks are visible also at both ends, indicating a crack propagating along the entire length of the specimen. In contrast, corda samples show a pseudoplastic indent with very few cracks around the impact area and no visible cracks through the thickness of the samples (see Figure 73). This behaviour suggests that the impact energy in the corda sample is mainly absorbed by elastic and plastic deformation of the sample. Extension of the indent is also strongly reduced because of the twisted arrangement, going from 28.507mm^2 for the unidirectional sample to 19.288 mm^2, with a decrease of more than 40% in the indent area.

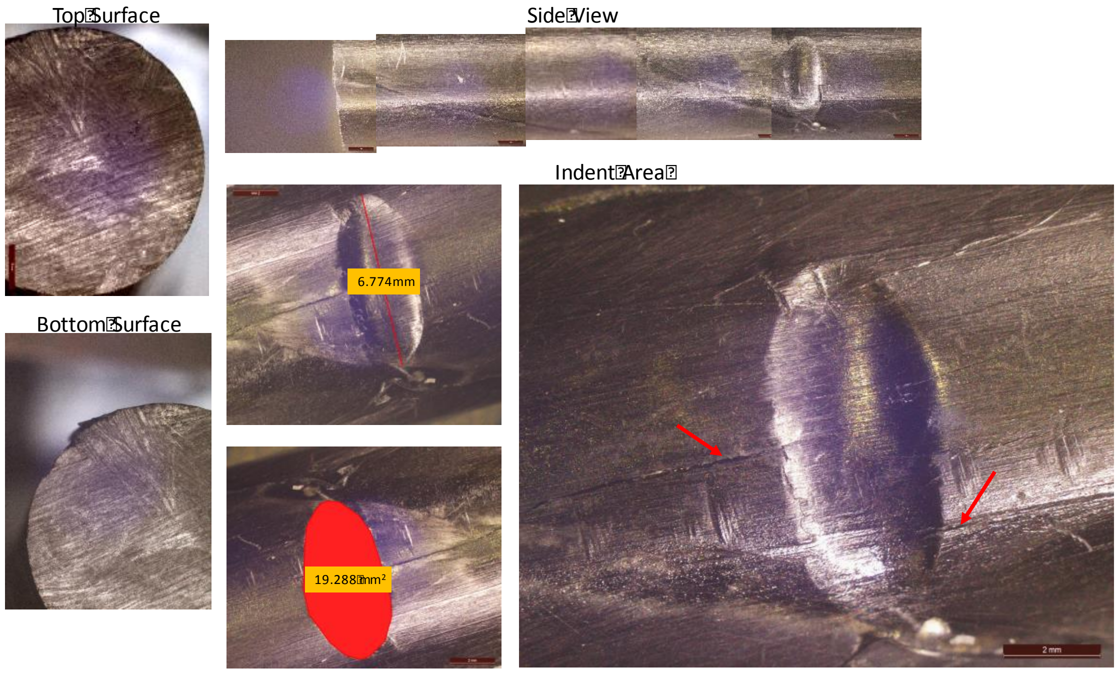

Figure 73 - Evaluation of indent area and cracks propagation for samples with twisted fibres with 12.6mm diameter – Pendulum Strike 5 Joule with a velocity of 3.8 m/s

As it is possible to see from the images above, the different disposition of the fibres along the axis of the sample strongly affects the behaviour of the material. The pseudoplastic behaviour of the corda samples shown during the three points bending test has been confirmed also for the Charpy test.

4.3.2.3 Crush test

The crush failure test gives information on the load/displacement response of the rods and their failure modes. The specimens were tested in axial compression between two flat platens on an Instron Machine 5585H. Six rods were tested, three unidirectional rods (UD) and three twisted rope based rods. Two samples for each type were compressed at a rate of 5 mm/min until 50%

of the compressive displacement while one of each type was conducted until 80%. Figure 74 shows the geometry of the rod test specimen.

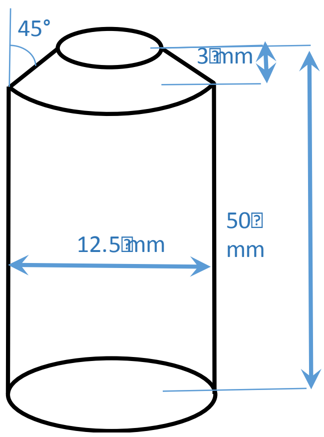

Figure 74 A geometric schematic drawing of the test specimen

To initiate progressive crushing from the top of the specimen without causing catastrophic failure each specimen rod was ground at one end to form a 45° chamfer by a lathe (as illustrated in Figure 74).

– *25 mm crush test (50 %)*

The UD rod failed by splaying mode, while the corda sample failed by progressive folding because it presented a pseudo ductile behaviour and hence was capable of large deformation. The difference in the crushing behaviour is evident from the pictures of the post crushed samples (see Figure 75). The fibres in the UD samples were fractured during the crushing process, while for the twisted arrangement the strands tend to untwist and fold on themselves. This brings to a higher post crush integrity for the corda sample. Moreover, the unidirectional rod caused catastrophically crack propagation along the fibres direction.

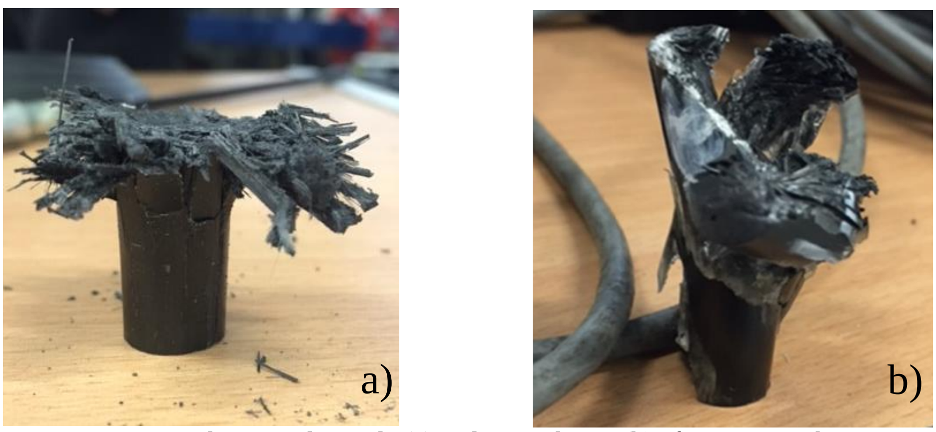

Figure 75 Unidirectional sample (a) and twisted rope (b) after 50% crush test

By examining the curves (Figure 77) it is noted that the two rod configurations crushed with two different failure modes. It is possible to suppose that while the UD samples are progressively crushed under the compressive load, the strands that make the twisted arrangement of the rope rod opened and tended to be compressed on themselves (see Figure 76).

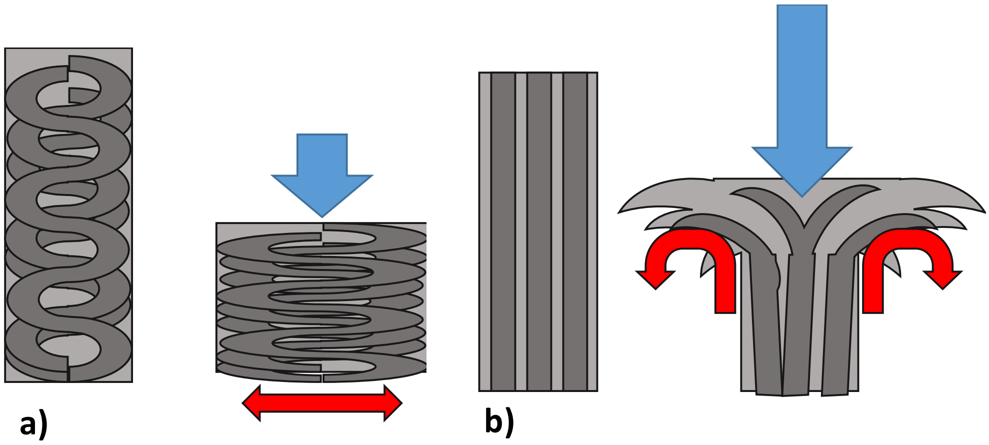

Figure 76 Schematic representation of the crushing mechanism for the twisted rope (a and for the unidirectional rod (b

The twisted arrangement behaves like "springs", lowering their stiffness in comparison with the UD samples, displaying a typical brittle behaviour. The UD samples exhibits the highest crush load throughout the crushing process, showing a maximum load of ~23kN, higher in respect to the corda samples (~8kN).

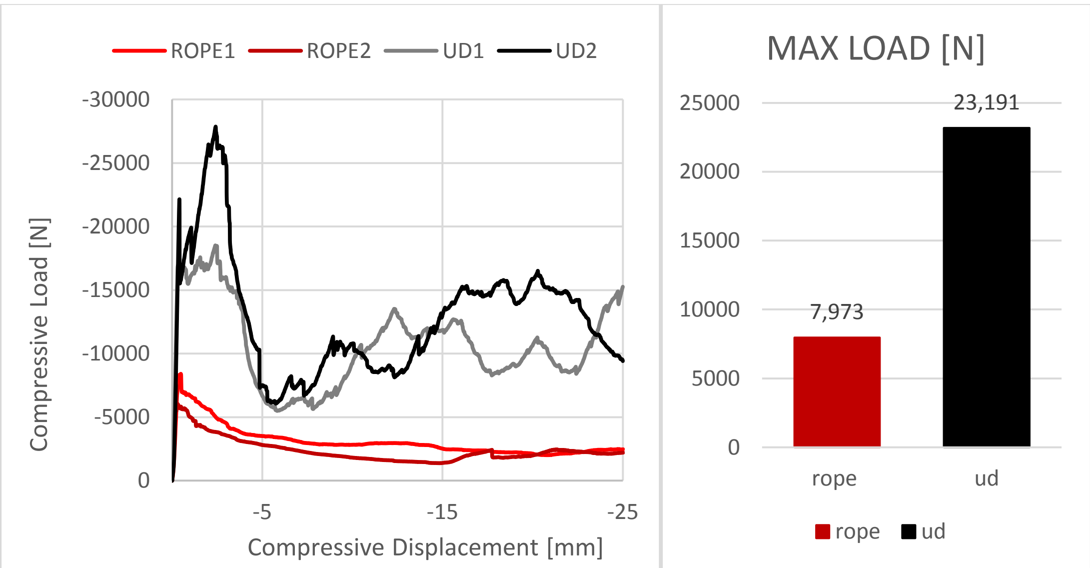

Figure 77 Crush load-displacement curves for UD and Corda composite rods.

– 40 mm crush test (80 %)

When the test is performed on longer compressive displacements (80% vs 50%) the benefits of the twisted arrangement become more evident. As it is possible to see from the curves (Figure 78), when the sample is compressed beyond a certain threshold (~65%) the twisted arrangement starts to oppose a higher resistance as the applied compressive load increases. This results in a higher stiffness and maximum load for the twisted arrangement.

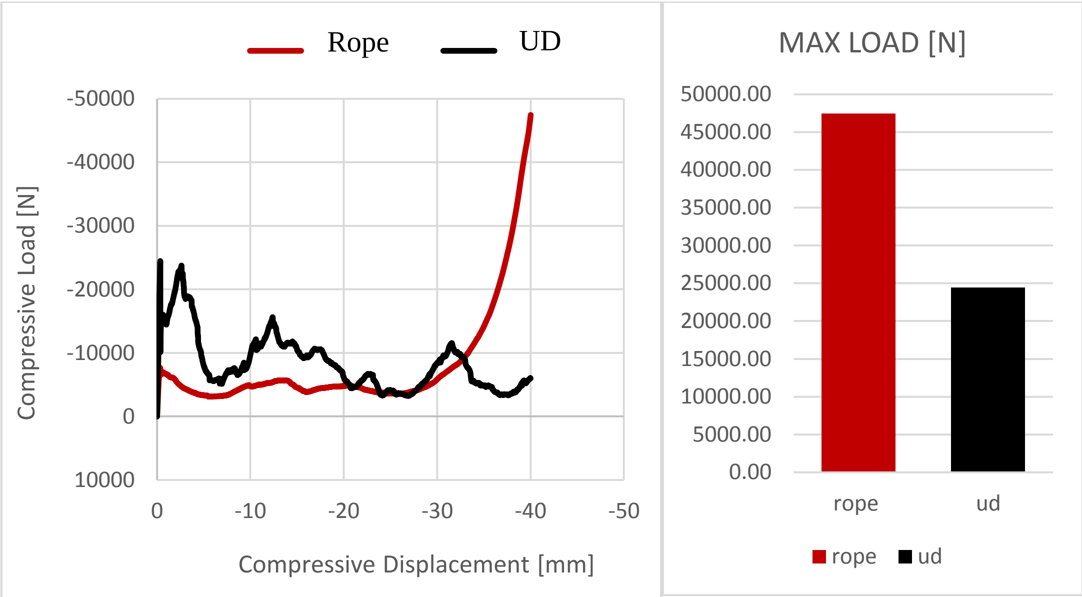

Figure 78 Crush load-displacement curves for UD and Corda composite rods.

Because the fibres were fractured during the crushing process for the UD sample, the post crush integrity was minimal as shown in Figure 79. The sample was almost disassembled showing no capacity to carry load. Instead, the twisted arrangement showed progressive crushing as the compressive load increased folding on themselves. The corda rod presents a post-crush integrity with the ability to oppose resistance to the compressive load.

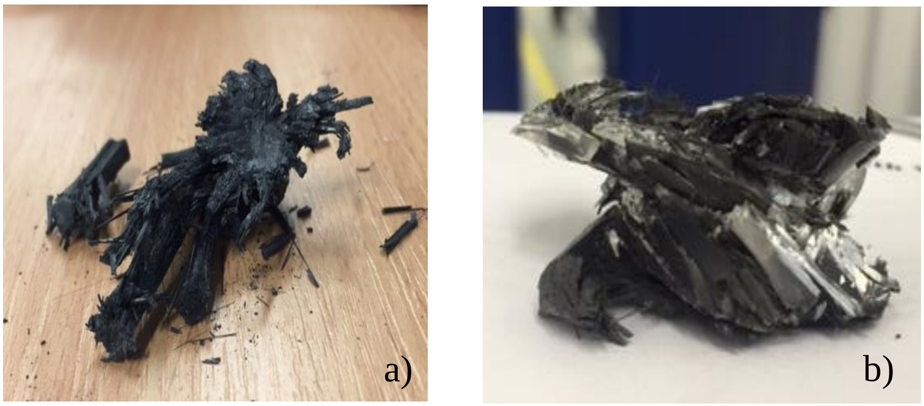

Figure 79 Unidirectional sample (a) and twisted rope (b) after 80% crush test

4.4 Composite laminate / Plate structure

Traditional composite manufacturing presupposes the fibre placement using several layers of fibre reinforcement until the desired thickness is achieved. Fibre placement involves the laying down of fibres along specific trajectories. The choice of the correct stacking sequence is one of the most important steps in the composite industry and directly affects structural properties, such as stiffness, dimensional stability, and strength of a composite laminate [200]. Fibres withstand loading and hence continuous fibres are recommended for structures that are strongly loaded. The use of highly directional strength of fibre reinforcement helps to maximize the performance of specific components. As described in the second chapter fibre reinforcement can be used in different forms such as unidirectional fibres, fabrics or 3D preform. The single fibre which constitutes the fibre reinforcement can be twisted or untwisted. Twisted yarns are normally used for increasing the lateral cohesion of the filaments and for ease of handling [205]. The good drapability of dry fabric reinforcement comes at the expense of possible fabric deformation modes. While the movement of fibres and yarns in the dry preform is favourable at the stage of the preform manufacture, it must be avoided in the final composite structures using resin or using stitching techniques. The movement of fibres can cause adverse effects such as wrinkling and thinning, which will lead to a decrease of the mechanical properties of the finished composite [206]. As reported by Jinlian [207], the interaction of structured yarns within the fabric can be grouped into eight micro-level deformation modes for textile fabrics (see Figure 80).

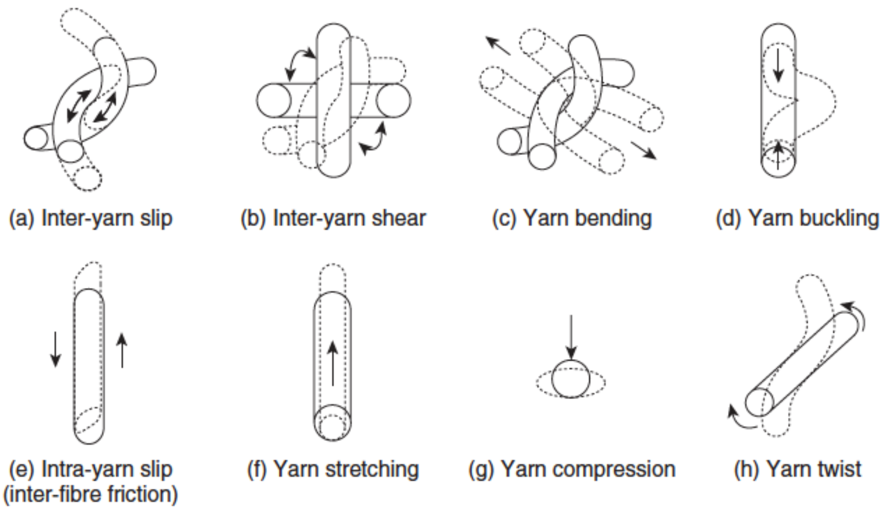

Figure 80 Micro-level fabric deformation modes, reproduced from [207].

The 3D helicoidally fabric presented in this work exploits the helical arrangement of several fibres to accomplish a 3D spatial distribution of the fibre, to increase, even more than simple twisted yarn, the lateral cohesion of fibres and provide to the final product ease of handling and distributed properties along the three directions (x,y and z). Moreover, varying the number of filaments within the single helicoidally twisted arrangement it is possible to achieve the desired thickness of the final product using a single fabric layer, with quasi isotropic properties. This simplifies the current manufacturing processes by reducing or eliminating the lamination process since a quasi-isotropic material configuration can be achieved using a single or fewer 3D twisted helicoidal fabric layers. All these specificities are of special interest for the composite manufacturing industry to reduce the time spent to layup the preform, obtain quasi isotropic properties, and avoid delamination in case of external impact. In addition, the experimental campaign presented herein shows that the innovative arrangement of fibre reinforcement confers to the structure a pseudo-ductile behaviour like metals.

4.4.1 Manufacturing process

3D helicoidal fibre fabrics were produced by weaving helicoidally twisted fibres using a traditional loom. Fabrics were weaved at MWright with a plain weave pattern. The fabric presents a density of almost 1.8 g/cm^3 and an average nominal thickness of 1.35 mm. The single helicoidal twisted fibres (rope) were obtained by twisting three strands together in a direction opposite to the direction used to twist carbon fibres to produce the individual strands. Each of the three strands was produced by twisting a tow containing 3000 individual carbon fibres (carbon fibre T300 3K from Toray) with a twist density (first twist density) of 120 tpm, at a speed of 1400 rpm and with a tow tension generated by a spring having a weight of 90 gr. The three strands were twisted together with a twist density (second twist density) of 100 tpm at a speed of 1400 rpm and a strand tension generated by a spring having a weight of 90 gr. The machine used to produce the individual strands and the ropes was a modified ring and doubling up twisting machine (see Figure 38). Fibre fabrics were subsequently consolidated with resin testing several techniques in order to validate the use of the innovative carbon reinforcement using traditional composite manufacturing techniques. Samples were manufactured by:

- vacuum resin infusion and resin transfer moulding using an epoxy resin (Araldite® LY5052/ Aradur® 5052 by HUNTSMAN) and curing the composite in oven;
- by stacking epoxy adhesive films (MTC510 from SHD Composites) and curing the sample in Autoclave following the curing cycle indicated by the resin producer,
- by using the fabric in form of prepreg. The samples were produced by SHD composite using VTC401 epoxy resin system. All fabrics were manufactured using an amount of epoxy resin approximately equal to the weight of the fibre reinforcement.

The innovative 3D helicoidal fabrics (labelled as 3DF samples) were compared with traditional composite obtained using the same type of fibres (traditional carbon tows from Toray having the same number of filaments), same resin system, same manufacturing process. Due to the different linear densities between the 3D fabrics and the traditional fabrics, the reference composites were manufactured imposing the same number of fibres per cross section. The 3D twisted helicoidal samples have been compared with traditional fabrics made with straight fibres (labelled as TF samples) for all mechanical tests. It is important to underline that since each of the twisted fibres of the 3DF fabric is obtained by twisting three different strands of carbon fibres tows, the final weight and thickness of a single 3DF fabric is three times bigger than the ones of a traditional TF fabric. In particular, as illustrated in Figure 81 one 3DF layer weighs 25.5g while three TF fabric layers weigh almost 24.5 g. Therefore, the comparison between the two materials was made by imposing the same fibres net weight for both the composites, hence three traditional TF fabrics were laminated together and compared with a single 3DF twisted fabric. For samples with greater thickness (multilayers), it was kept the same ratio of 3/1 between the TF and 3DF fabrics. By following this approach, it was possible to have the final samples of both batches (3DF and TF) characterised by the same final thickness value.

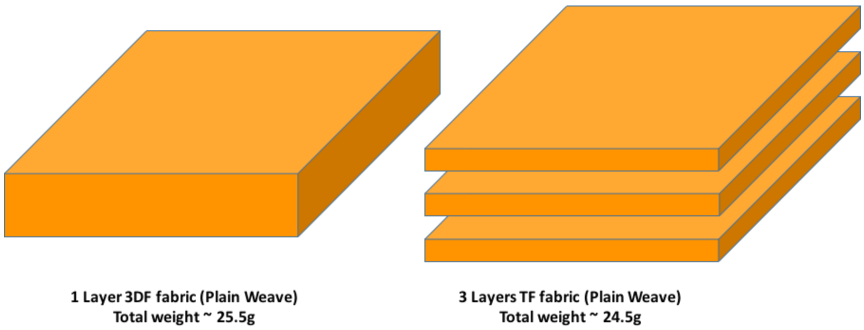

Figure 81 Schematic representation of the comparison between one layer of 3DF and three layers of TF fabrics.

To reduce uncertainty on the experimental campaign, all mechanical tests were performed on composite samples manufactured with prepregs, except if otherwise specified.

4.4.2 Mechanical test

The effect of the new helical twisted fibre reinforcement on fabric composite samples was evaluated by carrying out a test campaign aimed to identify the differences with the two different fibre reinforcement configurations. Five tests were performed:

1) Flexural behaviour was studied through three points bending tests identifying flexural modulus, flexural strength and flexural strain of the 3D helical fabrics against the TF samples.

2) Tensile behaviour was evaluated through tensile tests on tensile strips under tensile load.

3) Impact behaviour was studied through low velocity impact at different impact energies. Impact resistance and delamination area were evaluated for the 3DF composite plates and compared with the TF samples.

4) Energy absorbed was studied through charpy tests.

5) The elastic properties were evaluated by collecting vibration data from single cantilever samples subjected to an out-of-plane load F

4.4.2.1 Three points bending

The experimental campaign was conducted using an Instron Universal Tester (3369) and following the ASTM D790[208] standard on several samples in order to analyse the effect of the twisted geometry on the flexural behaviour of composite laminates. Each sample is placed on two supporting pins at a set distance apart and a third loading support is lowered from above at a constant rate until sample failure. The applied load generates tensile stress in the convex side of the specimen and compression stress in the concave side, with an area of shear stress along the midline. It is important to minimize the shear stress, in order to ensure that the primary failure of the specimens occurs from tensile or compression stress. This is done by controlling the span-to-depth ratio (the length of the outer span divided by the thickness of the specimen).

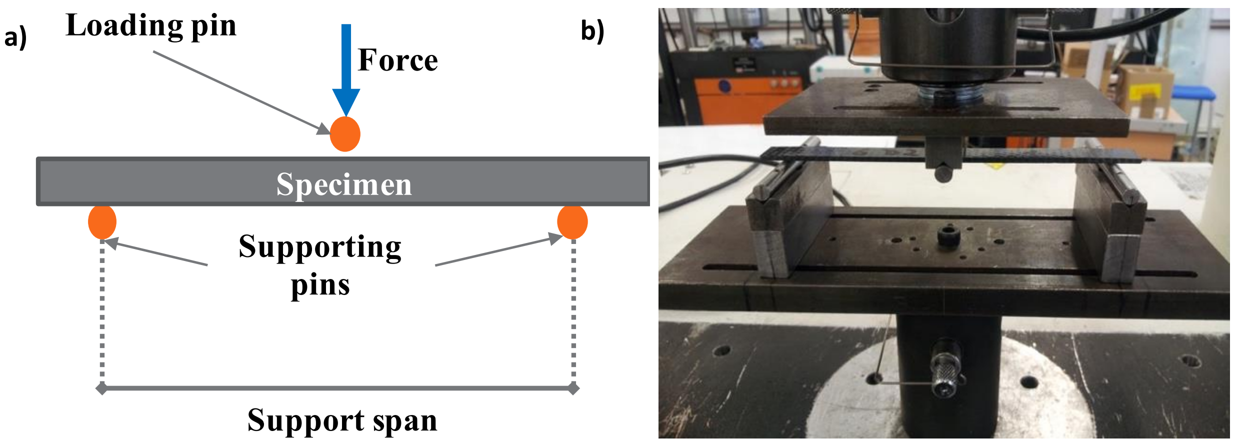

Figure 82 Three points bending setup: a) schematic of a traditional three points bending (TPB) test; b) real testing apparatus used for the testing campaign

The three-point bending flexural test provides values for the modulus of elasticity in bending E_b, the flexural stress σ_f and the flexural strain ε_f. Indeed, the flexural strength was evaluated from the load-displacement curves by following the equation:

$$\sigma_f = \frac{3PL}{2bd^2} \tag{8}$$

where:

- *P represents the value of the Load recorded by the machine during the test (kN),*
- *L is the span length between the two supporting pins (mm),*
- *d is the thickness of the specimen (mm),*
- *b is the the width of the sample tested.*

If the span-to-depth ratio is higher than 16, the moment acting on the specimens can be affected by significant end forces at the support pins. To take in account this end forces additional terms were included in the evaluation of the flexural stress, per the standard, as reported in the equation below:

$$\sigma_f = \frac{3PL}{2bd^2}[1 + 6(D/L)^2 - 4(d/L)(D/L)] \tag{9}$$

where *D* represents the vertical displacement recorded by the machine during the test (mm). The Flexural strain and the Bending modulus were evaluated by following the equations below:

$$\varepsilon_f = \frac{6(Dd)}{L^2} \tag{10}$$

$$E_b = \frac{L^3 m}{4bd^3} \tag{11}$$

where m is the slope of the tangent to the initial straight-line portion of the load-deflection curve (the area of interest in which the slope is evaluated is indicated by an arrow in the Load-displacement curve). The modulus determination can be seriously affected by the shear deflections during the test for small span-to-depth ratio. Indeed, in order to minimise the influence of the shear deformation, where it is possible, the specimens were divided in two batches per each thickness. A former batch for the modulus determination, in which the specimens were tested using a large span-to-depth ratio (at least 30) and a second batch with a shorter span in comparison to the first one, in order to induce tensile failure in the outer fibres of the sample along its lower face, for the evaluation of the flexural strength. Table 1 below lists the samples used during this test campaign. Dimensions were chosen according to the standard.

Table 7 - Samples used for the three points bending test campaign

Sample Label	Fibre Type	Number of layers	Width (mm)	Thickness (mm)
Thickness I				
D37-d3-1	Twisted	3	12.6	3.45
D37-d3-2	Twisted	3	12.53	3.55
D37-d3-3	Twisted	3	12.6	3.58
T32-t9-1	Traditional	9	12.7	3.65
T32-t9-2	Traditional	9	12.78	3.70
T32-t9-3	Traditional	9	12.88	3.65
Thickness II				
D36-d2-1	Twisted	2	12.8	2.30
D36-d2-2	Twisted	2	12.75	2.34
D36-d2-4	Twisted	2	12.7	2.38
D36-d2-5	Twisted	2	12.7	2.31
T31-t6-1	Traditional	6	13	2.10
T31-t6-2	Traditional	6	13	2.10
T31-t6-3	Traditional	6	12.8	2.14
T31-t6-4	Traditional	6	12.7	2.10
T31-t6-5	Traditional	6	13.08	2.17
T31-t6-6	Traditional	6	12.9	2.36
Thickness III				
D1-d1	Twisted	1	12.59	1.42
D2-d1	Twisted	1	12.5	1.43
T1-t1	Traditional	3	12.6	1.37
T2-t1	Traditional	3	12.58	1.34

Results are grouped in three main sections according to the thickness of the samples. 3D helicoidal specimens were compared with traditional ones imposing the same number of fibres per cross section. Considering that one 3D twisted fabric layer is equivalent to three traditional fabric layers, the sections were grouped as following:

- Thickness I (Single 3D layer versus Three traditional fabrics layers)
- Thickness II (Two 3D layers versus Six traditional fabrics layers)
- Thickness III (Three 3D layers versus Nine traditional fabrics layers)

4.4.2.1.1 Thickness I: Single 3D layer versus Three traditional fabrics layers

Being that the thickness of the samples is less than 1.6 mm, according to the standard, the support span cannot be modified and must be fixed at 25.4 mm. Due to the small span-to-depth ratio (~18), the modulus can be seriously affected by the shear deflections during the test. Therefore, the results shown for the bending modulus can be only used to point out the relative behaviour of the samples made with twisted fibres (3DT) in comparison with those produced using traditional unidirectional tows (TF).

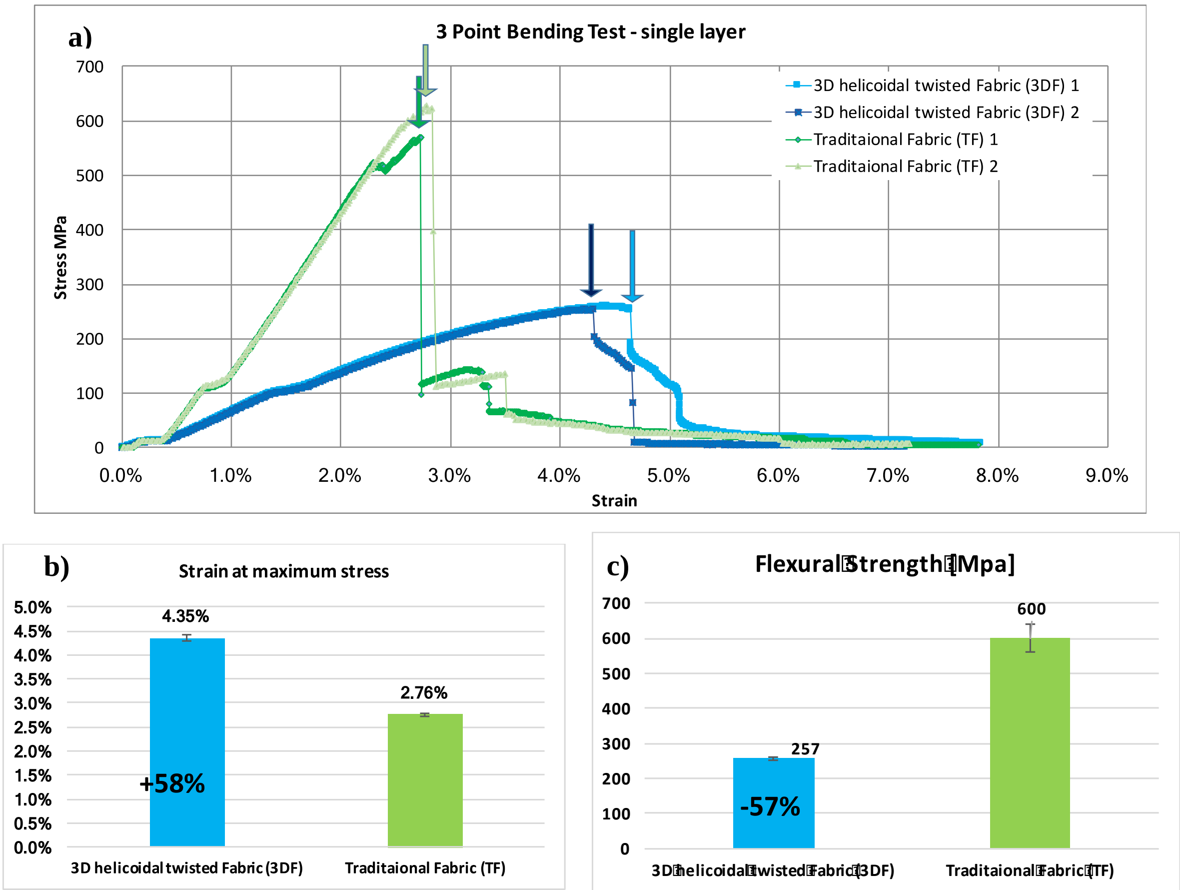

Figure 83 - Three-points-bending test: a) Stress strain curve, b) flexural strain, c) flexural strength

Figure 83 illustrates the stress-strain curve for the 3DF and TF samples. As it is possible to see from the different trends of the curves, the 3DF samples show lower values of the flexural strength than the TF ones, going from an average value of 600 MPa to 257 MPa (-57%). On the other side, the 3DF samples allow a larger deformation of the composite when it is subjected to an axial load going from a flexural strain of 2.8% for the TF to 4.4% of the 3DF ones (+58%). This behaviour can be explained with the presence of the twists along the axial direction which increases the total flexibility of the 3DF samples making them more susceptible to bending than the TF samples.

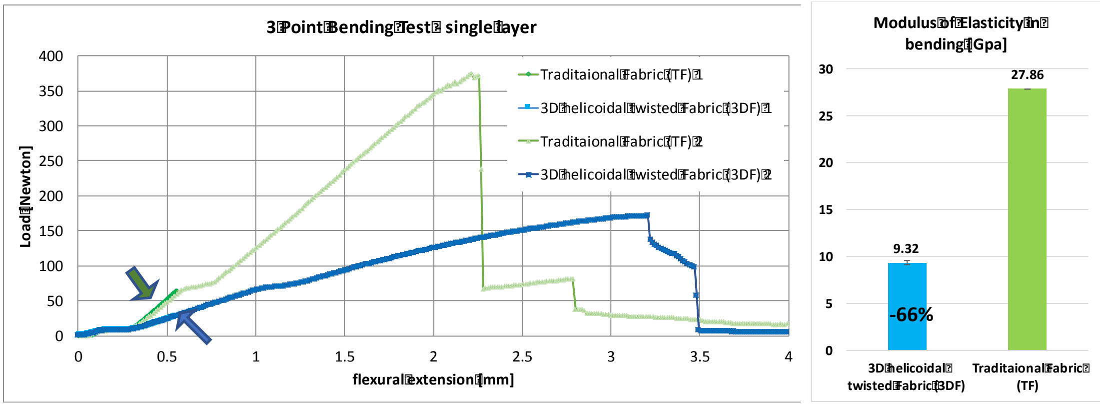

Figure 84 - Three-point-bending: bending modulus

The higher pliability of the 3DF samples is also reflected in the behaviour of the bending Modulus E_b, which shows a decrease in the passage from the TF specimens (27.8 GPa) to the 3DF ones (9.3 GPa) with a decrease of almost 66%. It is important to highlight that due to the small span-to-depth ratio (around 18 for these samples), the modulus can be affected by the shear deflections during the test. Therefore, the results obtained for the bending modulus can be only used to point out the relative behaviour of the samples.

4.4.2.1.2 Thickness II (Two 3D layers versus Six traditional fabrics layers)

- *First batch (Modulus evaluation)*

For the second thickness, to minimise the influence of the shear deformation on the evaluation of the bending modulus, the first batch of samples was tested with a span of 130 mm (span-to-depth ratio of almost ~60), as suggested by the standard. *Figure 85* illustrates the Load-displacement curves for the 3DF and TF samples tested with a span of 130 mm. The samples did not break and the tests were stopped when the samples reached 20 mm of displacement. After the load was removed both samples recuperate their original shape, therefore only the bending modulus was evaluated as reported in *Figure 85*. The 3DF specimens show a lower modulus than the traditional composites, passing from 44 GPa for the TF to 21 GPa for the 3DF (-53%).

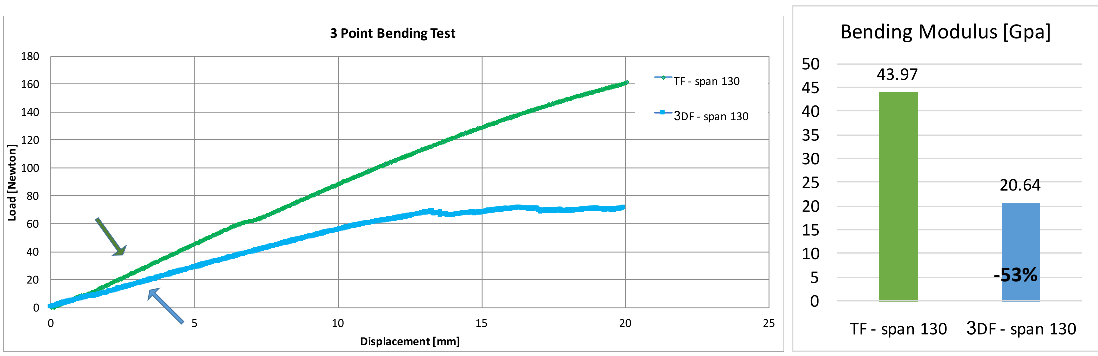

Figure 85 - Three-points-bending: bending modulus for the thickness II with a span of 130 mm

The bending modulus evaluated for the second thickness has been performed according to the standard and must be considered more accurate with respect to the one evaluated in the previous test using a shorter span. Indeed, the different value in respect to the first thickness samples, confirms the influence of shear deformation due to the small span-to-depth ratio.

- *Second batch (Flexural Strength evaluation)*

On a separate set of specimens, the flexural strength was determined setting the span at a lower span-to-depth ratio (~32) in order to induce tensile failure in the outer fibres of the sample along its lower face. The shorter span allows to bring the samples to the breaking point and evaluate the flexural strength. Being that the support span-to-depth ratio was still greater than 16 the stress was evaluated, as for the previous batch, per Equation *(9*.

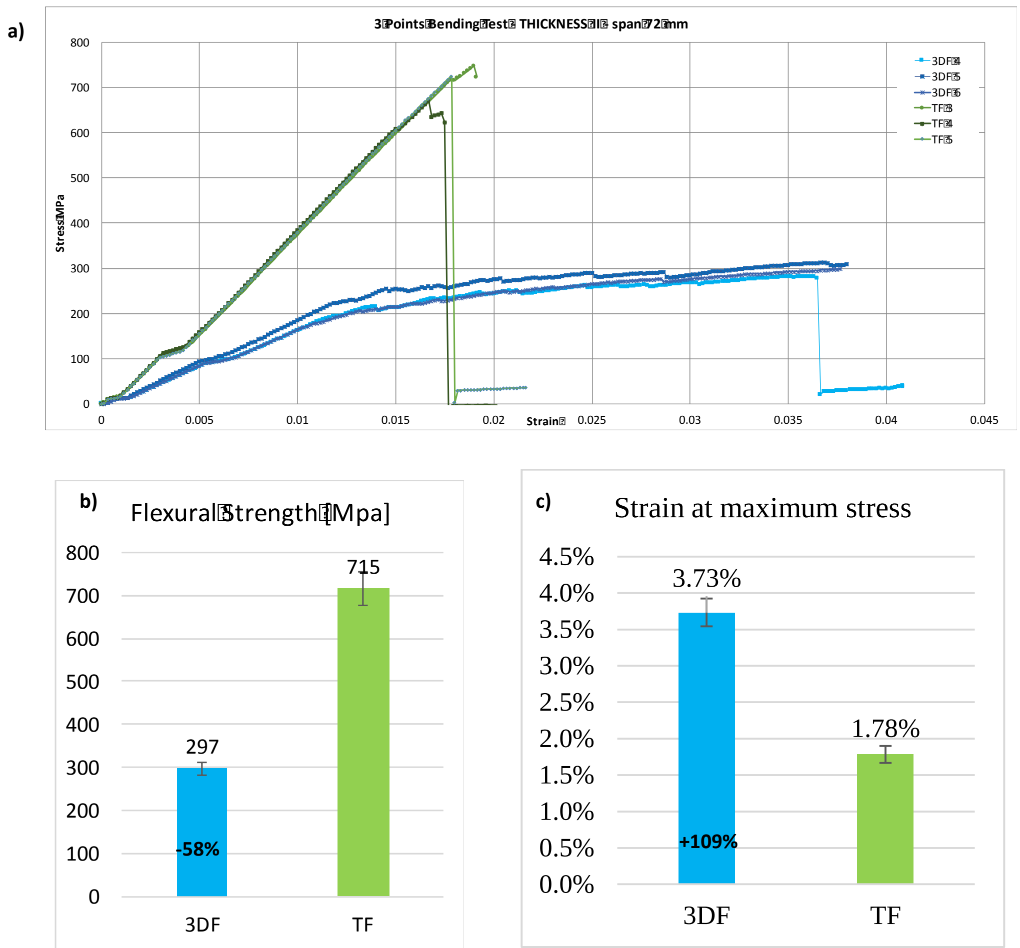

Figure 86 Three-points-bending: a) stress-strain curve for the thickness II with a span of 72 mm, b) flexural strength, c) flexural strain

Figure 86 illustrates the stress-strain curves for the 3DF and TF samples. As for the test performed on the first thickness, the 3DF specimens show lower values of the flexural strength than the TF ones, going from an average value of 715 MPa to 297 MPa (-58%). On the other side, the traditional composites present at the maximum stress a strain of 1.78% while the 3DF ones reach 3.73% (+109.35%). The different failure mechanisms for TF and 3DF samples are illustrated in the figures below. The 3D twisted helicoidal samples show a more pseudoplastic behaviour, having only the bottom part damaged, keeping the first layers almost intact. In some cases, it is possible to see only a plastic deformation of the sample, without the presence of any cracks but only some wrinkles on the top layer (see *Figure 87*b). It is important to underline that although the 3DF samples showed a very large displacement in comparison with the traditional samples, the final shape of the specimens showed a smaller bending angle due to elastic recovery that happens once the load is removed from the mid-section of the sample.

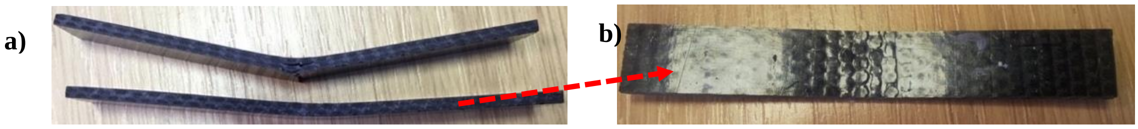

Figure 87 a) D36-D2-4 and D36-D2-5 after the test; b) 3DF sample D36-D2-4 front layer showing wrinkles due to plastic deformation

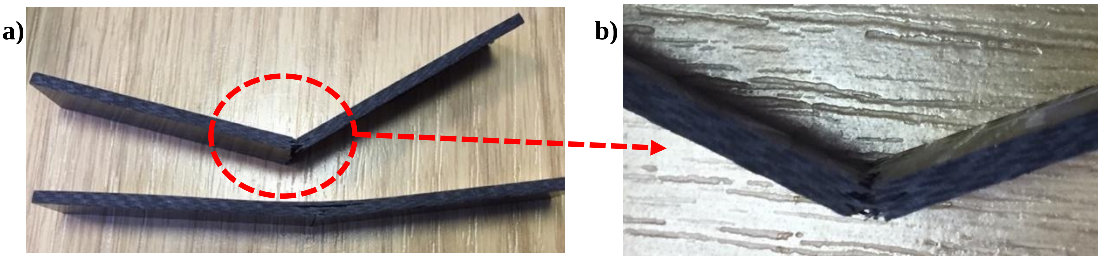

Figure 88 a) T31-T6-4 and T31-T6-5 after the test, b) TF sample T31-T6-4 showing the crack propagating through the thickness

The elastic modulus evaluated for the second batch agrees with the one calculated in the first batch. This indicates that the span to depth ratio was big enough to reduce the effect of the shear deformation.

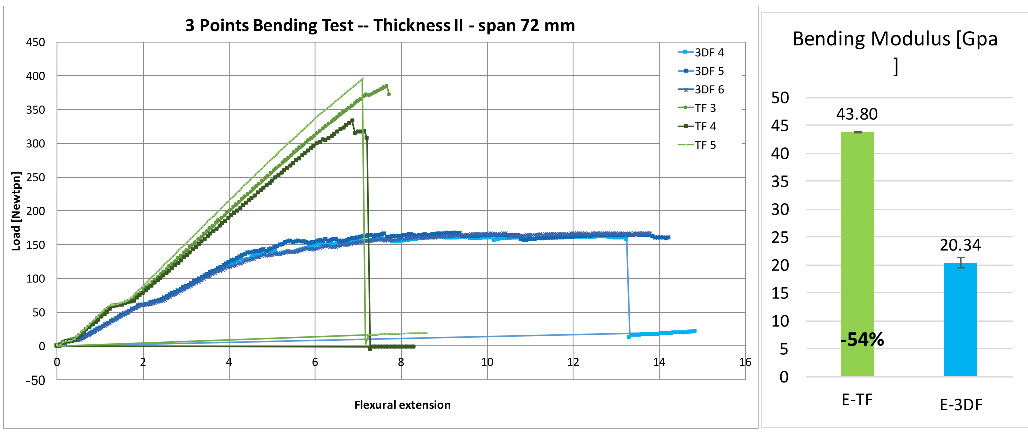

Figure 89 - Three-point-bending: bending modulus for the thickness 2 with a span of 72 mm

4.4.2.1.3 Thickness III (Three 3D layers versus Nine traditional fabrics layers)

- *First batch (Modulus evaluation)*

Figure 90 illustrates the stress-strain curves for the 3DF and TF samples. The span length was set at 112 (span-to-depth ratio ≃ 32). As for the previous tests, the 3DF specimens show a lower modulus with respect to the TF samples, passing from 39 GPa for the TF to 23 GPa for the 3DF (-40%), as reported in *Figure 91*. It is important to highlight that while the 3DF sample did not break, the TF sample broke catastrophically, presenting a strain at break of 1.8%.

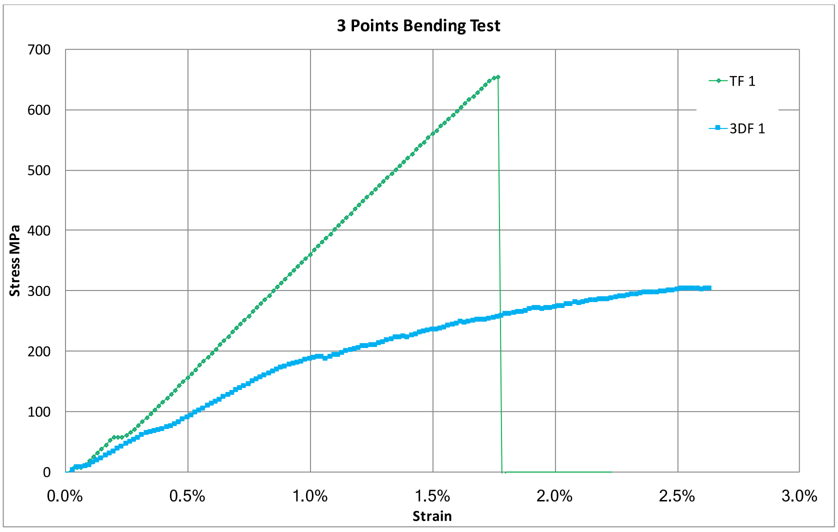

Figure 90 Three-point-bending: stress-strain curve for the thickness 3 with a span of 112 mm

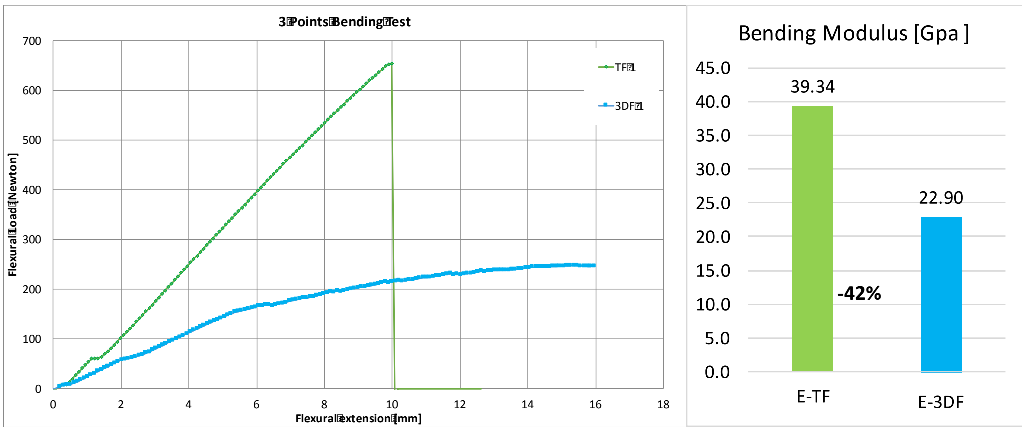

Figure 91 Three-point-bending: bending modulus for the thickness 3 with a span of 112 mm

- *Second batch (Flexural Strength evaluation)*

The second batch of specimens was tested using a span of 72 mm in order to bring both samples to the breaking point. Stress-strain curves for the 3DF and TF samples are reported in *Figure 92*a, while flexural strength and strain at break are illustrated in *Figure 92*b and c.

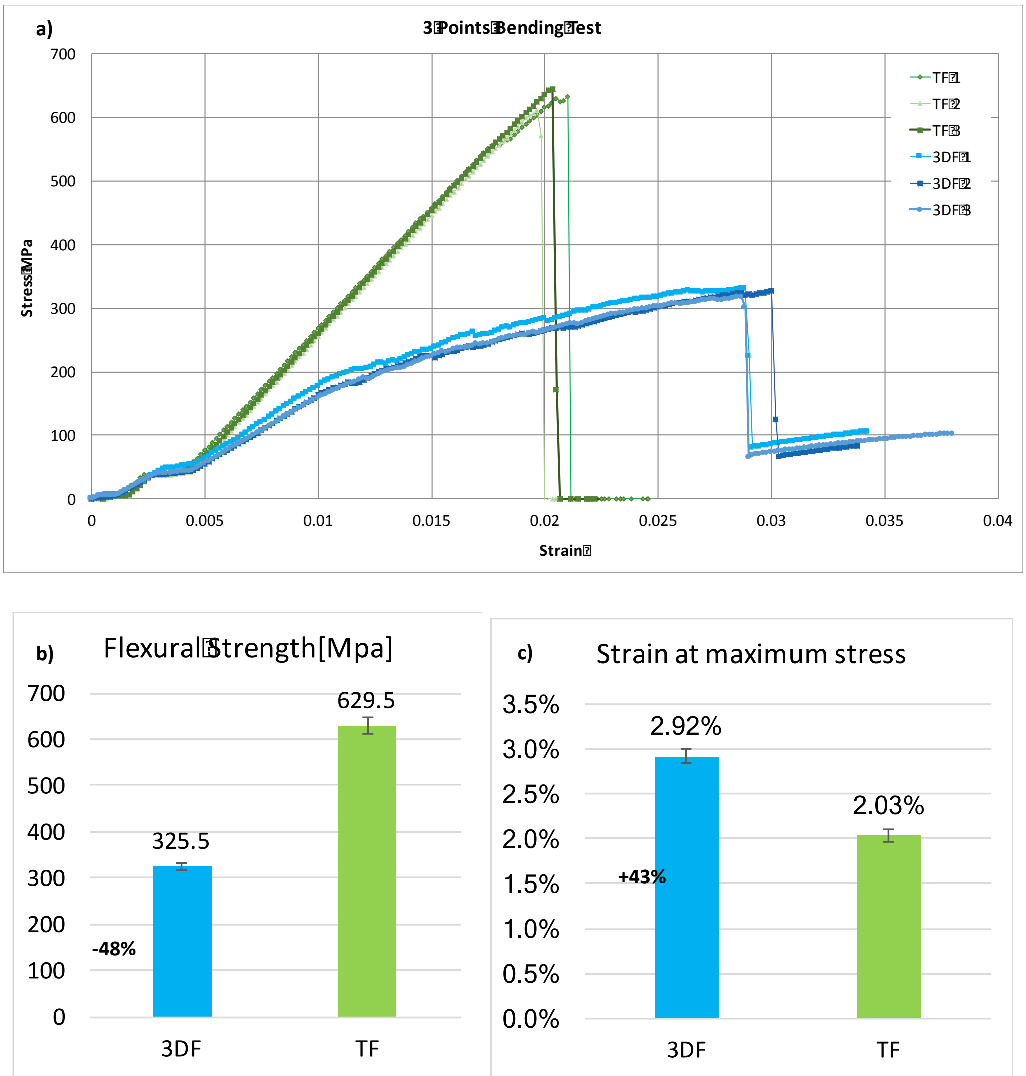

Figure 92 Three-point-bending for the thickness III with a span of 72 mm: a) stress-strain curve, b) flexural strength, c) flexural strain

Also for the third thickness, the 3DF specimens present a similar trend for the flexural strength, with a decrease in strength of nearly 48%, going from an average value of 629 MPa to 325 MPa for the TF. Also, the difference in flexural strain is similar to the previous cases, presenting a flexural strain of 2.03% for the TF specimens and to 2.92% of the 3DF ones, with an increment of +43%. It is important to underline that although the 3DF samples showed a very large displacement in comparison with the traditional samples, the final shape of the specimens showed a smaller bending angle due to the very large elastic recovery (almost 65%) that happens once the load is removed from the mid-section of the sample. Moreover, the 3DF specimens present only the bottom part damaged keeping the first two layers almost intact, while the TF samples present catastrophic failures (samples split in two parts).

Figure 93 T32-T9-1 and T32-T9-2 after the test

Figure 94 D37-D3-1, D37-D3-2 and D37-D3-3 after the test

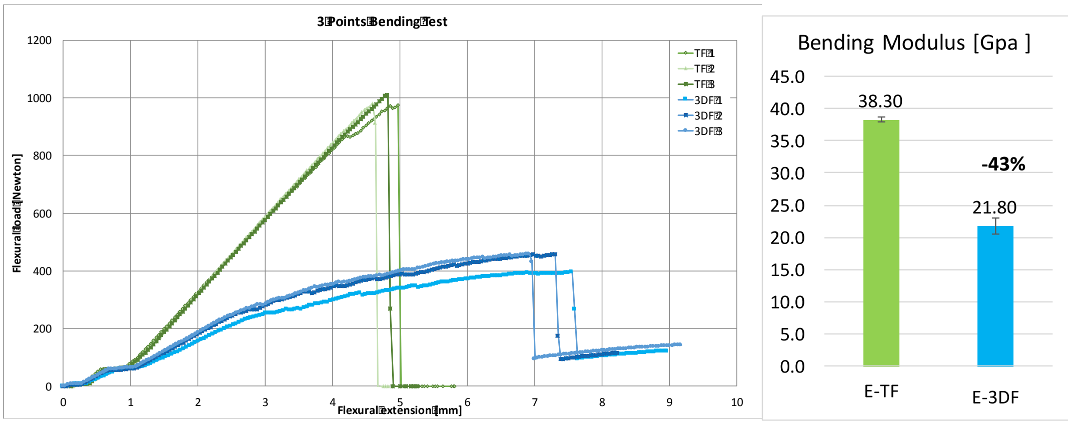

Figure 95 Three-point-bending: bending modulus for the thickness 3 with a span of 72 mm

The elastic modulus evaluated for the second batch is in agreement with the one calculated in the first batch. Indeed, the 3DF specimens show a lower modulus with respect to the TF samples, passing from 38 GPa for the TF to 22 GPa for the 3DF (-43%), as reported in *Figure 95*.

4.4.2.1.4 Comments

Analysing all the results listed above it is possible to conclude that the twisting procedure adopted for the 3DF samples, strongly affects the flexural behaviour of the composite laminates. In particular, the tested TF samples show fragile fracture which is typical of carbon composite structures with cracks propagating through the thickness of the specimens breaking the fibres in the area under tensile stress, and in the worst case bringing the sample to catastrophic failure (thickness 3). On the other hand, 3DF specimens show a pseudoplastic behaviour similar to the one observed in metals and polymers. Indeed, the sample is able to accommodate large displacements by deforming its structure due to the twisted carbon fibres that act as a sort of spring. This behaviour is confirmed by the large flexural strain shown for all three thicknesses, and by a very large elastic recovery that happens once the load is removed from the mid-section of the sample.

4.4.2.2 tensile test

The experimental campaign was conducted on several samples of rectangular cross section to analyse the effect of the twisted cordage on the tensile behaviour of composite laminates. Tensile tests were performed using an Instron Universal Tester (3369) and following the ASTM D3039 [208]. The test was conducted to evaluate the ultimate tensile strength and the modulus of elasticity of the tested laminates. To evaluate the Young's modulus of the samples the tests were conducted with strain transducers attached on the samples in order to obtain the stress-strain response of the material. Each sample is mounted in the grips of the Instron and loaded in tension. In order to protect the material from damage by the grips that clamp, and to increase the area of the loading region and reduce local stress concentrations, tabs were glued on both ends of the specimens as illustrated in Figure 96.

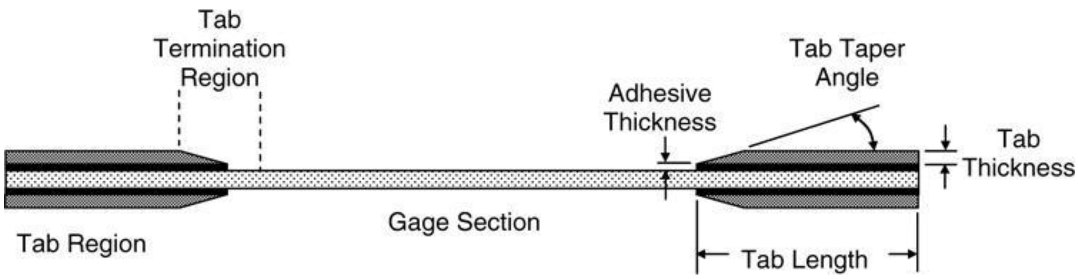

Figure 96 –Tabbed composite specimens for the tensile test

Tabs were made of aluminum with a thickness of 1.5 mm, length of 50 mm and width of 21 mm. The tabs increase the contact area over which the end loading is applied. Indeed, the axial load is introduced into the composite via shear, due to the frictional forces developed between the grip faces and the surfaces of the tabs. Thus, when local stress concentrations do occur at the ends, the maximum stress will hopefully still be less than that in the gage section of the specimen, resulting in gage section failures as desired. Strain transducers were instrumented to measure strain in both longitudinal and lateral directions for the evaluation of the modulus of elasticity. Possible bending of the specimens was monitored by measuring the longitudinal strain simultaneously on the opposite faces of the specimen. The applied load is measured by a load cell mounted between the specimen and the crosshead by converting forces into electrical signals that can be subsequently processed by the control system. A list of the samples used during this test campaign and their relative dimensions are reported in Table 8.

Table 8 - Samples used for the tensile bending test campaign

Sample Label	Fibre Type	Number of plies	Length (mm)	Width (mm)	Thickness (mm)
T6-33-1	Traditional (TF)	6	223	20.48	2.35
T6-33-2	Traditional (TF)	6	223	19.96	2.41
D2-38-1	Twisted (3DF)	2	221	20.32	2.13
D2-38-2	Twisted (3DF)	2	221	20.52	2.36
D2-38-4	Twisted (3DF)	2	221	20.56	2.20
D2-5-5	Twisted (3DF)	2	210	19.96	2.58

Figure 97 illustrates the initial area of the stress-strain curve for the 3DF and TF samples evaluated by strain gauges attached to the specimen and the load cell recorded by the Instron.

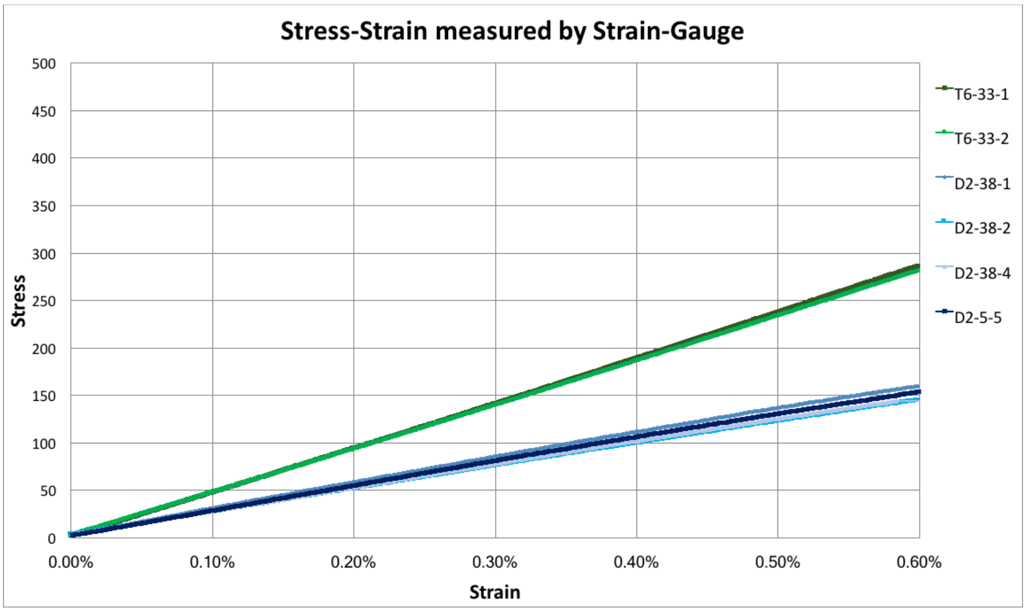

Figure 97 Stress-Strain diagram for 3DF and TF specimens evaluated using strain gauges.

The ultimate strength of the material was determined from the maximum load carried before failure. The ultimate tensile strength and the tensile stress were evaluated from the load-displacement curves by following the equation:

$$F^{tu} = \frac{P^{max}}{A} \tag{12}$$

$$\sigma_i = \frac{P_i}{A} \tag{13}$$

where F^{tu} represents the ultimate tensile strength in MPa, σ_i the tensile stress at ith data point, and A the average cross-sectional area of the specimen in square millimetre. Figure 98 illustrates the values of the ultimate tensile strength calculated for the 3DF and the TF samples.

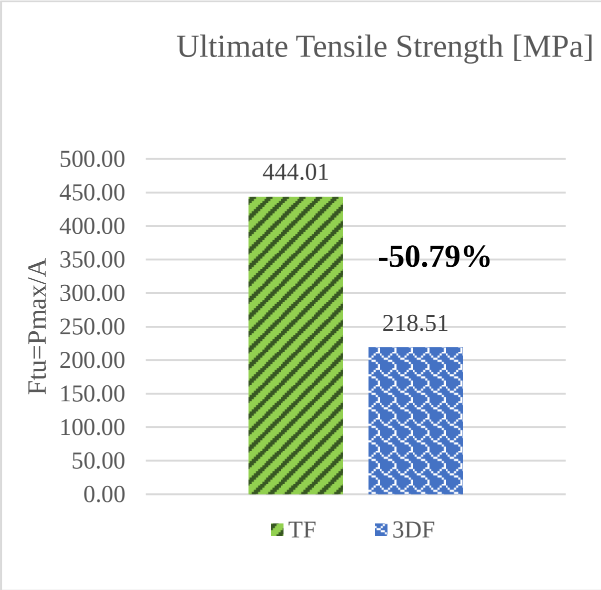

Figure 98 – Ultimate tensile strength

The 3DF samples tested in this work show a decrease of almost 50% in tensile strength with respect to the TF one. Fibres in the 3DF samples are not straight and so pulling on them causes contact pressure between the layers of strands, resulting in early failure. As explained in the paragraph 3.3, the tensile behaviour of twisted fibres is complex and can decrease, respect to an unidirectional bundle of fibres, the tensile strength of the structure. Additionally, due to the twisting operation on the fibres used for the manufacturing of the 3DF fabric, more cracks are present in the fibres, which lead to easy composite failure and then at a lower tensile strength

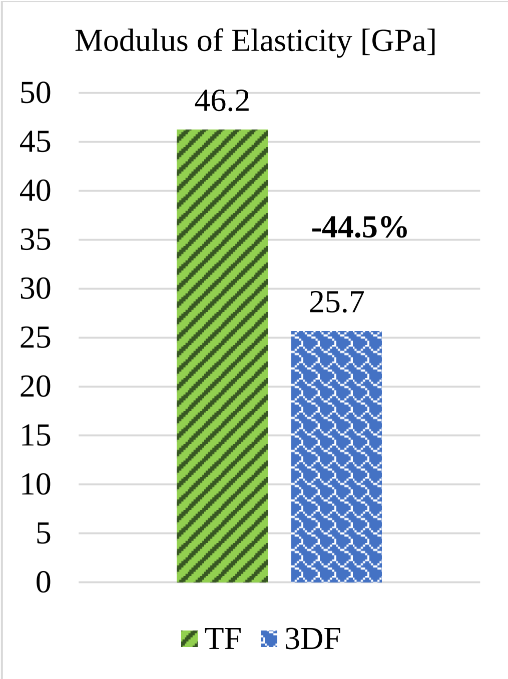

Figure 99 – Modulus of Elasticity

Tensile chord modulus of Elasticity was calculated according to the equation below:

$$E^{chord} = \frac{\Delta\sigma}{\Delta\epsilon} \tag{14}$$

The modulus achieved for the 3DF specimen is 44.5 % less than the modulus for the TF ones (see Figure 99). This is in agreement with earlier tests (three points bending). The reason behind this is that only a portion of the fibres run in the test direction. Along with this, twisting the fibres makes the fibre packing less efficient in the woven structure; which reduces the modulus of woven composites compared to the unidirectional composites. Moreover, the twisting operation affects also interfacial property between fibres and resin. Indeed, the permeability of the yarns and the impregnation of the fibres became more difficult with the increase of the number of twists. Consequently, the interfacial property between fibres and resin would be impaired dramatically resulting in poor mechanical properties.

The mechanical treatments undergone by fibres have to be mentioned to explain the scattering of the results and the lower strain at break for the 3DF specimens. The carbon fibres can be damaged during the manufacturing process that goes from the treatment of the single fibre to the weaving of the fabric. It is important to underline that the 3DF fabric presents an additional step during its manufacturing process, in which the fibres are twisted together before the weaving operation. The operation of twist insertion can cause fibres damage and hence cause premature failure, resulting in a lower strain. Moreover, the twisted fibres present a higher friction compared to the unidirectional ones, that can cause more fibre damage due to the friction and abrasion at every contact point of the fibres during weaving. In addition, all twisted fibres were wound from a metal bobbin to a cardboard bobbing using a winding machine, in order to be weaved. This operation can cause damage to the fibres and so can affect the mechanical properties of the fabric. Analysing all the results listed above it is possible to conclude that the twisting procedure adopted for the 3DF samples, strongly affects the mechanical properties of the composite laminates. In particular, the changes of orientation angles between reinforcing fibres and the applied load, the fibre damage introduced by the weaving and twisting process and the high fibre agglomeration, hence poor impregnation due to the twisting configuration all contributed to the decline of the mechanical properties for the 3DF specimens.

4.4.2.3 Impact test

In order to investigate the impact resistance of the 3D twisted helicoidal composite material, several samples were manufactured and subjected to low velocity impacts (LVI) at different impact energies. The impact curves recorded by the experimental apparatus were analysed and the characteristics of the impact properties were recorded together with the extent of the internal damage distribution. The 3D twisted helicoidal samples (labelled as 3DF samples) have been compared with traditional fabrics made with straight fibres (labelled as TF samples) for all the impact energies. Both the samples are a plain weave fabric manufactured using a traditional weaving machine and impregnated with the same epoxy resin system (VTC401 from SHD Composites).

In order to investigate the extent of the internal damaged area, each impacted sample was analysed with CT Scanner – Nikon XT H 225kV. X-ray computed tomography (X-ray CT) and computerized axial tomography scan (CAT scan) make use of computer-processed combinations of many X-ray images taken from different angles to produce cross-sectional (tomographic) images (virtual "slices") of the impacted samples, allowing precise assessment and identification of internal damaged areas. During the different analyses, the samples were analysed overlapping different specimens impacted at the same energy in order to have a direct comparison of the internal damage extension.

4.4.2.3.1 Single Layer Impact

3DF samples having one layer were compared with traditional composite having three layers and subjected to low velocity impacts (LVI) at different impact energies. The experimental campaign was conducted using a Drop-Weight LVI Impactor Dynatup 9250HV. The drop weight was of 4.415 kg and impactor's head was equipped with a hemispherical tip with a diameter of 20mm. Samples were dimensioned 100x150mm and clamped to a fixed support according to the BS EN ISO 6603-2:2000.

Figure 100 - Instron Dynatup 9250HV and clamping frame used during the experimental campaign

Because of the very low values of thickness of both 3DF and TF batches, some deviations from the standard were required in order to avoid complete perforation of the samples. In particular, the drop heights were less than 300 mm for the impact energies. In addition, since the 3DF-samples presented a slight curvature due to the autoclave curing, some of the samples might not have been totally in contact with the support plate outside the clamping window. Dimensions of the tested samples are listed in the Table below.

Table 9- weights and dimensions of the impacted samples (both 3DF and TF batches)

Straight fibres - TF Fabric					Twisted fibres – 3DF Fabric				
Label	**Length (mm)**	**Width (mm)**	**Thickness (mm)**	**Weight (g)**	**Label**	**Length (mm)**	**Width (mm)**	**Thickness (mm)**	**Weight (g)**
16 T	150.33	100.14	1.19	25.4	**7 D**	150.34	100.25	1.32	26.4
17 T	150.33	100.18	1.19	25.3	**9 D**	150.34	100.13	1.28	25.9
19 T	150.33	100.19	1.20	24.3	**10 D**	150.34	100.01	1.28	25.6

20 T	150.31	100.09	1.12	20.8	**11 D**	150.35	100.20	1.31	26.6
21 T	150.30	100.14	1.18	24.4	**12 D**	150.32	100.20	1.31	26.2
22 T	150.24	100.17	1.10	23.1	**13 D**	150.33	100.16	1.28	26.0
23 T	150.40	100.14	1.11	24.4	**14 D**	150.38	100.14	1.28	25.8
24 T	150.34	100.15	1.18	25.3	**25 D**	150.33	100.21	1.23	25.6

During the test the weight of the impactor was kept constant (4.415 kg), therefore in order to impact the samples at different energy levels, the velocity of the impact (v0) was tuned according to the equation:

$$v_0 = \sqrt{2\frac{E}{m}} \tag{15}$$

where m is the mass of the impactor and E is the required impact energy. The impact height was further adjusted by performing velocity tests on the rig in order to balance the error given by friction and mechanical inertia.

4.4.2.3.1.1 2J Impacts

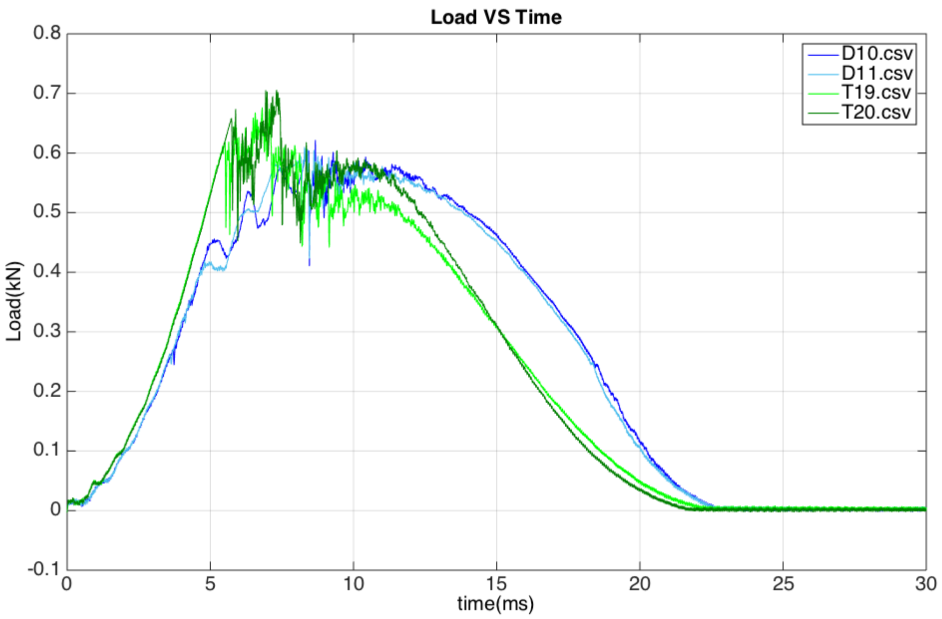

Figure 101 - Load VS Time curve for 2J impacts om samples TF and 3DF

The image above represents the load versus time curves collected from the load cell during the 2J impacts on the samples D10 and D11 (3DF) and T19 and T20 (TF). All samples survived the test with no perforation. From these data it is possible to evaluate the deflection of the test specimen by following the equation:

$$s(t) = v_0 - \frac{1}{m}\int_0^1 \left[\int_0^{t_1} F(t)dt_1\right] dt + \frac{1}{2}gt^2 \tag{16}$$

Where v0 is the impact velocity expressed in meters per second (0.933 for the 2J impacts), t is the time after impact at which the deflection is to be calculated (in seconds), F(t) is the force measured at any time after the initial impact expressed in Newtons, s(t) is the deflection expressed in meters, m is the weight of the falling mass of the impactor expressed in kilograms and g is the universal gravitational constant.

The data can then be expressed as Load versus Deflection curves which can be used to determine the area under the curve which represents the energy expended up to specific times tj from the equation:

$$E_j = \int_0^{t_j} F(s)ds \tag{17}$$

Where F(s) is the force at the deflection s, expressed in Newtons, s is the deflection (in meters) and J is a subscript that can denote different points in the curves such as Maximum (M), Puncture (P) or Yielding (Y). Load displacement curves obtained for samples D and T impacted at 2J are represented in the Figure below.

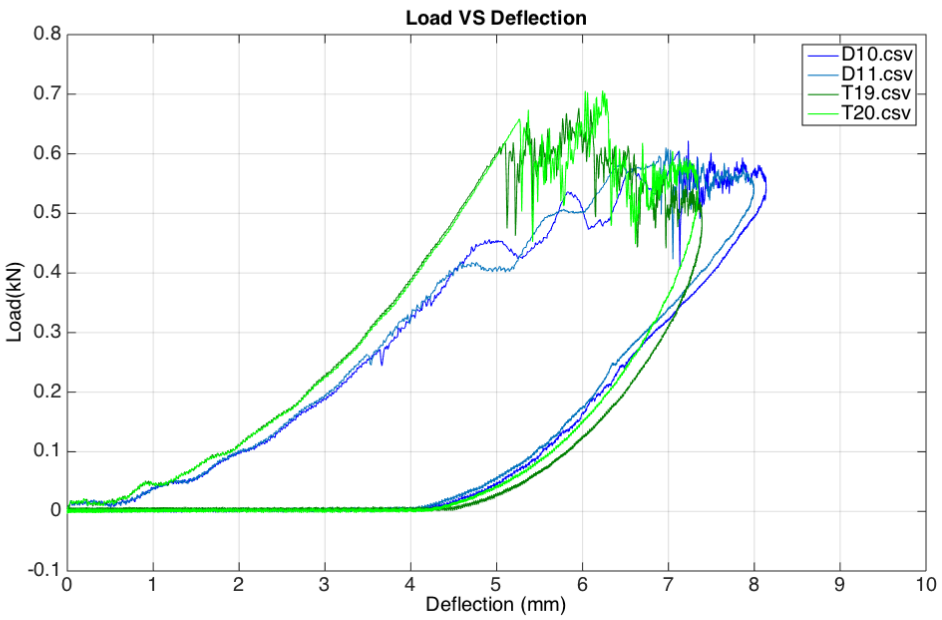

Figure 102 - Load VS Deflection curves for samples TF and 3DF impacted at 2J

Figure 103 shows the scan of the TF (labelled, in the picture, with the letter T) and 3DF (labelled, in the picture, with the letter D) samples impacted at 2J. The samples were sliced in three different orthogonal views to investigate the internal area around the impact location.

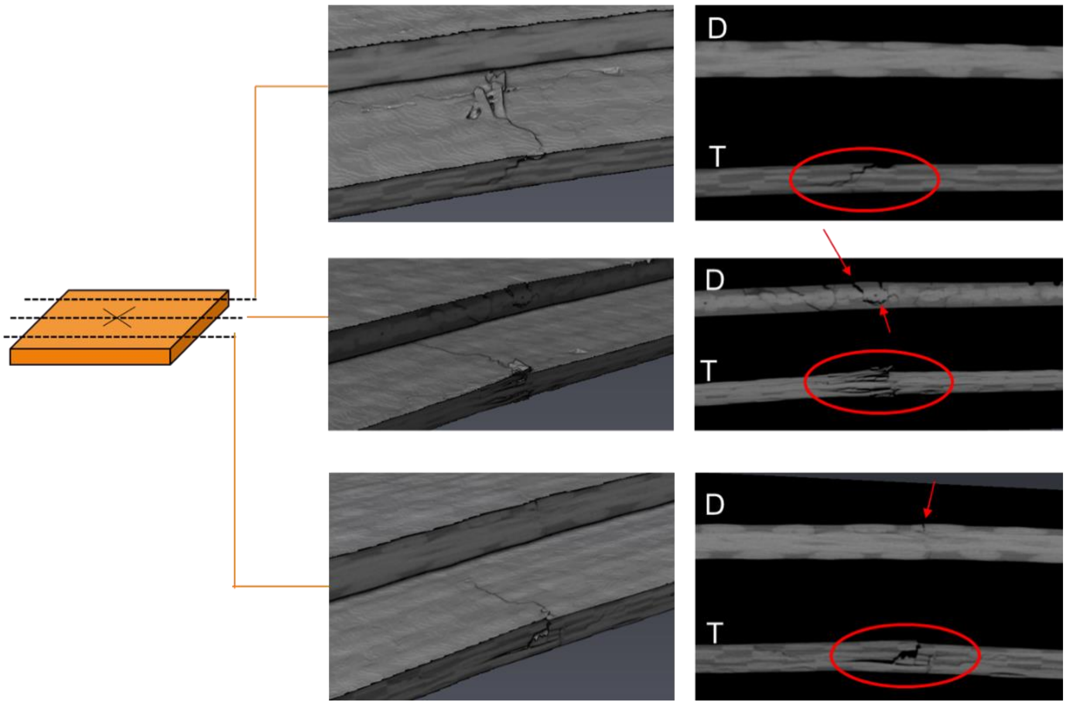

Figure 103 - CT scan images of samples 3DF and TF impacted at 2J

As it is possible to see from the images, the different geometry of the two typologies of fibrous reinforcement strongly affects the behaviour of the composite part when it is subjected to an out-of-plane impact load. Analysing the images of the TF sample it is possible to see the presence of internal delamination along the interface between the different laminae of the samples. Although they extend relatively far from the impact point, these delamination are not critical per se because of the low energy of the impact (2J), however they can act as stress intensification points during the normal operation in the working environment leading to sudden catastrophic failure of the part. On the other side the 3DF sample, because of its intrinsic "bulk" geometry (i.e. the absence of interlaminar interfaces generated from the twisted arrangement of the fibres that forms the single fabric used to manufacture the sample), shows a concentration of damage only in the impact area, showing only superficial cracks and no hidden internal damaged areas.

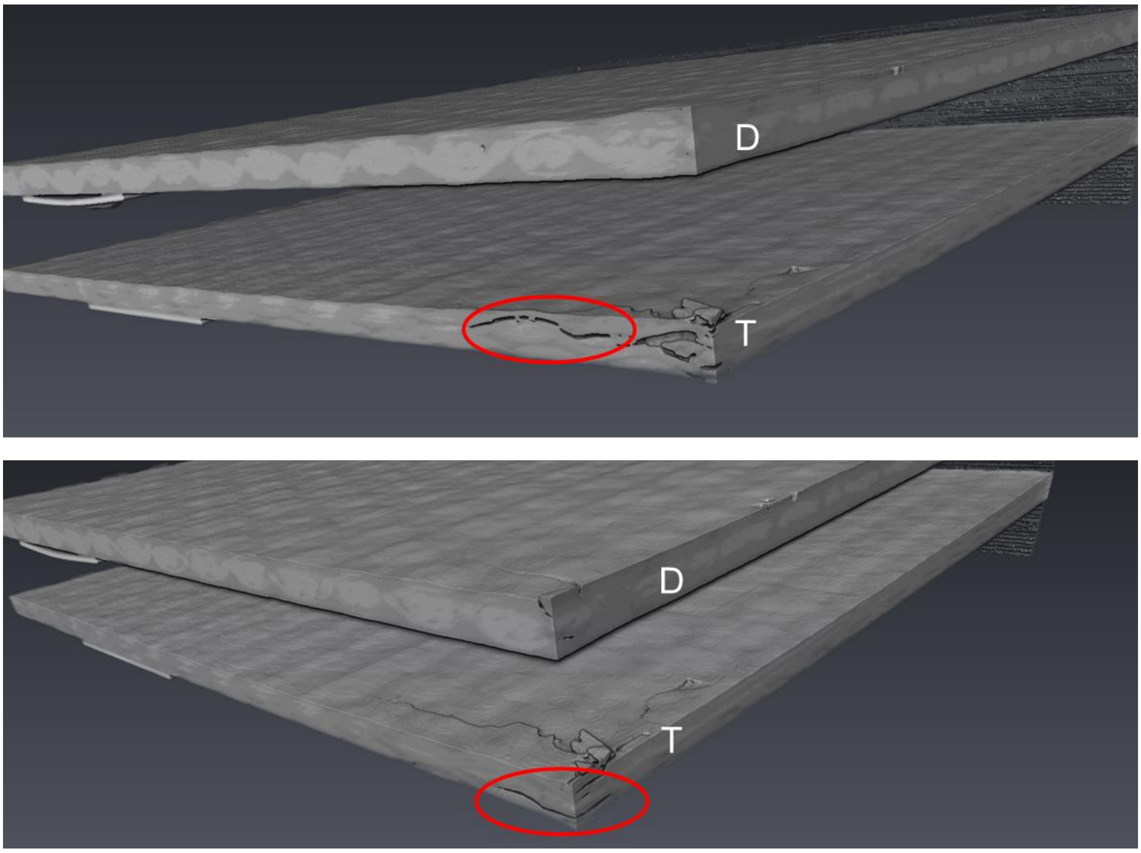

Figure 104 - Details of the internal delaminations within samples impacted at 2J

The presence of internal delamination for the TF sample is even more evident in Figure 104, where the propagation of the internal damage is represented in an orthogonal cross-section of the impacted area, as illustrated by the red circles in the images.

4.4.2.3.1.2 3J Impacts

Figure 105 illustrates the measured Load versus Time curves obtained from the load cell during the impact test on samples D12 and D13 (3DF) and T21 and T23 (TF) at 3J. The mean impact velocity was evaluated with a velocity sensor and measured 1.146 m/s. All samples survived the test with no perforation.

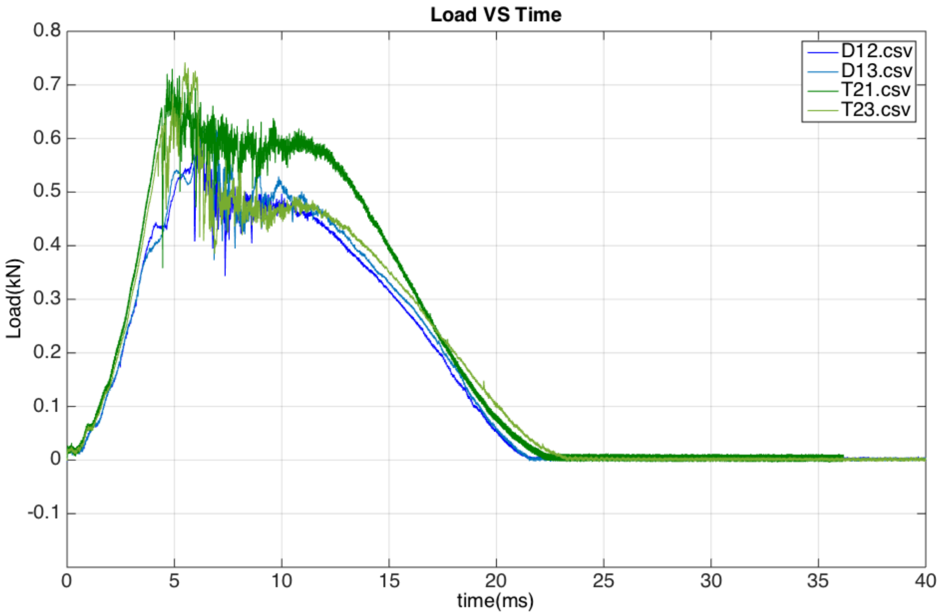

Figure 105 - Load VS Time curves for TF and 3DF samples impacted at 3J

The results from the tests were used to evaluate the Load versus Deflection curves, as illustrated in Figure 106 according to Equation (16)

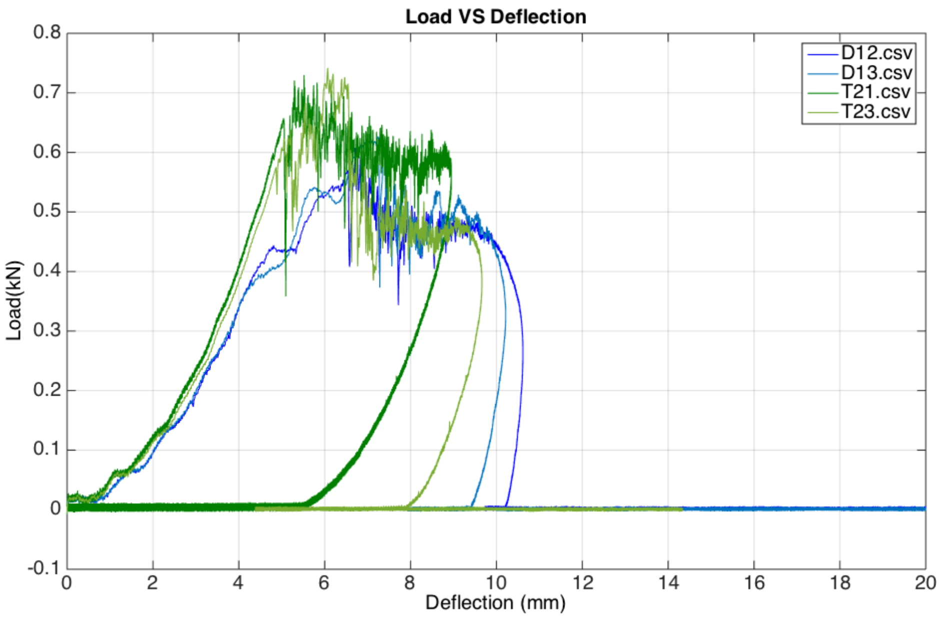

Figure 106 - Load VS Deflection curves for TF and 3DF samples impacted at 3J

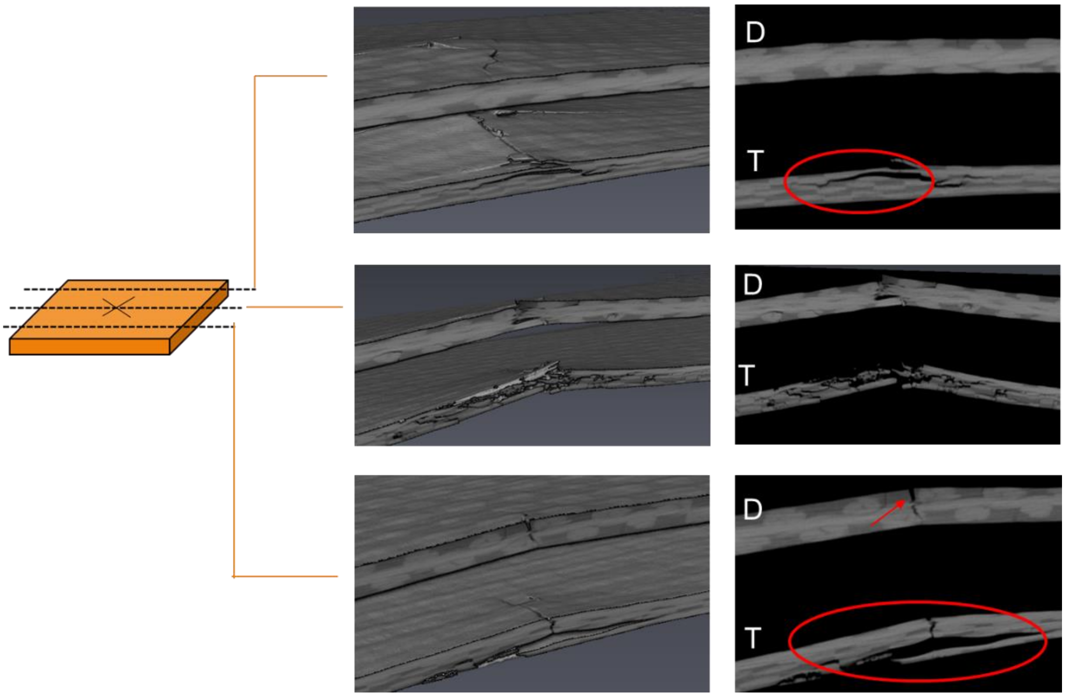

Figure 107 - CT-Scan Images captured for the TF and 3DF samples impacted at 3J

Figure 107 and Figure 108 represent the post-impact scans recorded for the impacted samples.

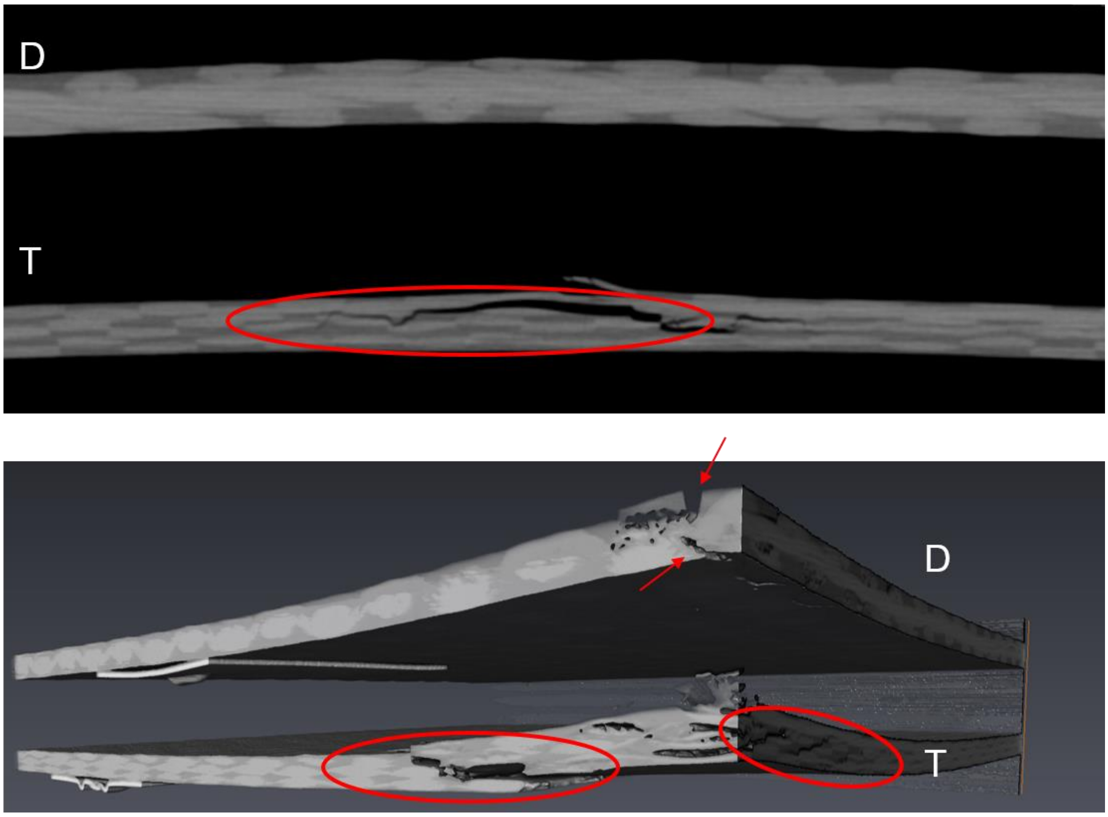

Figure 108 - Details of delaminated internal area close to the impact location for TF and 3DF samples impacted at 3J

The figures show the same trend observed in the previous scans for the 2J impacted samples. Indeed, as it is possible to see from the internal damage distribution, increasing the impact energy up to 3J increases the extent of the internal delaminations for the TF samples. On the other side, since the 3DF samples cannot dissipate impact energy through the opening of new internal surfaces (because of its twisted bulk structure), the twisted sample presents large superficial cracks strongly localised in the impact location as indicated by the red arrows in figures 8 and 9. Moving away from the impact area the presence of internal damaged areas is evident for the TF sample while the 3DF keeps its integrity (see Figure 108).

4.4.2.3.1.3 4J Impacts

Figure 109 illustrates the measured Load versus Time curves obtained from the load cell during the impact test on samples D7 and D9 (3DF) and T16 and T17 (TF) at 4J. The mean impact velocity was evaluated with a velocity sensor and measured 1.326 m/s. All samples survived the test with no perforation.

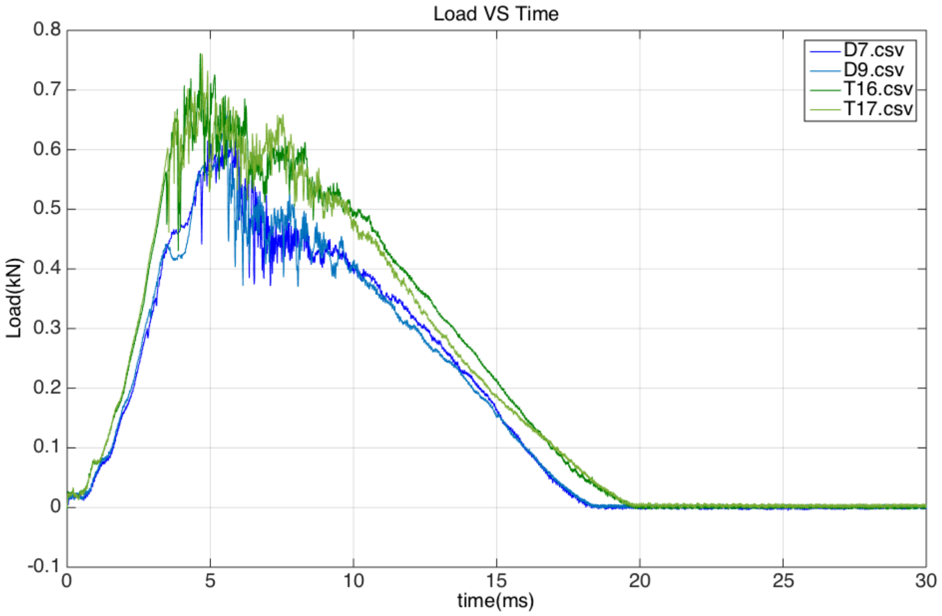

Figure 109 - Load VS Time curves for TF and 3DF samples impacted at 4J

As for the previous case the results from the tests were reported in Figure 110, per Equation (16, in the graph Load versus Deflection.

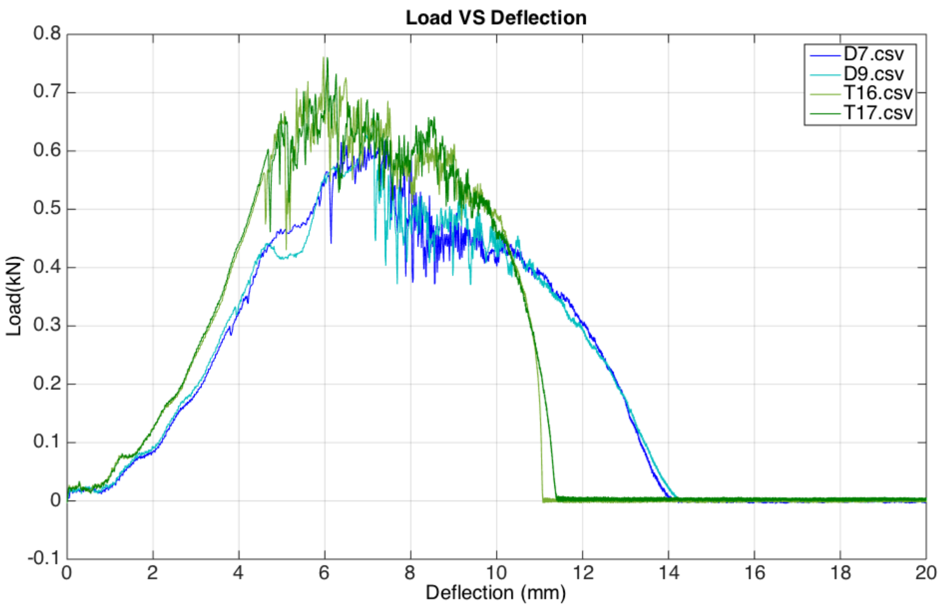

Figure 110 - Load VS Deflection curves obtained from TF and 3DF samples impacted at 4J

Figure 111 and Figure 112 below illustrate the internal damage distribution for the TF and 3DF samples impacted at 4J. Analysing the images, it is possible to observe the same behaviour observed for the impacts at lower energies, however in this case, because of the higher energy content of the impacts, the different mechanisms of energy dissipation during the impact time are more evident.

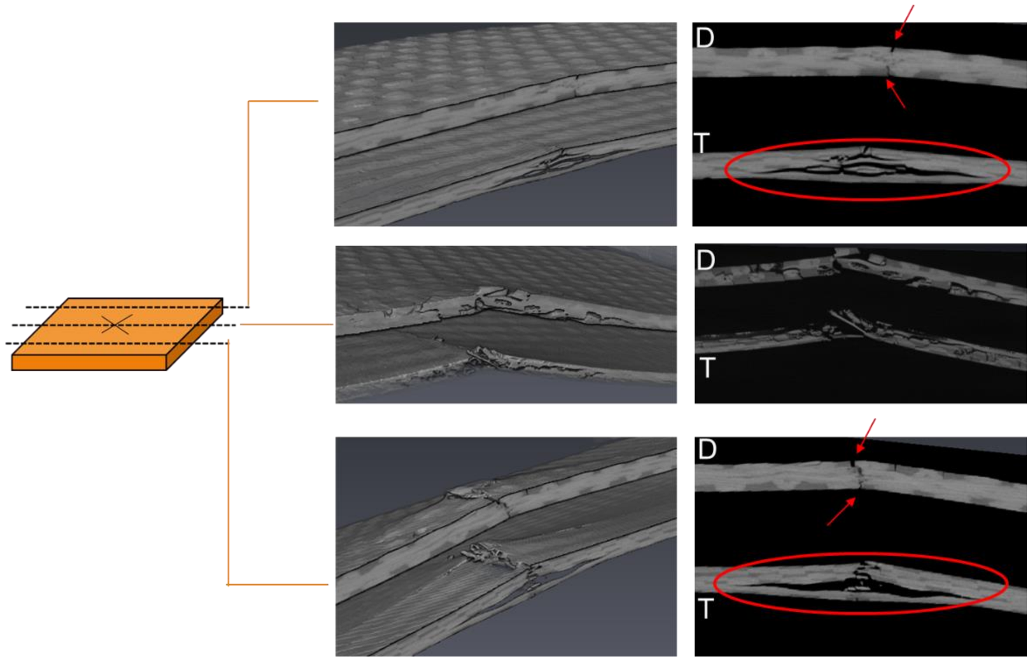

Figure 111 - CT-Scan images captured for samples TF and 3DF impacted at 4J

Analysing Figure 111, it is possible to see the presence of a very large delaminated area far from the impact location for sample TF which was generated by the contact with the impactor's head during the impact duration. The only way for the TF laminate to absorb the impact energy was to open new surfaces at the interface between two subsequent laminae, generating internal delaminated areas. This delamination extends far from the impact point along the length of the sample weakening it and reducing its residual properties.

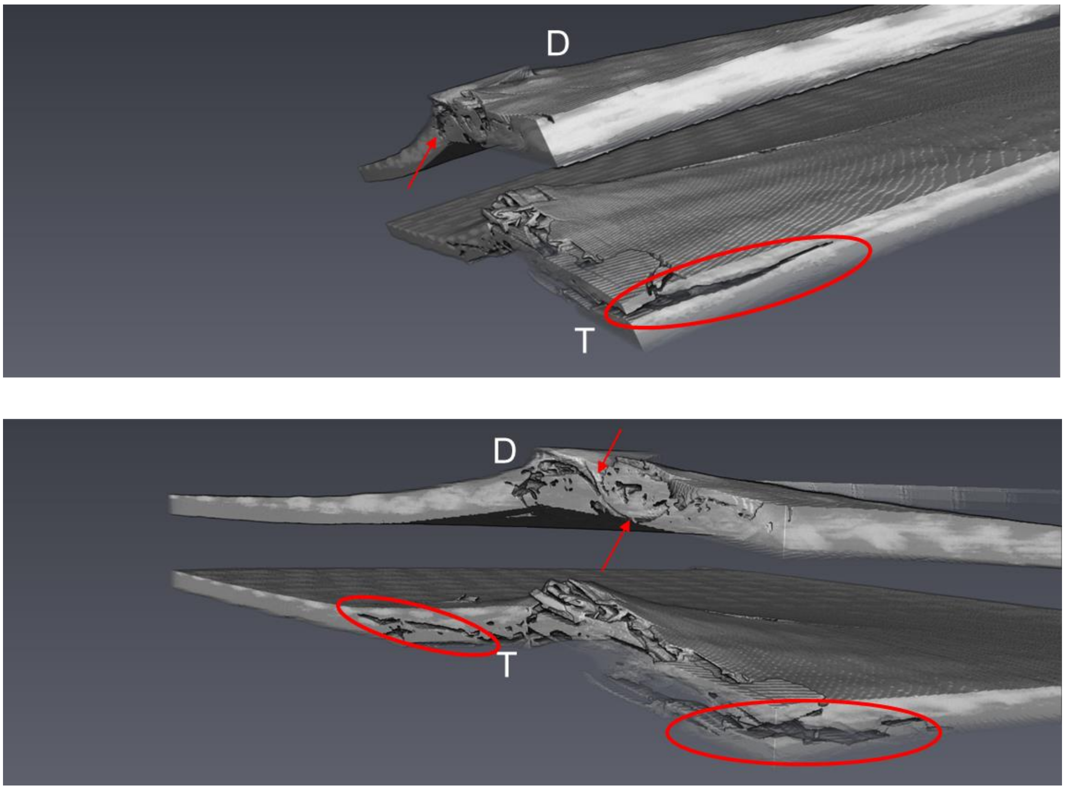

Figure 112 - Details of the different fracture behaviour of TF and 3DF samples impacted at 4J in correspondence with the impact location

Because of the twisted structure of the fabric, at the same position, sample D does not show any internal damage but only relatively large cracks which are generated on the surface because of the contact with the impactor's head. Since there is no possibility to dissipate the impact energy via the creation of delamination, these cracks become larger in correspondence with the impact location going along almost the entire thickness, with secondary cracks propagating from the impact location along the width of the sample (always visible from the top surface). Sample TF on the contrary appears shattered in the impact location with two out of three plies completely broken and an internal delamination running along a large portion of the sample's width. This different behaviour is clear in Figure 112 in which it is possible to see the large cracks on sample 3DF propagating from the impact area (red arrows in the images) compared with the internal delamination of sample TF indicated with the red circles in the two images.

4.4.2.3.1.4 5J Impacts

Figure 113 illustrates the measured Load versus Time curves obtained from the load cell during the impact test on samples D14 and D25 (3DF) and T22 and T24 (TF) at 5J. The mean impact velocity was evaluated with a velocity sensor and measured 1.477 m/s. All samples survived the test with no perforation.

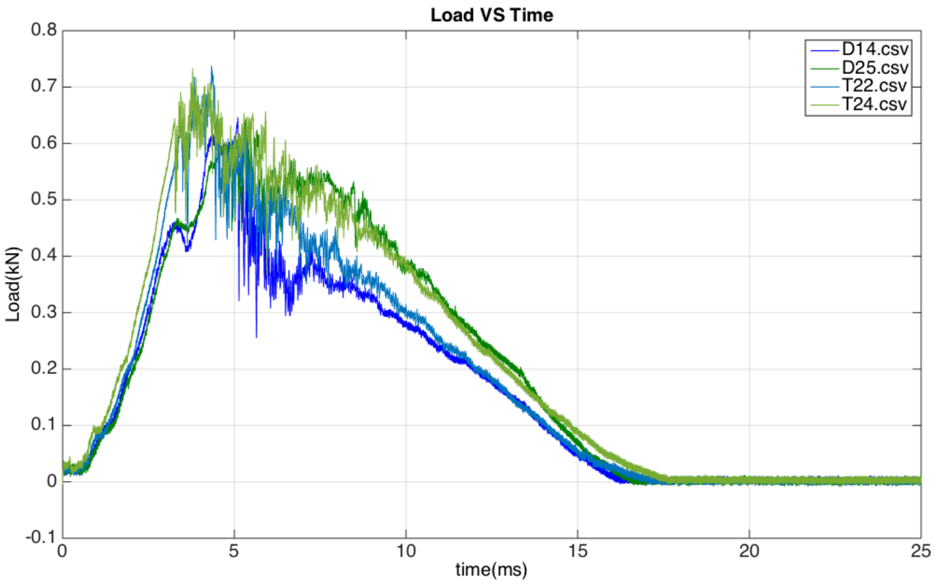

Figure 113 - Load VS Time curves for samples TF and 3DF impacted at 5J

As for the previous case the results from the tests were reported in Figure 114, per Equation (16, in the graph Load versus Deflection.

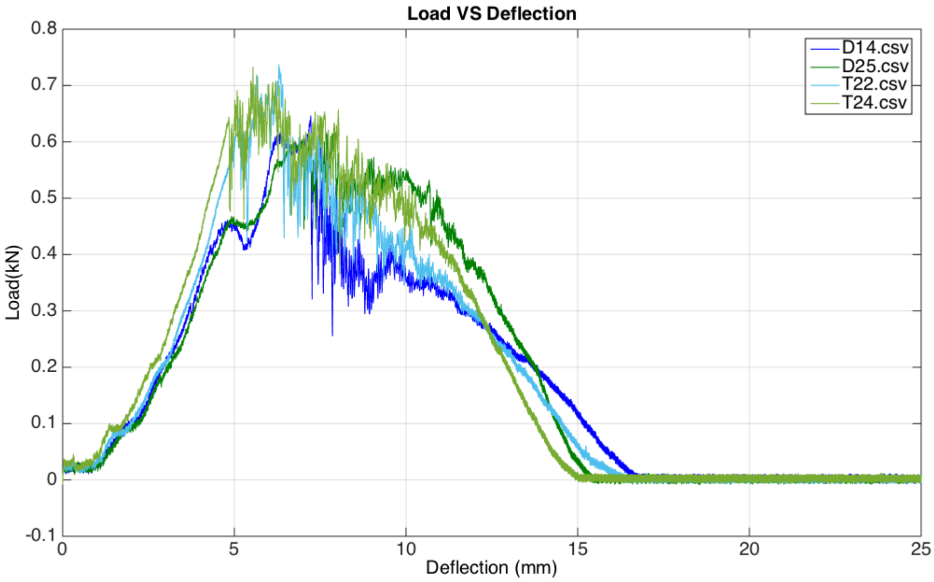

Figure 114 - Load VS Deflection curves for samples TF and 3DF impacted at 5J

The internal damage distribution captured with the CT-Scan is represented in Figure 115.

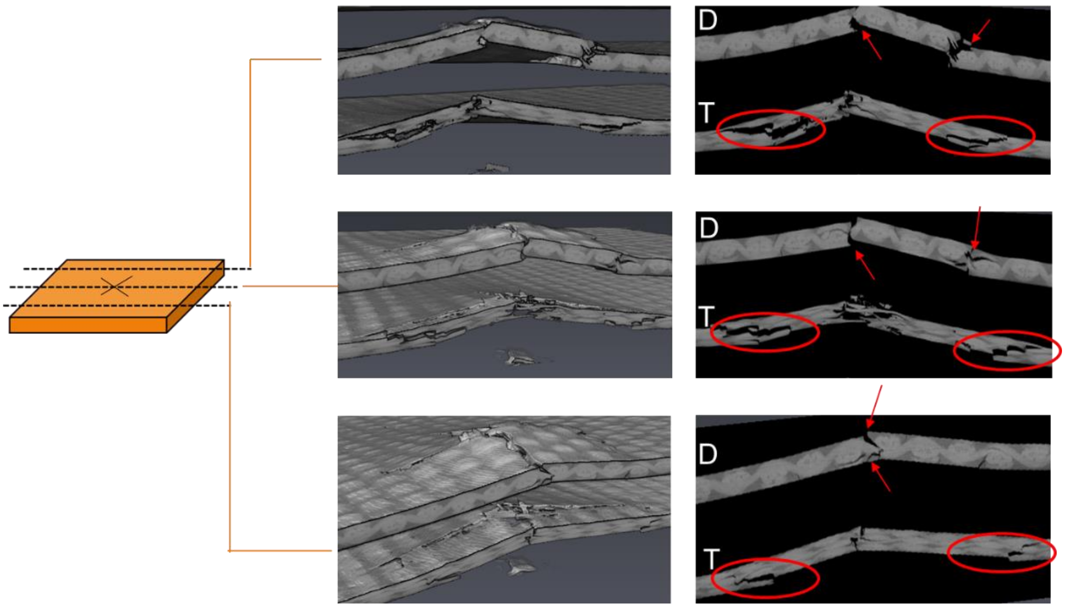

Figure 115 - CT Scan images acquired for samples TF and 3DF impacted at 5J

As it is possible to see from the different fracture mechanisms, in the area of the impact the effect of a 5J impact is far more catastrophic than at lower energies. Indeed at the impact location, sample 3DF presents large cracks that in some cases cross the entire thickness of the sample as indicated with the red arrows in the images. The cracks tend to go around the twisted fibres bundles and propagate through the matrix rich areas following the twists of the tows, leading to matrix-fibres debonding. Moving from the impact location the presence of these damages is reduced with no visible internal damages as it is possible to see from Figure 116.

As for sample TF, in the location of the impact, the delaminations are extended and propagate far from the impact area, shattering all the plies in correspondence with the impactor's head contact area (see Figure 116). In addition, as seen for the impacts at 4J, internal delaminations are not the only kind of damage generated from the impact, which are accompanied by large cracks that start from the surface and propagate through the entire sample. Secondary symmetrical cracks also open from the bottom surface far from the impact area (see Figure 115).

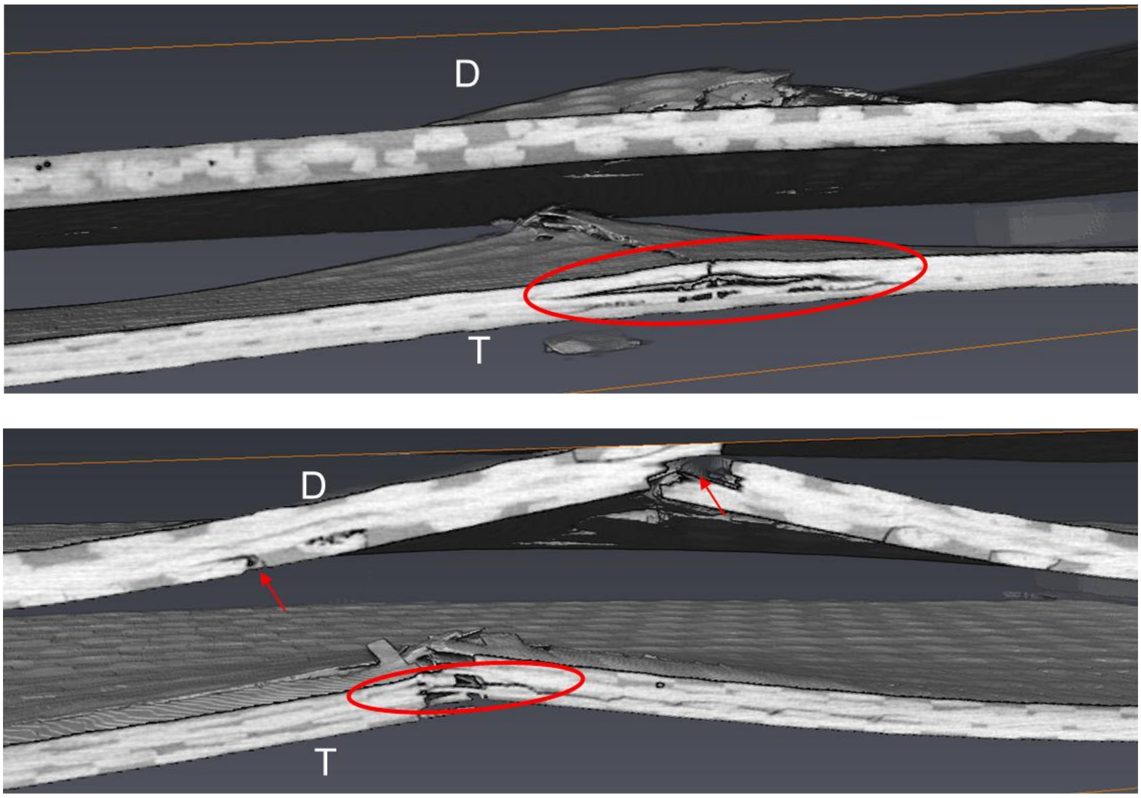

Figure 116 - Details of the different damage propagation in the proximity of the impact location for samples TF and 3DF impacted at 5J

4.4.2.3.1.5 7J Impacts

Figure 117 illustrates the measured Load versus Time curves obtained from the load cell during the impact test on samples D2 (3DF) and T18 (TF) at 4J. The mean impact velocity was evaluated with a velocity sensor and measured 1.743 m/s. All samples survived the test with no perforation.

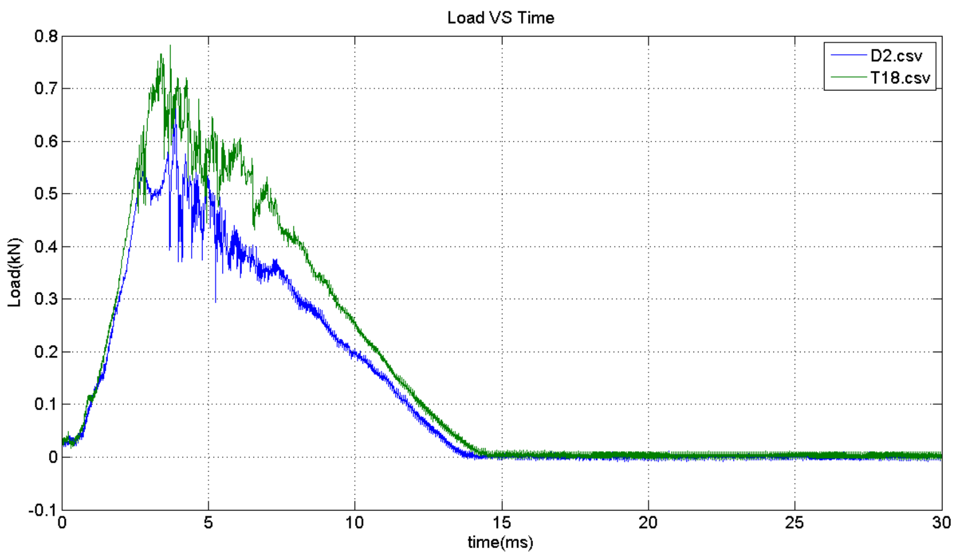

Figure 117 - Load VS Time curves for samples TF and 3DF impacted at 7J

As for the previous cases the results from the tests were reported in Figure 118 per Equation (16, in the graph Load versus Deflection.

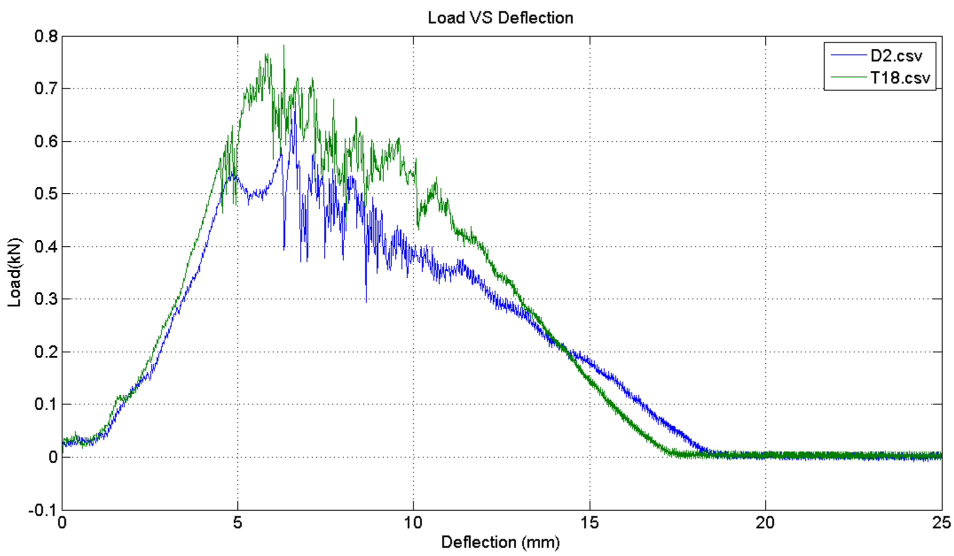

Figure 118 - Load VS Deflection curves for samples TF and 3DF impacted at 7J

Results from the CT-Scan analysis are represented in Figure 119 and Figure 120 below.

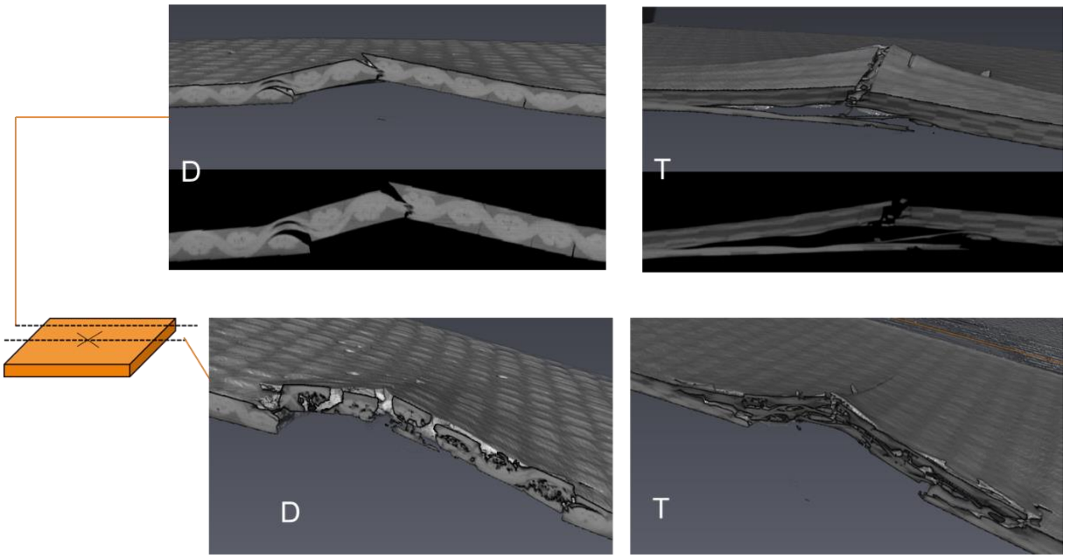

Figure 119 - CT-Scan images of samples TF and 3DF impacted at 7J

As for the 5J impacts, debonding at the fibres-matrix interface is observed for the 3DF samples with some fibres damages in correspondence with the impact location. Also in this case, the cracks on the surface tend to follow the twisted structure of the fibres tow, propagating through the matrix rich areas, although where the load is localised in a small area (i.e. the point in contact with the impactor's head) the twisted fibres bundle is split in two. Overall there are no internal damages or delamination far from the impact location with only some very small cracks that propagate for a small extent along the sample's thickness from the bottom surface. For this impact, it is observed that secondary perpendicular cracks start to form in the location of the impact which suggest that sample 3DF is reaching its impact resistance limit.

Sample TF presents a behaviour very similar to the one observed for the impacts at 4 and 5J. A large portion of the impact energy is absorbed by the opening of large delamination which are extended on a large area covering almost half of the sample (see Figure 120). In the impact area, the bottom layer is almost completely detached from the laminate and cracks propagate both in the matrix and in the fibres bundles with the classical tree pattern observed in traditional composite laminates.

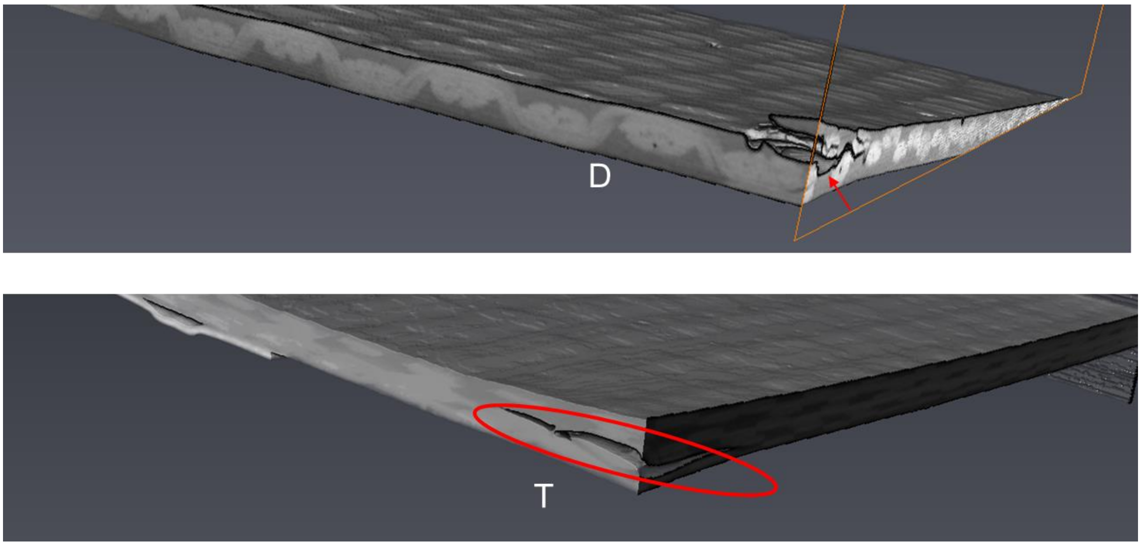

Figure 120 - Details of the internal damage distribution for samples TF and 3DF far from the impact location (7J)

4.4.2.3.1.6 Comments

The table below, summarises the results calculated from the Dynatup Instron machine.

Table 10 Impact data

EN TEST [J]	EN IMPACT [J]	VELOCITY [m/s]	MAX LOAD [kN]	EN MAX LOAD [J]	EN FAILURE [J]	DEFL MAX LOAD [mm]	DEF FAIL[mm]
TF							
2.000	1.919	0.932	0.691	1.719	2.061	6.096	6.036
3.000	2.908	1.148	0.736	1.570	3.171	5.796	8.126
4.000	3.877	1.325	0.761	1.805	4.544	6.012	11.092
5.000	4.876	1.486	0.756	1.756	5.077	5.637	12.989
7.000	6.730	1.746	0.783	2.081	5.921	6.321	14.820
3DF							
2.000	1.927	0.934	0.616	1.939	1.730	7.101	5.676
3.000	2.891	1.144	0.623	1.924	3.492	6.997	10.184
4.000	3.888	1.327	0.641	2.091	4.408	7.269	13.230
5.000	4.767	1.470	0.652	2.011	4.719	7.027	14.294
7.000	6.694	1.742	0.675	1.921	5.022	6.646	15.786

Figure 121 illustrates the trend of the maximum load recorded for all the impacts at different energies for both samples TF and 3DF. As it is possible to see, the traditional laminate shows higher value of the maximum load for all the impact, keeping an increase of around ~13% along all the different impact energies ranging between 0.7 to 0.8 kN for the TF samples and between 0.6 to 0.7 kN for the 3DF ones.

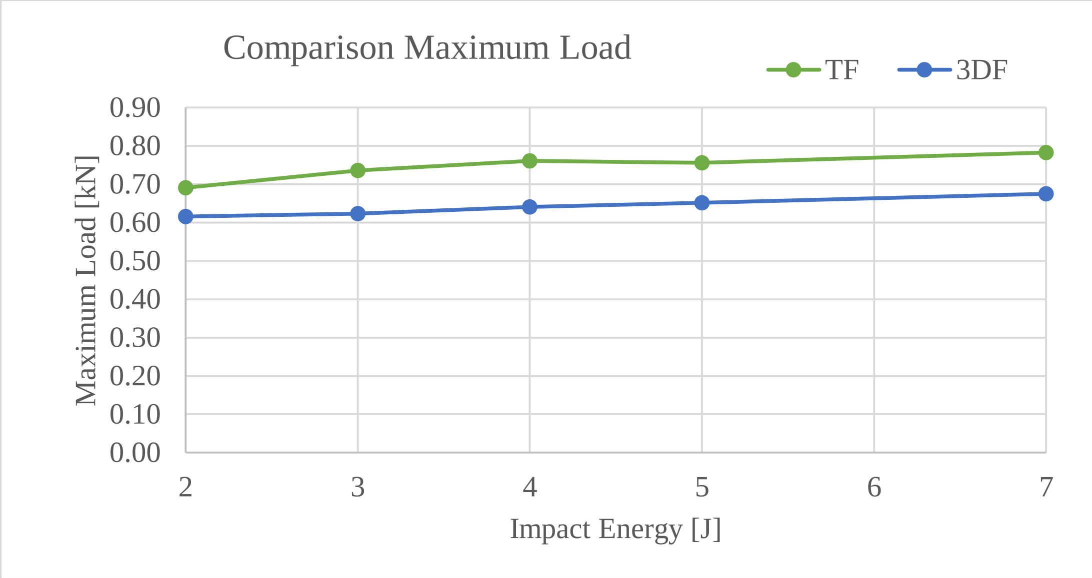

Figure 121 - Maximum load evaluated for the different impact energies for samples TF and 3DF during the entire experimental campaign

On the contrary, the deflection at failure of the sample shows an inverse behaviour, with the 3DF samples showing an increase in the maximum deflection with an average of ~15% from the impacts from 3 to 7J, while showing the same values for the 2J impacts.

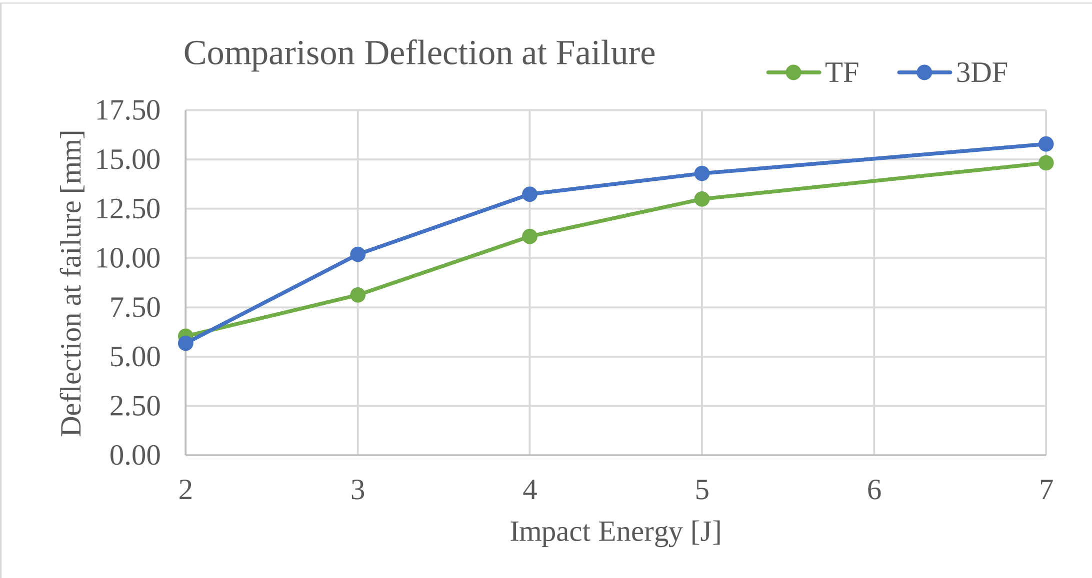

Figure 122 - Deflection at fracture evaluated for the different impact energies for samples T and D during the entire experimental campaign

Analysing the trends of both Maximum Load and Deflection at Failure, it appears that while the TF samples react with a high strength at low deflection, the 3DF material responds in an opposite way, by absorbing the impacts with higher values of deformation. These higher values of the deformation together with a lower value of strength confirm the results obtained with the flexural tests (three points bending on both rods and fabrics) in which same trends was observed.

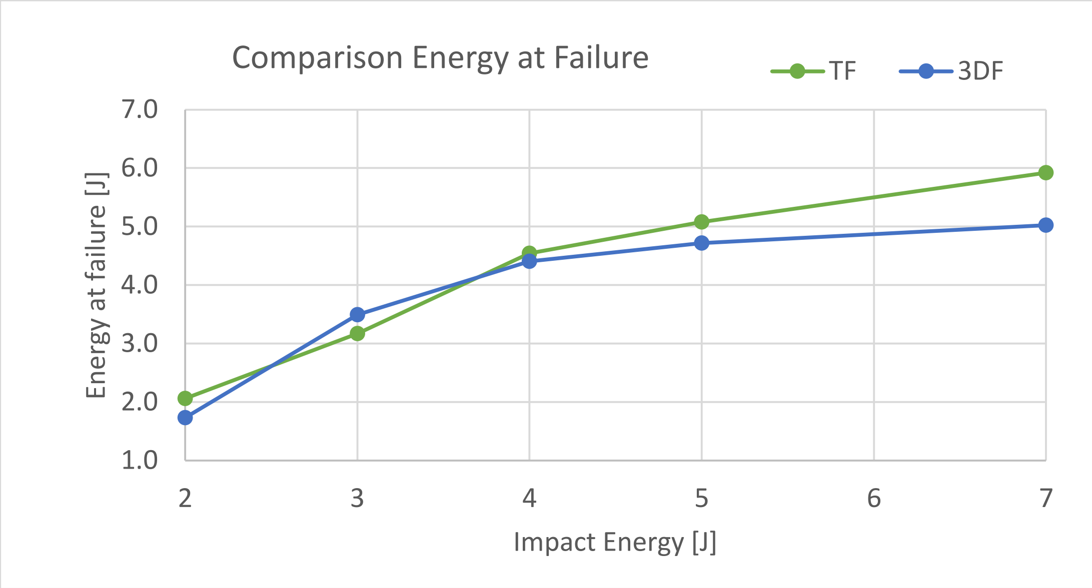

Figure 123 - Absorbed energy evaluated for the different impact energies for samples TF and 3DF during the entire experimental campaign

Figure 123 illustrates the values of the energy absorbed during the impact for all the samples (both TF and 3DF) at all the impact energies during the experimental campaign. Analysing the results, the different behaviour between the traditional straight fibres of samples TF and the twisted arrangement of samples 3DF seems to be opposite to what observed during the flexural tests, as the energy is more or less the same for the impacts at low energy levels (2 and 3J) and starts to diverge when it increases up to 7J, when the TF samples absorb almost 17% of energy more than samples 3DF. However, these results need to be compared with the internal damage assessment observed with the CT-Scan images.

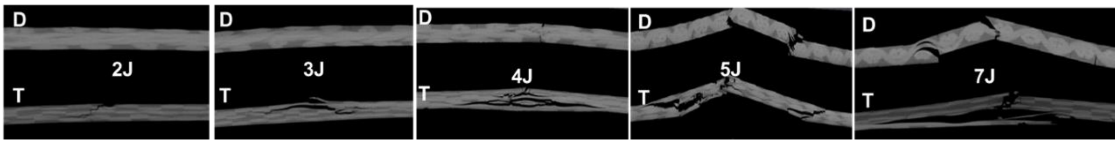

Figure 124 - Internal damage of samples TF and 3DF at different impact energies

As it is possible to see from the figure above, the intrinsic laminate structure of the TF samples leads to the generation of internal damage at the interface between two subsequent laminae. The opening of these new surfaces dissipates a large amount of energies but at the same time weakens the material, reducing its residual mechanical properties. At the same time, because these damaged areas are undetectable at naked eye being hidden inside the laminate structure of the material, they can lead to sudden critical failure of the part. Analysing the behaviour of the 3DF material, on the other side, it is possible to see that it reacts to an impact loading in a very different way by opening superficial cracks that can be easily detectable from the top surface. Increasing the impact energy these cracks can propagate following the twists of the fibrous reinforcement along the matrix rich areas. This generates a very localised damaged area in correspondence with the impact area while the zones far from the impact location stay undamaged.

4.4.2.3.2 Multilayer impact

In order to investigate the effect of impact resistance of the 3DF material having multiple layers respect to the traditional composite, several 3DF samples were manufactured with two and three layers respectively and subjected to low velocity impacts (LVI) at different impact energies. As for the impact on the single layer, the impact curves recorded by the experimental apparatus were analysed and the characteristics of the impacts properties were recorded together with the extent of the internal damage distribution. The results were compared with impacts performed at the same energies on traditional samples.

a) 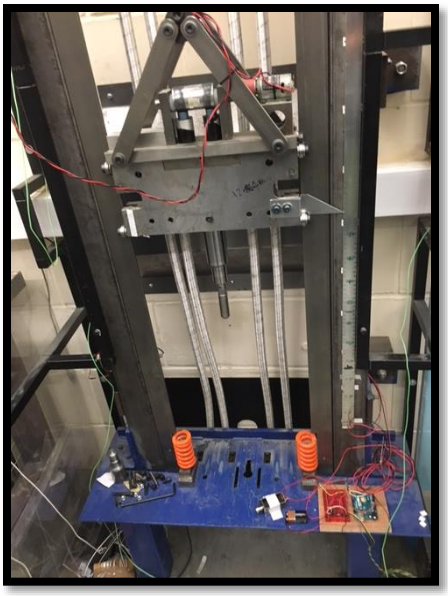 b) 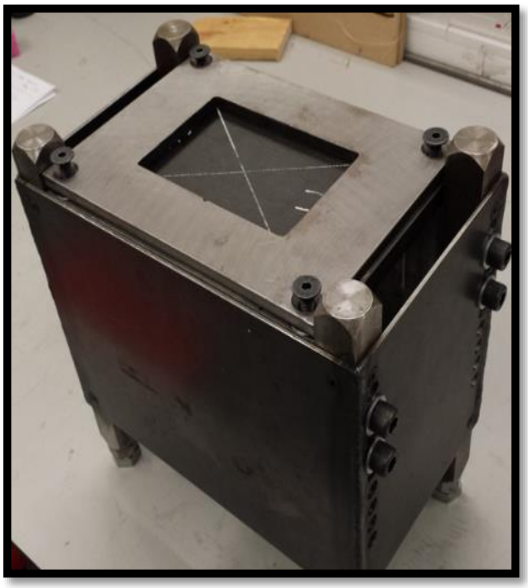

Figure 125 a) Drop-Weight Impactor tower b) Sample holder.

The experimental campaign was conducted using a Drop-Weight Impactor tower (see Figure 125*a*). The drop weight was of 12.864 kg and impactor's head was equipped with a hemispherical tip with a diameter of 20mm. The impact energy was varied by setting the drop height appropriately. Samples, according to the BS EN ISO 6603-2:2000, were dimensioned 100x150mm and clamped around their edges to a fixed metal structure with four screw allowing the test piece to be held on all four ends (see Figure 125*b*). During the test the weight of the impactor was kept constant, therefore in order to impact the samples at different energy levels, the velocity of the impact (v0) was tuned according to the equation (15. The impact height was further adjusted by performing velocity tests on the rig in order to balance the error given by friction and mechanical inertia.

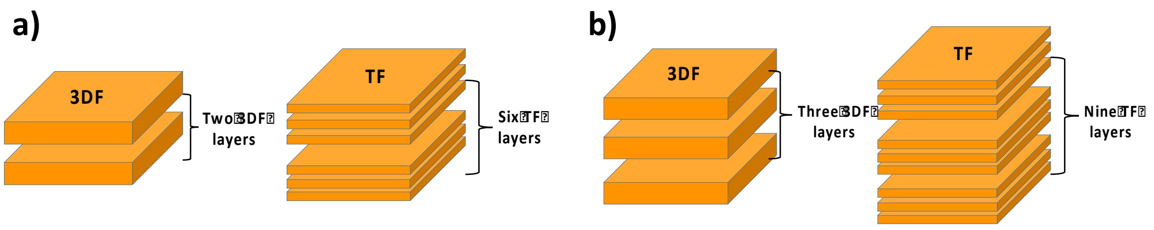

Figure 126 Schematic representation for 3DF and TF fabrics of the comparison between a) Thickness I, and b) Thickness II

As for the previous samples, due to the linear density of the two type of materials, the comparison between the two material was made by imposing the same fibres net weight for both composites, hence two and three 3DF twisted fabrics were laminated together and compared with three and nine traditional TF fabrics, respectively (see Figure 126). By following this approach, it was possible to have the final samples of both batches (3DF and TF) characterised by the same final thickness value (see Figure 127).

Table 11- weights and dimensions of the impacted samples (both 3DF and TF batches)

Label	Length (mm)	Width (mm)	Thickness (mm)	# plies	Impact Energy [J]	Height of impact [m]	Velocity of impact [m/s]
Thickness II							
D49 2	150.5	100.1	2.53	2 3DF	9	0.071	1.183
T45 6	150.5	100.0	2.59	6 TF	9	0.071	1.183
Thickness III							
D43 3	150.5	100.2	3.56	3 3DF	12	0.095	1.366
T39 9	150.5	100.0	3.84	9 TF	12	0.095	1.366

Because of the very low values of thickness of both 3DF and TF batches, some deviations from the standard were required in order to avoid complete perforation of the samples. In addition, since the D-samples presented a slight curvature due to the autoclave curing, some of the samples might not have been totally in contact with the support plate outside the clamping window. Dimensions of the tested samples are listed in the Table 11.

Figure 127 Samples for the multilayers impact test campaign

4.4.2.3.2.1 9J impact on 3DF double layers and equivalent TF samples

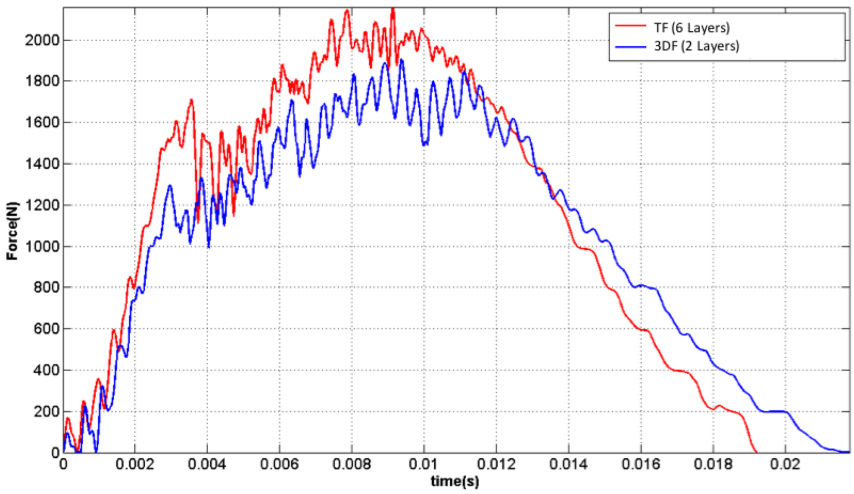

Figure 128 - Load VS Time curve for 9J impacts om samples T and D

The image above represents the load versus time curves collected from the load cell during 9J impacts on samples D49_2 (3DF) and T45_6 (TF). All samples survived the test with no perforation. As for the single layer impacts the results from the tests can be expressed as Load versus Displacement, using Equation (16. The data can be used to determine the area under the curve which represents the energy expended up to specific times tj from the equation (17. Load displacement curves obtained for samples 3DF and TF impacted at 9J are represented in Figure 129.

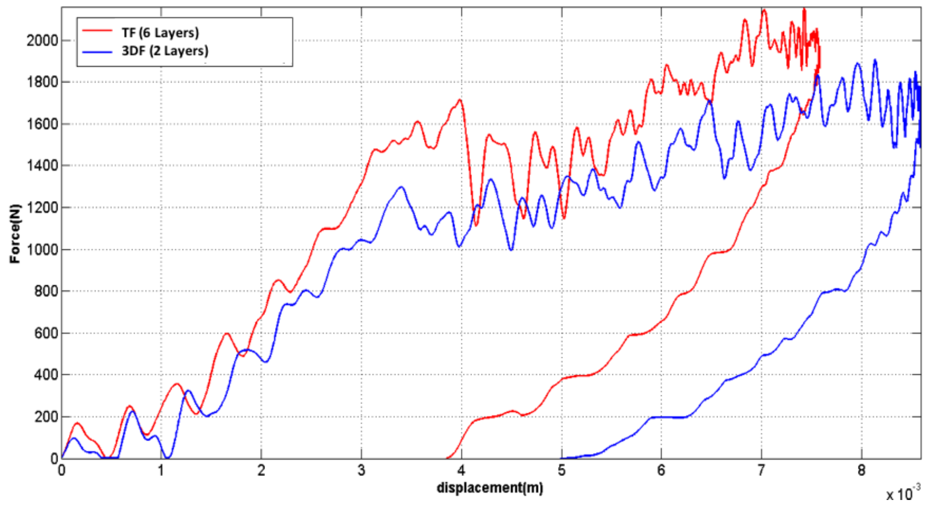

Figure 129 - Load VS Deflection curves for samples T and D impacted at 2J

Figure 130 shows the scans of the TF and 3DF samples impacted at 9J. The samples were sliced in two different orthogonal views in order to investigate the internal area around the impact location. Impacted samples were subjected to a CT-Scan analysis in order to investigate the extent of the internal delamination and the geometrical distribution of the cracks generated from the impact location.

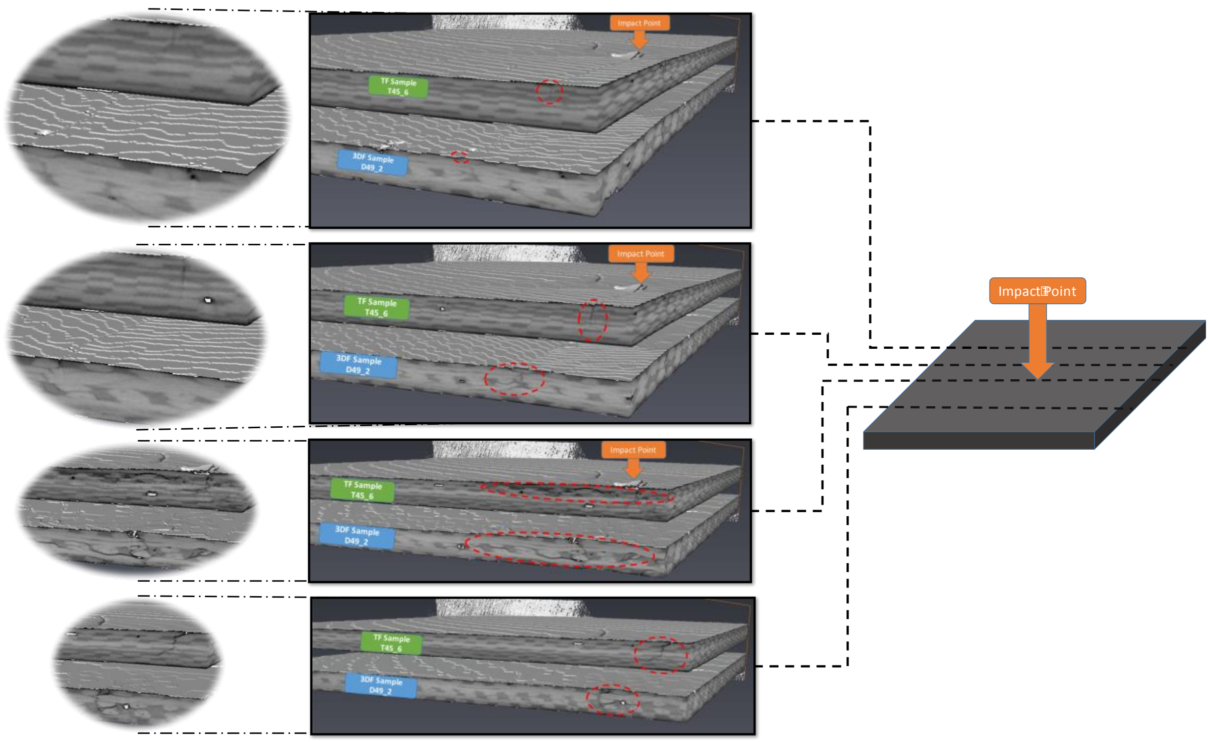

Figure 130 CT scan images of samples 3DF and TF impacted at 9J

As it is possible to see from the images, the different geometry of the two typologies of fibrous reinforcement strongly affects the behaviour of the composite part when it is subjected to an out-of-plane impact load. Analysing the images of the TF sample it is possible to see the crack extending through the thickness breaking the fibres or causing delamination. Instead, the crack on the 3DF sample tend to follow the twisted bundle, dissipating the impact energy through debonding of the interface fibre-resin. Moreover, due to the specific arrangement of the fibres in the 3DF samples, the crack tends either not to propagate as delamination or through the thickness breaking the fibres but tend to follow the twisted configuration and in most case generating multiple cracks. The creation of new cracks allows to dissipate more energy. Fibre breaking in the 3DF samples happens mainly in the proximity of the impact point were the impact energy is higher. Moreover, the cracks in the TF samples propagate far from the impact point respect to the 3DF sample. Indeed, as it is possible to see from figure 5 a), while for the TF sample the crack is present and cause also fibre breaking, in the 3DF sample the crack is barely visible and its only superficial.

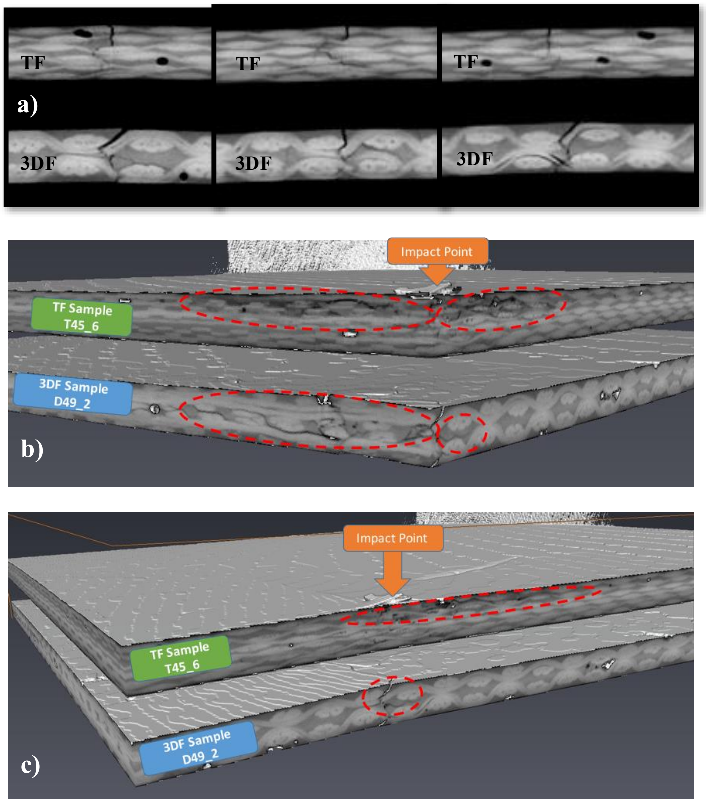

Figure 131 – Details of the crack propagation of samples 3DF and TF impacted at 9J, a) cross section of the impacted samples showing the different crack patterns, b) and c) cross section on the impact point

The presence of internal delamination for the traditional sample is even more evident in Figure 131b, where the propagation of the internal damage is represented in an orthogonal cross-section of the impacted area, as illustrated by the red circles in the images. The presence of debonding along the interface between twisted fibres and resin are less critical if compared to the type of damage present in the traditional samples. Indeed, the presence of large cracks and/or delamination can act as stress intensification points during the normal operation in the working environment leading to sudden catastrophic failure of the part. On the other side, the 3DF samples, presents small cracks with a complex pattern, mainly following the twisted arrangement of the fibres and hence the cracks in the 3DF samples require more energies to propagate and so the samples can withstand impacts better than traditional samples. Moreover, the 3DF samples dissipate impact energy also through higher maximum displacement respect to the TF samples (see Table 12).

4.4.2.3.2.2 12J Impacts on 3DF triple layers and equivalent TF samples

Figure 132 illustrates the measured Load versus Time curves obtained from the load cell during the impact test on samples D43_3 (3DF) and T39_9 (TF) at 12J. As for the previous test, all samples survived the test with no perforation.

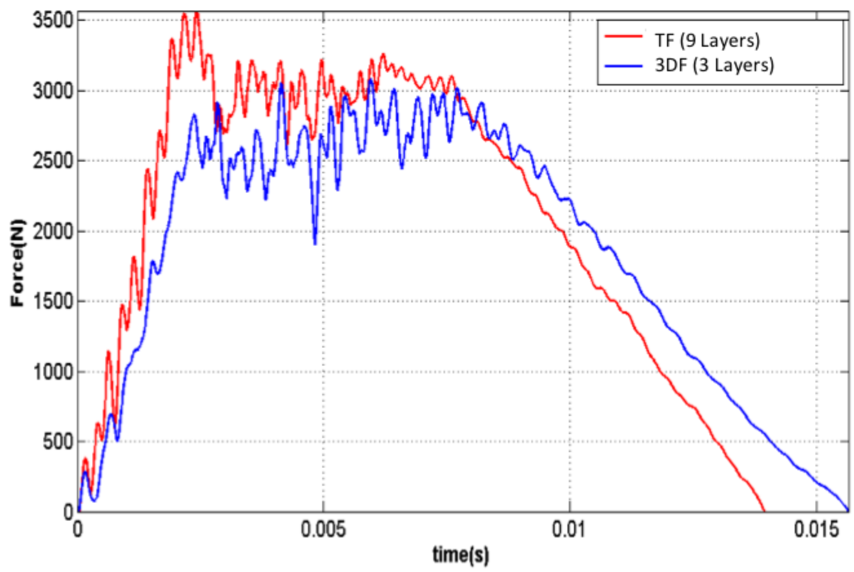

Figure 132 Load VS Time curves for TF and 3DF samples impacted at 12J

As for the previous impact energy, the results from the tests were expressed in Figure 129 as Load versus Displacement, using Equation (16).

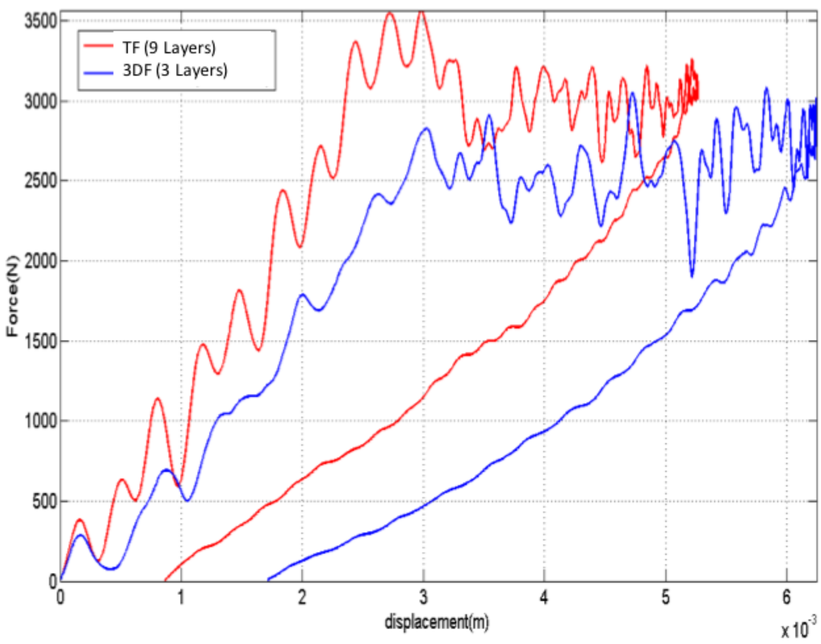

Figure 133 Load VS Deflection curves for TF and 3DF samples impacted at 12J

Figure 134 represent the post-impact scans recorded for the impacted samples. The figures show similar trend observed in the previous scans. As for the 9J impacts, debonding at the fibres-matrix interface is observed for the 3DF samples with some fibres damages in correspondence with the impact location.

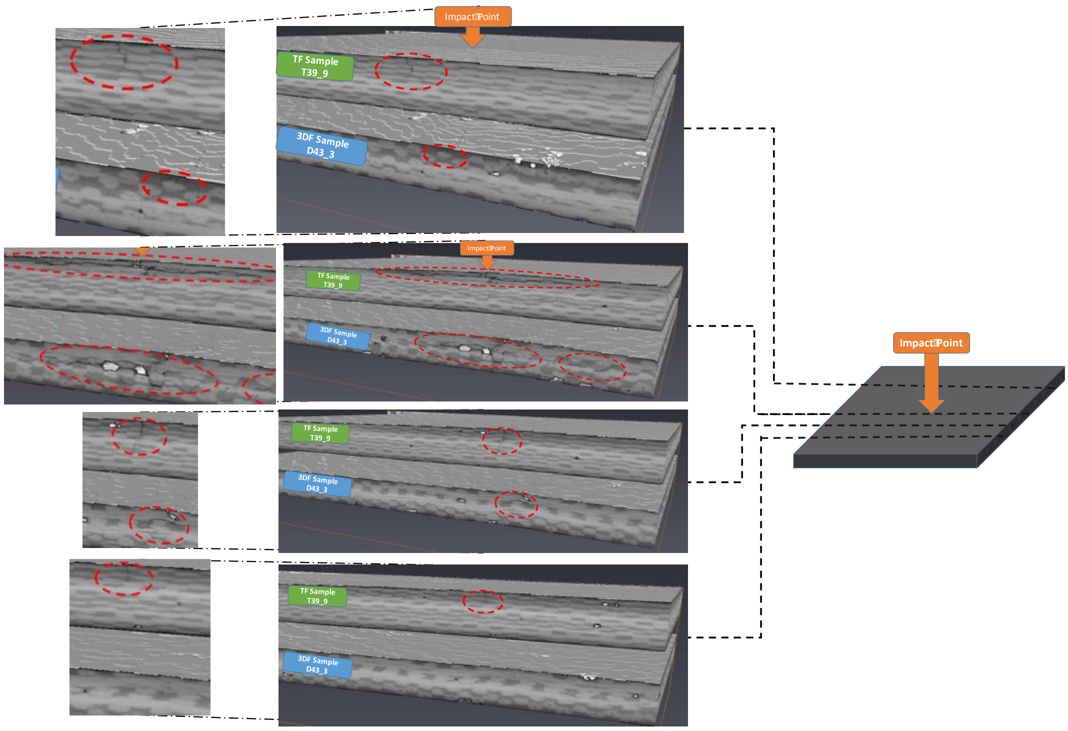

Figure 134 CT-Scan Images captured for the TF and 3DF samples impacted at 12J

Also in this case, due to the specific arrangement of the fibres in the 3DF sample, the crack does not tend to propagate as a delamination or through the thickness breaking the fibres, but tends to propagate through the matrix rich areas following the twists of the tows, leading to matrix-fibres debonding. This alternative zigzag crack pattern allows to dissipate impact energy, causing crack that are less critical compared to those present in the TF sample. Overall there are no internal damages or delamination far from the impact location while for the TF samples, cracks are still present and cause also fibre breaking, as illustrate by the red circle in the from Figure 134d).

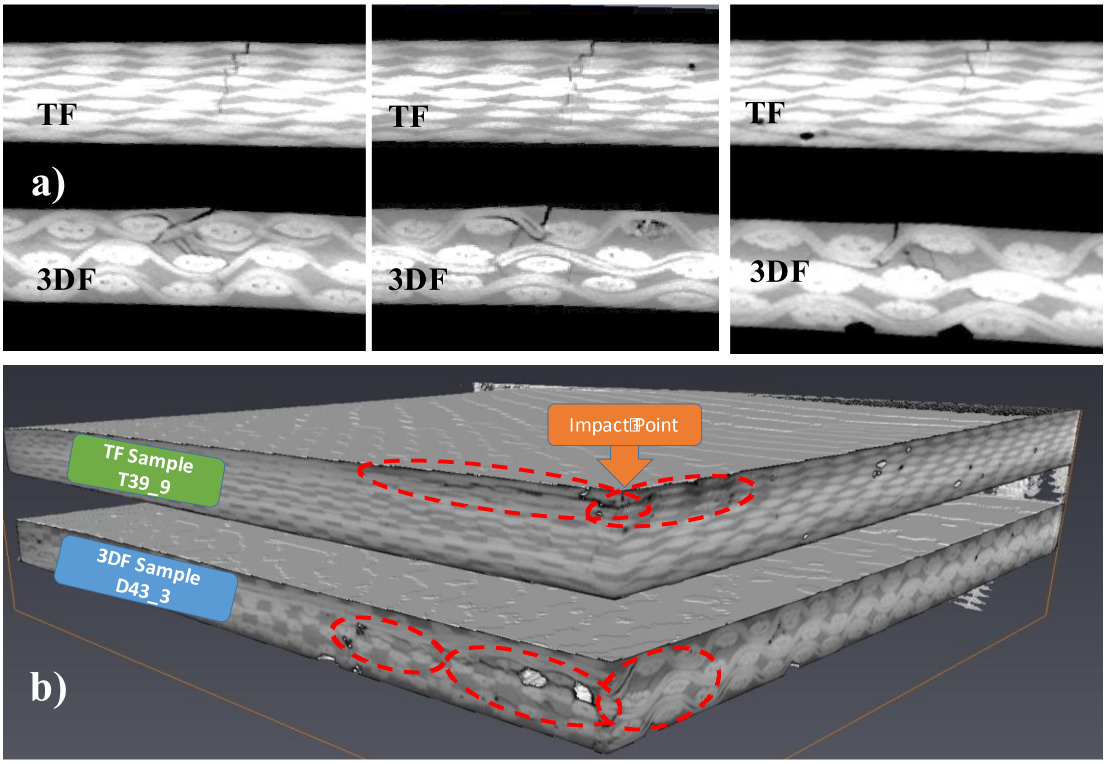

Figure 135 Details of the crack propagation of samples 3DF and TF impacted at 12J, a) cross section of the impacted samples showing the different crack patterns, b) cross section on the impact point

Analysing Figure 135, it is possible to see the presence of a very large delaminated area for sample TF which was generated by the contact with the impactor's head during the impact duration. The only way for the T laminate to absorb the impact energy was to open new surfaces at the interface between two subsequent laminae, generating internal delaminated areas. The delamination extends far from the impact point along the length of the sample weakening it and reducing its residual properties. On the other side, since the D samples present a 3D twisted configuration of the fibres, the impact energy is dissipated through the opening of new internal surfaces that follow in part the helical twisting. This is reflected in the sample in multi cracks and multi delamination of smaller length. The necessity to open new cracks and to follow complex patterns require higher energy consumption. This is reflected in the higher absorbing energy of the 3DF samples respect to the TF samples impacted at the same energy (Table 12).

Table 12 Summary of the impact campaign results on multilayer configurations for samples TF and 3DF

Label	#plies	Impact energy [J]	Velocity [m/s]	Max Force [kN]	Absorbed energy [J]	Residual displacement [mm]
Thickness II						
D49 2	2	9	1.183	1.91	7.23	1.72
T45 6	6	9	1.183	2.16	6.43	0.87
Thickness III						
D43 3	3	12	1.366	3.08	7.19	4.99
T39 9	9	12	1.366	3.57	6.34	3.85

Analysing the trends of both Maximum Load and Deflection at Failure, it appears that while the TF samples react with a high strength at low deflection, the 3DF material responds in an opposite way, by absorbing the impacts with higher values of deformation. The higher value of the deformation together with a lower value of strength confirm the results obtained with the flexural tests (three points bending on both rods and fabrics) in which the same trend was observed. The table below, summarises the results calculated from the impact campaign. Figure 136 illustrates the trend of the absorbed energy, the maximum force, and the residual displacement recorded for the 9J impacts for both samples TF and 3DF. As it is possible to see, the traditional laminate shows higher value of the maximum load, with a decrease of around ~12% for the 3DF sample. On the contrary, the deflection at failure of the samples shows an inverse behaviour, with the 3DF samples showing an increase in the residual displacement with an increment of ~30%. 3DF samples shows also a higher absorbed energy respect to the TF samples with an increment of ~12% for the samples impacted at 9 Joules.

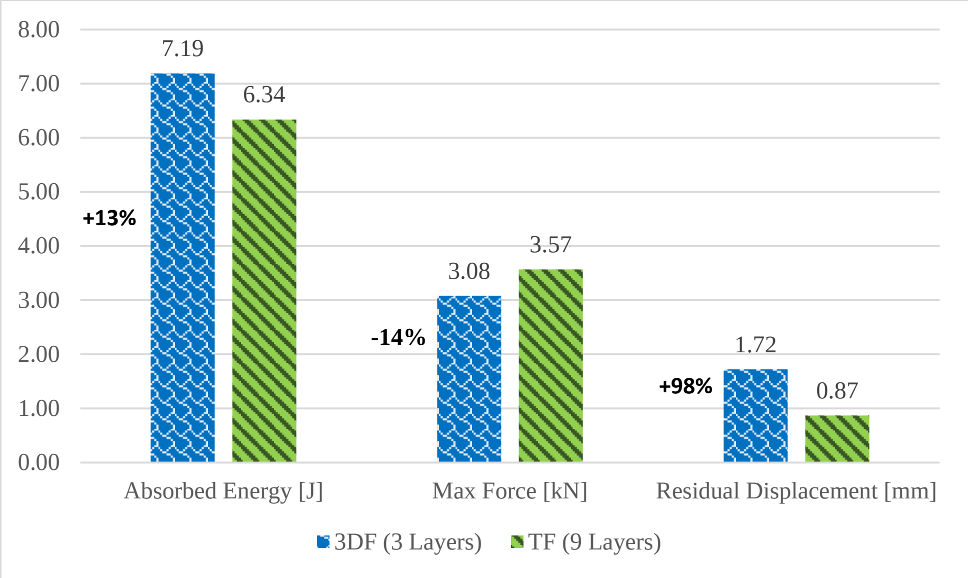

Figure 136 Comparison for samples TF and 3DF impacted at 9 Joules

Figure 137 illustrates the trend for the samples impacted at 12 Joules. As it is possible to see, the trend is very similar to the samples impacted at 9J, with a decrease of around ~13% of the maximum force for the 3DF samples and an increase of ~98% for the residual displacement. The absorbed energy is ~13% higher for the 3DF samples.

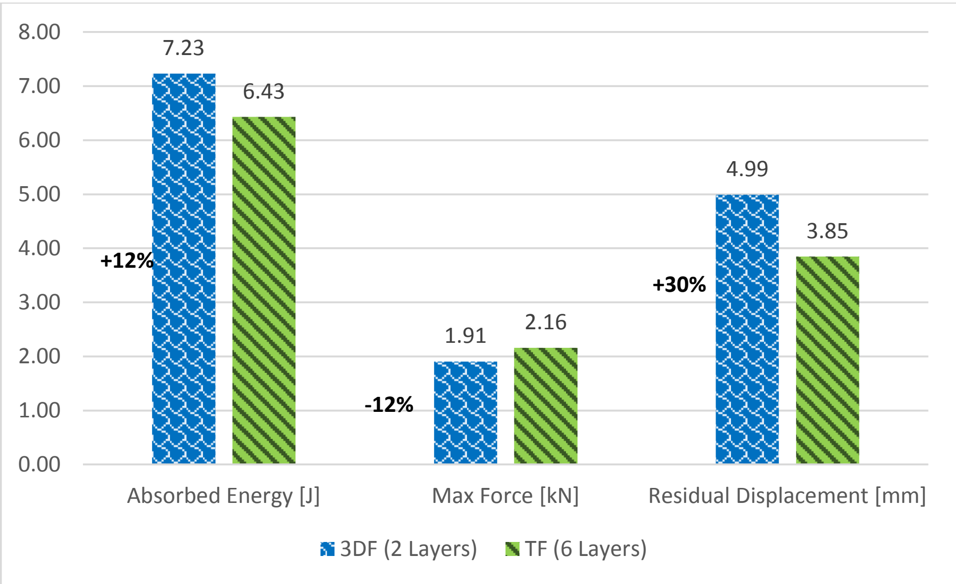

Figure 137 Comparison for samples TF and 3DF impacted at 12 Joules

As it is possible to see from the internal damage assessment observed with the CT-Scan images, the intrinsic laminate structure of the TF samples leads to the generation of internal damage at the interface between two subsequent laminae. The opening of these new surfaces dissipates a large amount of energies but at the same time weakens the material, reducing its residual mechanical properties. At the same time, because these damaged areas are undetectable at naked eye being hidden inside the laminate structure of the material, they can lead to sudden critical failure of the part. Analysing the behaviour of the 3DF material, on the other side, it is possible to see that it reacts to an impact loading in a very different way by opening superficial cracks that can be easily detectable from the top surface. Increasing the impact energy these cracks can propagate following the twists of the fibrous reinforcement along the matrix rich areas. This generates a very localised damaged area in correspondence with the impact area while the zones far from the impact location stay undamaged. Moreover, the presence of multiple layers on the 3DF samples, does not eliminate this advantage. Indeed, as it is possible to see from the internal damage distribution of 3DF samples for thickness II and III, although the samples are made with multiple layers still present benefit if compared with the traditional sample. The twisted configuration allows a different crack propagation from the one generated in the traditional samples.

4.4.2.4 charpy test

Charpy test is a standardised high-strain test able to evaluate the energy absorbed by a material during a fracture. The experimental apparatus consists in a pendulum of known mass and length (hence high inertia) that is dropped from a known length to impact a notched or unnotched (all the specimens used during this experimental campaign were unnotched) sample. The energy absorbed by the material during the impact can be evaluated by comparting the difference in the height reached by the hammer before and after the test (see Figure 138).

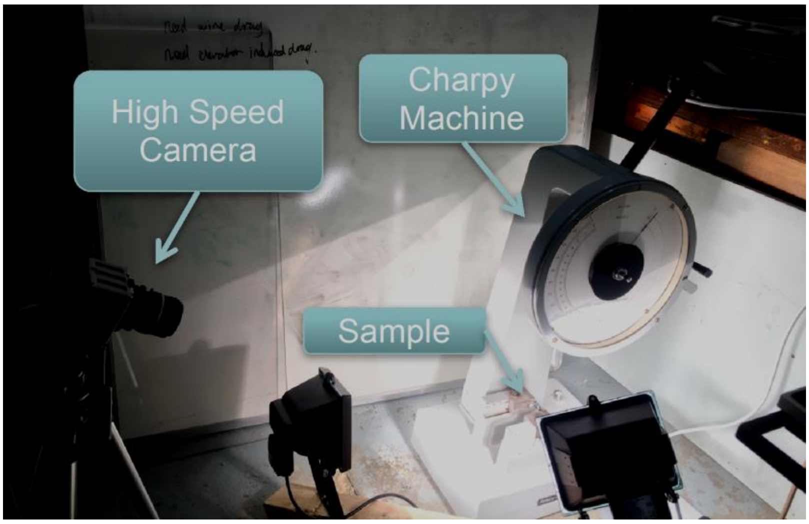

Figure 138- Charpy test: experimental apparatus and test setup

Samples were dimensioned based to the specification of the charpy impact machine used and the specific dimensions and weight are reported in the table 1. Calculation of the energy absorbed has been performed in accordance with the BS EN ISO 179-1-2010 [204]. Samples were manufactured using a prepreg layer produced by SHD composite with a VTC401 resin system and fabrics layers manufactured with a loom machine by Wright with a Plain Weave pattern using the T700 3K carbon fibres for the TF samples and the "corda" (manufactured from Galan using the same fibres) for the 3DF samples.

The thickness of our samples (reported in the table) was not in accordance with the standard EN ISO 179-1 therefore the results shown can be only used to point out the relative behaviour of the samples made with "CORDA" (3DF) in comparison with the sample produced using the traditional TF fibres. According to the specimens' dimensions, two different energies with two different charpy pendula were used during the test campaign. The first pendulum is characterised by a strike energy of 15J while the second has a strike energy of 1J.

Table 13 Samples characteristics

Specimen	#plies	Thickness (mm)	Length (mm)	Width (mm)	Weight (g)	Impact Energy [J]
Thickness II						
TF	6	2.51	127.5	19.9	8.7	15
3DF	2	2.45	127.4	19.9	8.6	15
Thickness I						
TF	3	1.31	59.4	10.0	1.1	1
3DF	1	1.38	59.4	10.0	1.1	1

It is important to underline that the size of the sample affects the calculated results, since the dimensions determine whether or not the material is in plane strain. This difference can greatly affect the test conditions therefore the results shown in the table below can be only used to point out the relative behaviour of the corda samples in comparison with traditional ones (represented by the TF samples). Test results are illustrated in the table below, which lists the tested samples, their dimensions and calculated Charpy impact strength of unnotched specimens a_{cU} evaluated according to the equation:

$$a_{cU} = \frac{E_c}{h*b} \times 10^3 \qquad (18)$$

where *Ec* is the corrected energy expressed in J recorded by the instrument during the test and *h* and *b* are the thickness and the width, in millimetres, of the test specimen. Since the samples presented a small variation in terms of weight due to the slight variation of resin in the samples, the absorbed energy was also evaluated in terms of energy absorbed per unit of weight.

Table 14 - Results from the Charpy test campaign

Specimen	#plies	Charpy Pendulum Strike Energy [J]	E/A [kJ/m^2]	E/W [J/g]
Thickness II				
TF	6	15	28.14	0.161
3DF	2	15	42.21	0.244
Thickness I				
TF	3	1	31.3	0.373
3DF	1	1	39.13	0.484

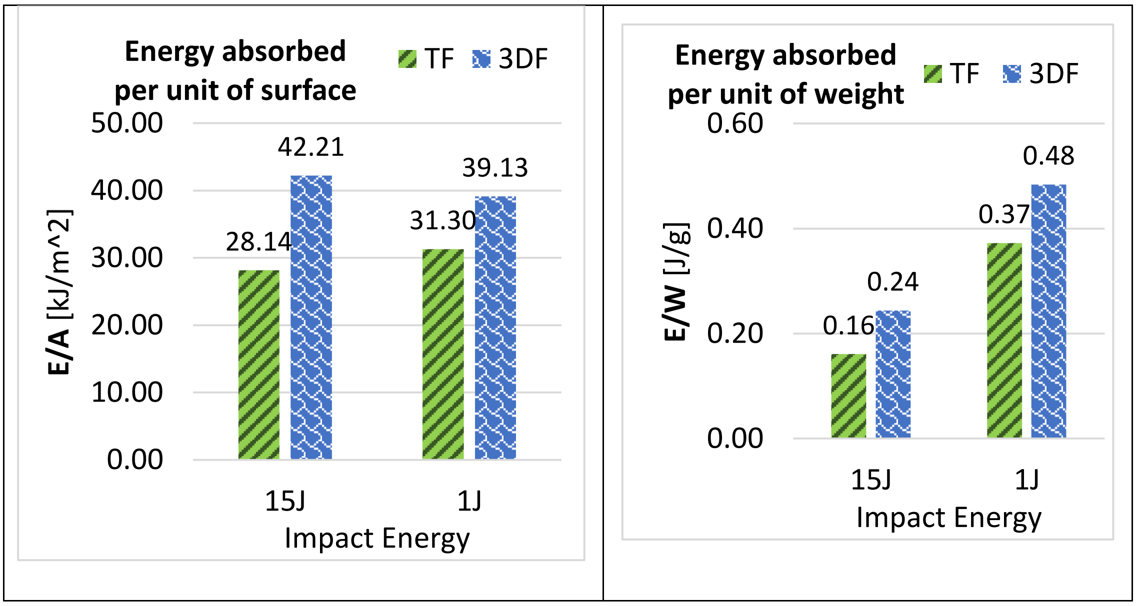

Figure 139 – Charpy test: difference in the absorbed energy (per unit surface and per unit mass) between TF and 3DF samples

Analysing the results in Table 14 it is possible to observe that corda samples show an enhancement in the energy absorbed by more than 50% for the samples impacted at 15 Joules and over 25% for the samples impacted at 1 Joule (see Figure 139). This behaviour confirms the large energy absorption property given by the twisted arrangement of the fibrous reinforcement shown in the three points bending tests.

4.4.2.5 Flexural Vibration Test of a Beam Elastically Restrained at one end.

The results obtained for the 3DF samples (labelled as D samples) have been compared with traditional fabrics made with straight fibres (labelled as TF samples) for all orientations. Both the samples are made from a plain weave fabric manufactured using a traditional weaving machine and impregnated with the same epoxy resin system (MTC510 from SHD Composites). It is important to underline that since each of the twisted fibres of the 3DF fabric is obtained by twisting three different strands of carbon fibres tows, the final weight and thickness of a single 3DF fabric are three times bigger than the ones of a traditional TF fabric. Therefore, the comparison between the two materials was made by imposing the same number of fibres per cross-section for both the composites, hence three traditional TF fabrics were laminated together and compared with a single 3DF twisted fabric (see Figure 140). By following this approach it was possible to have the final samples of both batches (3DF and TF) characterised by the same final thickness value.

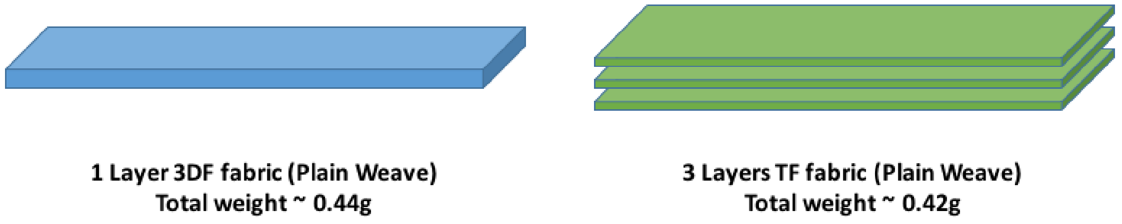

Figure 140 - Schematics of the TF and 3DF samples used during the experimental campaign

4.4.2.5.1 Young Modulus Evaluation

The elastic properties of the 3DF fabric were evaluated by collection vibration data from single cantilever samples subjected to an out-of-plane load F using a Laser displacement measuring system (*MicroEpsilon*) as illustrated in Figure 141.

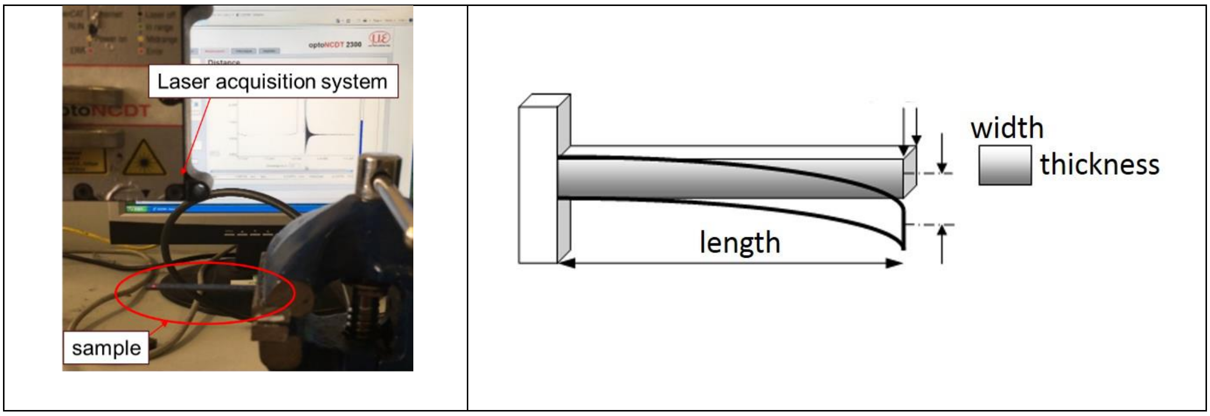

Figure 141 - single cantilever schematic and experimental setup of the vibrational tests

The displacement along the out-of-plane direction data were used to evaluate the natural frequency of the different samples from which it was then possible to calculate the Elastic Modulus along the sample's length knowing its geometry and density. Transverse or flexural motion of a homogeneous beam can be described by the Bernoulli-Euler equation:

$$-\frac{\partial^2}{\partial x^2}\left(EI\frac{\partial^2 w}{\partial x^2}\right) = \rho A\frac{\partial^2 w}{\partial t^2} \tag{19}$$

where I represents the moment of inertia of the cross section, E(x) is the modulus of elasticity of the beam, w(x,t) is its transverse displacement, x is the distance from the end of the beam, t is the time, A is the cross-sectional area of the beam and ρ is its mass density. Considering that EI is constant along the length it is possible to write Eq 1 as follows:

$$EI\frac{\partial^4 w}{\partial x^4} + \rho A\frac{\partial^2 w}{\partial t^2} = 0 \tag{20}$$

These equations can be used for specially orthotropic composites or laminates without coupling if the modulus E is replaced by the effective flexural Modulus Ef. However, since flexural modulus which is strongly influenced by the stacking sequence of the laminate, if there is no variation of the angle of the plies along the z direction (same orientation for each ply) the flexural Modulus Ef can be considered the same as Young's Modulus. In order to solve the Bernoulli equation, it is possible to consider a separation of variables solution for harmonic free vibration:

$$w(x,t) = W(x)e^{i\omega t} \tag{21}$$

where ω (=2πf) is the frequency and W(x) is the mode shape function.

By substituting (21 into (20, it is possible to write:

$$\frac{d^4W(x)}{dx^4} - k^4W(x) = 0 \qquad \text{with} \qquad k = \left(\frac{\omega^2\rho A}{EI}\right)^{1/4} \tag{22}$$

The solution of (22) can be written introducing some constants depending on the boundary conditions as:

$$W(x) = C_1\sin(kx) + C_2\cos(kx) + C_3\sinh(kx) + C_4\cosh(kx) \tag{23}$$

For a cantilever beam, these constants can be written as:

$W(x) = 0$ for $x = 0$ $\rightarrow$ $C_2 = -C_4$

$\frac{dW(x)}{dx} = 0$ for $w = 0 \rightarrow$ $C_1 = -C_3$

$\frac{d^2W(x)}{dx^2} = 0$ for $x = L \rightarrow C_1[sin(kL) + \sinh(kL)] + C_2[cos(kL) + \cosh(kL)] = 0$

$\frac{d^3W(x)}{dx^3} = 0$ for $x = L$ $\rightarrow C_1[cos(kL) + \cosh(kL)] + C_2[sin(kL) - \sinh(kL)] = 0$

For nontrivial solution C1 and C2 in the last two equations above, the determinant of the coefficients must be equal to zero, hence:

$$\cos(kL)\cosh(kL + 1) = 0 \tag{24}$$

Equation (24 represents the eigenvalue equation for the cantilever beam that is characterised by an infinite number of solutions k_nL, where the subscript n refers to the mode number. The values for the first three modes are:

$$k_1L = 1.875$$

$$k_2L = 4.694$$

$$k_3L = 7.855$$

By introducing the eigenvalue values in the expression of k in Equation (22), the frequency can be written as:

$$f_n = \frac{(k_nL)^2}{2\pi L^2}\sqrt{\left(\frac{EI}{\rho A}\right)} \tag{25}$$

The mode shapes for the first three modes are illustrated in the picture below:

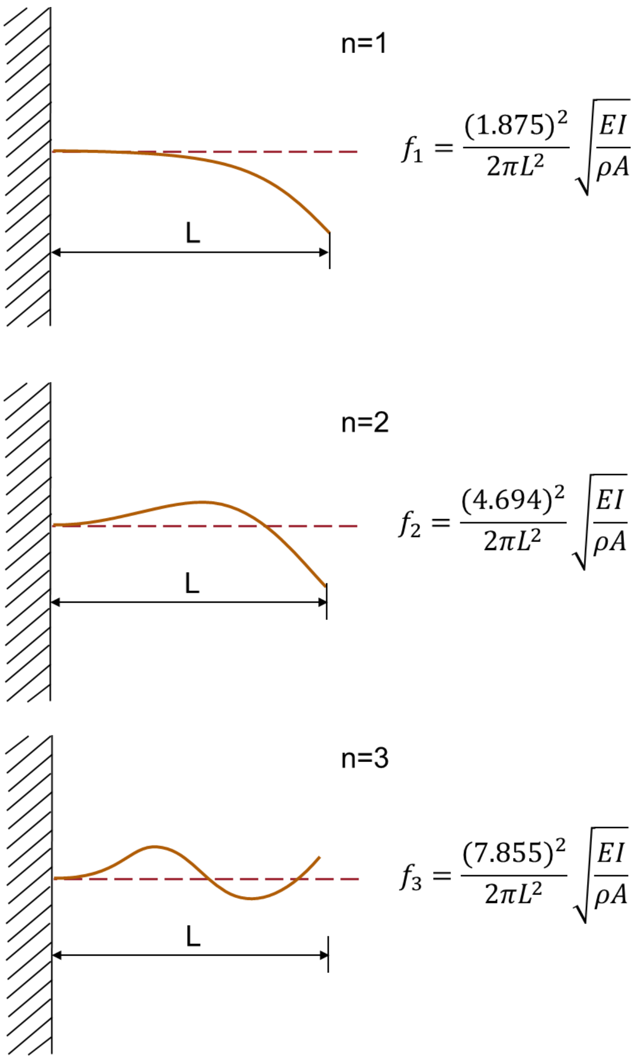

Figure 142 - Mode shapes for the first three modes for the vibration of a beam in a single cantilever configuration

Rearranging the terms of Equation (25) and considering that the moment of inertia for a rectangular bar is equal to $I = \frac{wt^3}{12}$ it is possible to express the Elastic Modulus along the length of the beam using the following equation:

$$E = \left(f_1 \frac{2\pi L^2}{(1.875)^2}\right)^2 \frac{\rho A}{I} \tag{26}$$

Therefore, in order to calculate the Elastic modulus along the length of the cantilever beam with Equation *(26)*, the natural frequencies of different samples were evaluated by extracting the frequency content of the Time-Displacement signals using the Fast Fourier Transform (FFT) of the collected data.

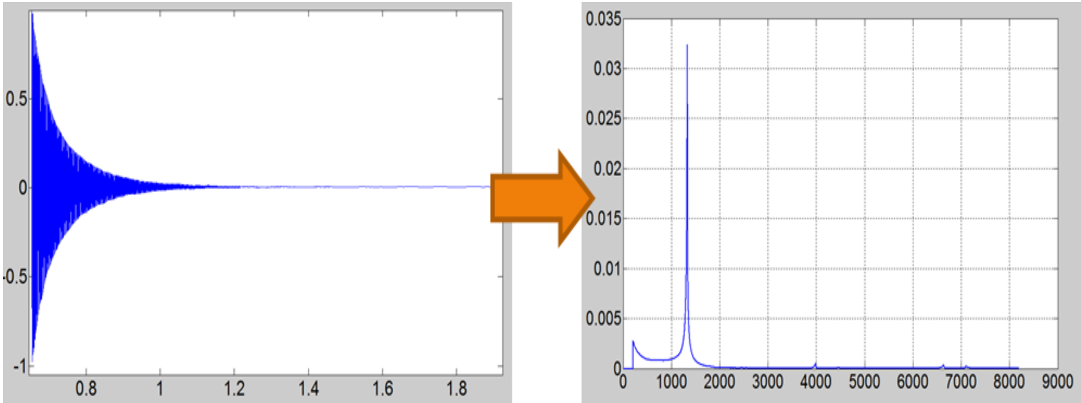

Figure 143 - Time VS Displacement signal collected from the laser measuring system during the tests and results from the FFT to identify the natural frequency of the sample

Since due to the twisted orientation of the fibres bundles the 3DF fabric is expected to show higher levels of in-plane isotropy, several samples were cut at 50x5mm at different angles in order to evaluate the elastic properties of the fabrics at different orientations. The direction chosen were 0, 30, 45, 60 and 90° as illustrated in the picture below (see Figure 144).

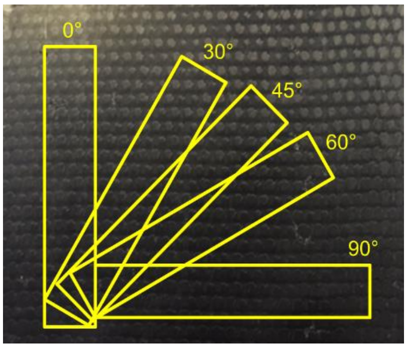

Figure 144 - orientation of the samples produced during the experimental campaign

The results obtained for the 3DF samples (labelled as D samples) have been compared with traditional fabrics made with straight fibres (labelled as TF samples) for all orientations. Results of the tests for the traditional straight fibre laminate (samples TF) are shown in the table below:

Table 15 - results of the vibration tests for samples TF

		length	width	thickness	weight	E (TEST 1)	E (TEST 2)	E (TEST 3)	average	Tot Average	st dev	decrease from 0°
	Sample I	50.93	5.076	1.096	0.4	2.60E+08	4.60E+10	4.60E+10	4.60E+10			
0	***Sample II***	50.95	5.03	1.108	0.4	4.79E+10	4.80E+10	4.78E+10	4.79E+10	4.44E+10	4516858237	
	Sample III	50.96	5.073	1.094	0.39	2.68E+08	3.53E+08	3.93E+10	3.93E+10			
30	***Sample I***	51.28	5.126	1.14	0.42	1.38E+10	1.39E+10	1.38E+10	1.38E+10			

	Sample II	51.263	5.126	1.147	0.42	1.28E+10	1.31E+10	1.32E+10	1.30E+10	1.28E+10	1214748869	-72%
	Sample III	51.233	5.03	1.144	0.41	1.05E+10	1.16E+10	1.22E+10	1.14E+10			
	Sample I	51.203	5.09	1.185	0.43	1.07E+10	1.07E+10	1.07E+10	1.07E+10			
45	***Sample II***	51.246	5.07	1.191	0.43	1.10E+10	1.09E+10	1.09E+10	1.09E+10	1.06E+10	367352893	-76%
	Sample III	51.206	5.1	1.19	0.43	1.02E+10	1.02E+10	1.03E+10	1.02E+10			
	Sample I	51.03	4.993	1.179	0.41	1.09E+10	1.11E+10	1.11E+10	1.10E+10			
60	***Sample II***	50.97	5.13	1.157	0.42	1.17E+10	1.19E+10	1.19E+10	1.18E+10	1.17E+10	633781274	-75%
	Sample III	50.95	5.136	1.183	0.43	1.22E+10	1.23E+10	1.24E+10	1.23E+10			
	Sample I	50.963	5.123	1.159	0.42	4.49E+10	4.50E+10	3.80E+10	4.26E+10			
90	***Sample II***	50.956	5.01	1.085	0.39	2.66E+08	4.35E+08	3.39E+10	3.39E+10	3.95E+10	4839660146	-11%
	Sample III	50.956	5.04	1.111	0.39	4.42E+10	4.07E+10	4.07E+10	4.18E+10			

The results are summarised in the bar chart below which illustrates the values of the Young's Modulus along different orientations:

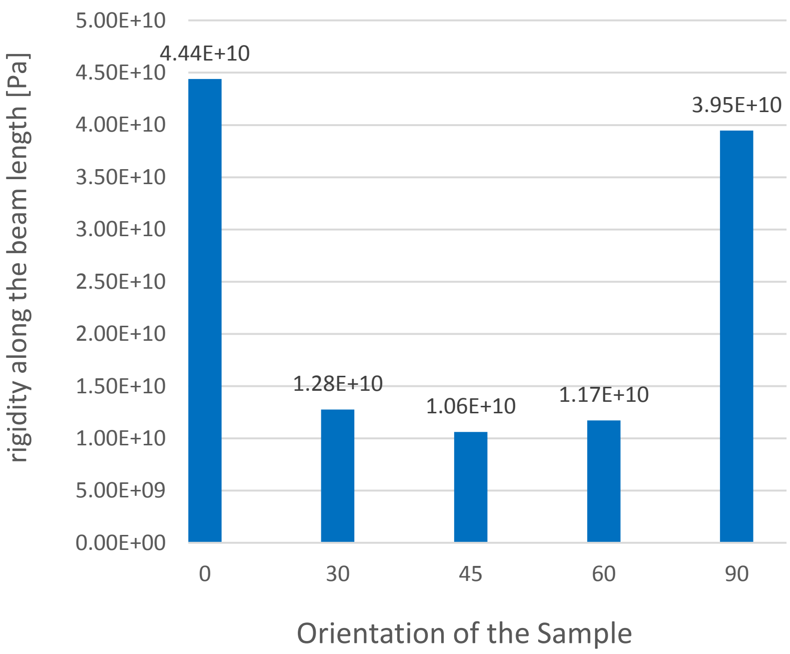

Figure 145 – Young's Modulus value for TF samples at different orientations (from 0 to 90°)

As it is possible to see from the chart, the elastic properties of the traditional straight fibres fabric T are strongly dependent on the orientation of the reinforcement. Indeed the mechanical properties strongly decrease for the samples cut at angles greater than 0°, dropping down by more than one fourth of the value of the Young's modulus for the samples cut at 45° and then slowly increasing when the angle goes from 45 to 90°. This trend represents the typical behaviour of a traditional fabric for which the mechanical properties are higher in the direction of the fibres (0 and 90° in our case because of the pattern of the plain weave fabric) and very low in the other directions. On the other side, observing the results obtained from the same tests on the 3DF samples, the behaviour seems completely different as it is possible to see from Table 16 below and the bar chart of Figure 146.

Table 16 - results of the vibration tests for samples 3DF

		length	width	thickness	weight	E (TEST 1)	E (TEST 2)	E (TEST 3)	average	Tot Average	st dev	decrease from 0°
0	***Sample I***	51.01	5.096	1.2	0.43	1.30E+10	1.31E+10	1.31E+10	1.31E+10			
	Sample II	51.05	5.1	1.22	0.44	1.28E+10	1.22E+10	1.22E+10	1.24E+10	1.28E+10	379778639	
	Sample III	51.07	5	1.21	0.43	1.30E+10	1.30E+10	1.30E+10	1.30E+10			
30	***Sample I***	51.053	5.11	1.219	0.43	9.44E+09	9.41E+09	1.18E+10	1.02E+10			
	Sample II	51	5.07	1.21	0.43	9.82E+09	9.84E+09	9.82E+09	9.83E+09	1.01E+10	200386941	-21%
	Sample III	51.056	5.023	1.226	0.44	1.01E+10	1.01E+10	1.02E+10	1.01E+10			
45	***Sample I***	51.31	5.066	1.2	0.44	1.01E+10	1.01E+10	1.01E+10	1.01E+10			
	Sample II	51.3	5.056	1.189	0.43	1.04E+10	1.04E+10	5.60E+08	1.04E+10	9.73E+09	881983027	-24%
	Sample III	51.24	5.04	1.216	0.43	2.11E+08	8.73E+09	8.72E+09	8.72E+09			
60	***Sample I***	51.03	5.033	1.234	0.44	2.03E+08	1.01E+10	1.02E+10	1.01E+10			
	Sample II	51.04	5.063	1.223	0.44	9.95E+09	9.93E+09	1.00E+10	9.97E+09	1.00E+10	123796157	-22%
	Sample III	50.98	4.933	1.219	0.43	9.93E+09	9.89E+09	2.10E+08	9.91E+09			
90	***Sample I***	51.17	5.05	1.221	0.43	9.96E+09	9.99E+09	9.99E+09	9.98E+09			
	Sample II	51.21	5.036	1.232	0.44	1.10E+10	1.11E+10	1.11E+10	1.10E+10	1.02E+10	702018412	-20%
	Sample III	51.22	4.973	1.168	0.4	9.65E+09	9.68E+09	9.74E+09	9.69E+09			

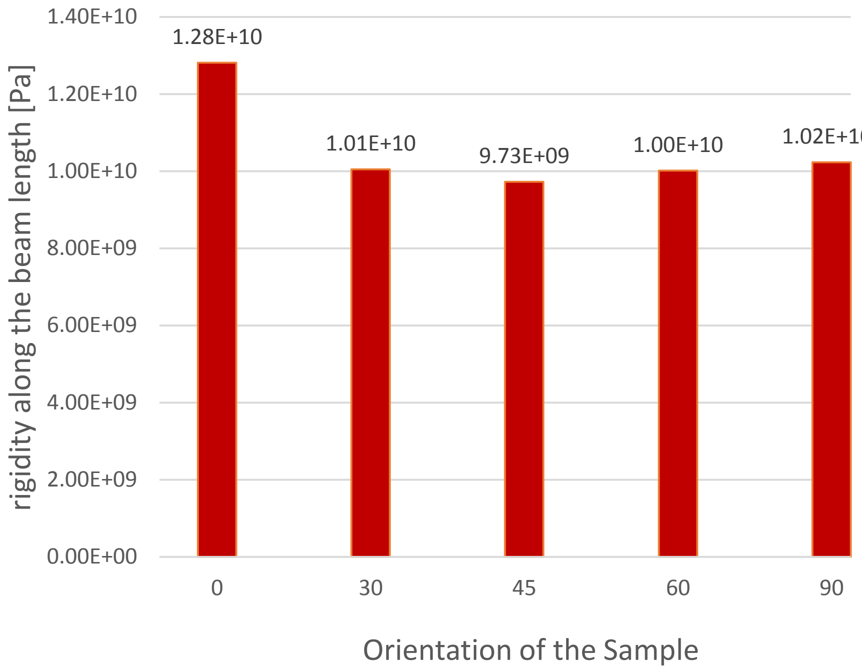

Figure 146 - Young's Modulus value for 3DF samples at different orientations (from 0 to 90°)

Indeed, analysing the results, it appears that the 3DF samples show a very high level of isotropy along the different direction, with a small change of 20% in the passage from the samples cut at 0° to the ones cut at 30° (~-20%) and no differences in the other angles. One possible explanation to this behaviour is given by the internal twisted structure of the fibrous reinforcement in which the fibres follow a helicoidal pattern which dispose them in a radial direction along the longitudinal axis of the tow (see Figure 8).

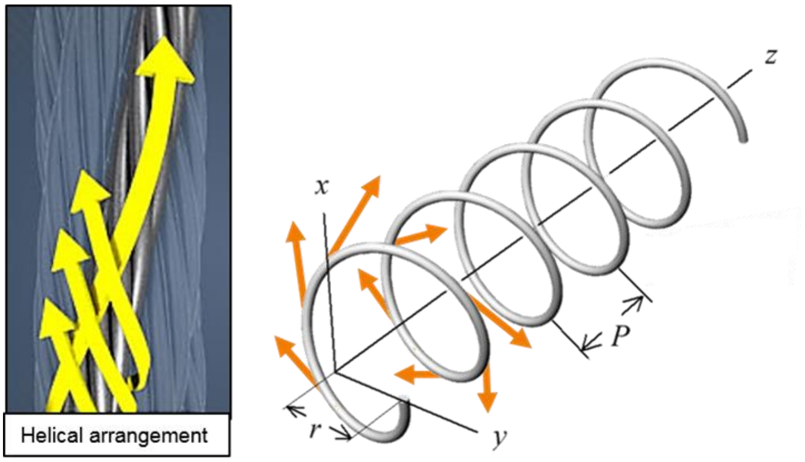

Figure 147 - Helical orientation of the twisted fibres along the tows length in the 3DF samples

Changing the orientation of the fibres from a fully longitudinal arrangement (0° degrees) to a radial disposition balances the in plane properties by decreasing the mechanical properties along the 0 direction and increasing the ones along other directions. This behaviour is more evident by comparing the results obtained from the two different composite panels (TF and 3DF) as shown in Figure 148 which shows a normalised comparison between the two orientations.

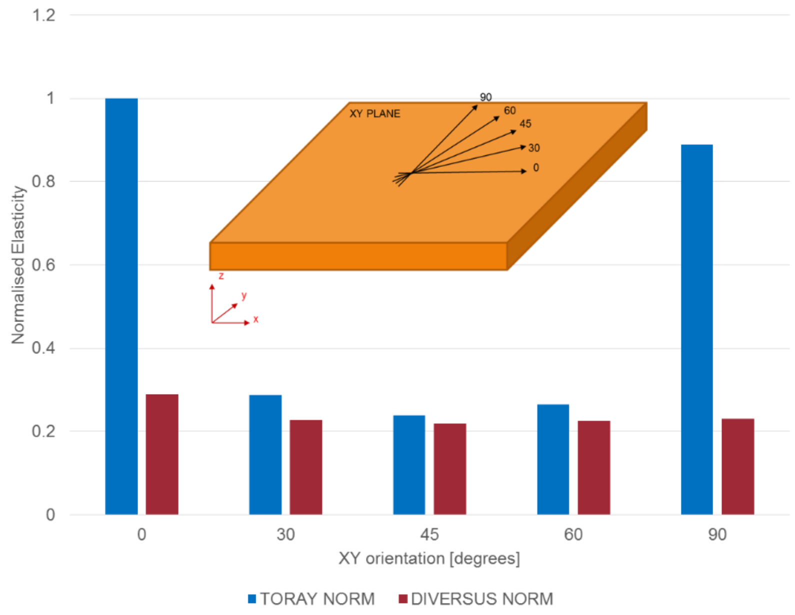

Figure 148 - Normalised comparison of the elastic moduli evaluated during the experimental campaign for both T and D samples

It is important to underline that the twisted structure of samples 3DF orients the fibres not only in the planar direction but also along the out-of-plane direction, having the fibres twisted in a fully 360° helix along the tow's length. This means that the isotropy of the material is not only in the planar direction such as in traditional quasi-isotropic laminates, but along all the three dimensions like in true homogeneous materials like metals.

On the other side, because of the plain weave pattern of the fabric, the traditional straight fibres (samples TF) concentrates all the strength given by the carbon material along the 0-90 directions, showing properties along the other planar directions which are a weaker combination of these two, while leaving the out-of-plane direction completely unreinforced (hence susceptible to cracks, delamination and other interlaminar damage). In other words, by changing the orientation of the fibres in the tows that form the fabric from a straight aligned configuration (samples TF) to a three-dimensional twisted one (samples 3DF) it is possible to modify how the strength of the fibrous reinforcement is distributed along all the three directions, balancing the elastic properties of the material. Although it was not possible to evaluate the elastic modulus of the laminates along the Z direction, these properties were evaluated indirectly by performing an impact test campaign, which will be the focus of another paragraph.

4.4.2.5.2 Evaluation of damping characteristics for different planar directions.

In order to fully understand how the twisted material would behave when subjected to a load in the out-of-plane direction, experiments were conducted to evaluate the damping characteristics of several 3D helicoidal twisted fabric (samples 3DF) oriented at different angles and a comparison was made with a traditional straight laminate (labelled samples TF).

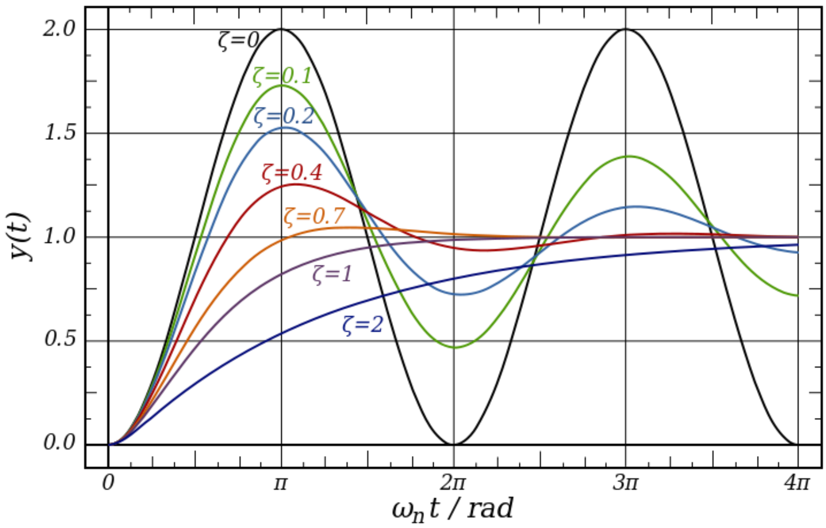

Figure 149 - effects given by different damping ratio values on a second-order system

Damping ratio can be defined a dimensionless measure describing how oscillations in a system decay after a disturbance. The damping ratio is a parameter, denoted by ζ (zeta), which characterises the frequency response of a second order ordinary differential equation.

The damping coefficient was evaluated from vibrational data collected using a Laser sensor by calculating the logarithmic decrement measured from different consecutive peaks. Logarithmic decrement was evaluated following the equation:

$$\delta = ln\frac{x_{n-w}}{x_n} \tag{27}$$

where x(n) is the amplitude of the vibration at the n^{th} peak, and x(n-w) is the amplitude recorded for a peak w periods away.

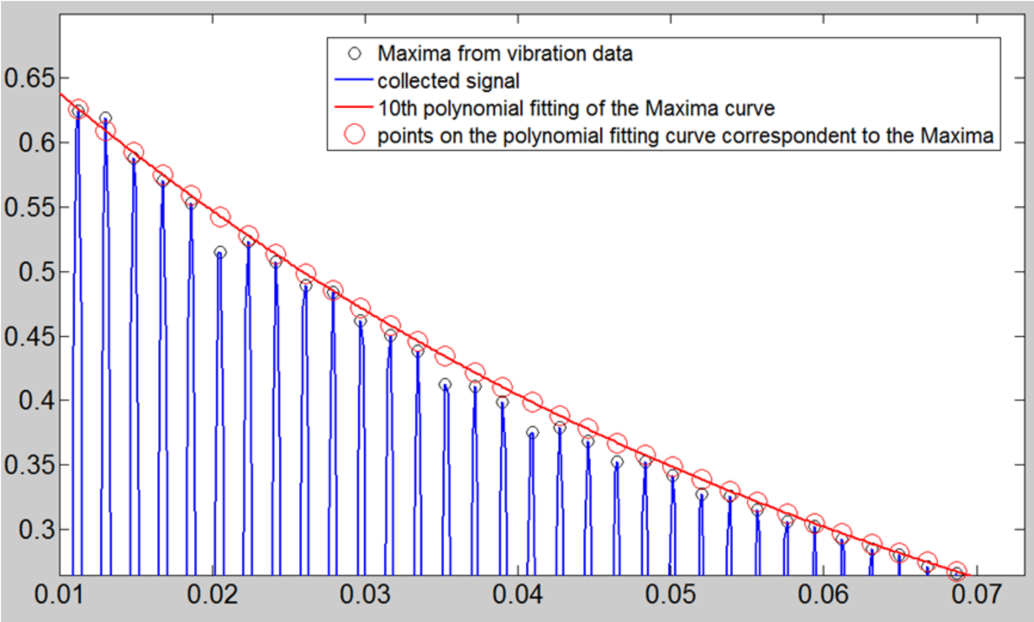

Figure 150 - details of the captured data during the damping test

Once the logarithmic factor δ was evaluated, it was possible to calculate the damping coefficient ζ by using the following equation:

$$\zeta = \frac{\delta}{\sqrt{(2\pi)^2+\delta^2}} \tag{28}$$

Data collected from the tests are presented in the table below for both samples TF and 3DF.

Table 17 - Logarithmic decrement and damping coefficient for both TF and 3DF samples collected during the experimental campaign

TF SAMPLES					3DF SAMPLES				
	DELTA	**DEV ST** (5 specimens)	**ZETA**	**DEV ST**		**DELTA**	**DEV ST** (5 specimens)	**ZETA**	**DEV ST**
0	0.0232	0.0047	0.0037	0.0007	**0**	0.039	0.003	0.00616	0.0005
30	0.0509	0.0036	0.008089	0.0006	**30**	0.035	0.009	0.00564	0.0014
45	0.0512	0.0063	0.0081	0.001	**45**	0.047	0.007	0.00754	0.0011
60	0.0485	0.0036	0.007722	0.0006	**60**	0.046	0.003	0.00724	0.0007
90	0.0178	0.0027	0.002844	0.0004	**90**	0.039	0.002	0.00603	0.0003

The behaviours of the two different sample batches is illustrated in Figure 151 which shows the effect given by the variation in the geometry of the fibrous reinforcement on the vibration dissipation.

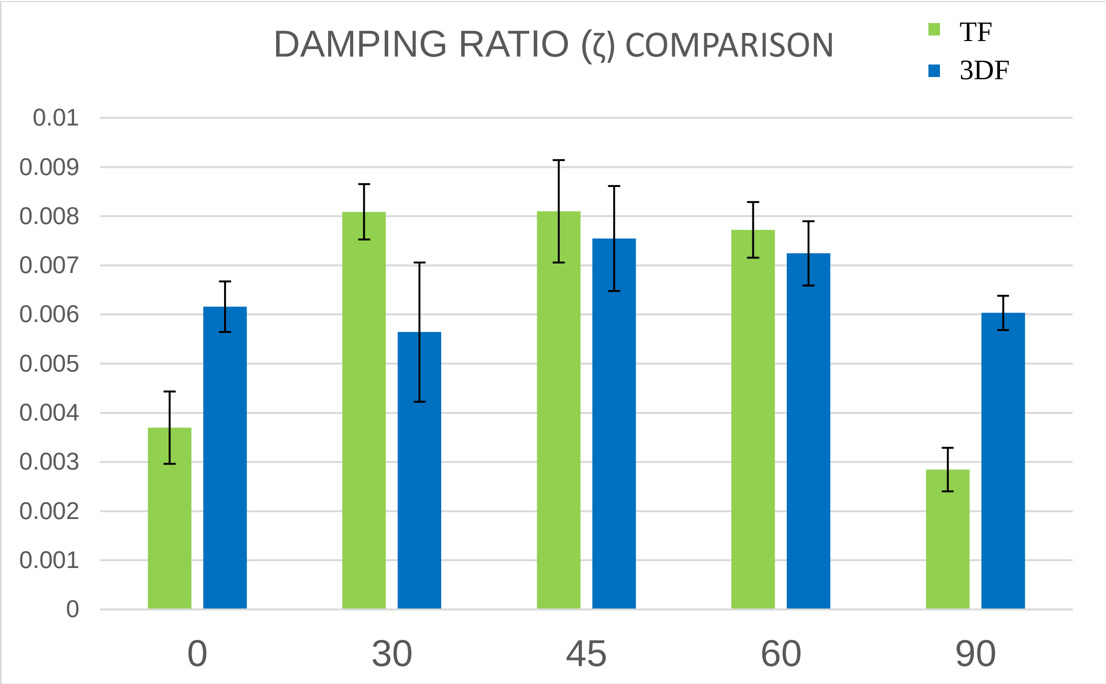

Figure 151 - comparison of the damping ratio evaluated for samples TF and 3DF at different orientations

Analysing the results, it is possible to observe that while the TF samples follow a trend which is highly variable with the orientation of the sample, the 3DF material, due to the helical disposition of the fibres along the tow's length, presents a much more isotropic behaviour, confirming the results observed with the vibration tests for the Young's Modulus evaluation.

4.4.2.6 Summary of the experimental results

RODS			
Flexural behaviour (Three points bending)			
	Flexural Stress (GPa)	**Flexural Strain**	**Bending Modulus [GPa]**
CORDA	0.436	14.60%	22.4
Traditional (unidirectional)	0.202	3.30%	31.7
Impact (Charpy test)			
	Energy absorbed per unit of surface [kJ/m^2]	Energy absorbed per unit of weight [J/g]	
CORDA	36.19	1.31	
Traditional (unidirectional)	9.98	0.4	
Crush test			
	25 mm crush test (50% compressive displacement)	40 mm crush test (80% compressive displacement)	
	Maximum Load [N]	Maximum Load [N]	

CORDA	7973	47458	
Traditional (unidirectional)	23191	24466	

FABRICS									
Flexural behaviour (Three points bending)									
	Flexural Strength (MPa)			Bending Modulus [GPa]			Flexural Strain		
configurations*	1	2	3	1	2	3	1	2	3
3DF (0/90 Fabric PW)	257	297	325.5	NA	20.64	22.9	4.35%	3.73%	2.92%
Traditional (0/90 Fabric PW)	600	715	629.5	NA	43.97	39.34	2.76%	1.78%	2.03%
Tensile Behaviour (Tensile test)									
	Ultimate Tensile Strength [MPa]			Modulus of Elasticity [GPa]			Tensile Strain		
3DF (0/90 Fabric PW)	218			25.7			NA		
Traditional (0/90 Fabric PW)	444			46.2			NA		
Impact Properties									
Low velocity Impact									
	Absorbed energy [J]			Max Force [kN]			Residual displacement [mm]		
configurations*	1	2	3	1	2	3	1	2	3
Energy [J]	7	9	12	7	9	12	7	9	12
3DF (0/90 Fabric PW)	5	7.23	7.19	0.67	1.91	3.08	6.6	1.72	4.99
Traditional (0/90 Fabric PW)	5.9	6.43	6.34	0.78	2.16	3.57	6.3	0.87	3.85
Charpy test									
	Energy absorbed per unit of surface [kJ/m^2]						Energy absorbed per unit of weight [J/g]		
configurations*	1		2				1		2
Energy [J]	1		15				1		15
3DF (0/90 Fabric PW)	39.13		42.21				0.484		0.244
Traditional (0/90 Fabric PW)	31.3		28.14				0.373		0.161
Elastic properties (Flexural vibration)									
Young Modulus Evaluation [GPa]**									
Angle	0		30		45		60		90

3DF (0/90 Fabric PW)	12.8		10.1		9.73		10		10.2	
Traditional (0/90 Fabric PW)	44		12.8		10.6		11.7		39.5	
Damping evaluation										
Angle	0		30		45		60		90	
Delta = logarithmic factor Zeta = damping coefficient	Delta	Zeta	Delta	Zeta	Delta	Zeta	Delta	Zeta	Delta	Zeta
3DF (0/90 Fabric PW)	0.039	0.0061	0.035	0.0056	0.047	0.0075	0.046	0.0072	0.039	0.006
Traditional (0/90 Fabric PW)	0.023	0.0037	0.051	0.0081	0.051	0.0081	0.048	0.0077	0.017	0.0028

*** Configurations:**	**3DF (0/90 Fabric PW)**	**Traditional (0/90 Fabric PW)**
1	one layer	three layers
2	two layers	six layers
3	three layers	nine layers

** composite samples were manufactured with a different resin than the one used for the Tensile test

4.5 Case Study Technology Validation

The proposed 3D helical fibre arrangement, in addition to several advantages seen in the previous paragraphs, present in his dry form a better drapability and ease of handling respect to traditional preform. In particular, in the “rope-like” shape the preform can be easily adjusted in the desired form keeping its structural properties. Moreover, the proposed solution introduces a low-cost and fast manufacturing process. To prove the advantages of the 3D helical fibre arrangement two products where investigated: D-lock and Helical-Spring.

The D-Lock (Figure 152) was made using a single twisted fibre preform for the shackle and by wrapping several 3D fabrics around the locking mechanism for the cross member. Both parts were manufactured by Resin Transfer Moulding technique.

Figure 152 D-Lock model made with 3D helical preform

A Perspex mould (Figure 153a) was manufactured for preliminary shackle manufacturing to guarantee a visual inspection of the resin flow during the injection process. Once all infusion parameters were optimized, a metal mould (Figure 153b) was used for the manufacturing process. The metal mould allows to cure the samples at higher temperature and have better surface finish.

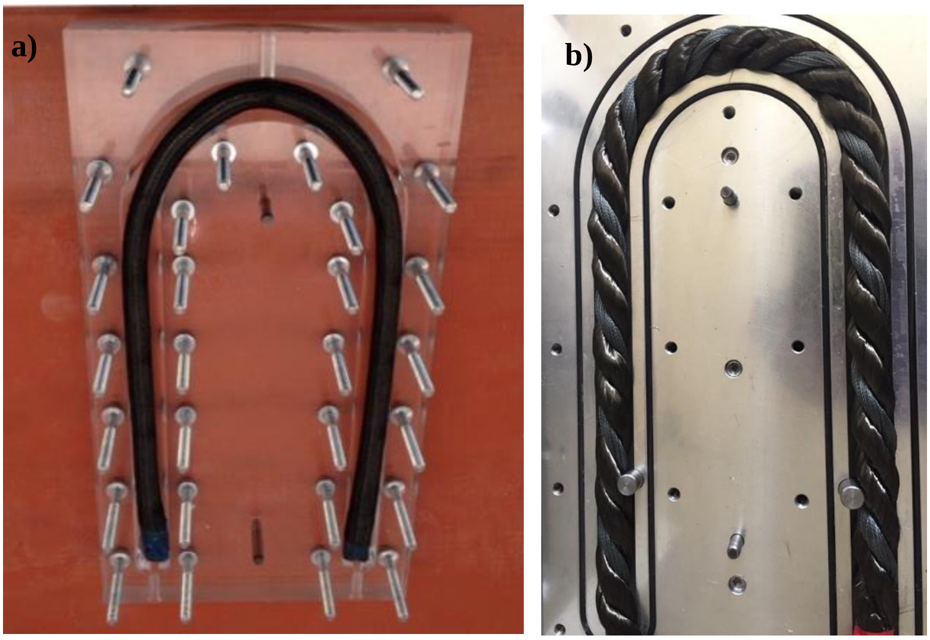

Figure 153 Shackle preform inside the: a) Perspex mould, b) metal mould

To satisfy the traditional lock requirements, such as resistance to theft attack (hacksaw, jack, crowbar, bolt cropper, freezing, hammers, etc.) whilst addressing the current D Lock weight issues several hybrid solutions were tested. The optimal hybrid configuration was found using carbon fibres strands and UHMWPE (Ultra High Molecular Weight PolyEthylene) fibres with metal inserts and a carbon fibres jacket. A D Lock solution was developed (Figure 154) and an experimental campaign was conducted where Gold Certificated (Sold Secure) were tested and successfully passed except for the hacksaw test, were the sample survived for almost two minutes instead of the 5 minutes' requirements.

Figure 154 D-Lock made using the 3D helical twisted fibre reinforcement

The second product investigated was a helical carbon spring (Figure 155). The sample was manufactured using a single 3D helical carbon rope covered by a silicone layer. The sample was obtained by a single step-process by injecting the resin directly in the silicone tube.

Figure 155 Helical-Spring made using the 3D helical twisted fibre reinforcement

5 Spiral Passive Electromagnetic Sensor

5.1 Introduction

There is a growing need for structural health monitoring (SHM) systems and NDT to reliably and accurately locate and quantify the presence of damage in composite material. Ideally the system should give information on the flaw appearance and its propagation before failure. Due to the extended variety of flaws that could be present within the structure, as illustrated in Figure 156, an effective monitoring of the system requires different types of sensor typically based on different physical phenomena, availing in most case the need of several techniques to detect and monitor all possible defects/damages [8, 145]. Furthermore, for an effective monitoring of the structure a large number of sensors distributed over a large area are required and the sensor should be able to detect the most likely flaws/damages.

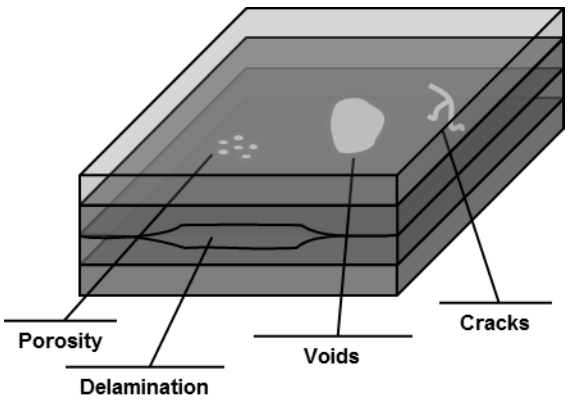

Figure 156 Typical flaws in a composite structure

Nowadays, with the steady increase of the use of composite materials in the aerospace industry, much attention has been devoted to smart material structures with embedded sensors, with the functionality to provide an early warning of the damage occurrence, resulting in efficient systems and in safer structures [11-14]. Given the complexity and weight penalties associated with the installation of wired sensors [9, 10], wireless sensors have become a promising solution to overcome design issues regarding structures that contain moving parts, or if the sensor has to be embedded within the material itself or placed in an inaccessible area of the structure. As a consequence, a number of studies are being conducted to design and manufacture passive wireless sensors [145, 146] despite the fact that wired sensors remain one of the most practical solutions for in-situ measurements. A key element in designing a wireless sensor is the type of power source being the leading factor for the lifetime of sensor and representing one of the main challenges in the sensor's design [144]. Indeed, a number of studies are being conducted to design and manufacture passive wireless sensors which work without the need of a battery [145, 146].

For many years engineers have been searching for ways to obtain information on how a structure is behaving in service by incorporating, at the time of construction or subsequently, sensing devices which can provide information about their health such as sensors that detect strain, temperature, humidity, and presence of defects (e.g. crack, delamination, porosity, etc.). In recent years structures and infrastructures tend to contain more integrated sensors in order to collect data on its health and/or on different environmental parameters [209, 210], and it is always preferred to have smart systems with the ability to cover more sensing operations in order to reduce the number of devices to install and eliminate problems of cross-talking between different devices. Whereas nowadays temperature measurements can be performed with a satisfactory accuracy, measurements of humidity are much more complex [211, 212]. Moisture is one of the largest concerns for building since it is the single most important agent of building deterioration [213]. Moreover the control of relative humidity and temperature is essential for improving aircraft cabin air quality [214]. The highest percentage of the current humidity sensors are based on the capacitive techniques, which have the feature of ease of fabrication, low power requirement and linear response [215, 216]. The objective of this research work was to create and validate a low-cost smart-sensor for non-destructive evaluation (NDE) and structural health monitoring (SHM) with the ability to detect temperature and humidity variations. Key elements in designing the new sensor are ability to work on glass and carbon fibres composites, to be easily surface mounted or embedded in complex geometries, able to detect flaws within the structure (most attention has been focused on delamination defects), low cost manufacturing process, ability to work wireless and without the need of a battery, and high robustness.

5.2 Spiral Passive Electromagnetic Sensor (SPES)

The Spiral Passive Electromagnetic Sensor (SPES), illustrated in Figure 157, represented a new design of inductor-capacitor (LC) resonant circuit sensor, which consists of a square planar spiral inductor, characterized by a single conductive trace (copper) on a dielectric substrate. The main idea was to transform a defect strain, crack, BVID, or a changing of the material properties or any alteration of the environment in the proximity of the sensor into a change of one of the following sensor’s parameters: resonant frequency, bandwidth, peak distribution, and amplitude of the SPES. Moreover, the sensor’s design allows reconfiguring the device in order to change correspondingly to the physical state for which the sensor is measuring, as pressure, temperature, PH [158, 160-162] and all physical characteristics affecting the parameter of the RLC circuit. In this work, the resonant frequency represents the principal parameter of investigation.

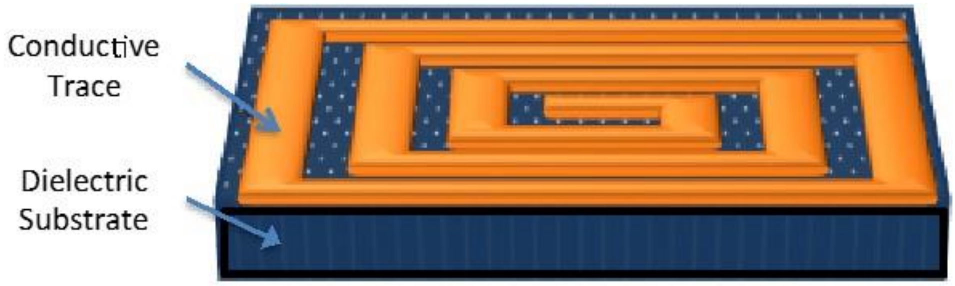

Figure 157 Illustration of the sensor

Another great advantage of the sensor presented in this work is the ability to monitor both conductive and non-conductive structure, one of the main challenges commonly encountered for resonant circuit sensor used for NDT [217, 218]. Two different techniques for the sensor's manufacturing have been adopted, using respectively a milling machine and an etching process. The latter method was chosen as it is the most widely used manufacturing technique to produce antennas or sensors. The sensor was realized etching a copper trace on a polyimide sheet, obtaining a flexible sensor with a thickness of only 110um. Instead the second manufacturing technique was investigated as a low-cost solution, obtaining a sensor with a thickness of 2mm, using a milling machine and a Printed Circuit Board (PCB) with FR4 as substrate and copper on the surface. The first sensor, due to its thickness, flexibility and resistivity of the polyimide substrate, offers the possibility to be easily embedded inside a laminated structure or bonded on complex structures, adapting easily to curved shapes.

The new sensor is lightweight, low cost, robust, flexible, portable, reliable, and offers the possibility to be tailored for the sensing application. In terms of reliability this technology offers several advantages with respect to other SHM/NDE devices, due to its simple design, which is less prone to failure of electrical circuit components, and can work in harsh environments. Moreover, the resonant sensor acting as an inductor with a single conductive trace, if damaged, could continue to work [159], resulting in a sensor with a lower number of turns, and hence the damage will result in a change of its own resonant frequency due to the reduced length of the conductive path. This characteristic is particular useful for identifying if the sensor itself has been hit and damaged.

The sensor presents the ability to work in two different configurations. In the first configuration (wireless setup) the SPES is interrogated by an external antenna connected to a spectrum analyser; while for the second setup (wired setup) the sensor is wired with the spectrum analyser acting directly as an antenna. The wired sensors could monitor structures in real time offering the possibility to work as a device for SHM; while the wireless systems, not requiring any direct connections between the sensor and the data processing is more suitable for ground inspection, acting as an NDE sensor, diagnosing the structure without the need to disassemble it. Moreover, the wireless devices have the advantage of not requiring a power supplier nor the precise alignment between sensor and the external antenna, needed in optical telemetry. Lack of need for bulky batteries and wire connections make passive sensors ideal candidates for applications where location of the sensors, or access to them, is prohibited. Difficulty to reach the sensor is often due to the remoteness of the system's location or by the harshness of the environment in which it is operated, such as: engine testing, landing gear in-flight or due to the presence of hazardous chemicals. The sensor can detect several physical parameters without incurring cross-talk and can both protect the structure from the presence of ice as well as remove the eventual presence of ice on the structure. The SPES presented a solution to address the need of a multi sensing device able to monitor and detect, wirelessly and without the need of a battery, defects and cracks within the structures as well as environmental parameters. The device, if wired to a power supply, could also be used to work as an anti-icing/de-icing device. The key advantage of the SPES is given by the new interrogation method and by its intrinsic multi-functionality given by its internal structure. Indeed, the use of polyimide allows to monitor humidity variations without the use of complex patterns [219-222] or additional coating [223, 224] that can affect the mechanical properties of the sensor and increase the manufacturing cost.

5.3 Sensor's principle of function

The sensors tested for the different interrogation methods present the following parameters (Figure 159): the outer length (l) of the square is ~100 mm, with eighteen turns spiral. The width (w) of each trace is 2mm and the spacing between the adjacent electrodes (g) is 0.2mm. The thickness of the sensor is related to the manufacturing process adopted, obtaining, for the sensors tested, a thickness of 110 μm using the etching process and 2 mm for the milling process.

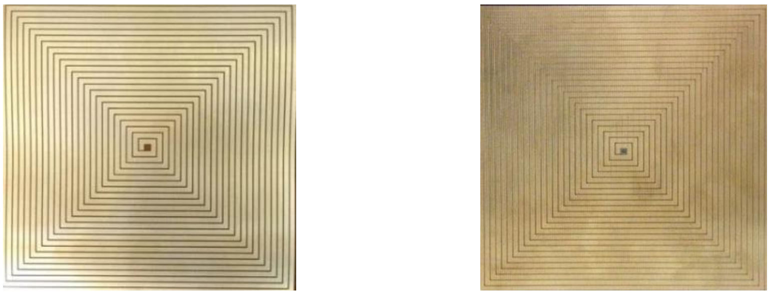

a) Copper trace on polyimide layer b) Copper trace on FR4 substrate

Figure 158 Spiral Resonant Sensors realized with different techniques

The first sensor was obtained using a single sided PCB (Printed circuit board) which has one ounce of copper on one side and a total thickness of 2mm. Instead the etched sensor was manufactured using one ounce of copper on one side as conductive trace and polyimide for the substrate using an etching technique. A silver finish was applied on the trace in order to protect the copper trace. The electrical properties of the etched sensor are reported in Table 18:

Table 18 Electrical properties for the SPES system on polyimide substrate.

Dielectric Strength	4.2 KV/mil
Dielectric Constant	3.5
Dissipation Factor	0.02
Surface Resistivity	10^{11} ohm/sq
Volume Resistivity	10^{11} ohm-m

The resonant frequencies of the sensor in free space are determined by wiring the sensors directly to the spectrum vector analyser and placing the sensor on wood supports to avoid interference. The sensor on the polyimide substrate, due to its slenderness and the easiness to bend itself, during the tests was fixed on polyethylene substrate (thickness of 1 mm), ensuring a uniform distance between the antenna, the sensor and the sample tested. The resonances of the sensors are 37 MHz for the sensor realized on polyimide substrate and 32 MHz for the one fabricated on FR4. The highest resonant frequency for the etched sensor with respect to the sensor on the FR4 is due to the polyimide substrate used as support that acts as dielectric increasing the resonant frequency.

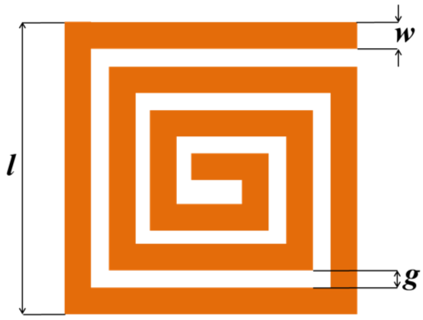

Figure 159 Example of geometry of the spiral sensor

The sensor is chipless and does not present any electronic circuit, but rather an inherent capacitance due to the geometric design and the inductance represented by the spiral metal trace. The sensor can be modelled as an inductor-capacitor (LC) tank circuit, where the copper coil forms both the inductor and the capacitor. When exposed to an external radiofrequency (RF) field, the sensor resonates. The sensor is powered and interrogated by magnetic field, using the return loss parameter as measured by a network analyser. This makes the sensor work wirelessly and passively. Figure 160 shows a 10 cm probe connected to a spectrum analyser (AGILENT N9913A 4 GHz FieldFox Handheld RF Combination Analyzer) to stimulate and remotely monitor the resonant frequency shift of the SPES device.

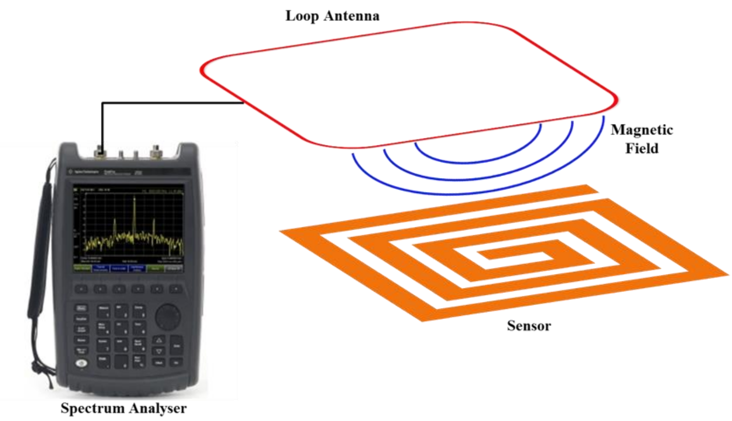

Figure 160 Loop antenna connected to a portable RF Network Analyzer powering and interrogating a SPES sensor

The resonant frequency is related to the inductance L and parasitic capacitance C of the spiral inductor as given:

$$f = \frac{1}{2\pi\sqrt{LC}} \tag{29}$$

When the SPES sensor is excited by a changing magnetic field, electromagnetic induction (described by the Farday's law) generates a current through the coil. Each copper trace of the sensor has a different voltage so, any turn's segment creates a potential difference between close parallel trace and thus an electric field. The electric and magnetic fields produced by the sensor when electromagnetically coupled with a substrate (i.e. the sample under test) will give information on the properties of the materials in the area surrounding the sensor. For the self-resonant coil, the equivalent lumped parameters, in accordance to the electric theory, can be calculated, as reported by Wang [15], using the equations below

$$L = \frac{\mu_0 \mu_r}{4\pi |I_0|^2} \iint \frac{J_{(r)} J_{(r)}'}{|r - r\prime|} dr dr' \tag{30}$$

$$C^{-1} = \frac{1}{4\pi \varepsilon_0 \varepsilon_r |q_0|^2} \iint \frac{\rho_{(r)} \rho_{(r)}'}{|r - r\prime|} dr dr' \tag{31}$$

where:

$L = Inductance$
$C = capacitance$
$\mu_0 = free\ space\ permeability$
$\mu_r = relative\ permeability$
$\varepsilon_0 = free\ space\ permittivity$
$\varepsilon_r = relative\ permittivity$
$J_{(r)} = current\ density\ functions$
$\rho_{(r)} = charge\ density\ functions$

Indeed, the presence of defects can be monitored by any changes of the sensor's resonance characteristics of frequency, amplitude, and bandwidth, in respect to the baseline of the undamaged samples. In particular, the variable parameters responsible for the shift of the resonant frequency when a change in the structure or in the material properties occurs are the inductance L and the capacitance C. The inductance is strictly related to the design characteristic of the sensor as the turns, the width (*w*) gap (*g*) side (*l*), as illustrated in Figure 159. The capacitance is related to the shape and the geometrical characteristic of the sensor, the permeability of the material used as substrate for the conductive trace and the sample under test. As reported by Boller et al. [143] the presence of damages within the structure induces locally significant variations of the electric conductivity and/ or dielectric permittivity. Moreover, the presence of flaws within the structure affects the current flows between the sensor's electrodes and so the capacitance.

A schematic representation of the sensing mechanism of the SPES is illustrated in Figure 161, although as reported in this paragraph, the equivalent electric representation is strictly related to the electrical properties of the material under exam. Indeed, the presence of flaws cause opposite effects on carbon and glass fibre composites depending on their electrical nature, resulting in a shift of the resonant frequency toward higher frequency for conductive samples as the defect increases, while in non-conductive structures the resonant frequency shift to lower frequencies.

The blue arcing lines in Figure 161 illustrate the electric force between parallel traces through the material (this is mirrored overhead the substrate). How deep electromagnetic radiation can penetrate into a material is a measure of a penetration depth and is strictly related to the design and the dimensions of the sensor as well as the permeability properties of the material. Indeed, Carbon fibre composites due to the electric conductivity of the fibres present a lower penetration depth in respect to glass fibre composites. Hence, monitoring thick or massive conductive composites can result in difficulty with the detection of defects due to a small penetration depth.

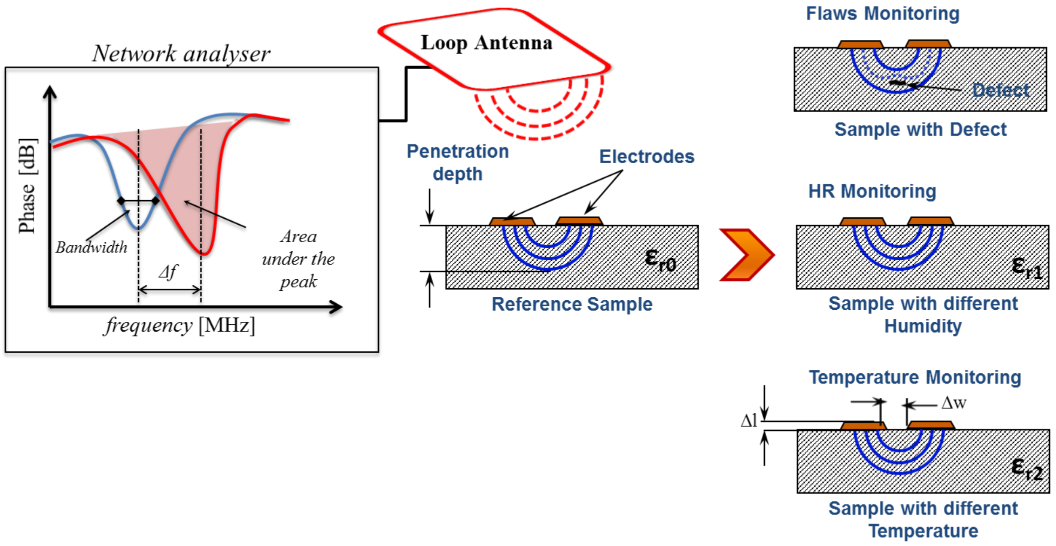

Figure 161 Schematic representation of the sensing mechanism of the SPES

Figure 162 shows a schematic representation of the basic principle of the SPES sensing mechanism. Indeed, any alteration of the sensor's response due to change in temperature, humidity and/or of the dielectric properties (e.g. ε_{ri}) of the materials in the proximity of the sensor can cause a shift or alteration of the sensor's resonance characteristics of frequency, amplitude, and bandwidth. So, any changes of the signal response of the sensor can be used to detect and correlate these variations with the presence of damage/flaws within the material, variation of environmental parameters or change in the property of materials in close proximity of the SPES.

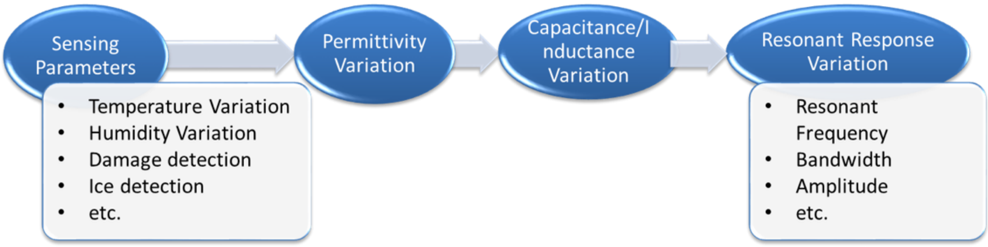

Figure 162 System block diagram of the SPES sensor

The understanding of the sensing function and the performance of the sensor are based on the estimation of the parameters of the sensors based on the equivalent electrical circuits. Indeed, the sensor can be represented by the lumped model of an LC tuned circuit, as showed in Figure 163a. Since the sensor itself is an inductor, the inevitable parasitic resistance and capacitance affect the parameters to be analysed. The inductance is generated by the sensor shape, in particular by the conductive trace, and is mainly related to the number of turns per given area. The capacitance is a result of the distance between the conductive trace and the sequence and properties of the underlying layers. The LC circuit, is a theoretical model, taking in account the real circuit, a resistance should be taken in account, in particular the one related to the conductive path. In Figure 163b a series resistance is added to the inductance to take in account the opposition to the current given by the conductive trace itself, related to its length and geometries.

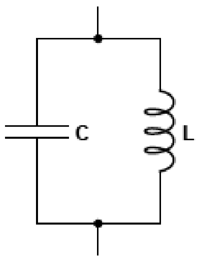

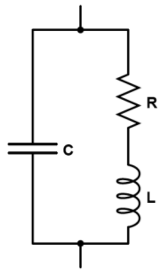

a) Equivalent circuit model

b) Equivalent model considering the real inductance

Figure 163 equivalent circuit model of the sensor, a) ideal LC tuned circuit, b) considering a real inductance

Resistance, Inductance and capacitance represent the sensor key parameters, and they will now be treated one by one. However, it is important to mention that with the sensor being attached only on one side of the sample, the dependency function between inductance and capacitance with the material's relative permeability and relative permittivity is not obvious. Based on the distributed parameters, the equivalent lumped parameters can be calculated, as reported by Kurs and Wang [148, 217]. The dependency function between the sensor parameters and the material relative permeability and permittivity is advised to be characterized and calibrated by experiments and/or computational methods.

5.3.1 Inductance

The inductance is the ratio of total magnetic flux (the magnetic flux multiplied by the number of turns N) to current through the inductor.

$$L = \frac{N\phi}{I} \tag{32}$$

The total inductance (L) of the coil is equal to the sum of the self-inductance (L_S) of each straight segment plus the mutual inductance (M) of the trace interaction as expressed in the formula (5). The mutual inductance is related to the mutually coupled magnetic fields of parallel traces, and depends on the distance of the trace, the direction of the current and the geometries of the conductive trace. In fact, due to the dependence of the mutual inductance on the directions of the current of the conductive traces considered, the mutual inductance is considered positive M_+, if the currents of the traces considered flow in the same direction, or negative M_- if they are in the opposite directions; while the self-inductance is the ratio between the current carrying conductor and the current passing through it.

$$L = L_s - (M_+ + M_-) \tag{33}$$

As highlighted by Neagu [225], using the formula (33) , of the self-inductance of a rectangle having diameter l, thickness w and height h (Figure 164); the self-inductance increases with decreasing the height of the trace:

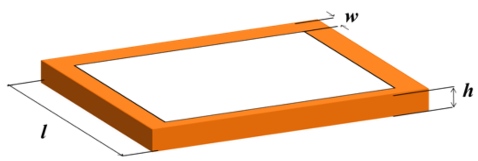

Figure 164 Rectangle with diameter l, thickness w and height h

$$L_{s(N=1)} = \frac{2\mu l}{\pi}\left[\ln\frac{4l}{w+h} + 0.894\frac{w+h}{4l} - 0.660\right] \tag{34}$$

It is reasonable to assume, that the formula keeps the same correlation with the increasing number of turns. On the contrary, the thickness *w* has its own correlation with the number of turns, bearing in mind that the number of possible spirals on the same area is strictly related to the width of the trace. This consideration on the self-inductance leads to the optimization of the inductance through the choice of a square spiral sensor rather than a circular one. Indeed, the square shape allow to increase the perimeter of the conductive trace keeping the total covered area constant.

5.3.2 Resistance

The physical parameters influencing the resistance of the sensors are the material properties of the conductive trace, indicated as series resistance, and the characteristics of the underlying layer, accounting as parallel resistance. The series resistance, consists of two terms that result differently from their dependence with the frequency. The frequency-independent term is the DC resistance of the wire, and could be expressed through the Ohm's law in the formula below, considering a conductive trace of length l, thickness h, with w and made of a material of resistance ρ.

$$R_s = \frac{\rho l}{hw} \tag{35}$$

The frequency-dependent contributions of the series resistance, are related to the eddy current and to the skin depth, strictly interconnected between each other. The eddy-currents are local currents travelling with opposite direction in respect to the applied current, arising from a changing of magnetic field. The eddy current will reinforce the current on the skin of the conductive trace resulting in cancelling the current in the middle. The tendency of the current to become distributed within a conductor is called skin-depth and denoted as δ_{trace}. According to the equation below, the skin-depth is related to the properties of the material and to the frequency of the current. In particular increasing the frequency, the current distribution change and tendency to concentrate on the edge of the wire. This parameter became relevant when its value is less than the dimension of the conductive trace.

$$\delta_{trace} = \sqrt{\frac{2\rho}{\omega\mu}} \tag{36}$$

Regarding our sensor, considering the copper as conductive trace and a frequency range of about 25-35MHz, the skin depth is $\delta_{trace} \approx 30\mu m$. Moreover, the magnetic field causes eddy currents also on the adjacent trace and in the underlying conductive substrate (in our case the carbon composite). This results in a different behaviour of the resonance frequency when CFRP or GFRP are tested. Regarding the eddy current on the underlying conductive layer, the magnetic field, can penetrate as seen before, only a limited distance, which as before could be evaluated through the penetration depth. As reported by Wang [217] the carbon composite for aerospace application presents a penetration depth $\delta_{ulayer} \approx 1mm$ at a frequency of 10MHz.

The parallel resistance is related to the insulating layer underneath the sensor, and is far less than that of the series resistance.

5.3.3 Capacitance

The use of samples with conductive and non-conductive properties requires the necessity to consider different capacitor components contributing to the total parasitic capacitance, as reported in Figure 166. The sensor's substrates (FR4 and polyimide) act both as a dielectric material; therefore they contribute similarly to the total parasitic capacitance (see Figure 165).

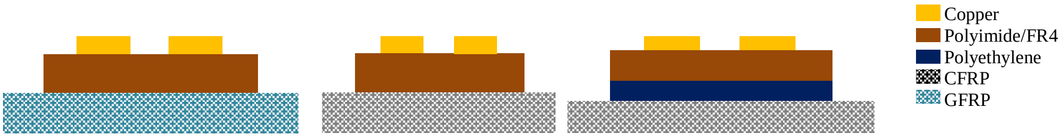

a) GFRP substrate   b) CFRP substrate   c) Polyethylene/CFRP substrate

Figure 165 Cross section of spiral sensor on different substrate

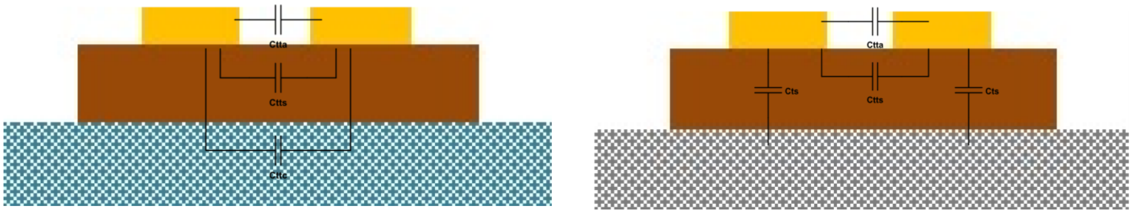

a) Parasitic Capacitance of the sensor attached on GFRP sample   b) Parasitic Capacitance of the sensor attached on CFRP sample

Figure 166 Cross section of spiral sensor on different substrate showing the parasitic capacitor components

In the first configuration (Figure 165a) the parasitic capacitance is a result of two different capacities, as reported in Figure 166a: the capacitance between adjacent turns C_{tta} , where the air gap act as a dielectric, and the capacitance between the coil's turn C_{tt} where the underlying layer act as a dielectric. The latter parameter is split in C_{ttc} and C_{tts} considering the GFRP and the FR4/polyethylene as dielectric layers respectively. The analysis of the C_{tt} parameter is relevant for the detection of the material's integrity, as reported by Klysz and Nassr [180, 226]. Instead the second configuration (Figure 165b) due to the conductivity of the CFRP, there are three parameters contributing to the parasitic capacitance, as reported in Figure 166b: the C_{tta} and the C_{tts} as the previous model, and the capacitance between the conductive trace and the CFRP C_{ts}. The formula for the evaluation of all defined parameters, and their dependence to the characteristics of the sensor and the material used are reported by Neagu and Jow [225, 227]. The third configuration (Figure 165c), having the polyethylene layer under the FR4, behaves as the previous, with the only difference of presenting, another capacitance C_{tp} added in series to C_{ts}, and another capacitance C_{ttp} in parallel to C_{tts}.

5.4 Experimental setup

5.4.1 Interrogation method

Based on the capacity of the resonant structures to act as antenna when excited, and then emitting radiation, it is possible to determine the self-resonance frequency of the SPES sensor, by using a spectrum analyser with an internal tracking generator, a loop antenna and a directional coupler, as reported by S. Roleson [228]. More precisely a swept input frequency was sent by the tracking generator to the loop probe. The loop antenna connected through the directional coupler, reflects most of the incident energy it receives, which is sent directly in to the spectrum analyser. This configuration can act as an absorption wave meter. Indeed, when a structure, with a natural resonant frequency within the swept-frequency range, is in the proximity of the probe its resonant frequency can be visualized as a dip in the spectrum trace. The presence of the change is caused by an incident RF absorbed by the structure. So when the resonant frequency is known, a short swept range has to be refined in order to increase the sensitivity of the sensor and allow the determining of a change in the structure due to the presence of a defect. Indeed, the comparison of resonant frequency of the same/similar samples before and after damage occurs offers the possibility to detect its presence. This effect is subtle and can easily be missed or misunderstood, so great accuracy is required, in order to compare the resonant frequency. It must be noted that a change in the instrumentation or the surrounding environments could affect the measurement leading to false alarm. Furthermore, regarding the distance between the loop antenna and the passive sensors, it is recommended to set the distance at 1/10 of the wavelength. Indeed, a current flowing into the coil (loop antenna) radiates a near-magnetic field that falls off with r^{-3}. Being the sensors designed to work mainly in aerospace sector, in order to avoid electromagnetic interference with the frequency adopted in the aeronautics, the SPES has been design to have work with frequencies less than 74.8 MHz (marker beacon).

5.4.2 Test plan

Two different samples were tested, a GFRP (non-conductive sample), and a CFRP (conductive sample). The spiral sensor was activated adopting both wireless and wired setups, using a Rohde & Schwarz spectrum analyser FSEK30 with an external coupler (the AGILENT FieldFox Handheld RF Combination Analyzer does not required the use of an external coupler). The sensor, due to its design geometries, could be considered as a resonant structure acting as an antenna. In the first method, (Figure 167) the magnetic field is induced in the sensor through a loop antenna connected, through a coupler, to the spectrum analyser.

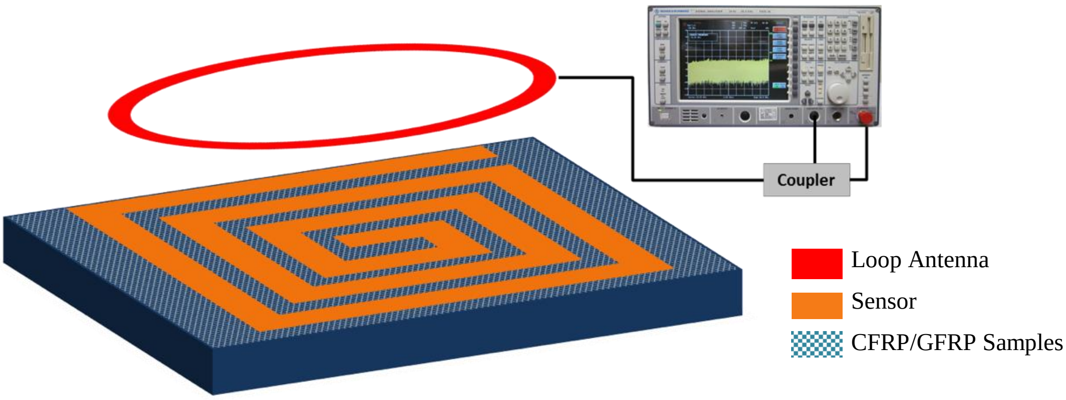

Figure 167 Wireless setup

In the second method the sensor is wired directly to both ends of the conductive trace and then connected directly to the output generator. The wired setup reduces the shielding of signal when conductive samples (CFRP) are tested. As reported in Figure 168 three different configurations were tested, connecting the sensor: to a coupler; to the generator output (acting as a transmitter); and to the input of the spectrum analyser (working as a receiver).

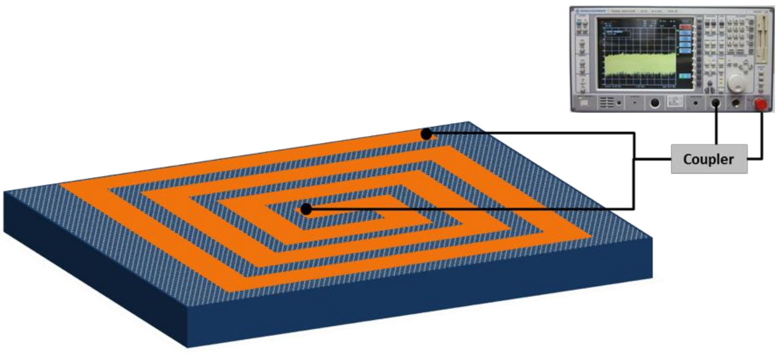

a) Sensor wired through a coupler

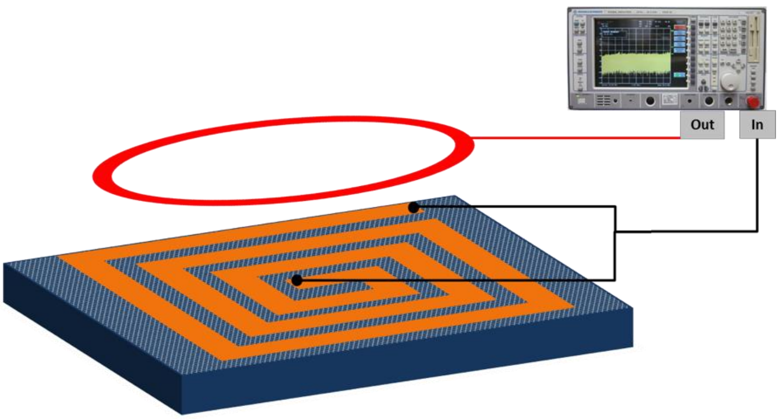

b) Sensor wired as a receiver

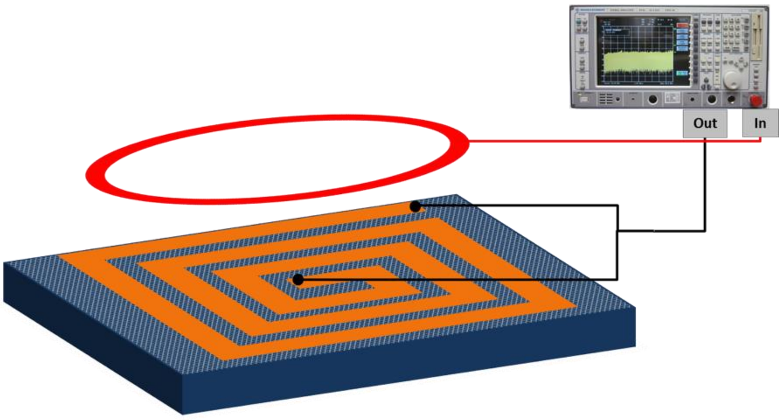

c) Sensor wired as a transmitter

Figure 168 Sensor wired to a spectrum analyser: a) through a coupler, b) to the input, c) to the generator output

In order to determine the presence of damage inside the samples, and to ensure the repeatability of the experiments, the following experimental procedure was followed. Different samples were manufactured using the autoclave in a single shot to ensure the consistency of the manufacturing method. After ensuring that all samples with the same characteristics present the same resonant frequency, different damages were performed on the samples, leaving one sample intact as reference. The sensor was placed on the non-damaged side of the composite and the new resonant frequency was reported and compared with the previous one, in order verify the presence of the damage. As reported in Table 19, two types of damage were investigated; holes obtained using a driller, and two impacts, at different energies, causing a barely visible impact damage and a visible crack on the opposite face to the impact (barely visible in the front impacted face), as illustrated in Figure 170. The characteristics of the samples and of the damages used are reported in Table 19.

Table 19 Samples and defects characteristic

	Material	Lamination sequence	Samples Thickness	Hole	Impact
Type 1	GFRP	$[0/90]_{5S}$	5.80mm	9 mm Φ	
Type 2	CFRP	$[(\pm45)_2/F/(\bar{F})]_S$	1.30mm	2 mm Φ	
Type 3	CFRP	$[(\pm45)_2/F/(\bar{F})]_S$	1.30mm	5 mm Φ	
Type 4	CFRP	$[(\pm45)_2/F/(\bar{F})]_S$	1.30mm		Impact 10 J

Type 5	CFRP	$[(\pm 45)_2/F/(\bar{F})]_S$	1.30mm		Impact 12 J

a) CFRP Intact b) CFRP Type 2 c) CFRP Type 3 d) CFRP Type 4 e) CFRP Type 5

f) GFRP Intact g) GFRP Type I

Figure 169 Composites panel tested

The impacted samples were also investigated using the infrared thermography to have a comparative NDT technique (Figure 170a) especially for the delaminated sample.

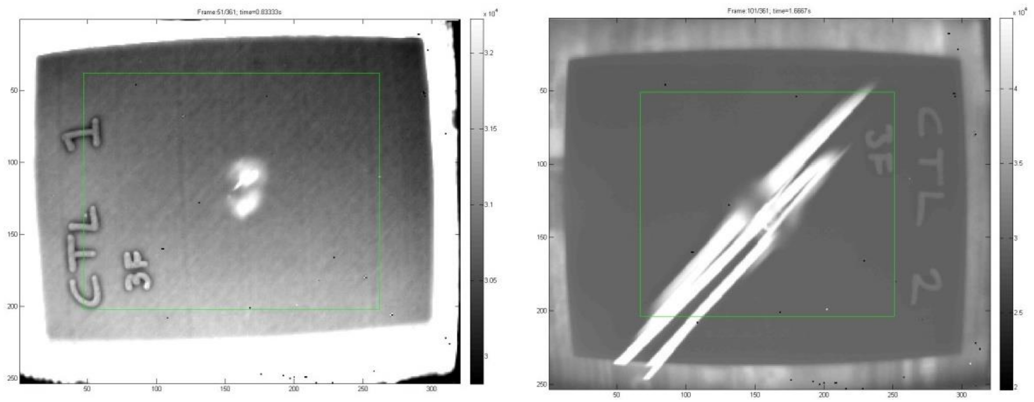

a) Delamination b) Crack

Figure 170 Thermography test: a) CFRP sample impacted with 10 J, showing a delamination in the middle; b) CFRP sample impacted with 12J showing a visible crack

5.4.3 Wireless setup:

As described before, the loop antenna is attached to the spectrum analyser through a coupler and the sensor (etched on polyimide) is placed on the sample under test. Two interrogation distances were investigated: 50 and 90 mm respectively. Due to the high sensitivity of the sensor, in order to minimize the interference with the surrounding environment the samples were positioned by minimizing the contact with other objects, using media that will support the sample only on the edges.

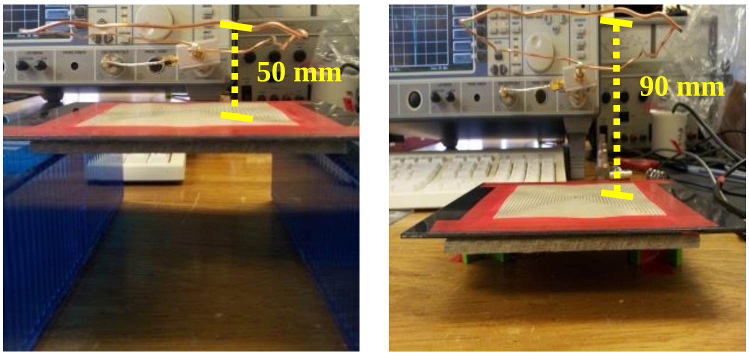

a) Interrogation distance of 50 mm

b) Interrogation distance of 90 mm

Figure 171 Wireless setup for two different interrogation distances: a) 50 mm; b) 90 mm.

The resonant frequency of the undamaged and the damaged composite, and using as reference the sensor in free-space, were analysed and compared. The graph in Figure 172 shows that the sensor resonant frequencies decrease when the sample is placed close to the sensor. The fiberglass, acting as a dielectric, causes an increase in the capacitance of the system and accordingly to the formula (1) a decrease of the resonance frequency. Furthermore, the presence of damage, as shown for the graph and the chart in Figure 171 cause a further decrease in the resonant frequency. The sensitivity of the sensor, illustrated in the figure 15b, was evaluated comparing the shift in resonant frequency (Δf) in respect to the intact sample. This allows comparing the different setups and choosing the most efficient. As reported in Figure 172c the sensitivity of the sensor slightly decreases as the interrogation distance increases.

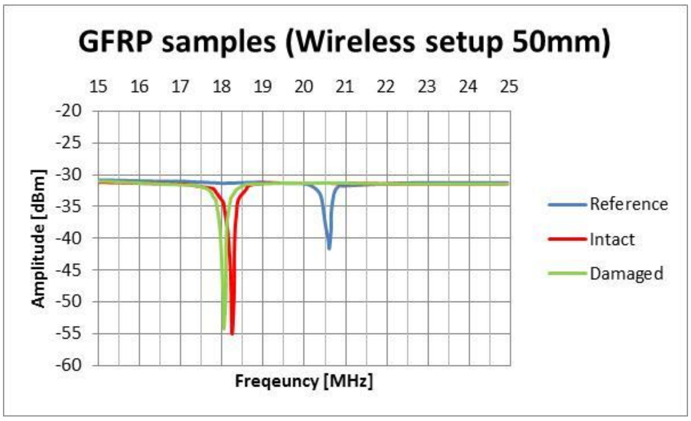

a) Spectrum analyser diagram of GFRP samples, interrogated wireless at 50mm from the samples

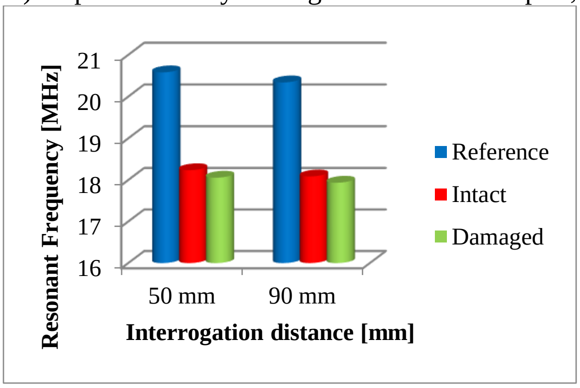

b) Comparison of resonant frequency for GFRP samples tested a two different interrogation distances

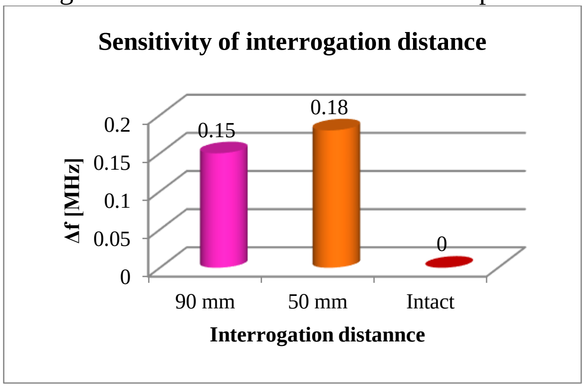

c) Sensitivity of the sensors tested a two different interrogation distances

Figure 172 Wireless interrogation of GFRP samples

5.4.4 Wired setup:

The wired setups allow the possibility to test conductive and non-conductive samples. Eliminating the factors related to the coupling with the antenna, more tests were performed with the wired system. Indeed, both typologies of sensors were tested (with FR4 and polyimide substrates), and as reported in Figure 168 three interrogation methods are investigated. The resonant frequencies of each relative configuration are reported below in Figure 173a, Figure 174, and Figure 175, grouping the results for the two typologies of material tested (CFRP and GFRP).

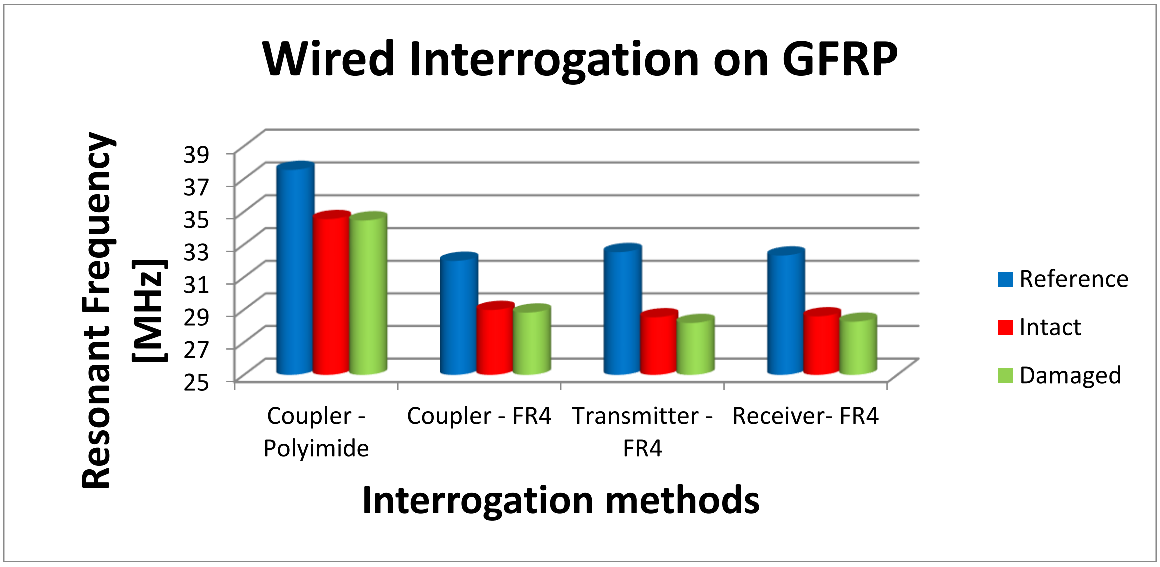

a) Resonant frequency for different interrogation methods

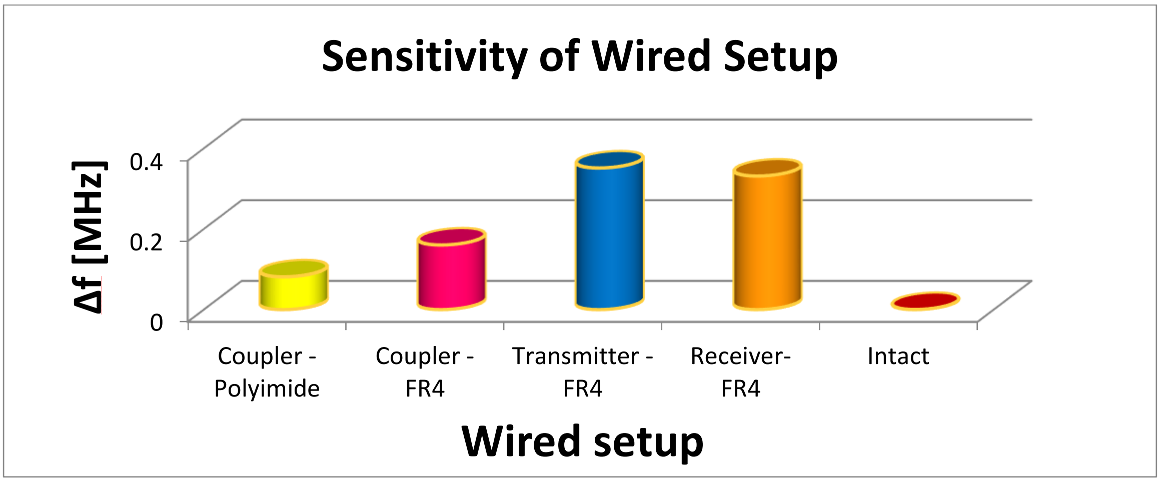

b) Sensitivity of the sensor for different interrogation methods on GFRP samples

Figure 173 Comparison of Wired Interrogation methods on GFRP samples

As for the wireless system, the resonant frequency presents the same trend, decreasing with the sample placed closer to the sensor, and with a further decrease caused by the presence of a damage within the GFRP samples. Instead the carbon composites, due to their different electrical properties, show an increase of the resonant frequency when the presence of damage is detected (Figure 174 and Figure 175).

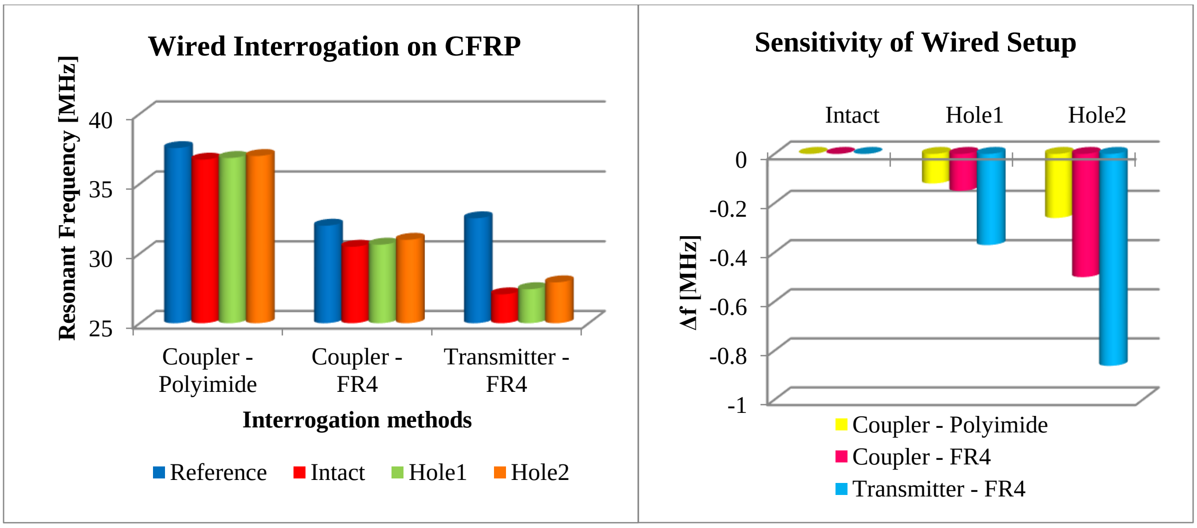

Figure 174 Comparison of Wired Interrogation methods on CFRP samples with hole

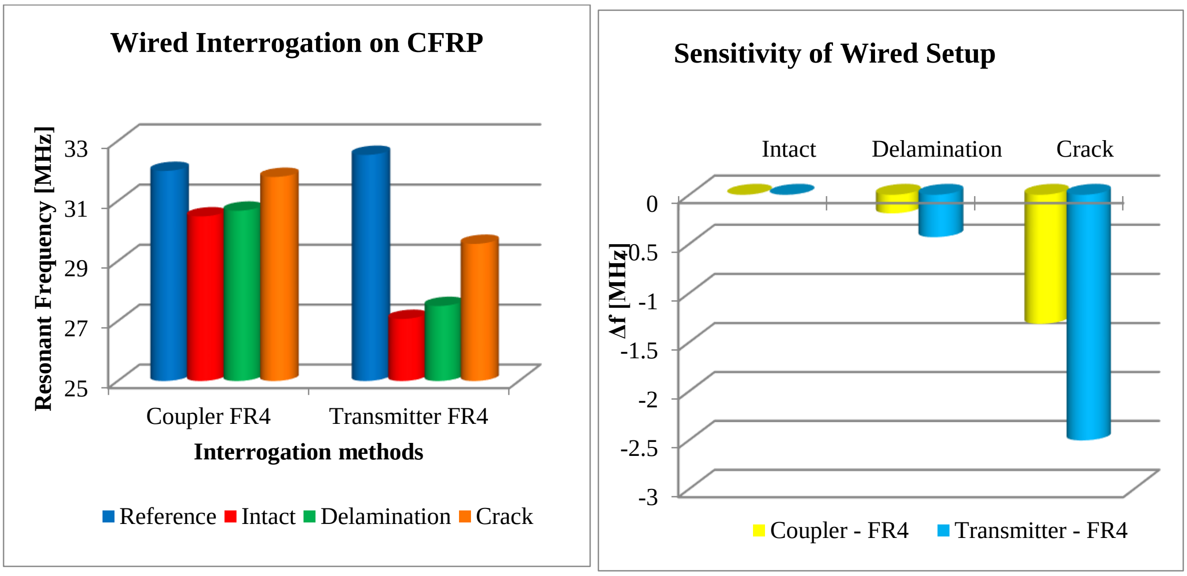

Figure 175 Comparison of Wired Interrogation methods on CFRP samples with delamination and crack

The chart in Figure 173b compares the different wired configurations, showing almost an equal sensitivity for the transmitter and receiver mode and an overall decrease in the resonant frequency when FR4 is used as substrate rather than polyimide. The transmitter mode is more perceptive to the presence of damage in respect to the coupler configuration. This is more clear from Figure 174 and Figure 175, where the sensitivity of the sensor for the samples with flaws is reported in respect to the intact samples, showing a higher sensitivity for the transmitter mode in comparison to the coupler-configurations. The sensitivity of the resonant frequency to the dimension of the defects has been shown, although the presence of defects affect also other parameters, like the bandwidth and the amplitude of the signal. Indeed, as showed in the Figure 176a, the samples impacted at 12J present a slightly increase in the resonant frequency in respect of the reference signal, although the value of amplitude and bandwidth is more relevant. This leads to planning further tests, in order to obtain a more accurate diagnosis of the sample by correlating the change of the mentioned parameters to the characteristic of the damage.

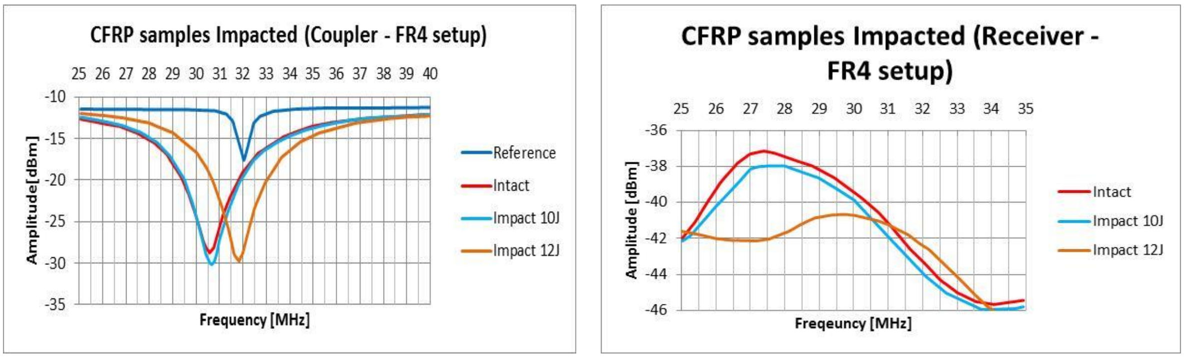

a) Sensor wired through a coupler

b) Sensor wired, working as receiver and interrogated by a loop antenna.

Figure 176 Spectrum analyser diagram of CFRP samples: a) sensor wired through a coupler to the spectrum analyser; b) sensor wired to the spectrum analyser as receiver and interrogated by a loop antenna (acting as transmitter).

The functionality of the wireless sensor is strictly related to the magnetic field strength and so is proportional to the interrogation distance. In order to optimize the sensitivity of the sensor and to increment the interrogation distance, more tests will be performed, based on different methods used to interrogate resonant circuits available [157-160].

5.5 Smart sensing

In order to exploit the smart sensing ability of the SPES five different setups were conceived for each individual sensing function: temperature sensing, humidity sensing, damage detection, anti/de-icing, structural change detection. All tests were performed using an AGILENT N9913A 4 GHz FieldFox Handheld RF Combination Analyzer.

5.5.1 Temperature Sensing

To measure temperature gradients, the electric field of the SPES must penetrate a material whose dielectric changes with temperature. As the temperature increases, the dimensions of the copper trace and the dielectric of the polyimide substrate change, affecting the sensor capacitance and inductance, consequently the resonant response of the sensor are modulated by the temperature. The characterization of the wireless passive temperature sensor was tested placing the sensor within a humidity chamber keeping the humidity fixed and changing the temperature. The resonant response parameters have been collected after different intervals of time in order to establish the time of response of the sensor to a temperature gradient. The

SPES device was activated wirelessly using a loop antenna of 100 mm diameter connected to the spectrum analyser placed at 100 mm of distance from the device. The setup is illustrated in Figure 177.

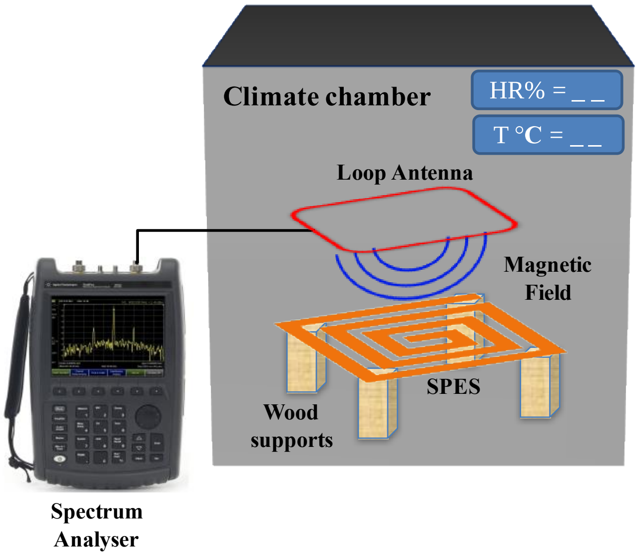

Figure 177 Temperature and Humidity sensing setup

The first test was conducted keeping the relative humidity constant at 40% and temperature at 25 degrees for 72 hours. The response recorded has been set as a starting point, assuming that the response of the sensor will not change after 72 hours. The temperature has been increased up to 50 degrees, keeping the humidity constant at 40%. The response of the sensor has been collected once the climate chamber has reached the desired temperature of 50 degrees, and recorded as time zero for the set temperature. Successive data have been recorded after 2, 5, 10, 15, 25, 30 minutes respectively, in order to monitor the sensor resonant frequency over different time intervals (see Figure 178).

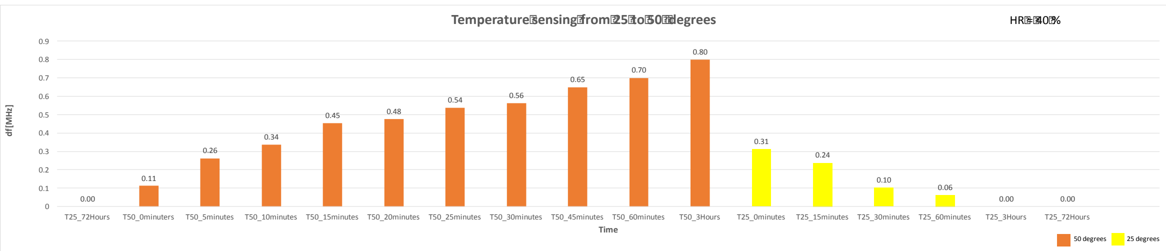

Figure 178 Temperature sensing from 25 to 50 degrees keeping the humidity constant at 40%. - Plot showing the shift in resonant frequency recorded at different temperatures for different time intervals.

If we consider the resonant frequency of the sensor after 72 hours, at the same value of humidity and temperature, as its correct value, we can set this number as 100% and see how much time the sensor requires to reach that value in terms of percentage starting from the value at the time zero. The shift in resonant frequency of the sensor at 50 degrees after 15 minutes (0.45 MHz) is already higher than the resonance shift at 25 degrees at the time zero (0.31 MHz). Therefore, it is possible to conclude from the first test that for the set parameters of humidity and temperature that the sensor requires at least 15 minutes in order to detect a drop or an increase in temperature and around 30 minutes to detect the exact resonance frequency correlated to the set temperature. More precisely, the correct value of resonance frequency is reached after three hours, although as shown in the graph below after 30 minutes the sensor reached almost 99% of its final value for an increase in temperature from 25 to 50 and almost 100.5% for a decrease from 50 to 25.

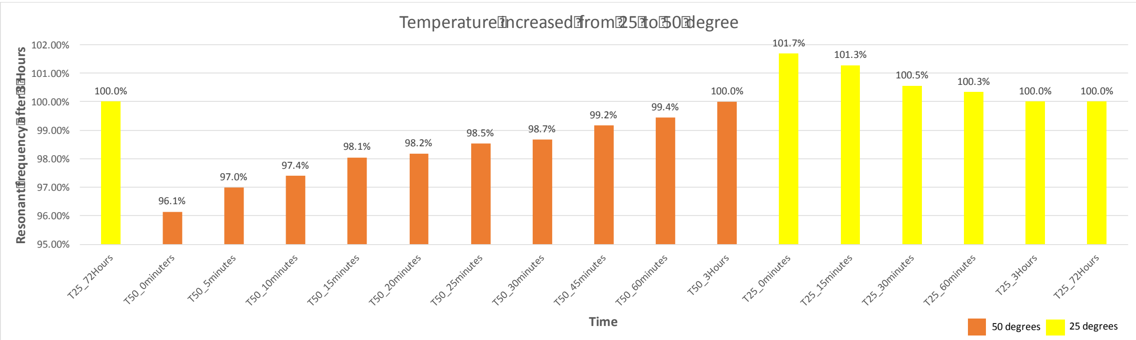

Figure 179 Temperature sensing from 25 to 50 degrees keeping the humidity constant at 40%.

A second test was performed raising the temperature from 20 to 65 degrees and keeping the relative humidity constant at 70 %. The sensor responses have been kept at the desired temperature for 30 minutes and the response registered after 2, 5, 10, 15, 25, 30 minutes respectively in order to get the response time at different external conditions. For clarity, we have reported in Figure 181 only the value of the resonant frequency after 30 minutes. The difference in resonant frequency between the previous temperature and the subsequent is not linear in the range tested and decreases as the temperature rises, although it is still possible to detect an increment of temperature with an increase of the resonant frequency shift.

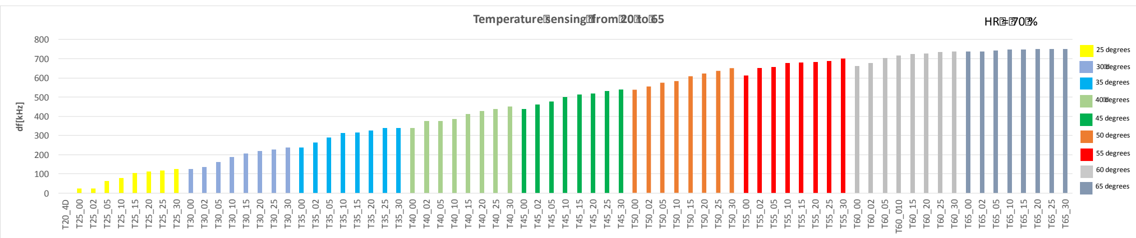

Figure 180 Temperature sensing from 20 to 65 degrees keeping the humidity constant at 70%.

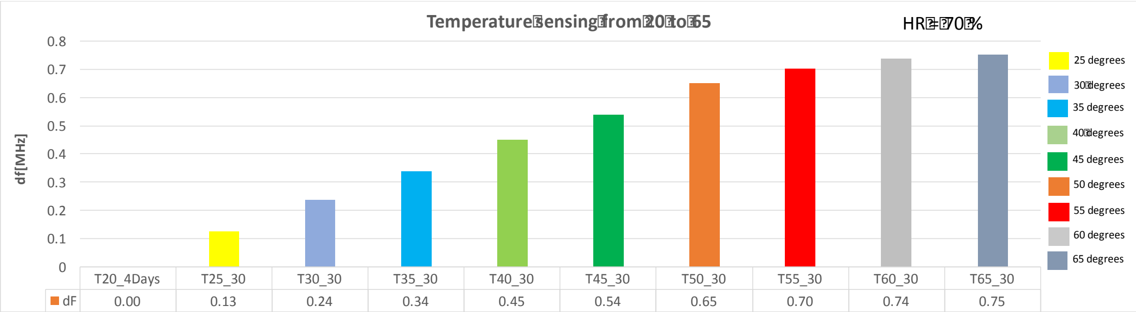

Figure 181 Temperature sensing from 20 to 65 degrees keeping the humidity constant at 70%.

As for the previous test we have measured the response of the sensor in percentage considering for this test the final value after 30 minutes at the set temperature (see Figure 182).

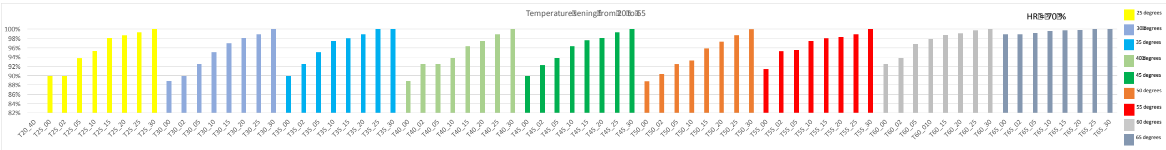

Figure 182 Temperature sensing from 20 to 65 degrees keeping the humidity constant at 70%.

From Figure 182 it is possible to conclude that the sensor requires the first 10 minutes to settle. Indeed, after 15 minutes the sensor reaches almost the 98% of the value at 30 minutes for all the temperature range analysed.

5.5.2 Humidity Sensing

Humidity monitoring is strictly related to the material used as substrate. Indeed, humidity variation does not affect the inductance of the sensor. In order to monitor humidity variation, as for the temperature sensing, the electric field of the SPES must penetrate a material whose dielectric is affected by humidity variations. As reported by Melcher et al. the polyimide absorbs water content changing its dielectric properties [229]. Indeed, the SPES device manufactured on a polyimide substrate shows the ability to monitor humidity variation. The device makes use of the coil interwinding capacitance (C_{int}) and substrate distributed capacitance (C_{dis}) as shown in the Figure 183. Moisture absorbed by the polyimide substrate causes a hydrolysis effect, which breaks the polyimide's internal carbon–nitrogen bonds. This alters the internal electrical polarization[230], which affects the permittivity of the polyimide. Therefore altering the distributed capacitance causing a shift in the resonant frequency.

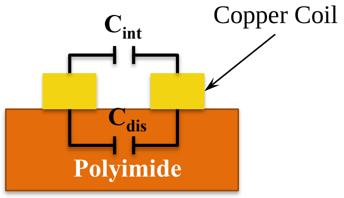

Figure 183 Schematic representation of the capacitance in the equivalent circuit of the senor for the humidity sensing.

The characterization of the humidity responses was carried out placing the SPES within the same climate chamber used for the previous test. The temperature was set at 28 degrees and the humidity raised from 35% to 70% and the data recorded once the climate chamber has reached the desired value of relative humidity, and recorded as time 0 and a successive value was recorded after 30 minutes. For the first measure the sample was kept at fixed temperature and humidity, HR 35% and 28 degrees, for 2 days. Only for the last value, the data were collected after 2 hours in order to monitor the sensor response on a longer time of exposure.

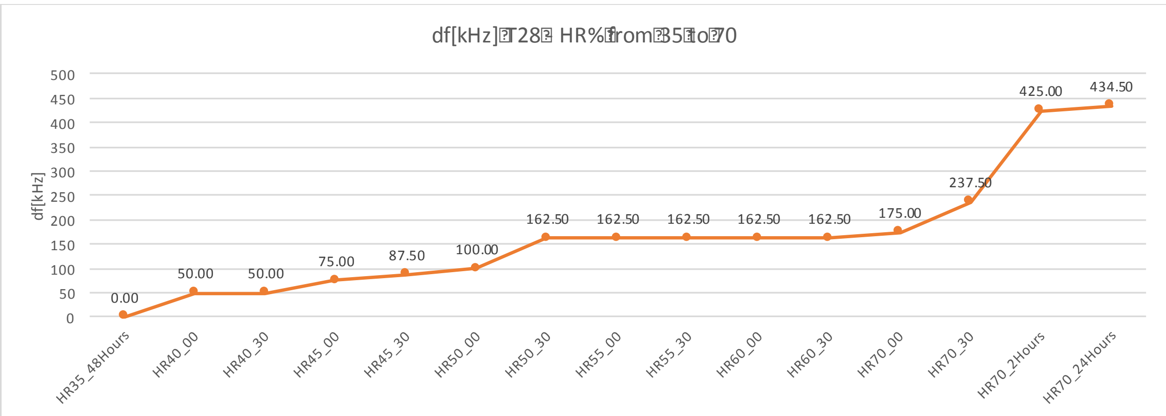

Figure 184 Humidity sensitivity of the SPES in a closed climate chamber - Plot showing the relative humidity vs. shift in resonant frequency using the sensor on polyimide substrate

From the graph above it is possible to conclude that although the resonant frequency of the sensor decreases as the humidity increase the trend is not linear and in particular as it is possible to see from the data collected at 70 HR%, the sensor requires more than an hour to detect the exact response, explaining also the nonlinear behaviour of the sensors. This behaviour can be correlated to the small environment in which the sensor was tested, and in which the flow of the air and hence the chemical interaction with the polyimide substrate of the sensor require more time to be completed. In order to confirm this hypothesis a second test was conducted in a larger environment. The sensor was tested within a Climate-Zone system (CTS Europe, Portsmouth, UK) with the air temperature kept constant at 19.0 ±0.5℃ and the humidity increased from 30% to 80% RH then decreased back to 30% RH. Increments of 10% and measurements are taken waiting five minutes once the chamber has reached the requested humidity, and before decreasing the humidity the sensor has been kept constant for 30 minutes at the humidity of 80%. The SPES device was activated wirelessly using a loop antenna of 100 mm diameter connected to the spectrum analyser placed at 55 mm of distance from the device. The setups are illustrated in the figures below.

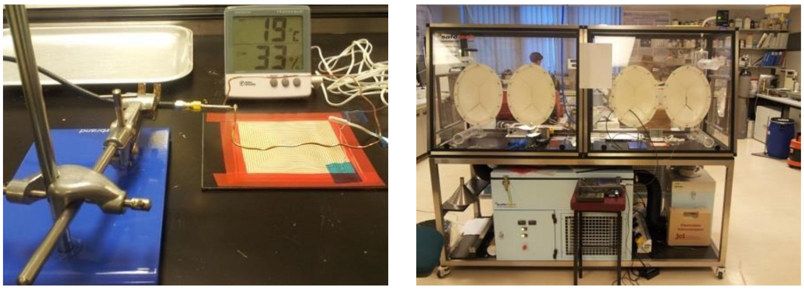

SPES on polyimide layer Humidity Chamber

Figure 185 Humidity Sensing Setup

Figure 186 presents the measured resonant frequency shift as a function of humidity range from 30 to 80 %H.R. As humidity increases, the overall dielectric constant of the polyimide increase and the resonant frequency of the sensor shifts to higher frequencies. In the whole test humidity range, resonant frequency changed about ~118 kHz, which means the sensitivity of the SPES is about ~2.3 kHz /%H.R.

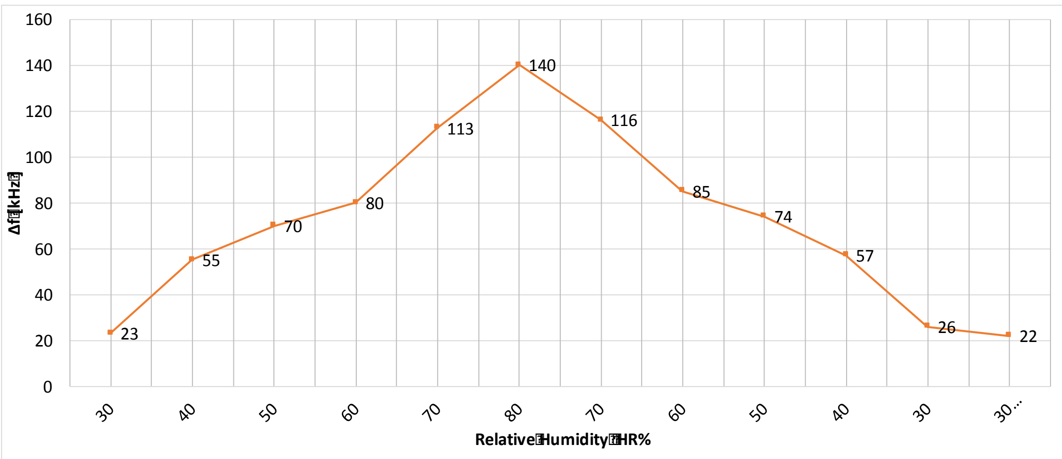

Figure 186 Humidity sensitivity of the SPES in an open climate chamber - Plot showing the relative humidity vs. shift in resonant frequency using the sensor on polyimide substrate

Moreover Figure 186 illustrates how by the polyimide layer required more time to detect a decrease in humidity respect to an increase the humidity absorption. Indeed, the shift of resonant frequency is slightly higher for the same relative humidity recorded previously increasing the humidity from 30 to 80 %. The same behaviour was observed when the sensor was placed at 30% HR and the data were collected 24 hours later. The resonant frequency shift at 30% of relative humidity after one day was close to the value collected at the beginning of the experiment (Δf of 23kHz).

5.5.3 Damage detection

The capability of the sensor to monitor damage was proved on laminated samples. In particular, composite structures can suffer from barely visible impact damage (BVID) [231, 232] caused by low-velocity impacts (energy level of 10–30 J) such as tool drops, bird strikes and hailstones[233, 234] that can cause a loss in structural integrity and it is a big challenge to detect the associated delamination or cracks. In order to determine the presence of damage inside the samples, and to ensure the repeatability of the experiments, the following experimental procedure was followed. Eight samples were manufactured in a single batch using VARTM (Vacuum assisted resin transfer moulding) process. Seven 'Triax' fabrics (+45°/90°/-45°) of 600gsm and one plain weave dry carbon fabric by Sigmatex were infused using an epoxy resin by Sika. The plate obtained from the infusion was cut using a diamond-coated disk on a table saw with guides, obtaining eight coupons. The resulting coupons were 150mm x 100mm with a thickness of 5.50 mm (with a standard deviation of 0.32 mm). After ensuring that all samples present the same resonant frequency, the coupons had to be damaged by means of a controlled manner. For this reason a low-velocity drop weight impact rig was used to induce damage to the laminates. Five different impacts were performed at different energies: 10, 20, 25, 30, 35 Joules respectively, leaving three intact samples as reference.

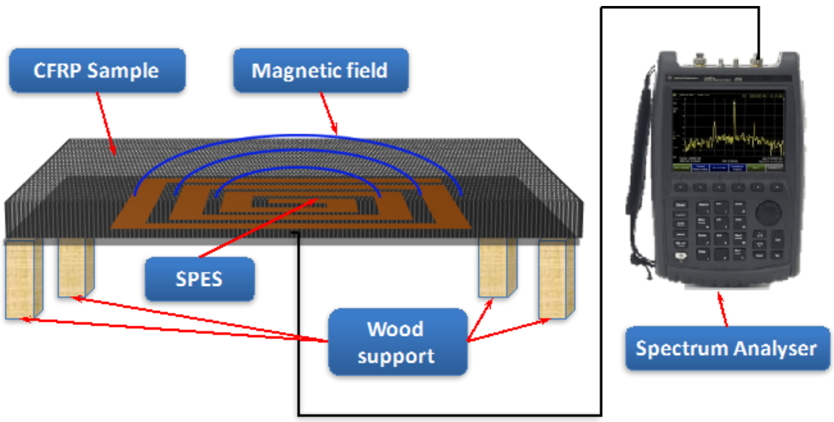

Figure 187 Interrogation Setup

The sensor was placed on the non-damaged side of the samples and the resonant frequency was reported and compared with the undamaged samples. The same sensor was used for all the samples, and in order to ensure a good adhesion to the sample and a repeatable measurement, the SPES device was fixed on a 1 mm polyethylene layer, ensuring a better and more uniform coupling between the antenna and the sensor (as illustrated in Figure 185a). To avoid interference, the SPES was placed at 4 cm from the ground. Figure 188 reports the resonant frequency for the different impacted samples, where the reference is the undamaged sample and the sensor represents the resonant frequency of the SPES in free air.

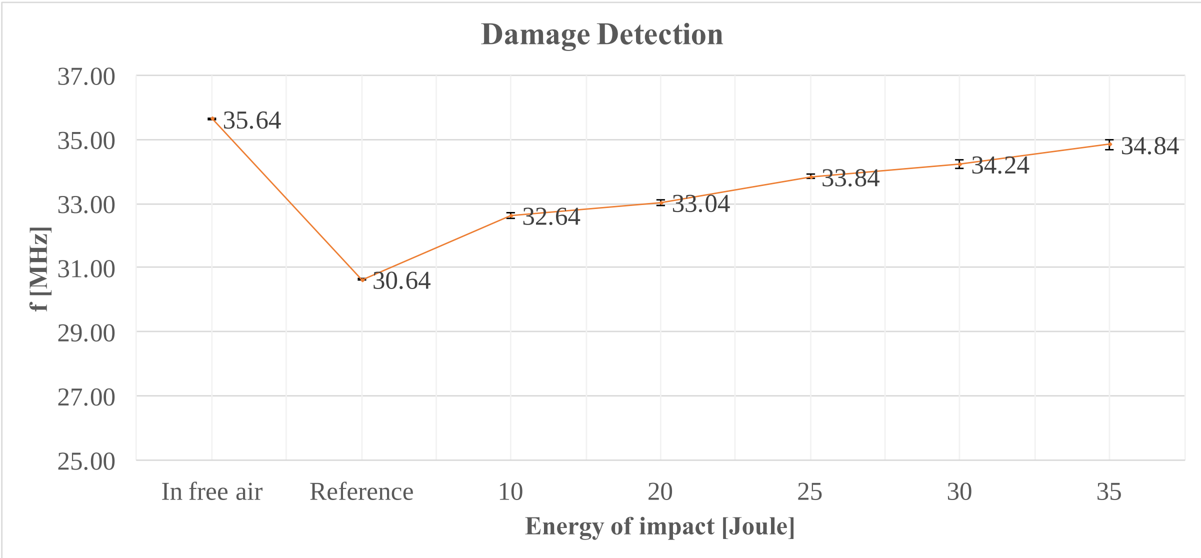

Figure 188 Comparison of resonant frequency for CFRP samples tested with different impact energy.

In the whole test, resonant frequency changed about 4.20 MHz, between the damaged (35J) and the undamaged one (Reference sample), which means the sensitivity of the SPES is almost ~0.12 MHz /Joule. The response of the sensor is repeatable, with a maximum standard deviation of ~0.15 MHz for the sample impacted at 35 J. The impacted samples were also investigated using the ultrasonic C-scan to have a comparative NDT technique (Figure 170a).

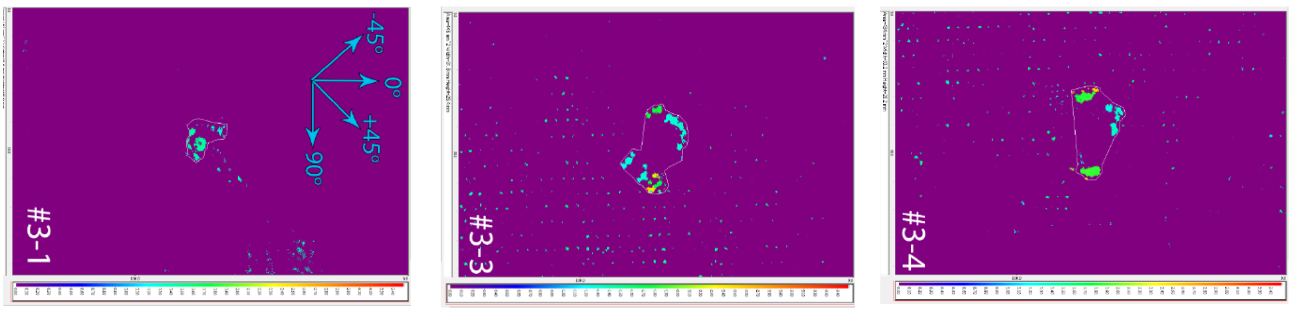

a) Sample Impacted at 10 Joule b) Sample Impacted at 20 Joule c) Sample Impacted at 25 Joule

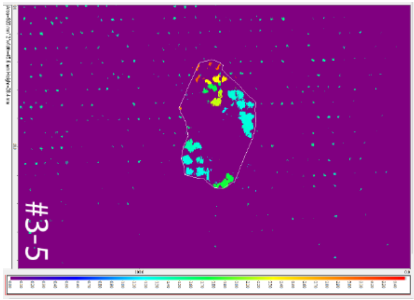

d) Sample Impacted at 30 Joule

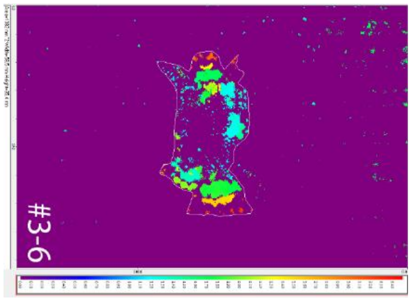

e) Sample Impacted at 35 Joule

Figure 189 Ultrasonic C-scan from the top surface (non damaged side): a) sample impacted with 10 J; b) sample impacted with 20J; c) sample impacted with 25 J; d) sample impacted with 30J; e) sample impacted with 35J.

5.5.4 De-icing and Anti-icing function

Due to its intrinsic nature, the SPES device has shown interesting properties that can be exploited for both de-icing and anti-icing applications. The SPES device can detect icing conditions, in particular, the presence of an ice layer can be detected with a shift of the resonant frequency due to change in the permittivity of the layer over the sensor, based on the higher dielectric constant of ice among the air [235]. Moreover, the SPES surface mounted or embedded within the composite structure can be used to rapidly increase the temperature of specific parts of the structure. Thus, the SPES device can be activated only in the critical parts of the aircraft to prevent icing conditions or where ice has been detected.

Figure 190 shows the setup for test the anti-icing/de-icing properties. The SPES device on polyimide layer was wired with crocodile pins at both ends of the conductive trace to a power supply.

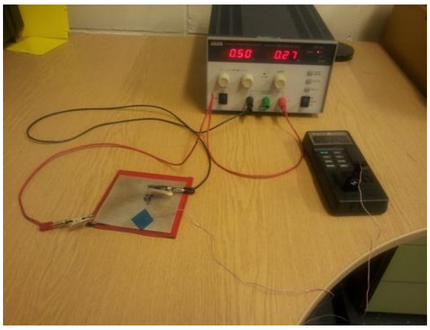

Figure 190 Anti-icing/De-icing setup

The test was conducted applying increasing values of voltages to the sensor. The graph in Figure 191 represents the evolution in time of the temperature recorded by the thermocouple attached on the copper trace of the SPES. The temperature measures were monitored at three different times: at the beginning of the test (t=0 min), after one minute (t=1 min), and after two minutes (t=2 min). The temperature was raised from room temperature up to almost 100℃ with a maximum voltage of 5.25 Volt.

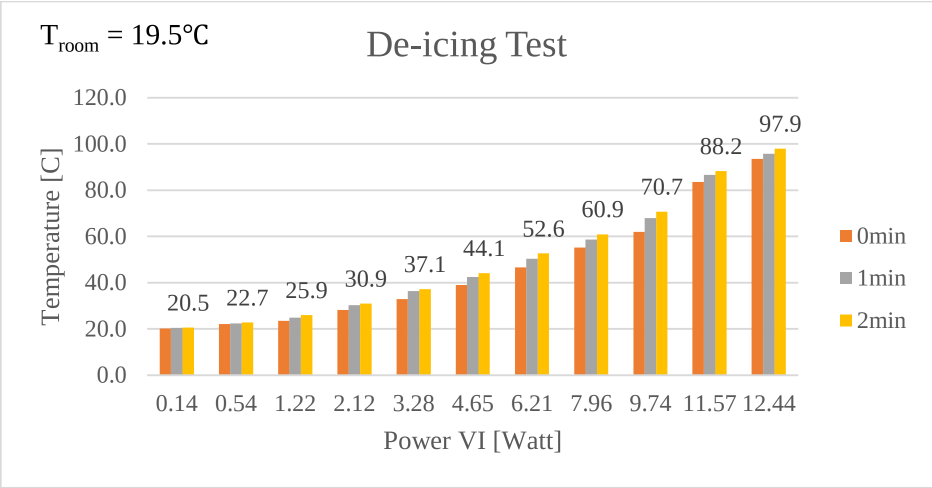

Figure 191 De-icing Test 1

In conclusion, results from the tests clearly show that SPES is very promising for both anti-icing and de-icing applications. Ice formation usually occurs when the static air temperature (SAT) is between -20 and +2℃, therefore a maximum increase in temperature of about ~25℃ is enough to melt the ice on the top surface of a structural component.

Tests performed at room temperature have shown that a temperature increase of 25℃ can be achieved when 3V are applied to the SPES, with a power consumption of ~5W (de-icing). Instead, icing conditions can be avoided using a power as low as ~0.5W (anti-icing). Since SPES temperature increase can show non-linear behaviour towards ambient temperature further measurements at ambient temperature as low as -20C need to be performed to confirm the data. It is important to underline that the SPES device can achieve a higher value of temperature adjusting the time window of the current excitation (see Figure 192). In this manner, the system can be optimized according to the external environmental conditions.

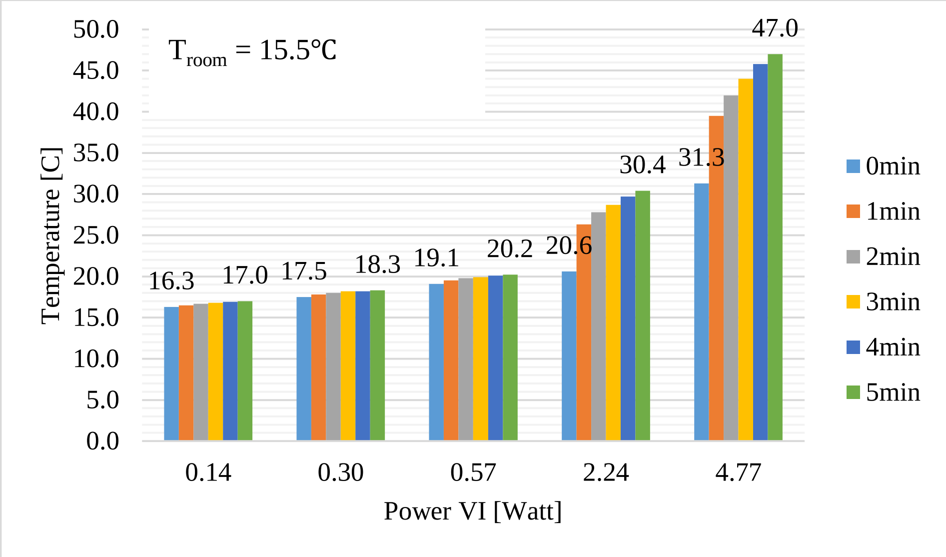

Figure 192 De-icing Test 2

5.5.5 Structural change detection and sensors' network

The SPES can identify and localize the presence of external structural variation simulated by the presence of excess material in the proximity of the sensor. Moreover, having more sensors close to each other by illuminating only one sensor, the signal response detects the presence and the position of sensors in the proximity. Three different sensor designs (K3, K6 and K10) were tested and embedded within glass fibre composite samples. Sensors' parameters are reported in the table below:

Table 20 Sensor's characteristics

Sensor label	Number of turns	Trace width [mm]	Total width of the sensor [mm]
K10	24	2	104.24
K6	13	2	63.6
K3	20	0.5	32.9

All the sensors were manufactured by etching process, having 75um of polyimide as a substrate and 35um of copper for the conductive pattern. In order to activate the sensor an external loop antenna having similar shape and dimensions has been connected to a spectrum analyser working as an absorption wave meter. In particular, two different square loop antennas were used, a 5 cm loop antenna for the K3 and K6 sensors, and a 12 cm antenna for the K10 sensor. The interrogating antenna was connected to the spectrum analyser that illuminated the sensor under test with a broadband frequency swept electromagnetic field from 10 to 70 MHz (the range was chosen in accordance to the geometrical design of the sensor). Based on the capacity of the resonant structures to act as antenna when illuminated by magnetic field, it is possible to determine the self-resonance parameters of the SPES.

For samples A and B two sensors were placed close to each other, while for sample C three K10 sensors were embedded aligned along the main length of the sample keeping the distance from the edge constant (70 mm). A representation of the number of sensors embedded within the sample and their location is reported in Figure 193.

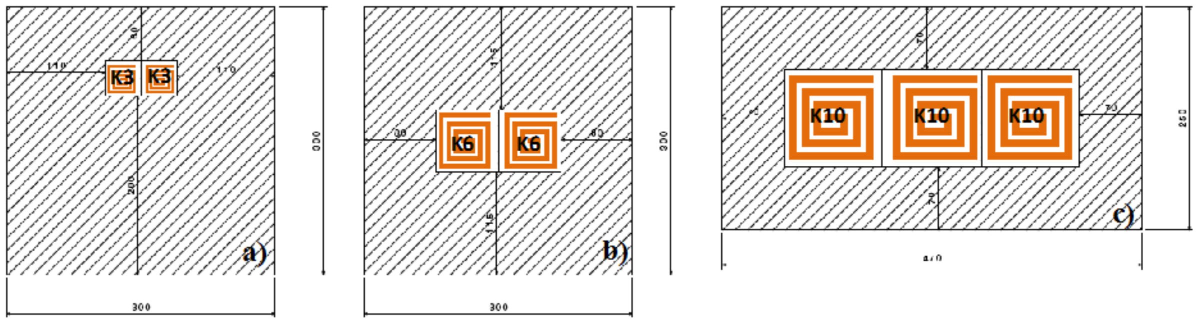

Figure 193 Location of the sensor within composite panels a) Sample A, b) Sample B, c) Sample C (all dimensions are in [mm]

All sensors were tested embedded within glass fibre composite structures. A standard hand lay-up and vacuum bagging process was used for manufacturing the samples. The basic layer employed for the fabrication of the laminates in the work was a glass fibre (type E) epoxy prepreg with fabric reinforcement (RP502) supplied by © Plastic Reinforcement Fabrics. Samples were cured according to the manufacturer's recommended cure cycle (5 degrees for minute up to 115 degrees, held for two hours then cooled inside the autoclave). The temperature and pressure cycle used in the autoclave for curing the specimens was per the manufacturer's material data sheet. Three sixteen-ply composite specimens with SPES sensors embedded between the fifteenth and sixteenth plies were manufactured. Experimental Configuration

All the sensors were tested before being embedded within the composite and resonant parameters (resonant frequency (f_r), amplitude and bandwidths evaluated at half height of the resonant frequency peak) recorded in Table 21. In order to avoid the error correlated to the setup environment, the system was dismantled and remounted before each measurement; three measurements for each sensor were recorded. Comparing the standard deviation error, it is possible to understand which parameters are more reliable. Over the three resonant parameters chosen, the resonance frequency and the amplitude were the values that showed a small standard deviation over the three measurements, so they were chosen as principal parameters of investigation. Due to the slenderness of the sensor, the sensor was fixed on a wood table while the distance between the sensor and the antenna was kept constant at 30 mm using external stand clamps, as reported in Figure 194. The effect of multiple sensors was tested placing the sensors close to each other having the antenna facing always the same sensor. As reported in Table 22, four configurations were tested for K10 sensor. In the first measurement, the sensor was left alone (K10-SingleSetup), when a second sensor of the same dimension was placed on the right side of the sensor (K10-OneRight) a decrease for both resonant frequency and amplitude occurred. Instead placing a second sensor on the left side (K10-OneLeft) the resonant frequency increased while the amplitude value decreased reaching a similar value to the previous configuration. As reported in the previous section, the Spectrum Analyser was used to detect the incident radiofrequencies (RF) absorbed by the structure. So, placing more sensors in the proximity causes a spread of the energy that is detected as a decrease in amplitude. Moreover, if the energy absorbed by the nearest sensor is enough to activate the resonant modes, the sensor will respond to the radiofrequency energy with its own resonant frequency. This will be shown in the spectrum trace as a shift of the resonant frequency or with the appearance of another peak on the same trace. To have a better understanding of the influence of multiple sensors, analysing the resonant parameters can lead to erroneous results. Indeed, the presence of a second sensor put in proximity of the first sensor can cause a shift in the resonant frequency as well as a bump in the signal trace revealing the direction in which the second sensor is placed (see Figure 195), or as a unique trace done by the interaction of the individual signal. According to how the resonant modes of the closest SPES interact between each other, the spectrum trace will be modified. For this reason, a visual inspection of the spectrum trace is advised.

The schematic of the different system configurations used for this study are shown in Figure 196. The probe connected to the spectrum analyser is positioned on top of the sensor under test. The capability of the sensor to monitor structural changes was proved positioning a 5cm square sample, named simulated change, having a thickness of 2.7 mm with the same properties of the laminated sample in the proximity of the SPES. The “simulated change” was moved while keeping the position of the antenna fixed on one of the sensors.

Configuration number one was studied following the same setup illustrated in Figure 194, while for configuration number 2 the sample was tested facing the layer with the SPES sensor embedded upwards. In configuration number 3 the antenna was placed beneath the sample facing directly the SPES while the simulated changes were placed on the opposite side of the sample. For all configurations, the distance from the loop antenna and the laminated sample was kept constant at 30 mm using an external stand clamp. In order to reduce interferences, the glass fibre sample was positioned at 50 mm from the ground through wood supports (see Figure 196).

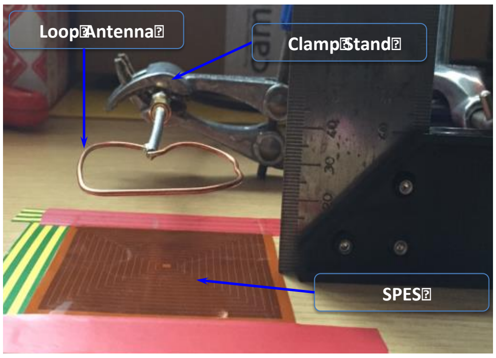

Figure 194 Sensor interrogation setup

Table 21 Sensor resonant parameters

Sensor label		**Resonant parameters**		
		Amplitude [dB]	**f [MHz]**	**Bandwidth**
K3	Average Value	1.37	57.05	164.97
	Standard deviation	0.09	0.08	17.66
K6	Average Value	2.15	45.28	79.65
	Standard deviation	0.03	0.06	0.84
K10	Average Value	7.99	17.29	21.61
	Standard deviation	0.50	0.10	1.15

Table 22 Sensor resonant parameters for multiple sensors configuration.

Sensor label	**Resonant parameters**		
	Amplitude [dB]	**f_r[MHz]**	**Bandwidths**
K10-SingleSetup	7.99	17.29	21.61
K10-OneRight	5.55	17.00	110.11
K10-OneLeft	5.57	17.41	110.38
K10-onBothSides (1st peak)	4.45	16.81	84.08
K10-onBothSides (2st peak)	4.08	17.58	62.16

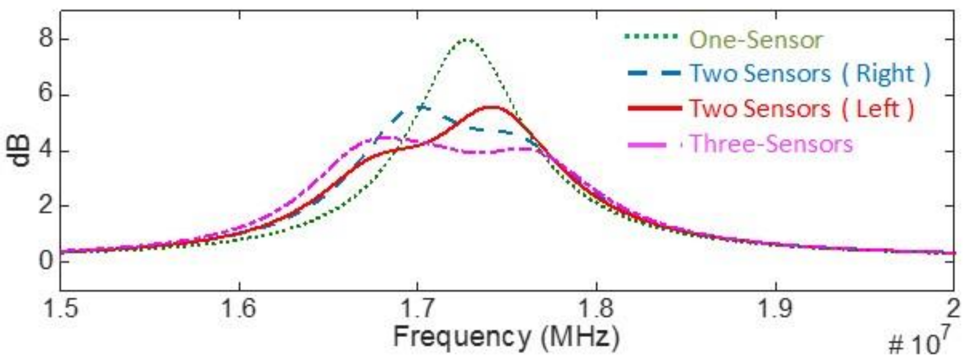

Figure 195 Sensors Spectrum Traces for multiple sensors configuration

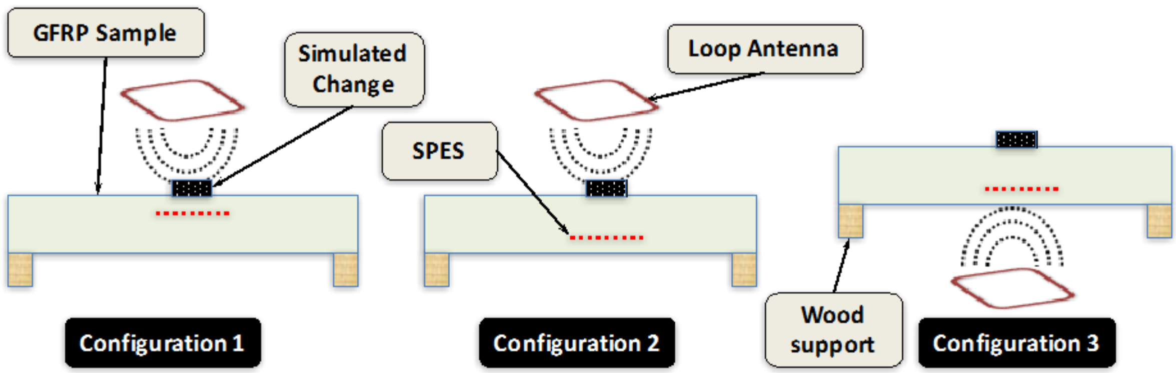

Figure 196 loop antenna powering and interrogating a SPES sensor in three different configurations.

5.5.5.1 Double sensors setup for K3 sensors (sample A)

Structural change monitoring of Sample A with two K3 sensors embedded was carried out using the configuration 1. The simulated change was moved in seven different positions, as illustrated in Figure 197, and a resonant frequency value recorded and compared with the reference value (resonant frequency of the embedded sensor). The loop antenna was placed upon the left sensor and resonant frequency recorded for all positions. A second test was repeated placing the antenna on the right sensor.

The simulated change, being made of fibre glass acts as dielectric, causing an increase in the capacitance of the system and accordingly to the formula 1) a decrease of the resonant frequency. Being the total capacitance a combination of the interaction between adjacent turns it is possible to localise the presence of structural changes by the comparison of the resonant frequency respect to the reference value. Indeed, as reported in the histograms below, where the Δf (given by formula (2) is plotted against the simulated change location, the resonant frequency changes as the simulated change was moved across the sample. Looking at the variation of the spectrum trace as the simulated-change moves across the sensor, the first peak decreases while second peak increases, for the configuration with the antenna on the left sensor.

The opposite trend is shown for the setup with the antenna on the right sensor. This leads to the possibility to localise on which position the structural change is located.

$$\Delta f = f_{reference} - f_{position} \tag{37}$$

It is interesting to note, that the sensor recognizes the presence of the simulated-change only when it overlaps at least part of the conductive trace of the SPES (see Figure 197). The shift of the resonance frequency has its maximum when the simulated structural change covers the centre of the nearby sensor. When the antenna is placed on the left sensor the maximum shift in resonant frequency is reached in position 7. This can be explained bearing in mind that the spectrum trace is given by the interaction of more than one resonant mode, and the second sensor results more sensitive to the presence of variation in the nearest area. A similar trend is shown for the antenna placed on the right sensor, having its maximum in position 3.

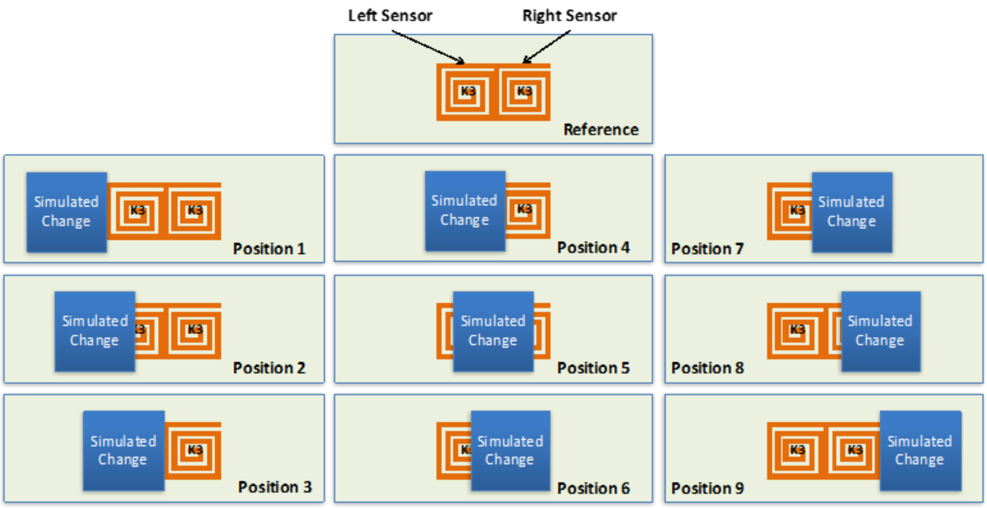

Figure 197 Simulated change positions for Sample A

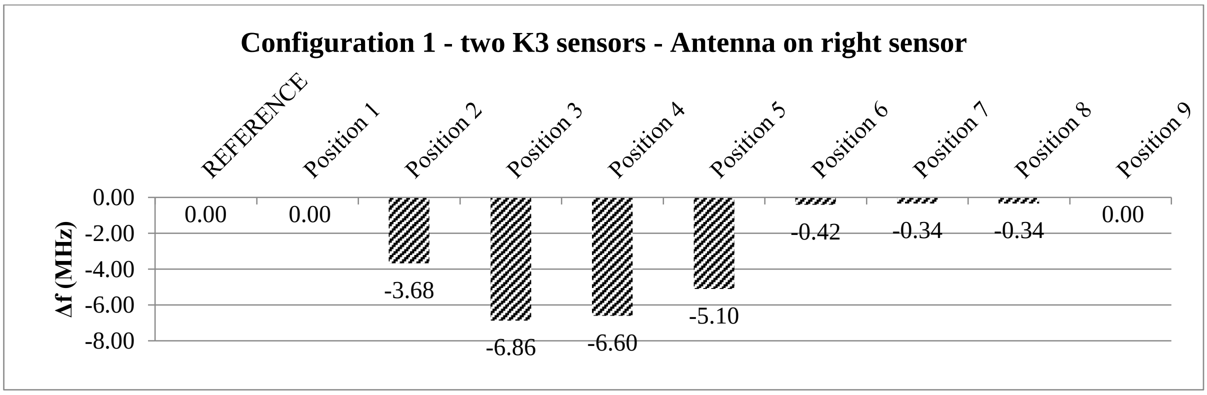

Figure 198 Δf for Configuration 1 - two K3 sensors - Antenna on right sensor

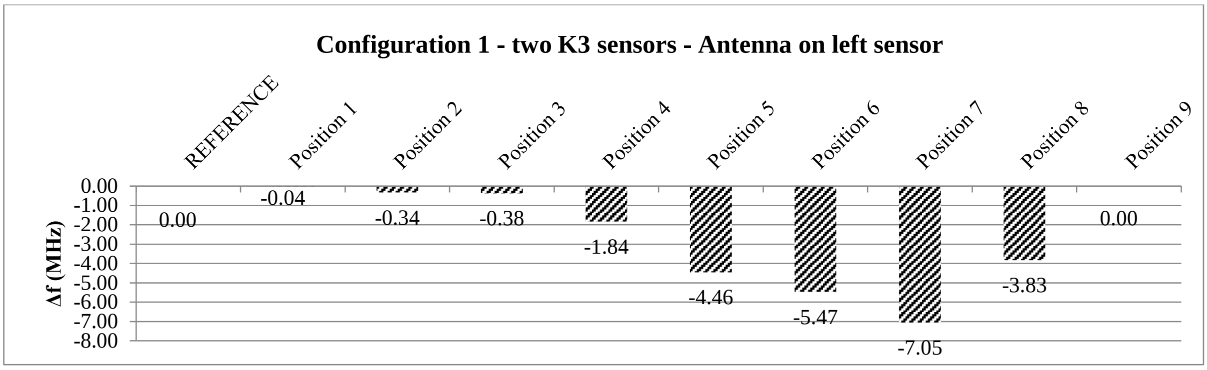

Figure 199 Δf for Configuration 1 - two K3 sensors - Antenna on left sensor

5.5.5.2 Double sensors setup for K6 sensors (sample B)

Monitoring of structural changes of Sample B with two K6 sensors embedded were carried out using the same setup adopted for K3 sensors (Configuration 1). The same simulated-change sample was used to check how different sensors respond to the same variation. The dimension of the simulated change was chosen in order to be bigger than the K3 sensor and smaller than the K6. Being that the sensor K6 is bigger than the K3, the number of different positions was increased from 9 to 11 (see Figure 200). Resonant frequencies for each sample position were recorded for the loop antenna placed on the right sensor firstly and secondly on the left one. For the K6 setup, the two sensors cause the presence of two peaks in the spectrum trace. Resonant frequencies of both peaks are reported in Figure 202 Figure 205.

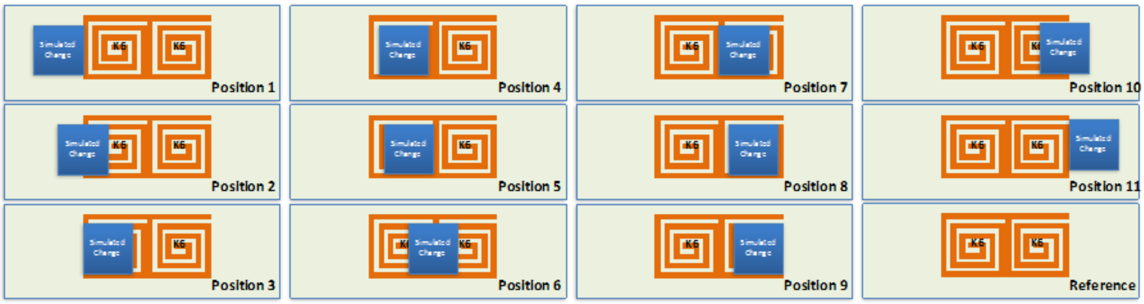

Figure 200 Simulated change positions for Sample B

As for the K3 sensors setup, a shift in the resonant frequency occurs as the structural change is on the SPES sensor. Analysing only the resonant frequency shift appears as simulated-change causing the same shift when it covers the left sensor or the right one. Instead, looking at the variation of the amplitude, for the setup with the antenna on the left sensor, the first peak decreases while the second peak increases as the simulated-change moves across the left sensor, while the first peak increases and the second decreases when the simulated structural change is on the right sensor (see Figure 202). The opposite trend is shown for the setup with the antenna on the right sensor (see Figure 205). This leads to the possibility to localize on which zone positions the structural change is located.

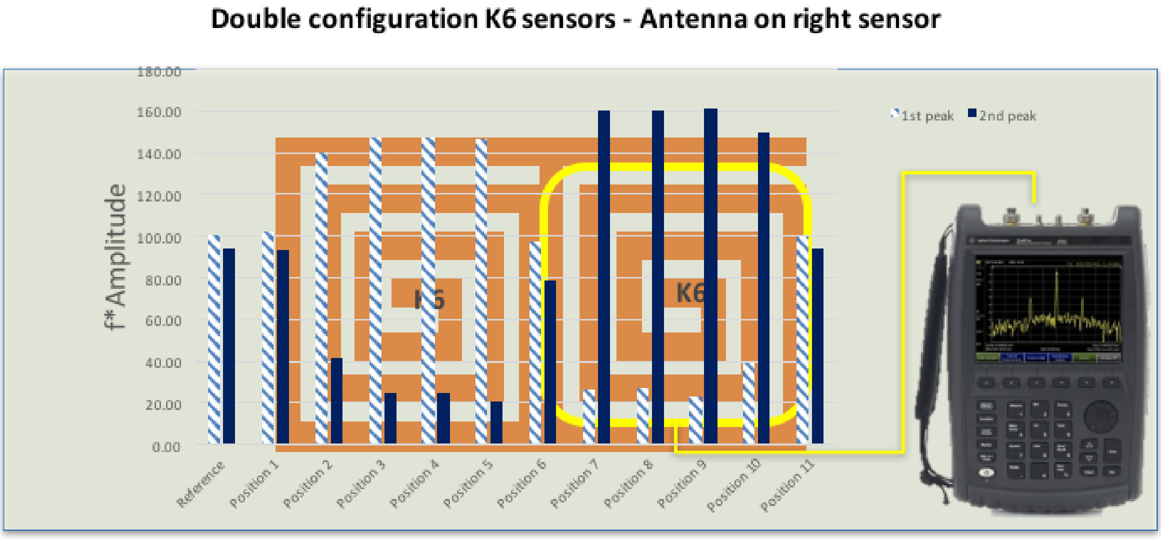

Figure 201 Frequency trend for Configuration 1 - two K6 sensors - Antenna on right sensor

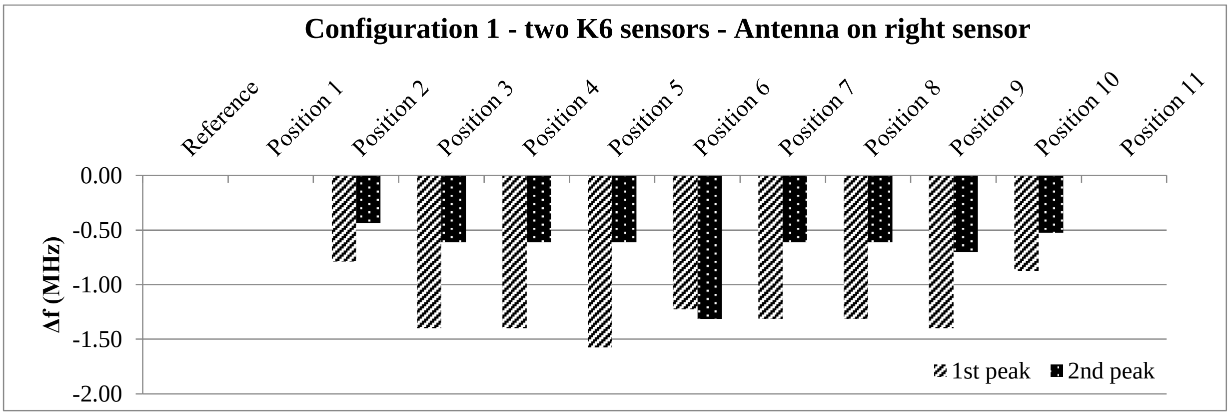

Figure 202 Δf for Configuration 1 - two K6 sensors - Antenna on right sensor

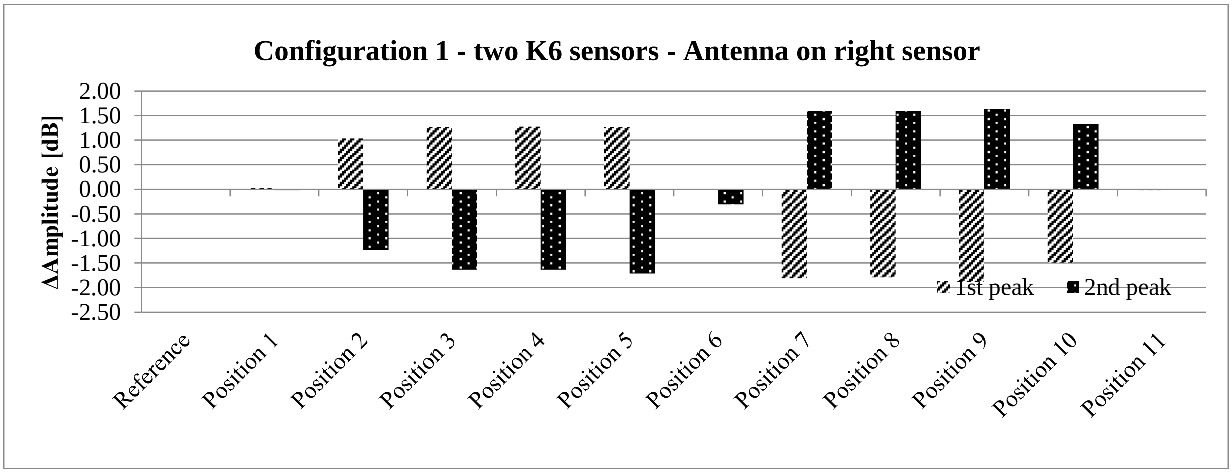

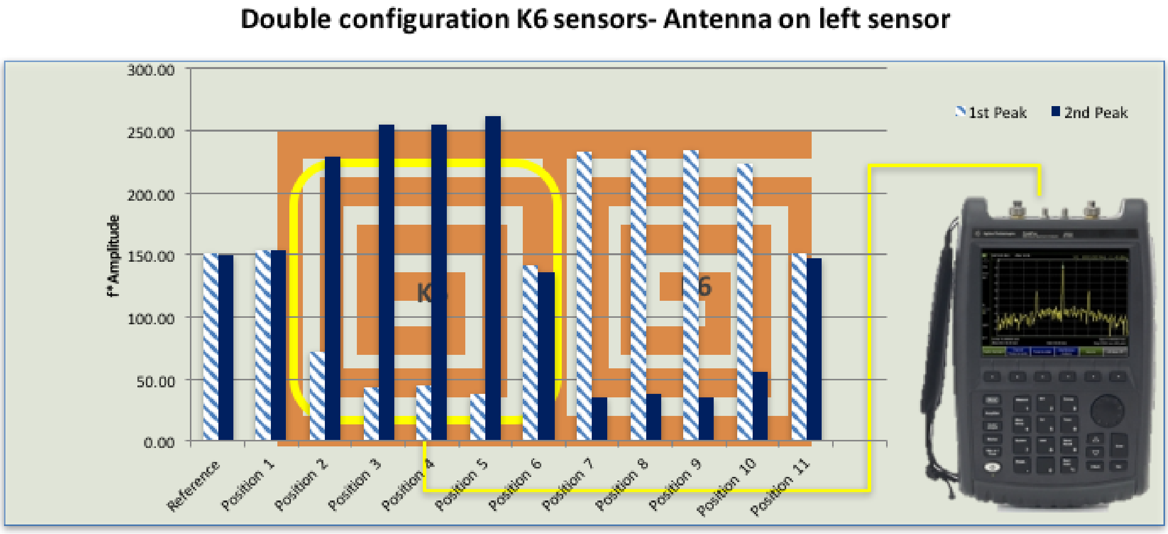

Figure 203 Frequency trend for Configuration 1 - two K6 sensors - Antenna on left sensor

Figure 204 ΔAmplitude for Configuration 1 - two K6 sensors - Antenna on right sensor

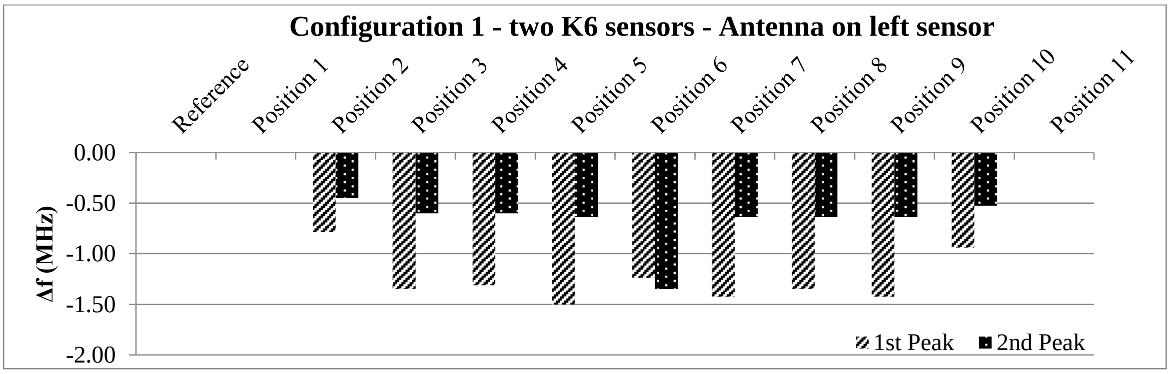

Figure 205 Δf for Configuration 1 - two K6 sensors - Antenna on left sensor

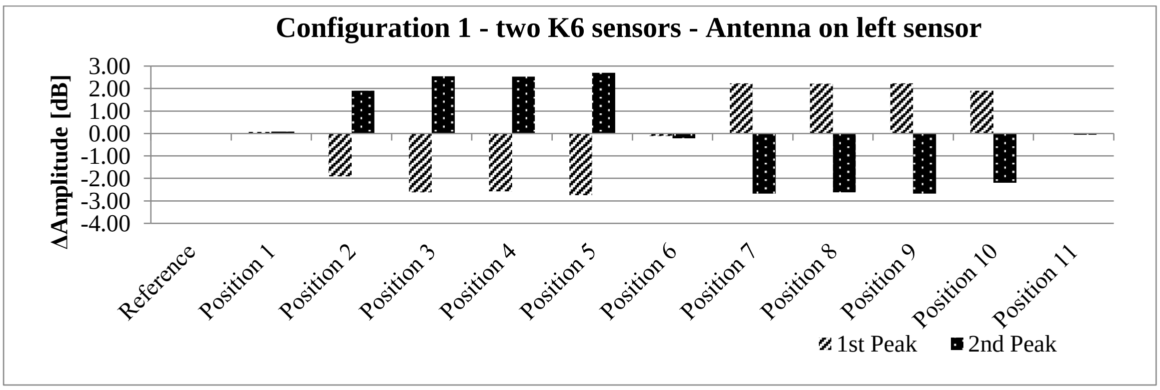

Figure 206 ΔAmplitude for Configuration 1 - two K6 sensors - Antenna on left sensor

5.5.5.3 Triple sensors setup for K10 sensors (sample C)

Monitoring of changes of sample C with three K10 sensors embedded were carried out using the three different configurations reported in Figure 196. For the K10 setup, the three sensors cause the presence of three peaks in the spectrum trace. Resonant frequencies for each sample position were recorded for the loop antenna placed on the middle sensor.

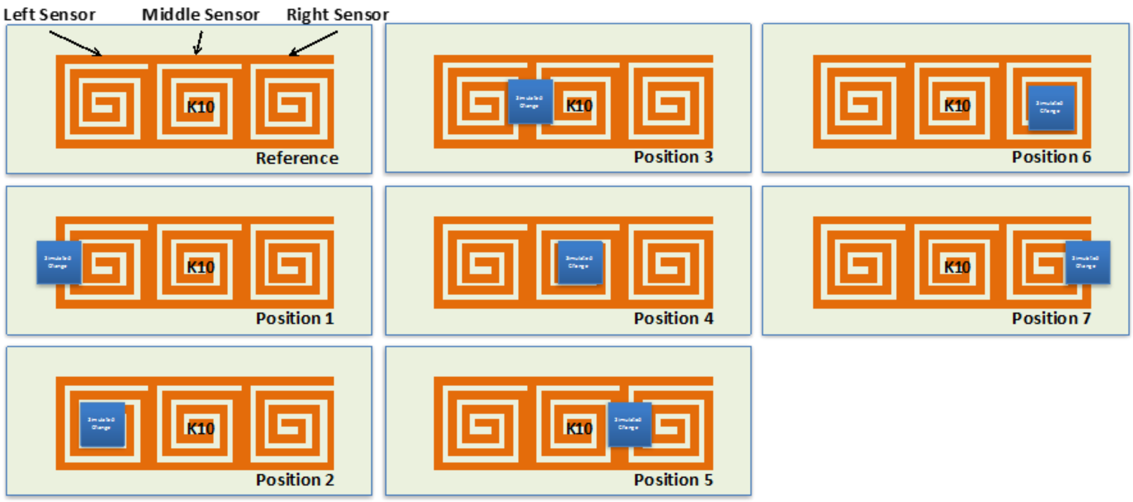

Figure 207 Simulated change positions for Sample C

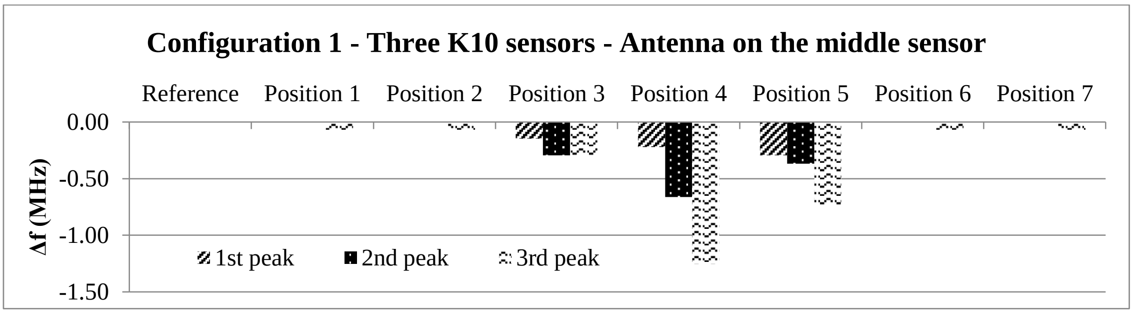

Figure 208 Δf (MHz) for Configuration 1 - Three K10 sensors - Antenna on the middle sensor

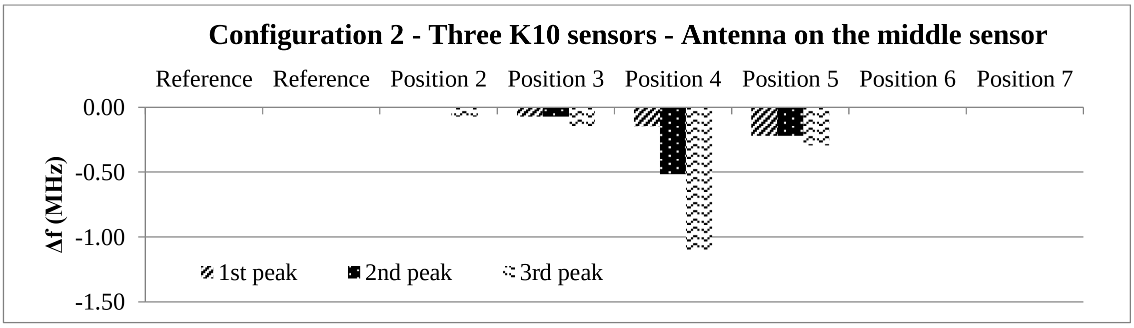

Figure 209 Δf (MHz) for Configuration 2 - Three K10 sensors - Antenna on the middle sensor

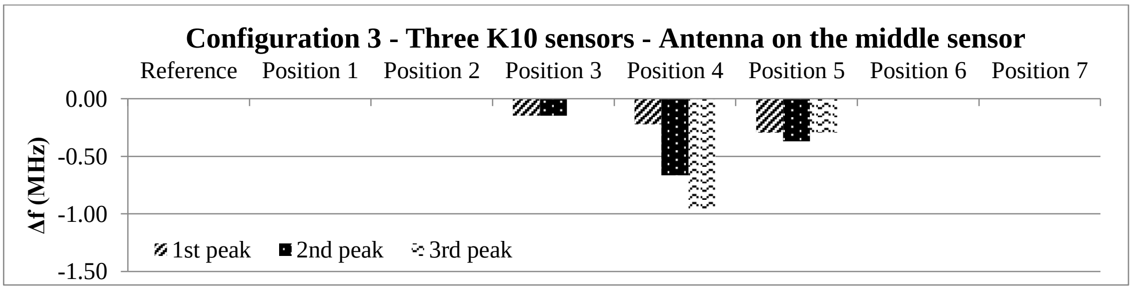

Figure 210 Δf (MHz) for Configuration 3 - Three K10 sensors - Antenna on the middle sensor

In all configurations the presence of structural changes was detected only when it was in the proximity of the middle sensor having the maximum shift in resonant frequency when it was exactly in the middle. Configuration 2 shows the ability to detect the structural change also if the SPES is positioned far from the surface, while configuration 3 denotes the capability to monitor variation on the surface opposite to the interrogated area.

5.6 Conclusions

The design and fabrication of a wireless, passive smart monitoring sensor for potential use in aerospace applications is presented. This simple and cost-effective sensor is based on a resonant circuit, with a spiral metal trace on a dielectric substrate. This configuration allows the sensor to detect the presence of flaws (cracks and delamination) and environmental changes as variation of temperature and humidity by measuring the changes in the resonant response of the SPES device (e.g.: sensor's resonant frequency). Data obtained from the tests exhibited a linear relationship between the resonant frequency of the SPES and the dimensions of the damaged area, with a sensitivity of the SPES of almost ~0.12 MHz /Joule.

The great advantage of the sensing system presented in this work is the ability to monitor different parameters using the same device. The sensor offers also the capability to work either wirelessly interrogated by a loop antenna or wired connected to a device able to detect its resonant response. Moreover, the electro thermal coupling effect of the copper trace was investigated in order to exploit the smart function of the SPES of detect the presence of ice as well as icing condition, and act as an ice protection system (de-icing/anti-icing). Indeed, the electrical resistance variation and the internal Joule heating source provided by the metal trace gives the possibility to reach ~50℃ with a power of ~5W, or up to 20℃ with just ~0.5W. All these characteristics make the SPES a competitive choice in structural health and environmental monitoring for use in the aerospace sector.

6 Concluding Remarks and Future Work

It is not straightforward to get good material properties in the out-of-plane direction using conventional designs of fibre reinforced composites. This limit has resulted in a significant research effort in recent years to provide a basis for new and improved damaged-tolerant structures. Typically, composite reinforcements take the form of unidirectional fibres or bidirectional/ fabric layers. These alternatives offer limited stiffness and strength in the z-direction. Developing new constituents and introducing them for primary load carrying applications in such sensitive industries as aerospace is exceptionally difficult and can take at least a decade, as was the case for current carbon fibre reinforced plastics. Instead, applying modified architectures of existing materials is faster and more straightforward and can lead to better properties in the out-of-plane direction. As reported in Chapter 2, there are numerous examples found in literature for structurally advanced 3D composite with enhanced mechanical properties. Current solutions to create 3-dimensional composites with quasi-isotropic strength and stiffness in all three directions are typically complex, lengthy, expensive, and to the detriment of in-plane properties. If multiple unidirectional plies or fabric layers are used to build up reinforcement in a z-direction, delamination problems can be introduced. Specific solutions, for example involving additional reinforcement stitched through in a z-direction lead to a more complex procedure requiring multiple stages of manufacture.

In this thesis, a new method to manufacture 3D preform through a twisted helical arrangement of fibres is presented. The novel technique is illustrated in Chapter 3 and validated through an experimental campaign reported in Chapter 4. The proposed solution shows enhanced mechanical properties in the out of plane direction, quasi-isotropic behaviour in all directions and a pseudo-ductile behaviour. It is worth nothing that while other techniques for 3D preform require complex equipment and additional stages of manufacturing the presented method can be easily realized making small adjustment to traditional machine used in the textile industries. In addition, the 3D fibres arrangement show good drapability and optimal wettability during resin infusion process. The proposed techniques allow the possibility to extend beyond the use of carbon fibres including within the structure yarn of metal or polymer fibres that can be shaped in the helical twisted arrangement without the need of further manufacturing steps. This will open to a new word of composite, in which many hybrid effect can be realised by blending, such as the use of different materials, or the use of the same material but with different modulus. Therefore, it is envisioned that the outcome of this research will lead to further studies and pave the way for the either the manufacturing of complex parts exploiting its drapability and wetting properties as well as the manufacturing of structural components requiring damage tolerance such as aircraft components (radome, fuselage, leading edge protection, etc.).

Another aspect, which is important to the damage tolerance approach, is a capability to detect damage or defects in structural components before they become a threat to the aircraft safety and performance. Whilst traditional non-destructive techniques have been successfully applied for several decades to detect the structural defects, they require complex sensors array and in the worst scenario to dismount part of the aircraft for inspection. Hence, novel techniques have been considered and investigated in the past decades. A novel sensor for damage detection is presented in Chapter 5. The sensor has shown the ability to detect and evaluate damage in either carbon or glass composite structures. The sensor is chipless and works passively without the need of power source, moreover consisting of a single metal trace on a dielectric substrate can be easily manufactured at low cost using conventional etching techniques. The SPES device has shown great potential also as multi-sensing device and as anti/de-icing device. Therefore, it is intended to validate the use of an array of SPES sensor as a smart-sensing skin to use for composite structures (e.g. aircraft). The following section summarises some of the original contributions, while several proposals for future work are provided in the last section that concludes this thesis.

6.1 Scope for Future Work

To conclude this thesis, a discussion of the future work considering both topics is provided next.

In Chapter 3, the twisted helical fibre arrangement is presented and several parameters of the manufacturing process investigated in order to find the optimal configuration. However, further studies are required to adjust the and setup the modified twisting machine and to get a better understanding of the setup parameters on the preform properties.

In Chapter 4, composite structures based on the novel fibre arrangement were manufactured and tested. Although the performed tests have successfully highlighted the enhanced impact resistance, pseudo-ductile behaviour and quasi isotropic properties further tests are advised for a deep characterization of the proposed fibre architecture. Furthermore, in the same chapter the 3D helical fibre arrangement has been validated for the manufacturing of commercial products: D-Lock and helical-spring. Future works will be addressed to investigated novel design and collect experimental data for process validation.

In Chapter 5, a chipless wireless sensor for SHM was developed and validated for damage detection on carbon and glass fibre composite laminates. The SPES successfully detected and evaluate the extent of delamination areas. In future work, it can be applied to more complex components with other damage types. The sensor will be tested as smart-sensing skin, in which multiple sensors will be distributed as an array and further sensing capabilities will be investigated (pressure, strain, etc.).

Although the novel 3D helical fibre arrangement will lead to produce lighter structure and reduce the safety factors for composite structure, there will still be the need of SHM system to monitor and check the integrity of the structure. This is particularly relevant for sensible sector (such as aerospace). Hence, future work will be focused on the manufacturing of composite structure based on the proposed fibre architecture with the SPES-skin applied. The final structure will allow to thinner and safer structures whilst having a lean manufacturing process.

7 Bibliography

[1] G. Hellard, "Composites in Airbus," Airbus (2008).
[2] E. Phil and C. Soutis, *Polymer composites in the aerospace industry*, Elsevier (2014).
[3] W. Cantwell and J. Morton, "The impact resistance of composite materials—a review," composites 22(5), 347-362 (1991)
[4] K. Dransfield, C. Baillie and Y.-W. Mai, "Improving the delamination resistance of CFRP by stitching—a review," Composites Science and Technology 50(3), 305-317 (1994)
[5] K. A. Dransfield, L. K. Jain and Y.-W. Mai, "On the effects of stitching in CFRPs—I. Mode I delamination toughness," Composites Science and Technology 58(6), 815-827 (1998)
[6] S. Abrate, *Impact on composite structures*, Cambridge university press (2005).
[7] M. Richardson and M. Wisheart, "Review of low-velocity impact properties of composite materials," Composites Part A: Applied Science and Manufacturing 27(12), 1123-1131 (1996)
[8] D. Balageas, *Structural health monitoring*, Wiley Online Library (2006).
[9] C. Farrar, "Historical overview of structural health monitoring," Lecture notes on structural health monitoring using statistical pattern recognition (2001)
[10] M. Celebi, "Seismic instrumentation of buildings (with emphasis on federal buildings)," Special GSA/USGS Project, an administrative report (2002)
[11] W. Staszewski, C. Boller and G. R. Tomlinson, *Health monitoring of aerospace structures: smart sensor technologies and signal processing*, Wiley. com (2004).
[12] M. Lin, X. Qing, A. Kumar and S. J. Beard, "SMART layer and SMART suitcase for structural health monitoring applications," in *SPIE's 8th Annual International Symposium on Smart Structures and Materials*, pp. 98-106, International Society for Optics and Photonics (2001).
[13] F.-K. Chang, *Structural Health Monitoring: The Demands and Challenges: Proceedings of the 3rd International Workshop on Structural Health Monitoring: the Demands and Challenges, Stanford University, Stanford, CA, September 12-14, 2001*, CRC Press (1999).
[14] S. W. Doebling, C. R. Farrar and M. B. Prime, "A summary review of vibration-based damage identification methods," Shock and vibration digest 30(2), 91-105 (1998)
[15] L. H. Baekeland, "The Synthesis, Constitution, and Uses of Bakelite," Industrial & Engineering Chemistry 1(3), 149-161 (1909)
[16] L. P. Biefeld, "Glass fiber strand," Google Patents (1946).
[17] S. Games and J. H. Thomas, "Glass fabric," Google Patents (1938).
[18] J.-K. Kim and Y.-W. Mai, *Engineered interfaces in fiber reinforced composites*, Elsevier (1998).
[19] A. FAA, "AC 20-107B, Composite Aircraft Structure," US Department of Transportation Federal Aviation Administration (2009)
[20] S. R. Reid and G. Zhou, *Impact behaviour of fibre-reinforced composite materials and structures*, Elsevier (2000).
[21] L. Tong, A. P. Mouritz and M. Bannister, *3D fibre reinforced polymer composites*, Elsevier (2002).
[22] R. T. Brown and E. C. Crow Jr, "Automatic through-the-thickness braiding," in *37th International SAMPE Symposium and Exhibition*, pp. 832-842 (1992).
[23] A. Mouritz, K. Leong and I. Herszberg, "A review of the effect of stitching on the in-plane mechanical properties of fibre-reinforced polymer composites," Composites Part A: applied science and manufacturing 28(12), 979-991 (1997)
[24] J. R. Reeder, "Stitching vs. a toughened matrix: compression strength effects," Journal of Composite Materials 29(18), 2464-2487 (1995)
[25] A. Mouritz, M. Bannister, P. Falzon and K. Leong, "Review of applications for advanced three-dimensional fibre textile composites," Composites Part A: applied science and manufacturing 30(12), 1445-1461 (1999)
[26] G. Czél and M. Wisnom, "Demonstration of pseudo-ductility in high performance glass/epoxy composites by hybridisation with thin-ply carbon prepreg," Composites Part A: Applied Science and Manufacturing 52(23-30 (2013)

[27] G. Czél, S. Pimenta, M. R. Wisnom and P. Robinson, "Demonstration of pseudo-ductility in unidirectional discontinuous carbon fibre/epoxy prepreg composites," Composites Science and Technology 106(110-119 (2015)
[28] N. F. Grace, G. Abdel-Sayed and W. F. Ragheb, "Strengthening of concrete beams using innovative ductile fiber-reinforced polymer fabric," ACI Structural Journal 99(5), 692-700 (2002)
[29] N. F. Grace, W. F. Ragheb and G. Abdel-Sayed, "Development and application of innovative triaxially braided ductile FRP fabric for strengthening concrete beams," Composite Structures 64(3), 521-530 (2004)
[30] G. I. Zagainov and G. Lozino-Lozinski, *Composite materials in aerospace design*, Springer Science & Business Media (2012).
[31] L. Nicolais, M. Meo and E. Milella, *Composite materials: a vision for the future*, Springer Science & Business Media (2011).
[32] E. Stover, W. Mark, I. Marfowitz and W. Mueller, "Preparation of an omniweave reinforced carbon-carbon cylinder as a candidate for evaluation in the advanced heat shield screening program," Technical Report AFML TR-70-283 (1971)
[33] C. Mullen and P. Roy, "Fabrication and properties description of Avco 3D carbon–carbon cylindrical composites," in *National SAMPE Symposium*, pp. 11-13 (1972).
[34] F. K. Ko and G. W. Du, "Textile Preforming," in *Handbook of Composites* S. T. Peters, Ed., pp. 397-424, Springer US, Boston, MA (1998).
[35] V. Ogale and R. Alagirusamy, "Textile preforms for advanced composites," Indian Journal of Fibre and Textile Research 29(366-378 (2004)
[36] M. Tsuzuki, "Three-dimensional woven fabric with varied thread orientations," Google Patents (1994).
[37] L. Bryn, M. A. Islam, W. L. Lowery Jr and H. D. Harries III, "Three-dimensional woven forms with integral bias fibers and bias weaving loom," Google Patents (2004).
[38] J. Goering, "Minimum distortion 3D woven preforms," Google Patents (2002).
[39] D. Raymond, "Weft-inserting devices for weaving looms," Google Patents (1957).
[40] D. Marsal and X. Millier, "Method for making a form party by 3d weaving, and resulting form part," Google Patents (2009).
[41] D. N. Betts, H. A. Kim and C. R. Bowen, "Design optimization of stiffness characteristics for bistable composite laminates," 52nd AIAA/ASME/ASCE/AHS/ASC Structures, Structural Dynamics and Materials Conference 19th AIAA/ASME/AHS Adaptive Structures Conference 13t. (2011)
[42] M. H. Mohamed, "Three-dimensional textiles," American Scientist 78(6), 530-541 (1990)
[43] M. A. A. Islam, "Bally Ribbon Mills, Bally, PA, USA," Advances in 3D Textiles 207 (2015)
[44] X. Chen and J. Hearle, "Developments in design, manufacture and use of 3D woven fabrics," in *Proceedings of TEXCOMP9 (International Conference on Textile Composites)* (2008).
[45] N. Khokar, "Second-generation woven profiled 3D fabrics from 3D-weaving," in *Proceedings of the 1st World Conferences in 3D Fabrics and Their Applications* (2008).
[46] X. Chen, *Advances in 3D Textiles*, Elsevier (2015).
[47] B. F. Smith and I. Block, *Textiles in perspective*, Prentice-Hall (1982).
[48] S. Ramakrishna, "Characterization and modeling of the tensile properties of plain weft-knit fabric-reinforced composites," Composites Science and Technology 57(1), 1-22 (1997)
[49] M. McGlockton, B. Cox and R. McMeeking, "A binary model of textile composites: III high failure strain and work of fracture in 3D weaves," Journal of the Mechanics and Physics of Solids 51(8), 1573-1600 (2003)
[50] P. Tan, L. Tong and G. Steven, "Modelling for predicting the mechanical properties of textile composites—A review," Composites Part A: Applied Science and Manufacturing 28(11), 903-922 (1997)
[51] B. Cox, W. Carter and N. Fleck, "A binary model of textile composites—I. Formulation," Acta metallurgica et materialia 42(10), 3463-3479 (1994)

[52] P. Tan, L. Tong, G. Steven and T. Ishikawa, "Behavior of 3D orthogonal woven CFRP composites. Part I. Experimental investigation," Composites Part A: Applied Science and Manufacturing 31(3), 259-271 (2000)
[53] P. Tan, L. Tong and G. P. Steven, "Micromechanics models for mechanical and thermomechanical properties of 3D through-the-thickness angle interlock woven composites," Composites Part A: Applied Science and Manufacturing 30(5), 637-648 (1999)
[54] N. Khokar, *3D-weaving and noobing: characterization of interlaced and non-interlaced 3D fabric forming principles*, Chalmers University of Technology (1997).
[55] N. Khokar, "3D fabric-forming processes: distinguishing between 2D-weaving, 3D-weaving and an unspecified non-interlacing process," Journal of the Textile Institute 87(1), 97-106 (1996)
[56] A. Mouritz and B. Cox, "A mechanistic approach to the properties of stitched laminates," Composites part A: applied science and manufacturing 31(1), 1-27 (2000)
[57] X. Ruan and T.-W. Chou, "Experimental and theoretical studies of the elastic behavior of knitted-fabric composites," Composites Science and Technology 56(12), 1391-1403 (1996)
[58] A. R. Horrocks and S. C. Anand, *Handbook of technical textiles*, Elsevier (2000).
[59] S. K. Batra and B. Pourdeyhimi, *Introduction to nonwovens technology*, DEStech Publications, Inc (2012).
[60] G. S. Bhat, "Nonwovens as three-dimensional textiles for composites," MATERIAL AND MANUFACTURING PROCESS 10(4), 667-688 (1995)
[61] J. W. Sawyer, "Effect of stitching on the strength of bonded composite single lap joints," AIAA journal 23(11), 1744-1748 (1985)
[62] Y. Tada and T. Ishikawa, "Experimental evaluation of the effects of stitching on CFRP laminate specimens with various shapes and loadings," in *Key Engineering Materials*, pp. 305-316, Trans Tech Publ (1989).
[63] D. Holt, "Future composite aircraft structures may be sewn together," Automotive Engineering 90(7), 46-49 (1982)
[64] C. Cacho-Negrete, "Integral composite skin and spar (ICSS) study program," in *AFWAL-TR-82-3053*, Flight Dynamics Laboratory, Wright Aeronautical Laboratories, Wright-Patterson Air Force Base Ohio (1982).
[65] C. Lee and D. Liu, "Tensile strength of stitching joint in woven glass fabrics," Journal of Engineering Materials and Technology 112(2), 125-130 (1990)
[66] D. D. Cartié, G. Dell'Anno, E. Poulin and I. K. Partridge, "3D reinforcement of stiffener-to-skin T-joints by Z-pinning and tufting," Engineering Fracture Mechanics 73(16), 2532-2540 (2006)
[67] G. Dell'Anno, "Effect of tufting on the mechanical behaviour of carbon fabric/epoxy composites," (2007)
[68] P. Deconinck, J. Capelle, V. Bouchart, P. Chevrier and F. Ravailler, "Delamination propagation analysis in tufted carbon fibre-reinforced plastic composites subjected to high-velocity impact," Journal of Reinforced Plastics and Composites 33(14), 1353-1363 (2014)
[69] P. Crothers, K. Drechsler, D. Feltin, I. Herszberg and T. Kruckenberg, "Tailored fibre placement to minimise stress concentrations," Composites Part A: Applied Science and Manufacturing 28(7), 619-625 (1997)
[70] "https://textlnfo.wordpress.com/tag/knitting-needle/."
[71] K. Leong, S. Ramakrishna, Z. Huang and G. Bibo, "The potential of knitting for engineering composites—a review," Composites Part A: applied science and manufacturing 31(3), 197-220 (2000)
[72] S. Ramakrishna and D. Hull, "Energy absorption capability of epoxy composite tubes with knitted carbon fibre fabric reinforcement," Composites Science and Technology 49(4), 349-356 (1993)
[73] S. Ramakrishna, H. Hamada, R. W. Rydin and T. Chou, "Impact damage resistance of knitted glass fiber fabric reinforced polypropylene composites," Science and engineering of composite materials 4(2), 61-72 (1995)
[74] P. Boisse, *Composite reinforcements for optimum performance*, Elsevier (2011).

[75] B. Gommers, I. Verpoest and P. Van Houtte, "Modelling the elastic properties of knitted-fabric-reinforced composites," Composites science and technology 56(6), 685-694 (1996)
[76] S. Huang, R. Richey and E. Deska, "Cross reinforcement in a GR/EP laminate," in *American Society of Mechanical Engineers, Winter Annual Meeting, San Francisco, Calif*, p. 1978 (1978).
[77] V. Tomashevskii, S. Y. Sitnikov, V. Shalygin and V. Yakovlev, "A method of calculating technological regimes of transversal reinforcement of composites with short-fiber microparticles," Mechanics of Composite Materials 25(3), 400-406 (1989)
[78] V. Krasnov, V. Kuznetsov and A. Y. Maksakov, "Automated method of transverse reinforcement of composites by short fibers," Mechanics of Composite Materials 23(3), 356-361 (1987)
[79] G. Frietas, C. Magee, J. Boyce and R. Bott, "Service tough composite structures using z-fiber process," in *Proceedings of the 9th DoD/NASA/FAA conference on fibrous composites, Lake Tahoe, Nevada* (1991).
[80] J. S. Boyce, G. A. Freitas, C. L. Magee, T. M. Fusco, J. J. Harris and E. Kunkel, "Ultrasonic fastening system and method," Google Patents (1998).
[81] I. Partridge, D. D. Cartie and T. Bonnington, "Manufacture and performance of z-pinned composites," Advanced polymeric composites, CRC Press, FL (2003)
[82] I. K. Partridge and S. R. Hallett, "Use of microfasteners to produce damage tolerant composite structures," Phil. Trans. R. Soc. A 374(2071), 20150277 (2016)
[83] P. Chang, A. Mouritz and B. Cox, "Tensile properties and failure mechanisms of z-pinned composite lap joints," Compos Sci Technol 66(2163-2176 (2006)
[84] A. Mouritz, "Review of z-pinned composite laminates," Composites Part A: applied science and manufacturing 38(12), 2383-2397 (2007)
[85] L. Anon, "Z-Pins strengthen the Super Hornet, save weight and cost," The integrator 3(1-2 (2001)
[86] J. Zhang and B. L. Fox, "Manufacturing influence on the delamination fracture behavior of the T800H/3900-2 carbon fiber reinforced polymer composites," Materials and manufacturing processes 22(6), 768-772 (2007)
[87] S.-Y. Fu, X.-Q. Feng, B. Lauke and Y.-W. Mai, "Effects of particle size, particle/matrix interface adhesion and particle loading on mechanical properties of particulate–polymer composites," Composites Part B: Engineering 39(6), 933-961 (2008)
[88] Y. Liu and S. Kumar, "Polymer/carbon nanotube nano composite fibers–a review," ACS applied materials & interfaces 6(9), 6069-6087 (2014)
[89] J. N. Coleman, U. Khan, W. J. Blau and Y. K. Gun'ko, "Small but strong: a review of the mechanical properties of carbon nanotube–polymer composites," Carbon 44(9), 1624-1652 (2006)
[90] M. Holzinger, J. Abraham, P. Whelan, R. Graupner, L. Ley, F. Hennrich, M. Kappes and A. Hirsch, "Functionalization of single-walled carbon nanotubes with (R-) oxycarbonyl nitrenes," Journal of the American Chemical Society 125(28), 8566-8580 (2003)
[91] C. Gao, H. He, L. Zhou, X. Zheng and Y. Zhang, "Scalable functional group engineering of carbon nanotubes by improved one-step nitrene chemistry," Chemistry of Materials 21(2), 360-370 (2008)
[92] M. Holzinger, O. Vostrowsky, A. Hirsch, F. Hennrich, M. Kappes, R. Weiss and F. Jellen, "Sidewall functionalization of carbon nanotubes," Angewandte Chemie International Edition 40(21), 4002-4005 (2001)
[93] T. Hasan, V. Scardaci, P. Tan, A. G. Rozhin, W. I. Milne and A. C. Ferrari, "Stabilization and "debundling" of single-wall carbon nanotube dispersions in N-methyl-2-pyrrolidone (NMP) by polyvinylpyrrolidone (PVP)," The Journal of Physical Chemistry C 111(34), 12594-12602 (2007)
[94] O. Iervolino, F. Pinto, M. Ingram, D. Mattia and M. Meo, "CNT Coating for Multiscale Carbon Fibre Composites," 9th International Conference on Composite Science and Technology: 2020 - Scientific and Industrial Challenges 330-343 (2013)
[95] J. Aveston and A. Kelly, "Tensile first cracking strain and strength of hybrid composites and laminates," Philosophical Transactions of the Royal Society of London A: Mathematical, Physical and Engineering Sciences 294(1411), 519-534 (1980)
[96] A. K. Kaw, *Mechanics of composite materials*, CRC press (2005).

[97] M. Grujicic, B. Pandurangan, K. Koudela and B. Cheeseman, "A computational analysis of the ballistic performance of light-weight hybrid composite armors," Applied Surface Science 253(2), 730-745 (2006)
[98] G. Marom, S. Fischer, F. Tuler and H. Wagner, "Hybrid effects in composites: conditions for positive or negative effects versus rule-of-mixtures behaviour," Journal of Materials Science 13(7), 1419-1426 (1978)
[99] P. Manders and M. Bader, "The strength of hybrid glass/carbon fibre composites," Journal of Materials Science 16(8), 2233-2245 (1981)
[100] Z. Wu, K. Sakamoto, K. Iwashita and Q. Yue, "Hybridization of continuous fiber sheets as structural composites," Journal of the Japan Society for Composite Materials 32(1), 12-21 (2006)
[101] H. Song and Z. Zhang, "Properties of unidirectional hybrid composites, hybrid fiber composites," Beijing: Beijing University of Aeronautics and Astronautics Press (1988).
[102] A. Bunsell and B. Harris, "Hybrid carbon and glass fibre composites," Composites 5(4), 157-164 (1974)
[103] N. Naik, R. Ramasimha, H. Arya, S. Prabhu and N. ShamaRao, "Impact response and damage tolerance characteristics of glass–carbon/epoxy hybrid composite plates," Composites Part B: Engineering 32(7), 565-574 (2001)
[104] F. Sarasini, J. Tirillò, L. Ferrante, M. Valente, T. Valente, L. Lampani, P. Gaudenzi, S. Cioffi, S. Iannace and L. Sorrentino, "Drop-weight impact behaviour of woven hybrid basalt–carbon/epoxy composites," Composites Part B: Engineering 59(204-220 (2014)
[105] A. Dorigato and A. Pegoretti, "Flexural and impact behaviour of carbon/basalt fibers hybrid laminates," Journal of Composite Materials 48(9), 1121-1130 (2014)
[106] F. Sarasini, J. Tirillò, M. Valente, T. Valente, S. Cioffi, S. Iannace and L. Sorrentino, "Effect of basalt fiber hybridization on the impact behavior under low impact velocity of glass/basalt woven fabric/epoxy resin composites," Composites Part A: Applied Science and Manufacturing 47(109-123 (2013)
[107] G. Marom, E. Drukker, A. Weinberg and J. Banbaji, "Impact behaviour of carbon/Kevlar hybrid composites," Composites 17(2), 150-153 (1986)
[108] A. Peijs and J. De Kok, "Hybrid composites based on polyethylene and carbon fibres. Part 6: Tensile and fatigue behaviour," Composites 24(1), 19-32 (1993)
[109] A. Peijs, R. Venderbosch and P. Lemstra, "Hybrid composites based on polyethylene and carbon fibres Part 3: Impact resistant structural composites through damage management," Composites 21(6), 522-530 (1990)
[110] A. Peijs, P. Catsman, L. Govaert and P. Lemstra, "Hybrid composites based on polyethylene and carbon fibres Part 2: influence of composition and adhesion level of polyethylene fibres on mechanical properties," Composites 21(6), 513-521 (1990)
[111] L. Vogelesang, R. Marissen and J. Schijve, "A new fatigue resistant material: Aramide Reinforced Aluminium Laminate (ARALL)," (1981)
[112] J. Gunnink, L. Vogelesang and J. Schijve, "Application of a new hybrid material (ARALL) in aircraft structures," in *Proceedings of the 13th Congress of the International Council of the Aeronautical Sciences (ICAS), Washington*, pp. 990-1000 (1982).
[113] A. Vlot, *Glare: history of the development of a new aircraft material*, Springer Science & Business Media (2001).
[114] A. Vlot, J. Gunnink, R. Alderliesten, W. Van der Hoeven, A. de Boer, W. Hart, C. van Hengel, P. Kuijpers, R. van Oost and G. Roebrocks, "Towards technology readiness of fibre metal laminates- Glare Technology Development(GTO) 1997-2000," in *ACUN- 3 International Composites Conference, Proceedings, Sydney, Australia, Feb. 5-9, 2001, Sydney 2052, Australia, University of New South Wales, 2001*, pp. 243-256 (2001).
[115] E. C. Botelho, R. A. Silva, L. C. Pardini and M. C. Rezende, "A review on the development and properties of continuous fiber/epoxy/aluminum hybrid composites for aircraft structures," Materials Research 9(3), 247-256 (2006)

[116] T. K. Tsotsis, "Interlayer toughening of composite materials," Polymer Composites 30(1), 70 (2009)
[117] R. Krieger Jr, "An adhesive interleaf to reduce stress concentration between plys of structural composites," Advanced Materials Technology'87 279-286 (1987)
[118] W. Hart‘t and L. Ubels, "Impact energy absorbing surface layers for protection of composite aircraft structures," in *8th European conference on composite materials, Naples* (1998).
[119] S. Petit, C. Bouvet, A. Bergerot and J.-J. Barrau, "Impact and compression after impact experimental study of a composite laminate with a cork thermal shield," Composites Science and Technology 67(15), 3286-3299 (2007)
[120] N. Pagano and R. B. Pipes, "The influence of stacking sequence on laminate strength," in *Mechanics of Composite Materials*, pp. 246-254, Springer (1994).
[121] R. F. Gibson, *Principles of composite material mechanics*, CRC press (2011).
[122] J. Tao and C. Sun, "Influence of ply orientation on delamination in composite laminates," Journal of Composite Materials 32(21), 1933-1947 (1998)
[123] F. Pinto, O. Iervolino, G. Scarselli, D. Ginzburg and M. Meo, "Bioinspired twisted composites based on Bouligand structures," pp. 97970E-97970E-97913 (2016).
[124] D. Ginzburg, F. Pinto, O. Iervolino and M. Meo, "Damage tolerance of bio-inspired helicoidal composites under low velocity impact," Composite Structures 161(187-203 (2017)
[125] P. Bradley and S. Harris, "Strategic reinforcement of hybrid carbon fibre-reinforced polymer composites," Journal of Materials Science 12(12), 2401-2410 (1977)
[126] J. S. Paine and C. A. Rogers, "The response of SMA hybrid composite materials to low velocity impact," Journal of Intelligent Material Systems and Structures 5(4), 530-535 (1994)
[127] M. Callens, L. Gorbatikh and I. Verpoest, "Ductile steel fibre composites with brittle and ductile matrices," Composites Part A: Applied Science and Manufacturing 61(235-244 (2014)
[128] M. G. Callens, P. De Cuyper, L. Gorbatikh and I. Verpoest, "Effect of fibre architecture on the tensile and impact behaviour of ductile stainless steel fibre polypropylene composites," Composite Structures 119(528-533 (2015)
[129] M. G. Callens, L. Gorbatikh, E. Bertels, B. Goderis, M. Smet and I. Verpoest, "Tensile behaviour of stainless steel fibre/epoxy composites with modified adhesion," Composites Part A: Applied Science and Manufacturing 69(208-218 (2015)
[130] T. Hayashi, K. Koyama, A. Yamazaki and M. Kihira, "Development of new material properties by hybrid composition," Fukugo Zairyo (composite materials) 1(1), 18-20 (1972)
[131] N. Svensson, R. Shishoo and M. Gilchrist, "Manufacturing of thermoplastic composites from commingled yarns-A review," Journal of Thermoplastic Composite Materials 11(1), 22-56 (1998)
[132] H. Diao, A. Bismarck, P. Robinson and M. Wisnom, "Pseudo-ductile behaviour of unidirectional fibre reinforced polyamide 12 composite by intra-tow hybridization," in *Proceedings of ECCM* (2012).
[133] G. Czél, M. Jalalvand, M. R. Wisnom and T. Czigány, "Design and characterisation of high performance, pseudo-ductile all-carbon/epoxy unidirectional hybrid composites," Composites Part B: Engineering 111(348-356 (2017)
[134] P. Curtis and M. Browne, "Cost-effective high performance composites," Composites 25(4), 273-280 (1994)
[135] H. Saito, M. Morita, K. Kawabe, M. Kanesaki, H. Takeuchi, M. Tanaka and I. Kimpara, "Effect of ply-thickness on impact damage morphology in CFRP laminates," Journal of Reinforced Plastics and Composites 30(13), 1097-1106 (2011)
[136] S. Sihn, R. Y. Kim, K. Kawabe and S. W. Tsai, "Experimental studies of thin-ply laminated composites," Composites Science and Technology 67(6), 996-1008 (2007)
[137] T. Yokozeki, Y. Aoki and T. Ogasawara, "Experimental characterization of strength and damage resistance properties of thin-ply carbon fiber/toughened epoxy laminates," Composite structures 82(3), 382-389 (2008)

[138] T. Yokozeki, A. Kuroda, A. Yoshimura, T. Ogasawara and T. Aoki, "Damage characterization in thin-ply composite laminates under out-of-plane transverse loadings," Composite Structures 93(1), 49-57 (2010)
[139] G. Czél, J. Etches, I. Bond and M. Wisnom, "Development and characterisation of pseudo-ductile hybrid carbon/glass–epoxy composites made of thin spread carbon tows," in *Proceedings of ECCM*.
[140] L. Harper, T. Turner, J. Martin and N. Warrior, "Fiber alignment in directed carbon fiber preforms–a feasibility study," Journal of Composite Materials (2008)
[141] A. Deivasigamani, A. Daliri, C. H. Wang and S. John, "A review of passive wireless sensors for structural health monitoring," Modern Applied Science 7(2), 57 (2013)
[142] K. Diamanti and C. Soutis, "Structural health monitoring techniques for aircraft composite structures," Progress in Aerospace Sciences 46(8), 342-352 (2010)
[143] C. Boller, F.-K. Chang and Y. Fujino, *Encyclopedia of structural health monitoring*, Wiley (2009).
[144] S. Roundy, D. Steingart, L. Frechette, P. Wright and J. Rabaey, "Power sources for wireless sensor networks," in *Wireless sensor networks*, pp. 1-17, Springer (2004).
[145] A. Deivasigamani, A. Daliri, C. H. Wang and S. John, "A Review of Passive Wireless Sensors for Structural Health Monitoring," Modern Applied Science 7(2), p57 (2013)
[146] J. P. Lynch, "A Summary Review of Wireless Sensors and Sensor Networks for Structural Health Monitoring," The Shock and Vibration Digest 38(2), 91-128 (2006)
[147] P. Si, A. P. Hu, S. Malpas and D. Budgett, "A frequency control method for regulating wireless power to implantable devices," Biomedical Circuits and Systems, IEEE Transactions on 2(1), 22-29 (2008)
[148] A. Kurs, A. Karalis, R. Moffatt, J. D. Joannopoulos, P. Fisher and M. Soljačić, "Wireless power transfer via strongly coupled magnetic resonances," science 317(5834), 83-86 (2007)
[149] P. Basset, A. Kaiser, B. Legrand, D. Collard and L. Buchaillot, "Complete system for wireless powering and remote control of electrostatic actuators by inductive coupling," Mechatronics, IEEE/ASME Transactions on 12(1), 23-31 (2007)
[150] C.-S. Wang, G. A. Covic and O. H. Stielau, "Power transfer capability and bifurcation phenomena of loosely coupled inductive power transfer systems," Industrial Electronics, IEEE Transactions on 51(1), 148-157 (2004)
[151] M. Ghovanloo and S. Atluri, "A wide-band power-efficient inductive wireless link for implantable microelectronic devices using multiple carriers," Circuits and Systems I: Regular Papers, IEEE Transactions on 54(10), 2211-2221 (2007)
[152] K. S. Rao, P. V. Nikitin and S. F. Lam, "Antenna design for UHF RFID tags: a review and a practical application," Antennas and Propagation, IEEE Transactions on 53(12), 3870-3876 (2005)
[153] R. K. Mongia and P. Bhartia, "Dielectric resonator antennas—a review and general design relations for resonant frequency and bandwidth," International Journal of Microwave and Millimeter-Wave Computer-Aided Engineering 4(3), 230-247 (1994)
[154] C. A. Grimes, S. C. Roy, S. Rani and Q. Cai, "Theory, instrumentation and applications of magnetoelastic resonance sensors: a review," Sensors (Basel) 11(3), 2809-2844 (2011)
[155] C. A. Grimes, C. S. Mungle, Z. F. Zeng, M. K. Jain, W. R. Dreschel, M. Paulose and K. G. Ong, "Wireless magnetoelastic resonance sensors: A critical review," Sensors 2(7), 294-313 (2002)
[156] A. D. Khazan, *Transducers and their elements: design and application*, PTR Prentice Hall (1994).
[157] M. G. Allen and J. M. English, "System and method for the wireless sensing of physical properties," Google Patents (2000).
[158] K. G. Ong, C. A. Grimes, C. L. Robbins and R. S. Singh, "Design and application of a wireless, passive, resonant-circuit environmental monitoring sensor," Sensors and Actuators A: Physical 93(1), 33-43 (2001)
[159] S. E. Woodard, B. D. Taylor, Q. A. Shams and R. G. Bryant, "Magnetic field response measurement acquisition system," Google Patents (2006).

[160] S. E. Woodard and B. D. Taylor, "Measurement of multiple unrelated physical quantities using a single magnetic field response sensor," Measurement Science and Technology 18(5), 1603-1613 (2007)
[161] S. E. Woodard, "SansEC sensing technology—A new tool for designing space systems and components," in *Aerospace Conference, 2011 IEEE*, pp. 1-11, IEEE (2011).
[162] K. J. Loh, J. P. Lynch and N. A. Kotov, "Passive wireless sensing using SWNT-based multifunctional thin film patches," International Journal of Applied Electromagnetics and Mechanics 28(1), 87-94 (2008)
[163] J. C. Butler, A. J. Vigliotti, F. W. Verdi and S. M. Walsh, "Wireless, passive, resonant-circuit, inductively coupled, inductive strain sensor," Sensors and Actuators A: Physical 102(1–2), 61-66 (2002)
[164] J. Chuang, D. Thomson and G. Bridges, "Embeddable wireless strain sensor based on resonant RF cavities," Review of scientific instruments 76(9), 094703 (2005)
[165] Y. Jia, K. Sun, F. J. Agosto and M. T. Quinones, "Design and characterization of a passive wireless strain sensor," Measurement Science and Technology 17(11), 2869 (2006)
[166] W. Wilson, D. Malocha, N. Kozlovski, D. Gallagher, B. Fisher, J. Pavlina, N. Saldanha, D. Puccio and G. Atkinson, "Orthogonal frequency coded SAW sensors for aerospace SHM applications," Sensors Journal, IEEE 9(11), 1546-1556 (2009)
[167] W. C. Wilson, D. F. Perey, G. M. Atkinson and R. O. Barclay, "Passive wireless SAW sensors for IVHM," in *Frequency Control Symposium, 2008 IEEE International*, pp. 273-277, IEEE (2008).
[168] U. Tata, H. Huang, R. Carter and J. Chiao, "Exploiting a patch antenna for strain measurements," Measurement Science and Technology 20(1), 015201 (2009)
[169] A. Daliri, A. Galehdar, S. John, W. Rowe and K. Ghorbani, "Circular microstrip patch antenna strain sensor for wireless structural health monitoring," in *Proceedings of the World Congress on Engineering* (2010).
[170] A. Daliri, A. Galehdar, W. S. Rowe, K. Ghorbani and S. John, "Utilising microstrip patch antenna strain sensors for structural health monitoring," Journal of Intelligent Material Systems and Structures 23(2), 169-182 (2012)
[171] X. Yi, T. Wu, Y. Wang, R. T. Leon, M. M. Tentzeris and G. Lantz, "Passive wireless smart-skin sensor using RFID-based folded patch antennas," International Journal of Smart and Nano Materials 2(1), 22-38 (2011)
[172] D. Watters, P. Jayaweera, A. Bahr and D. Huestis, "Design and performance of wireless sensors for structural health monitoring," in *AIP Conference Proceedings*, pp. 969-976, IOP INSTITUTE OF PHYSICS PUBLISHING LTD (2002).
[173] X. Yi, C. Cho, C.-H. Fang, J. Cooper, V. Lakafosis, R. Vyas, Y. Wang, R. Leon and M. Tentzeris, "Wireless strain and crack sensing using a folded patch antenna," in *Antennas and Propagation (EUCAP), 2012 6th European Conference on*, pp. 1678-1681, IEEE (2012).
[174] T. Chen, S. Li and H. Sun, "Metamaterials application in sensing," Sensors 12(3), 2742-2765 (2012)
[175] T. J. Cui, D. R. Smith and R. Liu, *Metamaterials: theory, design, and applications*, Springer (2009).
[176] R. Singh, C. Rockstuhl and W. Zhang, "Strong influence of packing density in terahertz metamaterials," Applied Physics Letters 97(24), 241108 (2010)
[177] R. Melik, E. Unal, N. K. Perkgoz, C. Puttlitz and H. V. Demir, "Metamaterial-based wireless strain sensors," Applied Physics Letters 95(1), 011106 (2009)
[178] R. Matsuzaki and A. Todoroki, "Wireless detection of internal delamination cracks in CFRP laminates using oscillating frequency changes," Composites science and technology 66(3), 407-416 (2006)
[179] R. Matsuzaki, M. Melnykowycz and A. Todoroki, "Antenna/sensor multifunctional composites for the wireless detection of damage," Composites Science and Technology 69(15–16), 2507-2513 (2009)
[180] A. A. Nassr and W. W. El-Dakhakhni, "Non-destructive evaluation of laminated composite plates using dielectrometry sensors," Smart Materials and Structures 18(5), 055014 (2009)

[181] C. H. Singer, E.J. Hall, A.R. (Eds.), *A History of Technology (Volumes 1. 3, 4 & 5)*, Published by Oxford Clarendon Press, 1957.
[182] E. Mackay, "Note on a New Tomb (No. 260) at Drah Abu'l Naga, Thebes," The Journal of Egyptian Archaeology 3(2/3), 125-126 (1916)
[183] H. A. McKenna, J. W. Hearle and N. O'Hear, *Handbook of fibre rope technology*, Elsevier (2004).
[184] M. J. Denton and P. N. Daniels, *Textile terms and definitions*, Textile Institute (2002).
[185] BSI, "BS EN ISO 1968:2004," in *Fibre ropes and cordage. Vocabulary*, BSI (22 November 2004).
[186] A. S. o. C. E. T. C. o. M. F. Rope, *Glossary of Marine Fiber Rope Terms: A Report of the Task Committee on Marine Fiber Rope of the Waterway, Port, Coastal and Ocean Division of the American Society of Civil Engineers*, The Society (1993).
[187] N. Pan and D. Brookstein, "Physical properties of twisted structures. II. Industrial yarns, cords, and ropes," Journal of applied polymer science 83(3), 610-630 (2002)
[188] R. Zhang, Y. Zhang, Q. Zhang, H. Xie, W. Qian and F. Wei, "Growth of half-meter long carbon nanotubes based on Schulz–Flory distribution," ACS nano 7(7), 6156-6161 (2013)
[189] T. C. Fitzgibbons, M. Guthrie, E.-s. Xu, V. H. Crespi, S. K. Davidowski, G. D. Cody, N. Alem and J. V. Badding, "Benzene-derived carbon nanothreads," Nature materials 14(1), 43-47 (2015)
[190] W. Oxenham, "The mechanics of wool structures R. Postle, GA Carnaby and S. de Jong, Ellis Horwood, Chichester, 1988. pp. 462, price£ 59.50. ISBN 0-7458-0322-9," British Polymer Journal 21(3), 279-279 (1989)
[191] J. W. Hearle, P. Grosberg and S. Backer, "Structural mechanics of fibers, yarns, and fabrics," (1969)
[192] J. W. Hearle, *Mechanics of flexible fibre assemblies*, Kluwer Academic Publishers (1980).
[193] P. Schwartz, *Structure and mechanics of textile fibre assemblies*, Elsevier (2008).
[194] G. Galilei, *Dialogues concerning two new sciences*, Dover (1914).
[195] D. Du Monceau, *Traité de la fabrique des manoeuvres pour les vaisseaux: ou, L'art de la corderie perfectionné*, chez Desaint (1769).
[196] "ISO 2:1973 Textiles," in *Designation of the direction of twist in yarns and related products, 1973*, International Organization for Standardization (ISO).
[197] PKM, "Yarn_twist.png," Y. t. S.-L. Z-Right.png, Ed., pp. "Twist" in spun yarns or ropes is often labeled Z-twist or Z-laid (for right-handed twist), S-twist or S-laid (for left-handed twist) due to the respective right and left slants of the central sections of those two letters. To visually determine the handedness of the twist of a rope/yarn/etc, sight down a length of it; the direction of the twists as they progress away from you, left or right, reveals their handedness., https://commons.wikimedia.org/wiki/File:Yarn_twist.png (2007).
[198] D. U. Shah, P. J. Schubel, P. Licence and M. J. Clifford, "Determining the minimum, critical and maximum fibre content for twisted yarn reinforced plant fibre composites," Composites Science and Technology 72(15), 1909-1917 (2012)
[199] D. Shah, P. Schubel, M. Clifford, P. Licence and N. Warrior, "Yarn optimisation and plant fibre surface treatment using hydroxyethylcellulose for the development of structural bio-based composites," in *18th International Conference on Composite Materials (ICCM-18)* (2011).
[200] P. Boisse, *Advances in Composites Manufacturing and Process Design*, Woodhead Publishing (2015).
[201] S. Mazumdar, *Composites manufacturing: materials, product, and process engineering*, CrC press (2001).
[202] M. Datasheet, "Araldite® LY 5052 / Aradur® 5052 datasheet."
[203] A. S. D. o. M. Properties, "Standard test methods for flexural properties of unreinforced and reinforced plastics and electrical insulating materials," American Society for Testing Materials (1997).
[204] B. Standard, "BS EN ISO 179-1:2010 Plastics. Determination of Charpy impact properties. Non-instrumented impact test," (2010)

[205] N. Naik and R. Kuchibhotla, "Analytical study of strength and failure behaviour of plain weave fabric composites made of twisted yarns," Composites Part A: Applied Science and Manufacturing 33(5), 697-708 (2002)
[206] J. R. Kaufmann, "Industrial applications of multiaxial warp knit composites," ACS Publications (1991).
[207] J. Hu, *3-D fibrous assemblies: properties, applications and modelling of three-dimensional textile structures*, Elsevier (2008).
[208] A. Standard, "D790 (2010) Standard test methods for flexural properties of unreinforced and reinforced plastics and electrical insulating materials," ASTM International, West Conshohocken (2010)
[209] N. Xu, S. Rangwala, K. K. Chintalapudi, D. Ganesan, A. Broad, R. Govindan and D. Estrin, "A wireless sensor network for structural monitoring," in *Proceedings of the 2nd international conference on Embedded networked sensor systems*, pp. 13-24, ACM (2004).
[210] J. Yick, B. Mukherjee and D. Ghosal, "Wireless sensor network survey," Computer networks 52(12), 2292-2330 (2008)
[211] Z. Chen and C. Lu, "Humidity sensors: a review of materials and mechanisms," Sensor letters 3(4), 274-295 (2005)
[212] L. Ruiz-Garcia, L. Lunadei, P. Barreiro and I. Robla, "A review of wireless sensor technologies and applications in agriculture and food industry: state of the art and current trends," Sensors 9(6), 4728-4750 (2009)
[213] J. F. Straube, "Moisture in Buildings," ASHRAE Journal 1 (2002)
[214] M. HODGSON, "Low relative humidity and aircraft cabin air quality," Indoor Air 11(3), 200-214 (2001)
[215] G. Scholz, "Marktanalyse: Sensoren und Meßgeräte für Gasfeuchte/Market analysis: Sensors and instruments for gas humidity," tm-Technisches Messen 59(3), 88-109 (1992)
[216] Y. Kanamori, E. Itoh and K. Miyairi, "Improvement of sensitivity and response speed of capacitive type humidity sensor using partially fluorinated polyimide thin film," Molecular Crystals and Liquid Crystals 472(1), 327/[717]-335/[725] (2007)
[217] C. Wang, K. L. Dudley and G. N. Szatkowski, "Open Circuit Resonant (SansEC) Sensor for Composite Damage Detection and Diagnosis in Aircraft Lightning Environments," in *4th AIAA Atmospheric and Space Environments Conference* (2012).
[218] J. J. Mielnik Jr, "Open Circuit Resonant Sensors for Composite Damage Detection and Diagnosis," (2011)
[219] A. Oprea, J. Courbat, N. Bârsan, D. Briand, N. De Rooij and U. Weimar, "Temperature, humidity and gas sensors integrated on plastic foil for low power applications," Sensors and Actuators B: Chemical 140(1), 227-232 (2009)
[220] A. D. DeHennis and K. D. Wise, "A wireless microsystem for the remote sensing of pressure, temperature, and relative humidity," Microelectromechanical Systems, Journal of 14(1), 12-22 (2005)
[221] Y. Wang, Y. Jia, Q. Chen and Y. Wang, "A passive wireless temperature sensor for harsh environment applications," Sensors 8(12), 7982-7995 (2008)
[222] W. Qu and W. Wlodarski, "A thin-film sensing element for ozone, humidity and temperature," Sensors and Actuators B: Chemical 64(1), 42-48 (2000)
[223] Q.-Y. Ren, J.-Q. Huang, L.-F. Wang, S. Wan, L.-T. Sun and Q.-A. Huang, "Temperature Sensing Properties of the Passive Wireless Sensor Based on Graphene Oxide Films,"
[224] C. Wang and B. D. Taylor, "SansEC temperature sensor for tire safety monitoring application," in *Future of Instrumentation International Workshop (FIIW), 2011*, pp. 146-149, IEEE (2011).
[225] C. Neagu, H. Jansen, A. Smith, J. Gardeniers and M. Elwenspoek, "Characterization of a planar microcoil for implantable microsystems," Sensors and Actuators A: Physical 62(1), 599-611 (1997)
[226] G. Klysz, J.-P. Balayssac, X. Dérobert and C. Aubagnac, "Evaluation of cover concrete by coupling some non-destructive techniques—Contribution of in-situ measurements," in *NDT-CE conf., Berlin* (2003).

[227] U.-M. Jow and M. Ghovanloo, "Design and optimization of printed spiral coils for efficient transcutaneous inductive power transmission," Biomedical Circuits and Systems, IEEE Transactions on 1(3), 193-202 (2007)
[228] S. Roleson, "Benchtop EMC testing techniques for medical equipment," Computer Standards & Interfaces 20(6), 483 (1999)
[229] J. Melcher, Y. Deben and G. Arlt, "Dielectric effects of moisture in polyimide," Electrical Insulation, IEEE Transactions on 24(1), 31-38 (1989)
[230] A. R. Ralston, C. F. Klein, P. E. Thoma and D. D. Denton, "A model for the relative environmental stability of a series of polyimide capacitance humidity sensors," Sensors and Actuators B: Chemical 34(1), 343-348 (1996)
[231] G. Zumpano and M. Meo, "Damage detection in an aircraft foam sandwich panel using nonlinear elastic wave spectroscopy," Computers & structures 86(3), 483-490 (2008)
[232] U. Polimeno and M. Meo, "Detecting barely visible impact damage detection on aircraft composites structures," Composite Structures 91(4), 398-402 (2009)
[233] M. Meo, A. Morris, R. Vignjevic and G. Marengo, "Numerical simulations of low-velocity impact on an aircraft sandwich panel," Composite Structures 62(3), 353-360 (2003)
[234] M. Alves, C. Chaves and R. S. Birch, "Impact on aircraft," in *Proceedings of the XVII Brazilian Congress of Mechanical Engineering* (2003).
[235] M. Hallikainen, "Dielectric properties of sea ice at microwave frequencies," NASA STI/Recon Technical Report N 78(11293 (1977)